

Methane stable carbon isotope dynamics spanning the Last Deglaciation

by

Joe R. Melton

B.Sc., University of Calgary, 2002

M.Sc., University of Calgary, 2004

A Dissertation Submitted in Partial Fulfillment  
of the Requirements for the Degree of

DOCTOR OF PHILOSOPHY

in the School of Earth and Ocean Sciences

© Joe R. Melton, 2009

University of Victoria

All rights reserved. This thesis may not be reproduced in whole or in part, by photocopy or other means, without the permission of the author.

Methane stable carbon isotope dynamics spanning the Last Deglaciation

by

Joe R. Melton

B.Sc, University of Calgary, 2002

M.Sc., University of Calgary, 2004

Supervisory Committee

Michael J. Whiticar (School of Earth and Ocean Sciences)

**Supervisor**

Ken Denman (Canadian Centre for Climate Modelling and Analysis)

**Departmental Member**

Andrew Weaver (School of Earth and Ocean Sciences)

**Departmental Member**

Dan Smith (Department of Geography)

**Outside Member**

Jed O. Kaplan (Ecole Polytechnique Fédéral de Lausanne)

**Additional Member**

## Abstract

Supervisory Committee

Michael J. Whiticar (School of Earth and Ocean Sciences)

**Supervisor**

Ken Denman (Canadian Centre for Climate Modelling and Analysis)

**Departmental Member**

Andrew Weaver (School of Earth and Ocean Sciences)

**Departmental Member**

Dan Smith (Department of Geography)

**Outside Member**

Jed O. Kaplan (Ecole Polytechnique Fédéral de Lausanne)

**Additional Member**

Polar ice core records reveal atmospheric methane mixing ratios ( $[\text{CH}_4]$ ) changing slowly over time scales the length of glacial-interglacial cycles, and also rapidly over a few decades. Measurement of the  $\delta^{13}\text{CH}_4$  value of gases entrained in glacial ice can help identify the sources of the observed  $[\text{CH}_4]$  changes.

To facilitate these measurements, an improved on-line extraction and continuous flow isotope ratio mass spectrometer (CF-IRMS) method was developed. Samples of outcropping ablation-zone ice from Pâkitsoq, Greenland were measured for  $\delta^{13}\text{CH}_4$  over the Last Glacial Maximum (LGM) to the Preboreal period (PB).

CF-IRMS measurement of the Pâkitsoq samples revealed an irregular, spot contamination consisting of elevated  $[\text{CH}_4]$  in the interstitial air, likely due to in-situ methanogenesis. All samples were then filtered to reject contaminated samples by comparison against contemporaneous  $[\text{CH}_4]$  from the GISP2 ice core. The filtered samples show more  $^{13}\text{C}$ -enriched  $\delta^{13}\text{CH}_4$  values during cold climatic periods, as well as a

potential shift to more  $^{13}\text{C}$ -enriched  $\delta^{13}\text{CH}_4$  values across the densely sampled Younger Dryas termination.

Interpretation of the stable time periods of the filtered record is aided by a data-constrained 4-box steady-state atmospheric  $\text{CH}_4$  model run in Monte Carlo mode. From the box model results, tropical wetlands show relatively consistent  $\text{CH}_4$  flux across all time periods except the YD. The cold, dry climates of the LGM and YD decreased wetland  $\text{CH}_4$  flux, however the LGM flux is likely compensated (increased) by the additional wetland area available on the exposed continental shelves. Boreal wetlands are an important source of  $^{13}\text{C}$ -depleted  $\text{CH}_4$  during warm periods, and their flux is likely predominantly from thermokarst lakes. Biomass burning  $\text{CH}_4$  flux increases throughout the deglaciation with fluxes in the Preboreal comparable to present-day. Gas hydrate releases indicate terrestrial hydrates are potentially more important than marine hydrates during the deglaciation.

The Pákitsoq  $\delta^{13}\text{CH}_4$  record of the abrupt YD termination suggests that the primary sources responsible for the initial  $[\text{CH}_4]$  increase were a mixture of biomass burning (~40%) and a boreal wetlands source (~60%), most likely thermokarst lakes. Perhaps surprisingly, this analysis found no important role for biogenic gas hydrates, or tropical wetlands, in the YD termination  $[\text{CH}_4]$  increase.

## Table of Contents

Title Page.....	ii
Abstract.....	iii
Table of Contents.....	v
List of Tables.....	vii
List of Figures.....	viii
Table of Acronyms and Abbreviations.....	xi
Acknowledgments.....	xii
Dedication.....	xiv
1.Introduction.....	1
1.1.The ice core record of atmospheric methane .....	2
1.2.Ice core studies of methane stable isotope dynamics.....	6
1.3.Research Objectives / Thesis Outline.....	11
1.4.Study sites.....	14
1.4.1.Påkitsoq, Greenland.....	14
1.4.2.GISP2, Greenland.....	16
2.Methods.....	17
2.1.Extraction line and isotope ratio mass spectrometer method.....	17
2.1.1.Experimental procedures.....	18
2.1.2.Post-combustion trapping.....	22
2.1.3.Methane concentration from the CF-IRMS.....	24
2.1.4.Instrumental setup performance.....	25
2.1.5.Further notes.....	29
2.2.Age scale.....	31
2.3.Corrections to isotope values.....	37
2.3.1.Gravitational and thermal fractionation correction .....	38
2.3.2.Firn diffusion correction .....	39
2.3.3.Atmosphere disequilibrium.....	40
2.4.Atmospheric box model Monte Carlo simulations.....	42
2.4.1.Description of 4-Box atmospheric model.....	42
3.Results.....	52
3.1.GISP2 $\delta^{13}\text{CH}_4$ measurements.....	52
3.2.Contaminated and compromised samples.....	54
3.3.Measurements spanning the LGM to Preboreal period.....	64
3.3.1. $\delta^{13}\text{CH}_4$ measurements for the most recent deglaciation.....	64
3.3.2.Younger Dryas – Preboreal transition.....	65
3.3.3.Younger Dryas Cold Interval.....	69
3.3.4.Oldest Dryas – Bølling transition.....	71
3.3.5.Time-slice observations.....	74
3.4.Box model Monte Carlo simulations.....	76
3.4.1.Modern Simulation .....	76
3.4.2.4-Box model simulation results across all time periods.....	77

3.4.3.Sensitivity tests.....	89
4.Discussion.....	95
4.1.Sources of contamination.....	95
4.2.Critique of Monte Carlo box model simulations.....	100
4.3.The $\delta^{13}\text{CH}_4$ record for the most recent deglaciation.....	102
4.3.1.Boreal Wetlands .....	105
4.3.2.Thermocarst Lakes.....	108
4.3.3.Tropical Wetlands.....	111
4.3.4.Gas Hydrates.....	116
4.3.5.Geologic Methane (GEM).....	121
4.3.6.Biomass burning.....	124
4.3.7.Ruminants.....	126
4.3.8.Aerobic Plant Methane (APM).....	126
4.3.9. $\text{CH}_4$ Atmospheric Lifetime.....	127
4.4.The Bølling-Allerød period $\delta^{13}\text{CH}_4$ record.....	129
4.5.The termination of the Younger Dryas.....	133
5.Conclusions.....	143
6.References.....	147
7.Appendix.....	161
7.1.Age scale tie points.....	161
7.2.Box model parameters.....	164
7.2.1.6-Box model description.....	164
7.2.2.4-Box model parameters.....	166
7.2.3.4-Box Model Algorithm.....	169
7.3.Ice core $\delta^{13}\text{CH}_4$ ratio measurement data.....	181

## List of Tables

Table 2.3.1: Parameters used as input for firn diffusion model.....	39
Table 2.4.1: Isotopic fractionation values for the three sink terms.....	46
Table 2.4.2: Box model stable time periods for Monte Carlo simulations.....	47
Table 2.4.3: Mean $\delta^{13}\text{CO}_2$ values for stable time periods simulated with atmospheric box model.....	49
Table 2.4.4: Source methane flux and stable isotope ratios for the 1990s simulation. ....	50
Table 3.2.1: Estimated uncertainties in comparison of CF-IRMS-derived $[\text{CH}_4]$ measurements to GISP2 $[\text{CH}_4]$ measurements.....	59
Table 3.3.1: Stable time period $\text{CH}_4$ observations.....	75
Table 3.4.1: Methane atmospheric lifetimes determined by 4-box atmosphere model Monte Carlo simulations. ....	79
Table 3.4.2: Results from the 4-box model, run as single simulation, for each time stable time period .....	80
Table 3.4.3: Monte Carlo 4-box model simulated $\text{CH}_4$ flux for hemisphere boxes and global total for all time periods investigated.....	81
Table 4.3.1: Summary of model studies, for both forward and inverse models, of the global wetland flux through different time periods.....	115
Table 4.5.1: Fractional contribution of each end-member of the 5 possible sources that could have contributed, along with biomass burning, to the $[\text{CH}_4]$ rise at the termination of the Younger Dryas. ....	138
Table 7.1.1: Age tie points for the Allerød to Preboreal period for the 2001 sampling trench.....	161
Table 7.1.2: Age tie points for the LGM to Allerød period for the 2003 to 2005 sampling trenches.....	162
Table 7.2.1: Air mass exchange rates between compartments of atmosphere 6-box model. ....	165
Table 7.2.2: Air mass exchange rates between compartments of atmosphere 4-box model. ....	166
Table 7.2.3: Source and sink distribution parameters for 4-box atmosphere methane model scenarios of 1990s .....	166
Table 7.2.4: 4-Box model simulation parameters for all time periods.....	167
Table 7.3.1: $\delta^{13}\text{CH}_4$ measurement values for samples from GISP2 core #139.....	181
Table 7.3.2: Complete Pákitsoq CF-IRMS measurement results.....	181
Table 7.3.3: Final results for Pákitsoq ice measurements of $\delta^{13}\text{CH}_4$ . ....	187

## List of Figures

Figure 1.1.1: Methane atmospheric concentrations from the Northern Hemisphere and the Southern Hemisphere with reconstructed temperature difference, relative to the average temperature of the last 1000 years, at the EPICA Dome C, Antarctica drilling site.....	2
Figure 1.2.1: Combination $\delta^{13}\text{CH}_4$ and $\delta\text{D-CH}_4$ plot for the major sources of $\text{CH}_4$ to the atmosphere.....	7
Figure 1.2.2: 2000 year record of $\delta^{13}\text{CH}_4$ , $\delta\text{D-CH}_4$ and $[\text{CH}_4]$ .....	9
Figure 1.3.1: $\delta^{13}\text{CH}_4$ , $\delta\text{D-CH}_4$ and $[\text{CH}_4]$ records spanning the most recent deglaciation.	11
Figure 1.3.2: Map of GISP2 drilling site, Pákitsoq snow deposition site and general flow path to Pákitsoq outcrop on the western Greenland margin.....	13
Figure 1.4.1: Cartoon of ice-sheet cross-section.....	14
Figure 1.4.2: Physical location of the Pákitsoq sampling site from the south.....	15
Figure 2.1.1: Schematic of CF-IRMS instrumental extraction and pre-concentration setup.....	22
Figure 2.1.2: Example mass spectrogram of a 10 ml sample of atmospheric air run through the setup of Schaefer and Whiticar (2007).....	25
Figure 2.1.3: Example mass spectrogram of an 8 ml sample of atmospheric air run through the instrumental set-up described here.....	27
Figure 2.2.1: Subset of Siple Dome $\delta^{18}\text{O}_{\text{atm}}$ dataset corrected for both gravitational and gas-loss fractionation .....	33
Figure 2.2.2: Example age tie-points for calendar age to Pákitsoq trench distance.....	34
Figure 2.3.1: Difference in age scale between Schaefer et al. (2006) and this work for the Schaefer et al. (2006) data.....	37
Figure 2.3.2: Younger Dryas - Preboreal transition methane isotope corrections for thermal, gravitational, and firn diffusional fractionation.....	40
Figure 2.4.1: Schematic of 6-box atmospheric methane model.....	42
Figure 2.4.2: 4-box model of atmosphere methane cycle.....	43
Figure 3.2.1: Pákitsoq IRMS-inferred $[\text{CH}_4]$ plotted against the contemporaneous GISP2 $[\text{CH}_4]$ .....	54
Figure 3.2.2: Pákitsoq methane concentration (as measured by GC-FID at OSU) versus GISP2 methane concentration for contemporaneous air.....	55
Figure 3.2.3: Pákitsoq $[\text{CH}_4]$ measured at OSU across 5 sampling seasons plotted on the same horizontal trench scale.....	56
Figure 3.2.4: Pákitsoq $\delta^{15}\text{N}$ of $\text{N}_2$ measured at Scripps Institute of Oceanography (SIO).	57
Figure 3.2.5: Histogram of the offset between the Pákitsoq IRMS-derived methane concentration and the contemporaneous GISP2 concentration.....	61
Figure 3.2.6: Pákitsoq IRMS-inferred $[\text{CH}_4]$ plotted against the contemporaneous GISP2 $[\text{CH}_4]$ . Also plotted are the boundaries of the upper and lower 100 ppbv filter.....	62
Figure 3.3.1: Pákitsoq $\delta^{13}\text{CH}_4$ and $\text{CH}_4$ concentration for the LGM to Preboreal time period .....	64
Figure 3.3.2: Pákitsoq $\delta^{13}\text{CH}_4$ and $\text{CH}_4$ concentration record during the transition of the Younger Dryas to the Preboreal.....	65

Figure 3.3.3: Abrupt temperature anomaly as recorded in the $\delta^{15}\text{N}$ values from the GISP2 core .....	67
Figure 3.3.4: Pákitsoq $\delta^{13}\text{CH}_4$ record from this work and Schaefer et al. (2006).....	68
Figure 3.3.5: Disequilibrium correction applied to the YD - Preboreal transition $\delta^{13}\text{CH}_4$ , $\delta\text{D-CH}_4$ and $[\text{CH}_4]$ values.....	69
Figure 3.3.6: The Younger Dryas Cold Interval methane concentration and $\delta^{13}\text{CH}_4$ from Pákitsoq.....	70
Figure 3.3.7: The Younger Dryas cold interval $\delta^{13}\text{CH}_4$ and $\text{CH}_4$ mixing ratio.....	71
Figure 3.3.8: The Oldest Dryas - Bølling transition $\delta^{13}\text{CH}_4$ and methane concentration record from Pákitsoq, Greenland.....	72
Figure 3.3.9: Oldest Dryas to Bølling transition $\delta^{13}\text{CH}_4$ record from Pákitsoq, Greenland and EDML, Antarctica.....	73
Figure 3.4.1: Monte Carlo box model simulation results for 1990s scenario.....	77
Figure 3.4.2: Probability distribution of atmospheric methane lifetime for the 6 time periods.....	78
Figure 3.4.3: Monte Carlo box model simulated $\text{CH}_4$ flux from the Northern and Southern Hemisphere across all time periods investigated.....	81
Figure 3.4.4: 4-Box model Monte Carlo simulation results for source strength over the stable time periods investigated.....	82
Figure 3.4.5: Normalized probability distribution of tropical wetland methane flux across all time periods.....	83
Figure 3.4.6: Normalized probability distribution of boreal wetland methane flux across all time periods.....	83
Figure 3.4.7: Normalized probability distribution of aerobic plant methane (APM) flux across all time periods.....	85
Figure 3.4.8: Normalized probability distribution of biomass burning methane flux across all time periods.....	85
Figure 3.4.9: Normalized probability distribution of biogenic marine gas hydrate methane flux across all time periods.....	87
Figure 3.4.10: Normalized probability distribution of ruminant methane flux across all time periods.....	88
Figure 3.4.11: Normalized probability distribution of geologic methane (GEM) flux across all time periods.....	88
Figure 3.4.12: Normalized probability distributions of sensitivity tests for 4-Box Monte Carlo model.....	90
Figure 3.4.13: Normalized probability distributions of sensitivity tests for 4-Box Monte Carlo model.....	91
Figure 3.4.14: Sensitivity test for the effect of a marine versus terrestrial hydrate source $\delta\text{D-CH}_4$ value across all time periods.....	94
Figure 4.3.1: $\delta^{13}\text{CH}_4$ , $\delta\text{D-CH}_4$ and $\text{CH}_4$ concentration records spanning the LGM through the Holocene.....	104
Figure 4.3.2: Continental ice sheet extents for the LGM, Bølling, and Preboreal time periods.....	105
Figure 4.3.3: Plot of 1) $\delta^{13}\text{CH}_4$ , 2) thermokarst $^{14}\text{C}$ basal initiation dates, 3) number of thermokarst $^{14}\text{C}$ basal initiation dates binned every 500 years, 4) boreal peatland $^{14}\text{C}$ basal initiation dates, 5) number of boreal peatland $^{14}\text{C}$ basal initiation dates binned	

every 500 years, 6) inter-polar gradient (IPG) of [CH <sub>4</sub> ], and 7) CH <sub>4</sub> concentration data. .....	110
Figure 4.3.4: Collected global records of moisture and temperature. ....	113
Figure 4.3.5: Map of exposed continental shelf at the YD and LGM.....	114
Figure 4.3.6: Exposed continental shelf during the LGM.....	120
Figure 4.3.7: Map of present day onshore and marine seeps of geologic methane.....	122
Figure 4.4.1: Uncertainty envelopes for the δ <sup>13</sup> CH <sub>4</sub> record spanning the Oldest Dryas to Bølling transition.....	129
Figure 4.4.2: Uncertainty envelopes for the δ <sup>13</sup> CH <sub>4</sub> record spanning the LGM to the start of the Holocene.....	130
Figure 4.5.1: Uncertainty envelopes for the δ <sup>13</sup> CH <sub>4</sub> record over the transition from the Younger Dryas to the Preboreal period.....	133
Figure 4.5.2: Combination δ <sup>13</sup> CH <sub>4</sub> and δD-CH <sub>4</sub> for the major sources of methane to the atmosphere, and the calculated value of the source responsible for the YD-Preboreal transition CH <sub>4</sub> increase.....	139

### Table of Acronyms and Abbreviations

APM	Aerobic Plant Methane
BA	Bølling-Allerød
BB	Box model sensitivity test with a biomass burning $\delta^{13}\text{CH}_4$ value of -20 ‰
BP	Before 1950 A.D.
DCH	Diffusive Column Height
FEN	Box model sensitivity test using a fen wetland $\delta^{13}\text{CH}_4$ value
FID	Flame Ionization Detector
G-25	Box model sensitivity test with a GEM $\delta^{13}\text{CH}_4$ value of -25 ‰
G-50	Box model sensitivity test with a GEM $\delta^{13}\text{CH}_4$ value of -50 ‰
GC	Gas Chromatography
GCM	General Circulation Model
GEM	Geologic Emissions of Methane
IPG	Inter-Polar Gradient
ka	1000 years
LGM	Last Glacial Maximum
$\text{IN}_2$	Liquid Nitrogen
MWP-1A	Meltwater Pulse 1A
NH	Northern Hemisphere
NPD	Normalized Probability Distribution
o.d.	Outer diameter
OD-B	Oldest Dryas – Bølling
PB	Preboreal
PIH	Preindustrial Holocene
PLOT	Porous layer open tubular
ppbv	Parts per billion by volume
SH	Southern Hemisphere
TK	Box model sensitivity test using a thermokarst $\delta^{13}\text{CH}_4$ value
VPDB	Vienna PeeDee Belemnite
VSMOW	Vienna Standard Mean Ocean Water
YD	Younger Dryas

## Acknowledgments

I have very much enjoyed the many people I was able to work with over the course of this project, and definitely owe some thanks.

First, I would like to thank my supervisor, Michael Whiticar, for being patient with the sometimes agonizingly slow progress on the 'machine'. Michael, thankfully, understands the technical difficulty of these measurements and was always forgiving, even when I had months with nothing but 'leak checking' to report. I also greatly appreciated Michael's willingness to let me lead this project where it needed to go. I enjoyed the freedom and believe I am a better, more independent scientist as a result.

I also owe a huge thanks to Jed Kaplan. Jed has taught me everything I know about modelling (95% of which doesn't appear in this thesis) and has shared with me his great enthusiasm for science. I have been most fortunate to spend long periods working side-by-side with Jed, and I feel I have profited greatly. I am also indebted to Jed and Helga for making me welcome into their home when I made the treks to work in Lausanne.

Hinrich Schaefer has been a great mentor during my studies. I had a great time in Pâkitsoq with Hinrich and enjoyed the numerous discussions that we have had over the years. Hinrich was also kind enough to provide his firm diffusion model.

This project is largely possible due to the work of Vas Petrenko, Jeff Severinghaus, Ed Brook, and the late Niels Reeh. Niels Reeh was the first person to suggest that outcropping ice could be a valuable resource for ancient ice and worked hard to demonstrate that fact. For this project, I have really built upon the foundation that was carefully laid by the Brook and Severinghaus labs. All the methane concentration work was performed at OSU in the Brook lab, all  $\delta^{15}\text{N}$  and  $\delta^{18}\text{O}_{\text{atm}}$  data were measured in the Severinghaus lab, mostly by Vas. Without these measurements and the initial pioneering work by Vas, Ed, Jeff, Hinrich, and Niels, I would not have a thesis. Jeff, Vas, and Ed have been very helpful in answering my questions and sharing data. I had a lot of fun with Vas in Pâkitsoq and in our discussions since then. I definitely look forward to any opportunities to work with all of them again.

Paul Eby is a great lab manager and friend who made going into the, maddeningly loud, lab actually fun each day. I owe a lot to Paul for ensuring that our mass spec didn't die a horrible death, and now know what I always need to do if the Hip come on the radio.

I thank my committee members: Ken Denman, Andrew Weaver, and Dan Smith. Ken and Andrew have been there from the beginning with guidance and advice, and Dan was kind enough to step in at the end with short notice. Katrin Meissner, before moving from UVic, was a great committee member who was very helpful and supportive. Katrin and Andrew provided me with time on their cluster computer, without which my simulations would still be running on my little laptop. Vivek Arora was kind enough to join my committee when we thought I was going to write up my vegetation modelling work, and has always been willing to answer my questions.

During this thesis, I have had numerous helpful discussions. Rita Wania has been great for dissuading me from going on wild goose chases, Charles Curry suggested the box model formulation, Giuseppe Etiope was helpful in understanding geologic

emissions, Keith Lassey provided his disequilibrium model. Glen MacDonald and Konstantin Kremenetski were kind enough to provide me with their  $^{14}\text{C}$  peatland basal initiation dates. The National Ice Core Laboratory of the United States made GISP2 ice available through their deaccession program.

Various people going through the Whiticar lab made my time there a lot more fun. Special thanks to Kern Lee for our daily foosball game, and for swearing profusely each time I won. My friend, Matt Henderson, was greatly appreciated as a fellow grad student to gripe with about the state of our research.

I want to thank my family for their support and commiseration/celebration when things were going poorly/well. Lastly, I want to thank my wife Catrin for her understanding and support, especially the last year of this project. I am very lucky to have such a wife as her.

## **Dedication**

To my wife Catrin for her love, caring, and patience.

## 1. Introduction

The atmospheric mixing ratio of methane ( $\text{CH}_4$ ) has more than doubled since the PreIndustrial period (before 1850 A.D.; Figures 1.1.1 and 1.2.2) [Denman et al., 2007]. The present  $\text{CH}_4$  atmospheric mixing ratio is significantly higher than at any time in the last 800,000 years [Loulergue et al., 2008], and continues to increase [Rigby et al., 2008]. This rapid increase is disconcerting, as atmospheric  $\text{CH}_4$  plays an important role in the climate system.

Methane is the second most important troposphere sink for the OH radical, which is the principle determinant of the oxidizing capacity of the Earth's atmosphere, and the primary source of water vapour to the stratosphere [Lelieveld et al., 1993]. Additionally, the present atmospheric concentration of methane (ca. 1.8 ppm) contributes  $0.48 \pm 0.05$   $\text{W m}^{-2}$  of direct forcing to the total  $2.63 \pm 0.26$  from long-lived greenhouse gases [Forster et al., 2007], with an additional indirect forcing (due to formation of  $\text{O}_3$  in the troposphere and  $\text{H}_2\text{O}$  in the stratosphere) estimated to be between  $0.13 - 0.8$   $\text{W m}^{-2}$  [Lelieveld et al., 1998]. Due to the importance of methane, an understanding of the non-anthropogenic controls on  $\text{CH}_4$  formation and destruction is essential for projections of the role of  $\text{CH}_4$  in future climate. The ice core record has proven to be an excellent source of information about  $\text{CH}_4$  dynamics through changing climatic regimes.

Since the first high-resolution polar ice core  $\text{CH}_4$  record was published [Chappellaz et al., 1990], the mechanisms behind the observed abrupt changes in  $\text{CH}_4$  concentration have been intensely debated. Particular attention has been paid to abrupt concentration increases (Figure 1.1.1), as the ice core record has demonstrated numerous

events where the rate of change in the atmospheric methane concentration ( $[CH_4]$ ) approaches those of the industrial period [e.g. Brook et al., 2000].

### 1.1. The ice core record of atmospheric methane

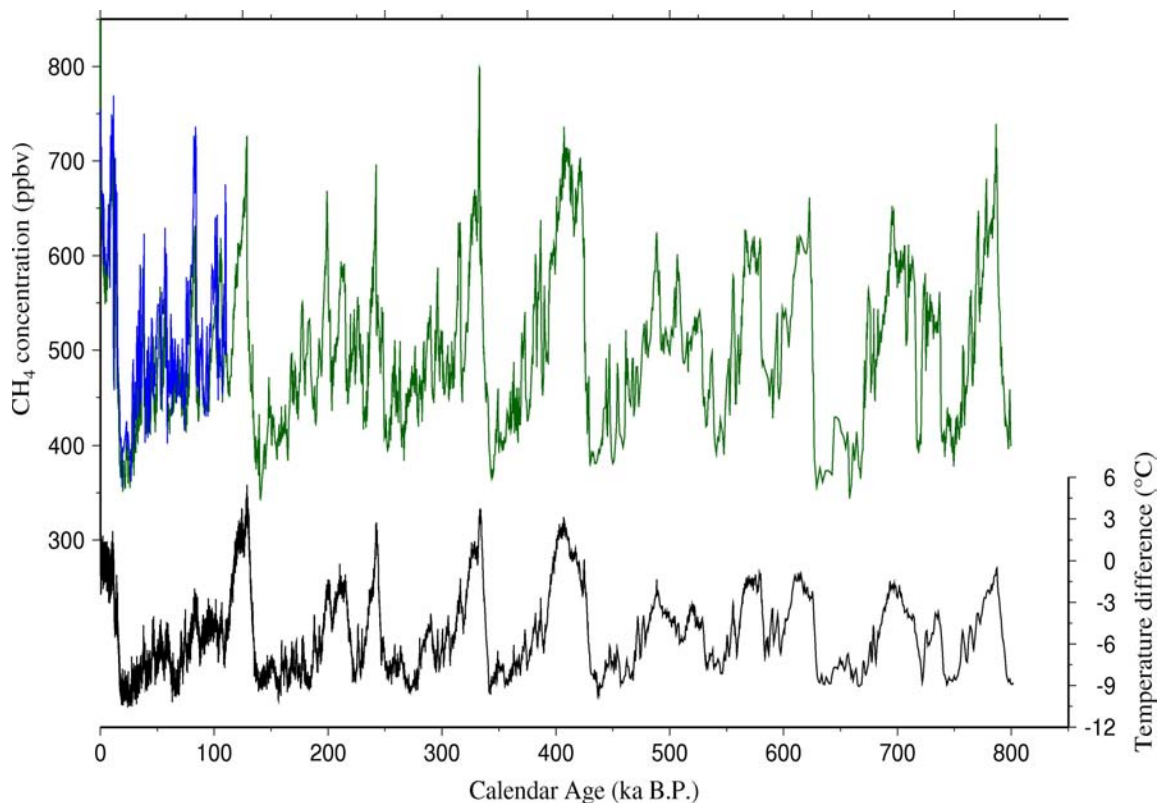


Figure 1.1.1: (top) Methane atmospheric concentrations from the Northern Hemisphere (blue) (GISP2; Brook et al., 1996) and the Southern Hemisphere (green)(EPICA Dome C; Loulergue et al., 2008). (bottom) Reconstructed temperature difference, relative to the average temperature of the last 1000 years, at the EPICA Dome C, Antarctica drilling site (Jouzel et al., 2007). Temperature reconstruction is based upon  $\delta D_{ice}$  measurements.

Methane records, along with paleo-temperature proxies, from both Antarctica [Petit et al., 1999; Flückiger et al., 2004] and Greenland [Chappellaz et al., 1990, 1993a, 1997; Brook et al., 2000, 2005] reveal the close correlation between methane and millennial-scale warming and cooling (Figure 1.1.1). Indeed,  $CH_4$  more closely parallels the rapid variations of polar temperature records than any other measured gas [Chappellaz et al., 1993a]. Numerous hypotheses have been put forward to explain the

CH<sub>4</sub> dynamics observed on time scales of decades to glacial-interglacial changes [e.g. Chappellaz et al., 1993b; Kennett et al., 2003; Luyendyk et al., 2005; Walter et al., 2007]. The hypotheses can be grouped into two categories: one for hypotheses that address the rapid changes in atmospheric methane concentration, and the other that addresses methane concentration changes that occur over glacial to interglacial cycles. The major distinction between the two categories, as many of the abrupt methane hypotheses are equally valid for the glacial-interglacial changes, is the assumed ability of the proposed mechanism to rapidly increase atmospheric methane concentration.

Three main hypotheses have been proposed as responsible for the large abrupt methane concentration changes observed in the ice core record:

1. Wetlands [Chappellaz et al., 1993b; Brook et al., 2000]
2. Methane hydrates [Nisbet, 1990; Kennett et al., 2003]
3. Thermokarst lakes [Walter et al., 2007]

Wetlands are the most important natural methane source at present, and are estimated to account for approximately 75% of the global methane burden in the Preindustrial Holocene (PIH) [Chappellaz et al., 1993b; Wuebbles and Hayhoe, 2002]. Due to wetlands' apparent importance, one hypothesis purports that an invigorated hydrologic cycle with higher precipitation allows expansion of wetland areal extent, and increased wetland methane emissions, particularly in the tropics [Brook et al., 1996]. Indeed, Severinghaus and Brook (1999) have found the increase in methane concentration to be synchronous, or possibly slightly lagging, the surface temperature increase over Greenland for two large abrupt warming events during the most recent

deglaciation. This suggests increased methane emissions to be a product of warmer temperatures (also see Severinghaus et al., 1998).

The methane clathrate (gas hydrate) release hypotheses have envisioned several scenarios. One contends that marine clathrates situated on the continental margins are capable of episodic destabilization events triggered by the warming of the upper thermocline waters. This scenario assumes that the majority of the CH<sub>4</sub> released passes through the water column, without oxidation, to the atmosphere [Kennett et al., 2003]. Another variation relies upon low sea-level to decrease the isostatic pressure on deep oceanic clathrates, thus destabilizing them and promoting massive sediment slumping. This slumping would release large volumes of gas hydrate from the hydrate stability zone and eventually to atmosphere [Nisbet, 1990; Paull et al., 1996]. A recent update on this hypothesis, based upon preserved tar records in sediments from the Santa Barbara basin, proposes that methane hydrates may act as a 'climate sensitive valve system for thermogenic hydrocarbons', i.e. clathrate release allows for the increased release of methane from hydrocarbon seeps [Hill et al., 2006].

Thermokarst lakes have recently been shown by Walter et al. (2006) to release large amounts of CH<sub>4</sub> from point-source locations. Some hotspots are observed to produce almost 50 g CH<sub>4</sub> m<sup>-2</sup> yr<sup>-1</sup>, and the present-day global flux is estimated at 24.2 ± 10.5 Tg CH<sub>4</sub> yr<sup>-1</sup> [Walter et al., 2007]. The large amount of available carbon [Romanovskii et al., 2004], and proven methane production, has lead to thermokarst lakes being postulated as playing a substantive role in past abrupt climate changes [Walter et al., 2007].

Two additional hypotheses have been proposed, in addition to the three previously mentioned, to explain methane dynamics on the slower glacial-interglacial time scale. One hypothesis concerns biogenic volatile organic compounds (BVOCs) interaction with OH radicals [Valdes et al., 2005; Kaplan et al. 2006], and the other involves geologic emissions of methane (GEM). [Luyendyk et al., 2005; Etiope et al., 2008a].

OH radicals are formed via the action of solar radiation on ozone and water vapour:



Methane can then react with the formed OH:



OH concentrations are not constant in the atmosphere, and will vary diurnally, seasonally, and spatially. This is largely related to solar radiation fluxes [Rohrer and Berresheim, 2006], as well as the concentrations of the OH radical's source/sink gases [Prinn, 2003]. BVOCs are also oxidized in the troposphere, primarily by OH radicals. As such, changes to BVOC atmospheric concentrations through time are expected to influence OH concentrations. As the OH sink is responsible for about 85 to 90% of the troposphere methane oxidation [Dlugokencky et al., 1994; Wuebbles and Hayhoe, 2002], changes to OH will influence atmospheric CH<sub>4</sub> concentrations.

GEM sources include terrestrial and marine seeps of thermogenic gas and geothermal/volcanic emissions from the Earth's crust. Luyendyk et al. (2005) propose periods of glacial low sea level cause marine seeps on the continental shelves to become

sub-aerial. These seeps, under higher sea levels, vent into the water column and therefore much of the CH<sub>4</sub> is oxidized before reaching the surface [Luyendyk et al., 2005]. Thus, Luyendyk et al. (2005) estimate that seeping CH<sub>4</sub> could contribute double the present day emissions during glacial times, if the gas is able to avoid water column oxidation.

Etioppe et al. (2008a) argue that while off-shore seeps are important, on-shore GEM appear to have higher CH<sub>4</sub> emissions. Due to primarily endogenic (geodynamic) controls on gas flow, variations in the flux of GEM sources are insensitive to negative feedbacks, such as the effect of cooling temperatures on biogenic CH<sub>4</sub> production. The release of this geologic CH<sub>4</sub>, while accounting for some minor sensitivity to exogenic (surface) conditions, is not anticipated to be necessarily catastrophic or abrupt. Etioppe et al. (2008a) suggest that due to the thermogenic nature of this CH<sub>4</sub>, periodic enhanced degassing of geologic CH<sub>4</sub> could have contributed to higher than expected  $\delta^{13}\text{CH}_4$  values observed since the last deglaciation [Schaefer et al., 2006; Fischer et al., 2008].

To allow distinction between these different hypotheses, methane's stable isotopes of both carbon and hydrogen can be used to constrain possible changes in source/sink fluxes, as was first proposed in 1982 [Stevens and Rust, 1982](Figure 1.2.1).

## **1.2. Ice core studies of methane stable isotope dynamics**

The pioneering work of Craig et al. (1988), provided the first measurements of methane stable carbon isotopes from ice cores. However, due to the technology available at the time, the amount of gas required, and hence sample size, was very large (25 kg/sample). The large amount of ice needed (length of ice core) meant that temporal resolution was much lower than desired for investigations of rapid atmospheric methane

dynamics [Craig et al., 1988]. It took almost 20 years, with the second ice core study published in 2005 [Ferretti et al., 2005], for technical barriers to be overcome thus allowing analysis of small samples, with high-temporal resolution suitable for investigating abrupt climate events.

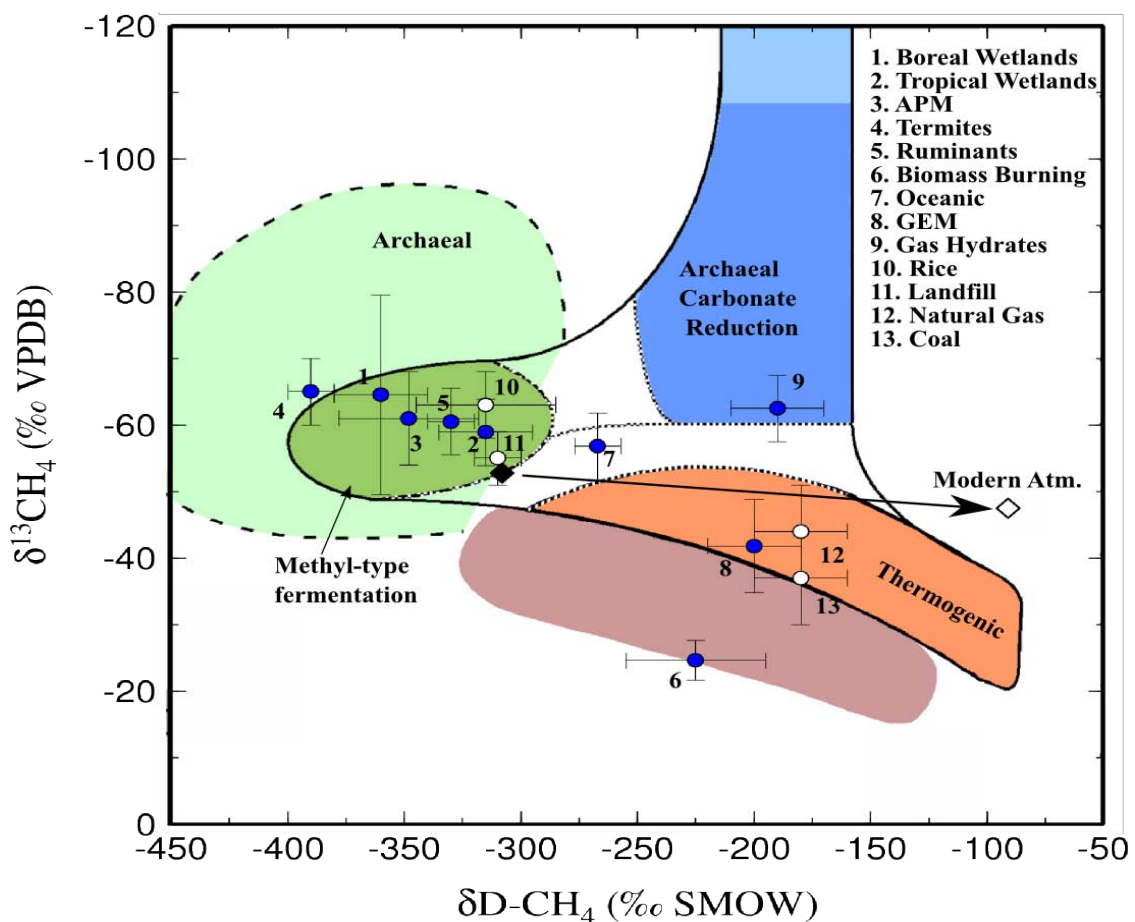


Figure 1.2.1: Combination  $\delta^{13}\text{CH}_4$  and  $\delta\text{D-CH}_4$  plot for the major sources of  $\text{CH}_4$  to the atmosphere. Anthropogenic sources are unfilled circles. The methane hydrate stable isotope values are typical for a marine biogenic gas hydrate. Shaded regions denote methanogenic pathways (after Whiticar, 1999). The modern atmosphere measured stable isotope value is the unfilled diamond. Sink fractionation changes the integrated source  $\delta^{13}\text{CH}_4$  and  $\delta\text{D-CH}_4$  to the measured value (direction of fractionation from integrated source value is indicated by the arrow). Source stable isotope values and standard deviations are based upon Quay et al., 1999; Whiticar, 1999; Milkov, 2005; Keppler et al., 2006; Vignano et al., 2009.

Ferretti et al. (2005) report a high-resolution  $\delta^{13}\text{CH}_4$  record spanning the period from 0 to 2000 A.D. The Ferretti et al. (2005) record is a composite of Law Dome,

Antarctica ice samples, Antarctic firm air, and Southern Hemisphere archived and ambient air samples (Figure 1.2.2). Ferretti et al. (2005) use modelled methane source partitioning and CO concentration data to suggest that biomass burning emissions are high from 0 to 1000 A.D. then reduce by almost 40% over the next 700 years, with the change attributed to a combination of human activities and natural climate change. Ferretti and coworkers' 2005 report clearly demonstrates the power of isotope analysis to determine source changes and reveal insights, sometimes unexpected. Mischler et al. (2009) recently confirmed the measurements of Ferretti et al. (2005) and supported their conclusions of changing biomass burning methane emissions.

Following shortly after the Ferretti and coworkers study, Schaefer et al. (2006) investigated the Younger Dryas – Preboreal (YD-PB) transition (11.57 ka BP; ka B.P refers to thousand years before 1950 A.D.) through measurements of  $\delta^{13}\text{C}_{\text{CH}_4}$ . That same year, Sowers (2006) used  $\delta\text{D-CH}_4$  measurements to study the same transition (YD-PB), the Oldest Dryas-Bølling transition (OD-B; ~14.7 ka BP), the onset of Interstadial #8 (38.5 to 38.0 ka BP), as well as a coarse resolution (every 500 yr) survey from the Last Glacial Maximum (LGM) to 8 ka BP. Both papers showed some surprising results (Figure 1.3.1). Perhaps most interesting is the relatively constant  $\delta^{13}\text{C}_{\text{CH}_4}$  value of -46 ‰ found by Schaefer et al. (2006) over the YD-PB transition, which is about 5.5 ‰ more  $^{13}\text{C}$ -enriched than was anticipated (and 1 ‰ more enriched than the modern atmosphere). Stable  $\delta^{13}\text{C}_{\text{CH}_4}$  values over the transition were believed to be consistent with additional emissions from tropical wetlands, aerobic plant methane (APM) emissions or a multisource scenario, while ruling out a large marine biogenic clathrate source [Schaefer et al., 2006].

Sowers' study (2006) also found no evidence to suggest a marine clathrate source from the  $\delta D-CH_4$  record, which demonstrated no change, or possibly a slight decrease in  $\delta D-CH_4$  values (more  $^2H$ -depleted) over the increasing  $CH_4$  concentrations of the YD-PB transition. A similar pattern is found for the OD-B and Interstadial #8 warming events ruling out marine gas hydrate release, which would increase  $\delta D-CH_4$

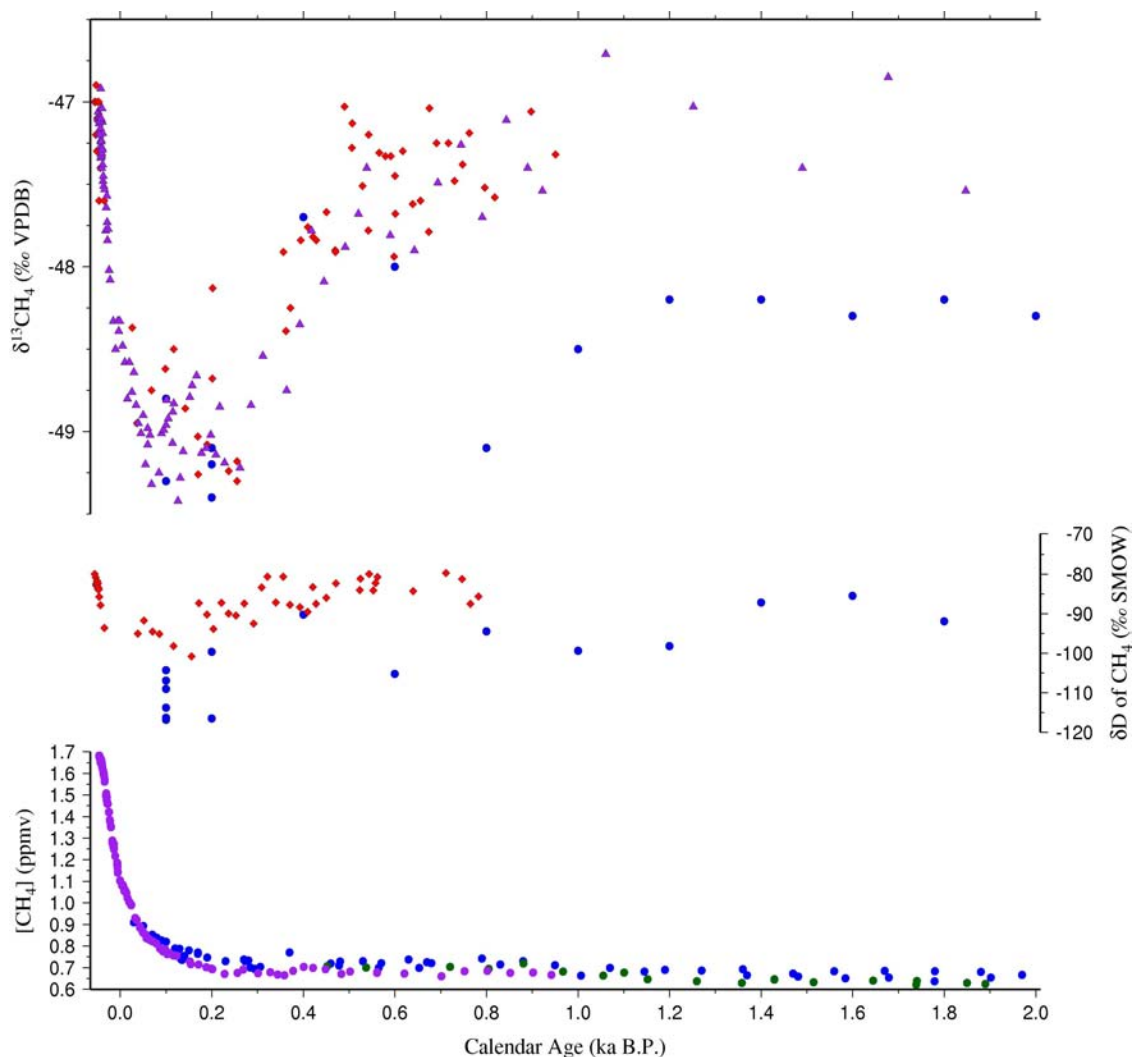


Figure 1.2.2: 2000 year record of  $\delta^{13}CH_4$  (top),  $\delta D-CH_4$  (middle) and  $[CH_4]$  (bottom).  $\delta^{13}CH_4$  data are from Law Dome, Antarctica (purple triangles) [Ferretti et al., 2005], West Antarctica Ice Sheet (WAIS) Divide (red diamonds) [Mischler et al., 2009], and GISP2, Greenland (blue dots) [Sowers, 2009].  $\delta D-CH_4$  data are from WAIS Divide (red diamonds) [Mischler et al., 2009] and GISP2 (blue dots) [Sowers, 2009]. Concentration data are from EDML, Antarctica (green dots) [EPICA Community Members, 2006], GISP2 (blue dots) [Brook et al., 2005], and a combined record from Law Dome ice, firn air and atmospheric archived and ambient air samples (purple triangles) [Etheridge et al. 1998]

values [Sowers, 2006]. Sowers (2006) suggests that the more  $^2\text{H}$ -enriched glacial  $\delta\text{D-CH}_4$  is a result of a lower ratio of net to gross wetland methane emissions and increased thermogenic emissions. Changing the ratio of net to gross wetland emissions exerts a strong control on the methane hydrogen isotope values due to the kinetic isotope effect (KIE) associated with methane oxidation near the soil-atmosphere interface. Thermogenic emissions are also implicated due to their relatively  $^2\text{H}$ -enriched isotope signature. Whiticar and Schaefer (2007) use the combined YD-PB records of  $\delta\text{D-CH}_4$  [Sowers, 2005] and  $\delta^{13}\text{CH}_4$  [Schaefer et al., 2006] to also suggest thermogenic clathrate releases, or natural gas seeps, in the time period prior to the YD termination.

Fischer et al. (2008) recently reported  $\delta^{13}\text{CH}_4$  measurements spanning the most recent deglaciation from the EDML, Antarctica ice core (Figure 1.3.1). A Monte Carlo steady-state box model was used to quantitatively interpret their measurements. Their box model results indicate an increase in the atmospheric lifetime of  $\text{CH}_4$  and the boreal wetland source as the deglaciation progressed. Biomass burning was found to be relatively constant over the deglaciation.

These first studies using the stable isotopes of  $\text{CH}_4$  demonstrate the powerful probe that stable isotopes provide for understanding the natural methane system. However, the present datasets provide only small, incomplete, glimpses of the time periods of interest. Further studies are required to fully elucidate the source and sink dynamics underlying the observed changes in  $\text{CH}_4$  atmospheric mixing ratio. This thesis will address some of the present gaps in our knowledge of the underlying methane source and sink behaviour during the most recent deglaciation, as well as during examples of abrupt climate change events.

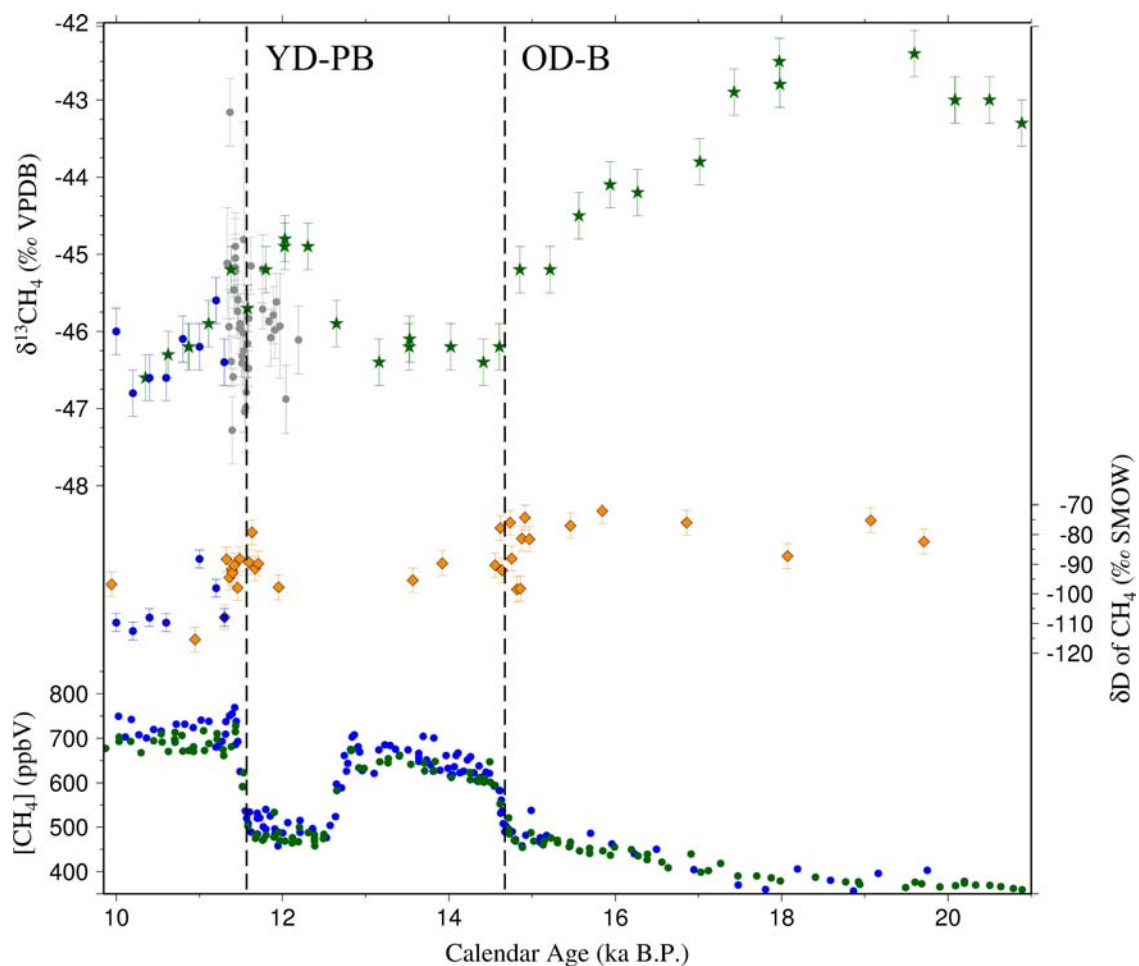


Figure 1.3.1:  $\delta^{13}\text{CH}_4$  (top),  $\delta\text{D-CH}_4$  (middle) and  $[\text{CH}_4]$  (bottom) records spanning the most recent deglaciation.  $\delta^{13}\text{CH}_4$  data sources (top) include Fischer et al. (2008)(green stars; EDML, Antarctica), Schaefer et al. (2006)(grey circles; Pákitsoq, Greenland), and Sowers (2009)(blue dots; GISP2, Greenland). GISP2  $\delta\text{D-CH}_4$  data are from Sowers (2006)(orange diamonds) and Sowers (2009)(blue dots).  $\text{CH}_4$  concentration data are from Brook et al., 1996 (blue dots; GISP2, Greenland), and EPICA Community Members (2006)(green dots; EDML, Antarctica). Dashed lines indicate the YD-PB transition (11.57 ka BP) and OD-B (14.7 ka BP) transition.

### 1.3. Research Objectives / Thesis Outline

This thesis aims to improve our understanding of methane dynamics through the most recent deglaciation. The approach used for this investigation involves the measurement and interpretation of the  $\delta^{13}\text{CH}_4$  record from methane occluded in ablation-zone ice from Pákitsoq, Greenland spanning the Last Glacial Maximum (LGM; ca. 21 ka BP) to the Preboreal period (PB; ca. 10 ka BP). The use of Greenland ice will fill a gap in

the presently available data. While most methane sources are terrestrial, and predominantly in the Northern Hemisphere, the only  $\delta^{13}\text{CH}_4$  record available for the deglaciation is from the Southern Hemisphere [Fischer et al., 2008]. The analysis of a Northern Hemisphere record in this thesis provides an archive located closer, and thus perhaps more sensitive to changes in, the proximal  $\text{CH}_4$  sources. Additionally, measurement of a Northern Hemisphere  $\delta^{13}\text{CH}_4$  record enables further information to be gleaned through the inter-polar gradient (IPG) in  $\delta^{13}\text{CH}_4$  values. The  $\delta^{13}\text{CH}_4$  IPG provides unique information about the hemispheric location of the sources contributing to changes observed in the atmospheric methane mixing ratio.

The most recent deglaciation, while an important example of methane dynamics between glacial and interglacial periods, also contains climatic events where the atmospheric  $\text{CH}_4$  mixing ratio changes rapidly on decadal time scales. Two climate events are of particular interest, the OD-B transition and the YD Cold Interval. The OD-B transition occurred early in the deglaciation with extensive ice sheets and globally low-sea levels still in place, while the YD cold interval marked a rapid climate reversal to almost glacial conditions lasting over a millennia [Alley, 2000].

These two climatic transitions are well-suited to aid understanding of how different warming events impact upon which  $\text{CH}_4$  sources are responsible for the abrupt increases in  $[\text{CH}_4]$ . The hypothesized trigger for the YD termination is the rerouting of runoff from the Laurentide Ice sheet [Broecker et al., 1989; Fanning and Weaver, 1997], whereas the OD-B transition is related to the Meltwater Pulse 1A (MWP-1A) with its source of freshwater from the Antarctic shelf [Clark et al., 2001; Weaver et al., 2003].

This thesis details the development and implementation of an improved extraction line, partitioning, and continuous flow-isotope ratio mass spectrometer measurement procedure for the  $^{13}\text{C}/^{12}\text{C}$  determination of  $\text{CH}_4$  from air occluded in samples of glacial ice. These  $^{13}\text{C}/^{12}\text{C}$  ratios (reported as  $\delta^{13}\text{CH}_4$  values) span the most recent deglaciation. They are interpreted with the aid of a steady-state 4-box atmospheric methane Monte Carlo model. The results of the box model simulations then define probability distributions of the source fluxes and methane atmospheric lifetime for the

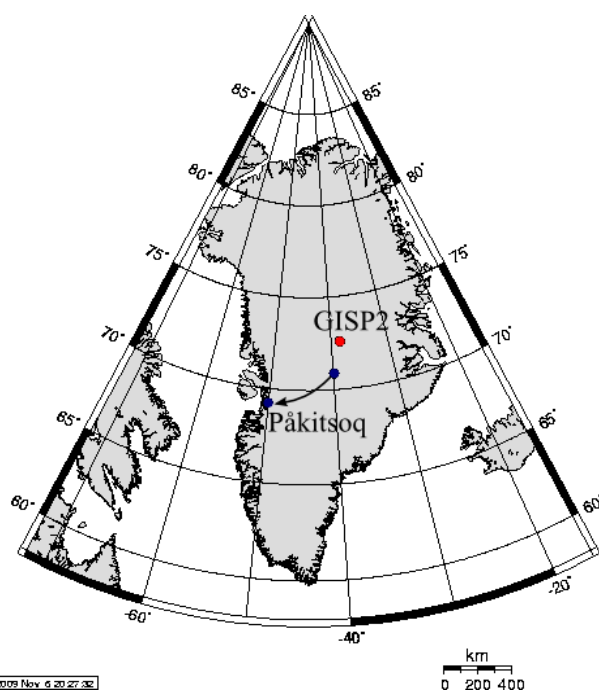


Figure 1.3.2: Map of GISP2 drilling site (red dot), Pákitsoq snow deposition site (blue dot) and general flow path to Pákitsoq outcrop on the western Greenland margin.

stable periods investigated. The times of rapid change are treated separately using a mass balance approach informed by the  $\delta^{13}\text{CH}_4$ ,  $\delta\text{D-CH}_4$  and  $^{14}\text{CH}_4$  records, where available.

The remainder of Chapter 1 describes the ice sampling locations. Chapter 2 describes: 1) the improved instrumental method to extract and measure the Pákitsoq and GISP2 interstitial air  $\delta^{13}\text{CH}_4$  values, 2)

sample age determination, and 3) corrections applied to adjust for fractionating firn processes. Chapter 2 also describes the steady-state atmospheric box model used to interpret the Pákitsoq  $\delta^{13}\text{CH}_4$  record over the deglaciation. Chapter 3 describes the results of  $\delta^{13}\text{CH}_4$  measurements from GISP2 and Pákitsoq using the improved instrumental

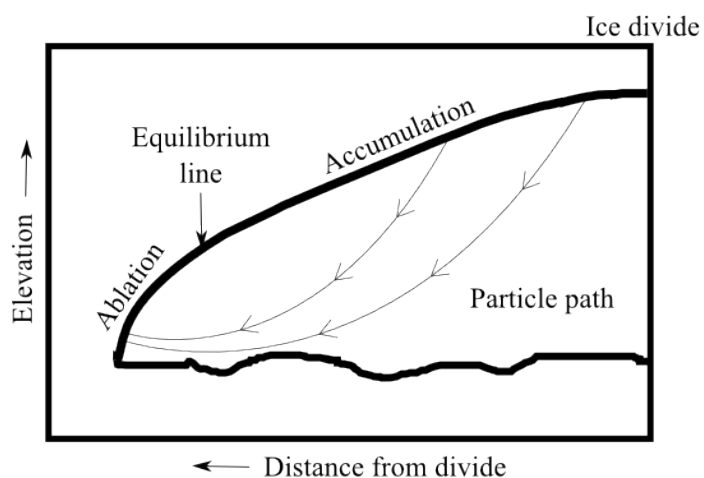
setup. The box model simulation results for each time period investigated are also described. Chapter 4 discusses the results from the measurements and box model simulations in the context of current knowledge and previous work by other researchers. Chapter 5 presents the main findings of this thesis. Chapter 6 and 7 are references cited and appendices, respectively.

## 1.4. Study sites

### 1.4.1. Pâkitsoq, Greenland

The Pâkitsoq ice sampling site is located at 69°25.83'N 50°15.20'W, approximately 40 km northeast of the town of Illulisat, Greenland (Figure 1.3.2). The Pâkitsoq site is ideally situated in a region where ice flowing from the accumulation zone, near the Summit of the Greenland ice sheet, outcrops due to the presence of a compression zone created

by a mountain range (Figure 1.4.1). The ice ablates at the rate of 2 – 3 m yr<sup>-1</sup> with a flow rate of approximately 17 m yr<sup>-1</sup> 1 km inland and almost zero at the margin [Petrenko et



al., 2006; Reeh and Thomsen, 1994]. The area

Figure 1.4.1: Cartoon of ice-sheet cross-section. Particle paths recreate ice flow through the ice sheet from the accumulation zone to the ablation zone. Pâkitsoq is within the ablation zone. Adapted from Reeh et al. (2002)

presently is in negative mass balance, with the vertical surface loss of 9 m over the 12 year period from 1994 to 2006 [Reeh et al., 2005].

The area has been extensively studied starting with the glaciological work by N. Reeh [Reeh and Thomsen, 1994; Reeh et al., 2002], and expanded with methane gas

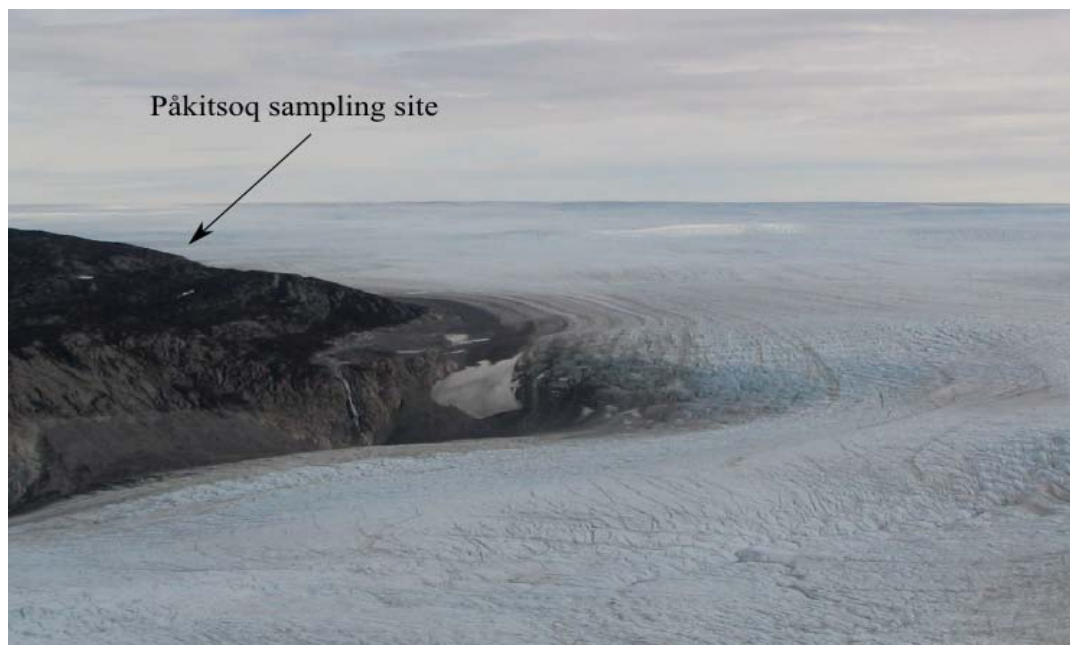


Figure 1.4.2: Physical location of the Pâkitsoq sampling site from the south. Note the alternating bands of dark (sediment rich ice from cold climate periods) and light ice (from periods of warmer climate) as the ice outcrops against the mountain range. Actual sampling site is out of sight behind the mountain ridge.

and stratigraphy work [Schaefer, 2005; Schaefer et al., 2006; Petrenko et al., 2006; Petrenko, 2008; Schaefer et al., 2009]. Pâkitsoq has been targeted due to the presence of ice dating from the LGM through to the Preboreal available in virtually unlimited quantities at the surface. This ice exists in horizontal strata that visibly denote cold and warm periods by sections of darker and lighter ice, respectively (Figure 1.4.2). Detailed information on the age scale is presented in Section 2.2. The ice contains sections of altered ice termed 'blue' bands (bubble-free ice) and dust bands (sections with high sediment content). These sections have been proven to contain anomalously elevated [CH<sub>4</sub>] in the gas trapped in the ice [Schaefer, 2005; Petrenko et al., 2006] and thus must be avoided.

#### 1.4.2. *GISP2, Greenland*

The GISP2 drilling site is located close to the summit of the Greenland ice sheet (Figure 1.3.2; 72.58°N ; 38.48°W)[Grootes and Stuiver, 1997]. Drilling was completed in 1993 and the core section analysed here is #139, originally cored for analysis of cosmogenic particles. The section is from a depth interval of 141.0 to 142.2 m with an age of approximately 220 to 230 yr BP (see Section 2.2). The GISP2 ice core drill site is located at 3208 m above sea level with a present day mean annual temperature of -31 °C and snow accumulation rate of 0.24 m ice yr<sup>-1</sup> [Meese et al., 1997]. These conditions give a firn (compressed snow) to ice transition depth of approximately 80 m [Severinghaus et al., 1998]. Below this depth, the air trapped within the ice matrix is no longer able to communicate with atmosphere.

## 2. Methods

An improved method to determine the  $^{13}\text{C}/^{12}\text{C}$  ratio of methane from ice cores and small air samples was developed and is described here (Section 2.1).

Procedures for the assignment of gas age for the Pákitsoq ice samples are described in Section 2.2. Due to processes that cause separation of the isotopologues in the firn layer, several corrections are necessary to determine the original atmosphere value of the  $\delta^{13}\text{CH}_4$  or  $\delta\text{D-CH}_4$ . An additional correction for the disequilibrium that can occur between the measured atmospheric concentration and stable isotope values, and the values of the aggregated sources, outside of the firn column, is also described. These corrections are outlined in Section 2.3.

Two box models were developed to interpret changes in the global source budget during the different stable time periods investigated. These models are described in Section 2.4.

### 2.1. Extraction line and isotope ratio mass spectrometer method

Measurement of the  $\delta^{13}\text{CH}_4$  value from gases entrained in ice presents several challenges:

1. The concentration of methane in ancient ice is low, varying between ca. 350 ppbv (parts per billion by volume) during the Last Glacial Maximum (LGM) to as high as 800 ppbv prior to Industrialization [Brook et al., 2000]. In contrast, present day atmospheric methane mixing ratios are presently ca. 1860 ppbv [Dlugokencky et al., 2009].

2. Sample sizes of acceptable age resolution for investigating abrupt events are commonly between 100 and 200 grams assuming a 10 % air content by volume [Raynaud et al., 1997], this allows between 200 and 400 pmol of CH<sub>4</sub>, which is on the limit of instrumental sensitivity.
3. Access to the gases in the ice samples requires an extraction procedure that can effectively separate the gas from the ice matrix in a manner that preserves the gas content and isotope ratio.
4. Lastly, to be of utility in determining past changes in the global methane budget, the measurements must be of sufficient accuracy and precision to allow detection of changes in source and sink configuration, likely on the order of  $\pm 0.3 \text{ ‰}$  to  $\pm 0.5 \text{ ‰}$  [Schaefer and Whiticar, 2007].

To accommodate these analytical challenges, an online extraction system with several innovations was developed. The procedure follows three main steps: 1) liberate gas from the ice through a wet extraction; 2) isolate and convert the CH<sub>4</sub> to carbon dioxide (CO<sub>2</sub>) and; 3) introduce the target gas (CO<sub>2</sub>) into the CF-IRMS. The performance of this setup is described in Section 2.1.4.

#### *2.1.1. Experimental procedures*

The initial procedure follows that of Schaefer and Whiticar (2007). First, the outer 2 – 3 mm of an ice sample (ca. 100 – 150 g) is removed to prevent surface contamination. The ice is then weighed and sealed within a pre-chilled 570 ml stainless steel extraction chamber fitted with a Viton<sup>®</sup> O-ring (schematic is presented in Figure 2.1.1). The chamber has been designed to withstand both a vacuum and mild overpressure. To remove ambient air contamination, a rotary vacuum pump evacuates the chamber for 5

minutes down to the vapour pressure of ice. The chamber is then sealed from the vacuum pump using a Nupro<sup>®</sup> bellows valve, and heated by a hot water bath. Melting of the ice sample is monitored via a window built into the extraction chamber (pyrex glass sealed with a Viton<sup>®</sup> O-ring). Ice melting time averages between 4 and 7 minutes (sample-size dependent), allowing for one minute equilibration time. The melting releases the occluded gas, and the gas partitions into the evacuated headspace. Once the equilibration is complete, helium (He) gas is allowed to fill the chamber at a rate of 160 ml min<sup>-1</sup>. The He stream enters the chamber through a short length of tubing, within the meltwater, allowing stripping of the dissolved CH<sub>4</sub> and flushing of the headspace. The pressure on the He gas line entering the chamber is monitored via a pressure gauge. As soon as the chamber reaches atmospheric pressure, the outflow valve is opened to allow gas to flow onto the pre-concentration setup.

Post-chamber, the gas enters a series of traps. Due to bubbling of the He stream through the meltwater, significant amounts of water vapour are carried with the helium stream necessitating efficient water removal. The water trap, placed immediately downstream of the chamber, is composed of an open stainless steel tube (20 cm of 6 mm diameter plus 40 cm of 2 mm) maintained at -70 °C with a liquid nitrogen (LN<sub>2</sub>; -190 °C) cooled - ethanol slurry. The length of the water trap efficiently strips the gas stream of water but necessitates effective drying procedures between samples (outlined in Section 2.1.5).

The dried gas stream then passes through two traps to remove carbon monoxide (CO). CO must be removed from the gas stream to prevent the CO from being included in the methane signal later in the extraction line (particularly for the post-combustion

trapping step; section 2.1.2). Un-trapped CO will be converted into CO<sub>2</sub> within the combustion oven and is very difficult to separate from the CH<sub>4</sub> (which is also combusted to CO<sub>2</sub>). The first CO trap is a 6 cm length of 6 mm outer diameter (o.d.) stainless steel tubing packed with Sofnocat™ 514, a highly-active promoted platinum, palladium, and tin oxide catalyst. The second CO trap is a 15 cm length of 6 mm o.d. stainless steel tubing packed with Schutze reagent (iodine pentoxide on granular silica gel). The Schutze reagent is consumable and needs to be periodically replaced. The Sofnocat™ 514 can be refreshed with periodic heating.

The gas stream then enters a Valco® 6-way gas sample valve to be cryogenically trapped. The cryogenic trap preferentially captures CH<sub>4</sub> and CO<sub>2</sub> as well as other gases with higher boiling points (allowing oxygen and nitrogen to flow to waste). The trap is HayeSep® D absorbent (divinylbenzene, 80 - 100 mesh) packed into a 10 cm length of 1/8 in. o.d. tubing, and maintained at -125 °C by a cryogenic trap design detailed in Schaefer and Whiticar (2007). The gas stream flushes the extraction chamber for 10 min (equivalent to approximately 5 headspace volumes, determined to be sufficient for quantitative extraction through performance tests; Section 2.1.4) quantitatively extracting and trapping the CH<sub>4</sub>. This trapping time is optimized to ensure complete transfer of the sample gas, while preventing excessive water vapour from transferring as well. Excessive water vapour adversely affects instrument performance [Merritt et al., 1995; Schaefer, 2005].

After the 10 minute trapping elapses, the valve is turned to allow a separate He gas stream (set at the same pressure; ca. 15 psi) to carry the CH<sub>4</sub> off the Haye-sep®. Release of this trapped CH<sub>4</sub> from the Haye-sep® requires warming of the trap to room

temperature, at which point the trapped methane is rapidly released. Since the CO<sub>2</sub>, that is also trapped on the Haye-sep<sup>®</sup>, takes a significant amount of time to elute from the columns further along in the set-up (and presents a complication to the post combustion focus; Section 2.1.2), it is trapped separately than the CH<sub>4</sub> by inserting a double loop of blank capillary into liquid nitrogen before the second Valco<sup>®</sup> 6-way gas sample valve. The methane is then trapped on section of gas chromatography (GC) capillary tubing (GSQ<sup>®</sup> PLOT; 0.32 mm ID) immersed in LN<sub>2</sub>.

The methane quantitatively transfers from the Haysep<sup>®</sup> D to the GSQ trap within 5 minutes. After the methane has transferred, the 6-way valve is turned from trapping to injection mode, and the GSQ loop is removed from the LN<sub>2</sub>, releasing the CH<sub>4</sub>. Since the GSQ loop is located on a different port of the 6-way valve than the CO<sub>2</sub> double-loops; it allows the release of the CH<sub>4</sub> onto the following GC columns while releasing the CO<sub>2</sub> to atmosphere.

Further isolation of CH<sub>4</sub> from other remaining gases is accomplished via two GC columns with a combustion oven in between. The GC columns are kept inside GC ovens, the first oven contains a room temperature 30 m long 0.53 mm inner diameter (ID) GSQ<sup>®</sup> PLOT capillary column with a He carrier gas flow rate of ca. 1 ml min<sup>-1</sup>. This first GC column allows good separation of CH<sub>4</sub> from any remnant CO and CO<sub>2</sub> but not N<sub>2</sub>O. After the first column, the sample passes into a micro-combustion oven containing a nickel-platinum catalyst at 1080 °C. The oven maintains an oxidative environment through a trickle flow of 1% O<sub>2</sub> in He make-up gas (0.5 ml min<sup>-1</sup>)[Dias et al., 2002; Schaefer and Whiticar, 2007], allowing the quantitative conversion of CH<sub>4</sub> to CO<sub>2</sub> and H<sub>2</sub>O. To remove

the water created during the combustion a Nafion<sup>®</sup> trap [Leckrone and Hayes, 1997] with He counterflow is used.

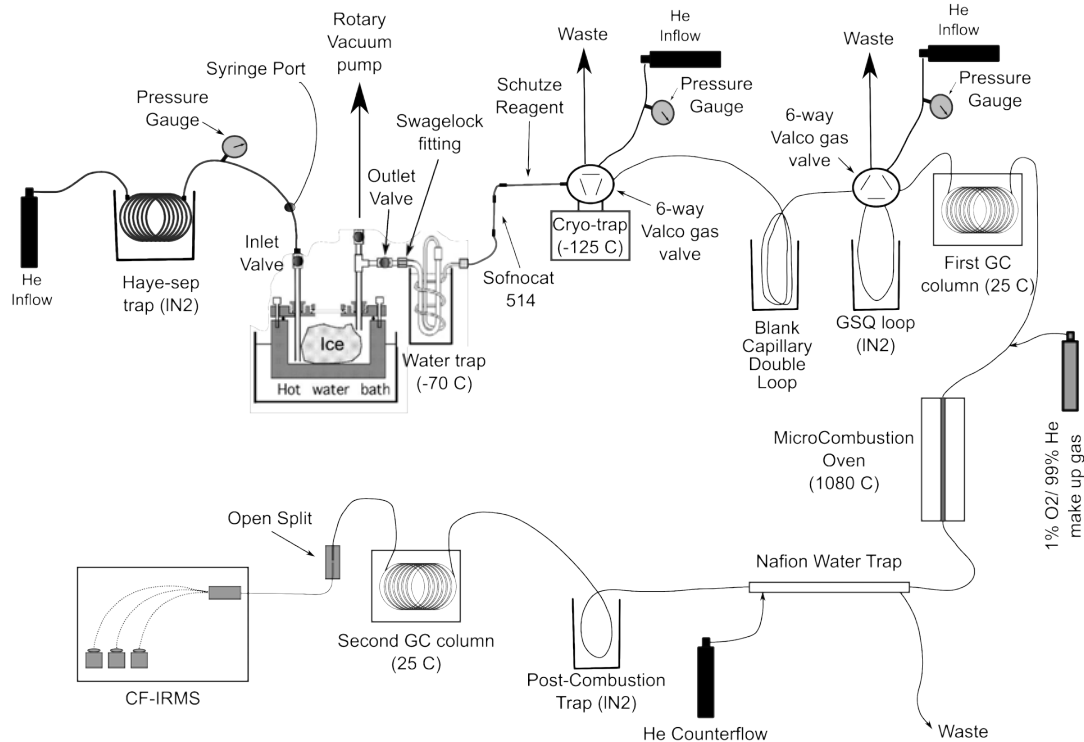


Figure 2.1.1: Schematic of CF-IRMS instrumental extraction and pre-concentration setup.

### 2.1.2. Post-combustion trapping

The introduction of a post-combustion trapping step is the most important change from the procedure outlined in Schaefer and Whiticar (2007) and will be described in detail here. This trapping requires the addition of CO traps and the removal of CO<sub>2</sub> from the gas stream. The procedures for these two changes are described in the previous section.

The larger internal volume of the micro combustion oven, as compared to the GC column capillary tubing, allows for spreading of the CH<sub>4</sub> peak and subsequently lower

peak heights for detection in the CF-IRMS. To maintain a tight, high-amplitude peak, which is desirable to ensure sample signal is significantly above the instrument shot noise threshold, a post-combustion trap technique was developed. The shot noise threshold was determined for our instrument to be a  $m/z$  44 peak of  $> 290$  mV, [Schaefer and Whiticar, 2007](0.97 nA at a resistor value of 300 M $\Omega$  for the  $m/z$  44 detector). The post-combustion trapping occurs on blank capillary tubing immersed in  $\text{IN}_2$  immediately after the Nafion water trap. The trapping is initiated after the  $\text{N}_2\text{O}$  peak has passed and was determined to be sufficient, after only a 1 minute long hold, to completely trap the  $\text{CH}_4$  signal (now combusted to  $\text{CO}_2$ ; referred to hereafter as methane- $\text{CO}_2$  for clarity). This technique also necessitates He gas pre-scrubbing as described in Section 2.1.5.

Once the minute-long trap is complete, and the capillary tubing is released from the  $\text{IN}_2$ , the sample then passes into a second room-temperature GC (30 m length 0.53 mm ID GSQ Poraplot<sup>®</sup> column). The second column functions to further separate the methane- $\text{CO}_2$  signal from the  $\text{N}_2\text{O}$ , which has a tendency to tail excessively in the CF-IRMS. Post-columns, the methane- $\text{CO}_2$  flows into an open-split, which acts to decrease the gas volume, and finally into the CF-IRMS. The CF-IRMS used for all measurements presented here was a Finnigan MAT 252 with Isodat<sup>™</sup> software for peak detection and interpretation. Note that many of the CF-IRMS instrumental limits and procedures were therefore adopted as determined by Schaefer, (2005) and Schaefer and Whiticar, (2007) including shot noise threshold (reliable detection limit) and linearity of system response to differing methane concentrations. As a result, samples with  $m/z$  44 peak size below 290 mV (0.97 nA) were discarded (Appendix 7.3).

The methane-CO<sub>2</sub> stable carbon isotope ratios are measured as the ratio between  $m/z$  44 (<sup>12</sup>C<sup>16</sup>O<sup>16</sup>O) and 45 (<sup>13</sup>C<sup>16</sup>O<sup>16</sup>O). The  $m/z$  46 (essentially <sup>12</sup>C<sup>18</sup>O<sup>16</sup>O) signal, is also recorded to correct for the <sup>12</sup>C<sup>17</sup>O<sup>16</sup>O isobaric contamination of <sup>13</sup>C<sup>16</sup>O<sup>16</sup>O that occurs at  $m/z$  45, (e.g. [Assonov and Brenninkmeijer, 2003]). The isotope ratios are referenced against a laboratory CO<sub>2</sub> working standard pulsed into the CF-IRMS at the start of the run and after the methane signal has been recorded (calibrated against the Vienna PeeDee Belemnite (VPDB)-CO<sub>2</sub> standard gas from the International Atomic Energy Agency, IAEA). All stable carbon isotope ratios of methane are reported in the standard  $\delta$ -notation as per mil (‰) values (with the deuterium ratio formulated similarly):

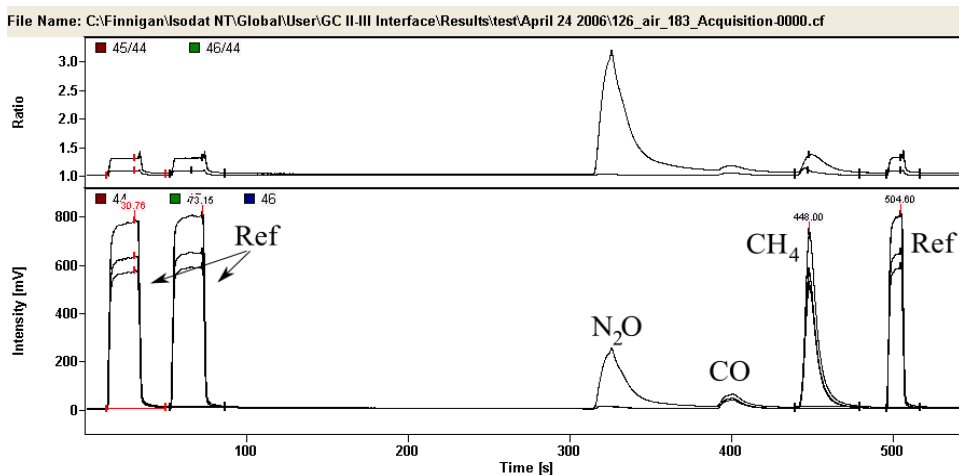
$$(2.1.2.) \quad \delta^{13}CH_4 = \left( \frac{{}^{13}C/{}^{12}C_{sample}}{{}^{13}C/{}^{12}C_{VPDB}} - 1 \right) \times 1000$$

### 2.1.3. Methane concentration from the CF-IRMS

Methane concentrations for ice samples can be calculated using the  $m/z$  44 peak height and sample mass, provided the ice-bubble air content is known and the ionization efficiency of the mass spectrometer remains constant. Testing has shown that the  $m/z$  44 peak is as suitable as using the peak area ( $\mu V$  s) under the  $m/z$  44 peak [Schaefer and Whiticar, 2007]. The instrumental response is determined using air samples of known volume and methane concentration to parameterize instrumental signal response to CH<sub>4</sub> carbon (mV signal /  $\mu g$  C). Since the CF-IRMS technique utilizes flushing of the headspace gas from the sample chamber, we achieve quantitative transfer of the gas from the sample chamber to the remainder of the extraction line. This is in contrast to the common technique of expanding the gases onto a sample loop, thus losing the sample gases that remain in the melting chamber and transfer lines. The ability to quantify the

sample concentration is useful for detecting compromised samples (see Section 3.2), which is otherwise difficult due to the destructive nature of the analysis.

#### 2.1.4. Instrumental setup performance



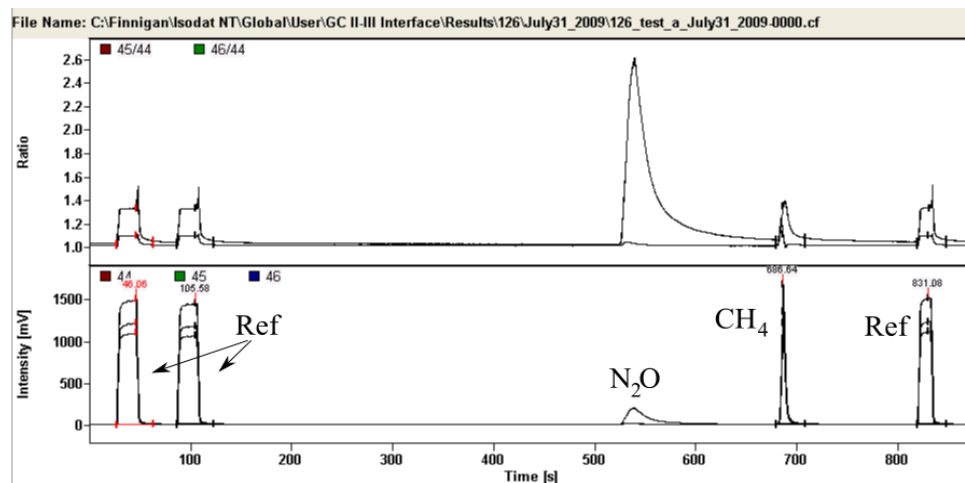
Peak No.	Start (s)	Rt (s)	Width (s)	Ampl. 44 (mV)	Ampl. 45 (mV)	Ampl. 46 (mV)	Area All (Vs)	$\delta^{13}\text{C}/^{12}\text{C}$ (‰ VPDB)
1 (Ref)	13.8	30.8	36.6	575	635	783	11.18	-49.44*
2 (Ref)	53.2	73.2	33.8	586	647	797	11.78	-50.14
3 (CH <sub>4</sub> )	439.8	448	39.8	512	567	728	4.58	-47.68
4 (Ref)	496.1	504.6	20.6	589	650	802	5.34	-49.56

Figure 2.1.2: Example mass spectrogram of a 10 ml sample of atmospheric air run through the setup of Schaefer and Whiticar (2007). The spectrogram shows the three measured ion intensities of the sample ( $m/z$  44, 45, and 46 in mV, listed as Ampl. in the data table above). The first two flat-top peaks are reference gas pulsed into the IRMS (the first peak is assigned a known value of -49.44 ‰, note on this run the second peak is 0.6 ‰ off of the first peak. This is accounted for later with the following reference peak). The peak at ~320 s is N<sub>2</sub>O, closely followed by CO and then CH<sub>4</sub>. The reference gas is pulsed into the IRMS after the CH<sub>4</sub> has eluted to account for any drift in instrument response. The instrument response (mV /  $\mu\text{g C}$ ) for this run was 28.21.

The improved extraction line setup has an approximate increase in sensitivity of 2.5 times, on a mV /  $\mu\text{g C}$  basis, versus that of Schaefer and Whiticar (2007)(see example Figures 2.1.2 and 2.1.3). Validation of the precision and accuracy for  $\delta^{13}\text{C}/^{12}\text{C}$  measurements from gases occluded in glacial ice using the improved instrumental set-up

is, however, not as straight-forward. The main challenges lie in the processes that occlude the air in the ice matrix (that of firm compaction through time, which is difficult to replicate for artificial samples) and the lack of readily available, uncompromised glacial ice for repeated measurements. To establish the precision and accuracy of the method outlined in Sections 2.1.1 and 2.1.2, several techniques were used including: 1) blank tests, 2) introduction of atmospheric air samples via the syringe port, 3) measurement of ice samples made by equilibrating atmospheric air with distilled water, and 4) measurement of a small number of samples from the GISP2 ice core (described in Section 3.1).

Basic blank tests with the complete extraction procedure (including post-combustion trapping) initially yielded values consistently larger than 100 mV (0.33 nA) ( $m/z$  44 peak size), which is greater than 33 % of the stated minimum permissible sample signal (290 mV; 0.97 nA). This situation was corrected by the implementation of He gas pre-scrubbing (described in Section 2.1.5). During the course of regular analysis, the dry blanks were consistently below 65 mV (0.22 nA) and more commonly below 40 mV (0.13 nA). The slight increase in blank values from Schaefer (2005) is a result of the post-combustion trapping, which, as previously described, serves to increase peak height approximately 2.5 times that of non-post-combustion trapped samples (see Figures 2.1.2 and 2.1.3). The increase in both blank and sample size then results in the same relative contribution of the blank to the measured signal for non-trapped, and post-combustion trapped, analyses. The maximum blank contribution was ca. 5 % of the sample signal, while more commonly  $< 3$  %. Samples were corrected for the blank as per Schaefer and Whiticar (2007).



Peak No.	Start (s)	Rt (s)	Width (s)	Ampl.	Ampl.	Ampl.	Area All	$\delta^{13}\text{C}/^{12}\text{C}$
				44 (mV)	45 (mV)	46 (mV)	(Vs)	(‰ VPDB)
1 (Ref)	26.8	46.1	37	1100	1218	1495	21.76	-47.5
2 (Ref)	86.6	105.6	36.8	1063	1177	1444	21.41	-47.53
3 (CH <sub>4</sub> )	680.5	686.6	28.3	1215	1347	1670	5.19	-47.57
4 (Ref)	819.7	831.1	29.1	1112	1230	1510	14.91	-49.5

Figure 2.1.3: Example mass spectrogram of an 8 ml sample of atmospheric air run through the instrumental set-up described here. The spectrogram shows the three measured ion intensities of the sample ( $m/z$  44, 45, and 46 in mV, listed as Ampl. in the data table above). The first two flat-top peaks are reference gas pulsed into the IRMS. The peak at  $\sim 520$  s is  $\text{N}_2\text{O}$ , and then the  $\text{CH}_4$  peak. Note the lack of CO peak in both the intensity (bottom) and ratio (top) plots. The reference gas is pulsed into the IRMS after the  $\text{CH}_4$  has eluted to account for any drift in instrument response. The instrument response (mV /  $\mu\text{g C}$ ) for this run was 83.68, or 2.9 times that of the example trace in Figure 2.1.2.

Wet blank analysis has been examined by Schaefer and Whiticar (2007) and has not been reexamined on the basis that the instrumental set-up has not been greatly modified in the sample chamber and water trap, and thus similar performance is anticipated. Schaefer and Whiticar (2007) noted a slight increase in blank values when measuring methane-free ice samples (30 – 50 mV). This was attributed to the possibility of residual  $\text{CH}_4$  in the blank sample water (one set was from water that had been extensively boiled to degas it, and the other set was from meltwater refrozen from

previous extractions) or the from incomplete extraction during the previous run. The isotope effect was assumed to be  $\leq 0.15$  ‰. Other causes of high blanks reported by Schaefer and Whiticar (2007) were carefully avoided, such as overheating of the sample chamber and excessive water build up in the extraction line.

While the measurement of an introduced gas, into a dry sample chamber, does not recreate many of the unique conditions that are present in an ice extraction (gas interaction with melt water, water accumulation in the water trap, sample chamber heating and cooling cycles, and time period of the gas in the sample chamber), it does form an effective test of the accuracy of the set-up in less challenging conditions, and can help with understanding of the possible biases introduced into the system during ice measurements. As an initial test, 23 replicates were performed over a 5 day period through injections of outside air of varying amounts (7 – 10 ml; ca. 800 – 1000 pmol) giving a mean  $\delta^{13}\text{CH}_4$  value of  $-47.65 \pm 0.21$  ‰ ( $1\sigma$  standard deviation). Additionally, air samples were measured at the start and end of every sampling day, as well as regularly in-between samples. These samples had a mean  $\delta^{13}\text{CH}_4$  value of  $-47.51 \pm 0.29$  ‰ ( $n = 48$ ). The standard deviation will be elevated above its true value due to no attempt to correct for the  $\delta^{13}\text{CH}_4$  seasonal cycle (measured for the nearby Olympic Peninsula to have an amplitude of 0.11 ‰ [Quay et al., 1999]). The actual value of the seasonal cycle at the laboratory location is unknown.

To recreate the conditions of a natural sample ice extraction, artificial ice samples were created and analysed. The samples are made from deionized water first equilibrated with atmospheric air, outside of our laboratory, by lengthy stirring (usually greater than 12 hours). The water samples are then frozen in plastic containers (between ca. 150 – 250

g of water). The artificial ice samples do not present the ideal test, as they are not glacial ice. However, Schaefer (2005) demonstrates that these artificial samples are internally consistent, and are consistent with the air with which they were equilibrated. The artificial ice was measured routinely when running glacial ice samples to ensure system performance ( $\delta^{13}\text{CH}_4$  of  $-47.51 \pm 0.29$  ‰;  $n = 32$ ; no correction for seasonal variations). The identical accuracy and precision of the ice samples compared to the air samples demonstrates that artificial ice samples faithfully record the atmospheric  $\delta^{13}\text{CH}_4$  value, and that the extraction set-up does not introduce any artifacts during wet extractions.

#### *2.1.5. Further notes*

Due to the numerous steps, small sample size, and lengthy trapping times of the gas stream employed, it is important that the extraction line is performing well to ensure precise and accurate measurements. Two key innovations deserve mention here: 1) helium stream pre-scrubbing, and 2) effective post- sample clean out procedures.

During the extraction procedure the gas stream is focused upon a HayeSep<sup>®</sup> D loop for 10 minutes to trap the sample  $\text{CH}_4$ . With a flow rate of  $160 \text{ ml gas min}^{-1}$ , 1.6 L of gas passes through the trap. If that gas has contaminant  $\text{CH}_4$ , that  $\text{CH}_4$  will contribute to higher blank values. Testing of 10 ultra-purity grade 5.0 He tanks delivered to our lab found the tank methane concentrations to vary from  $< 5$  ppbv to  $> 40$  ppbv (measured with Isometric Instruments GYRO<sup>™</sup> laser-based spectrometer). The most contaminated tank would cause an increase in blank signal of up to 200 mV (0.67 nA) ( $m/z$  44 peak) using the post-combustion technique. To protect against the higher methane concentration tanks, a scrubbing-HayeSep<sup>®</sup> D trap (100 g in 70 cm of  $1/8^{\text{th}}$  inch diameter coiled stainless

steel tubing) was installed upstream of the pre-concentration set-up (Figure 2.1.1). This scrubbing-HayeSep<sup>®</sup> D trap is immersed in LN<sub>2</sub> and only released at the end of the measurement day. The large capacity of the scrubbing trap, and relatively small contaminant concentration, allow for efficient removal of gas stream methane without risk of overloading, or 'break-through', of the contaminant CH<sub>4</sub>.

The second innovation deals with the large amounts of water vapour carried by the gas stream leaving the extraction chamber. It is vital to ensure this water is removed from the instrumental set-up after each ice extraction. To accomplish this, the first step is to stop the flow of He immediately after the gas flow through the HayeSep<sup>®</sup> D has been switched from the load position to inject. This prevents more water vapour from transferring to the water trap. The sample chamber is then opened, the meltwater removed, and the chamber wiped dry. Once the chamber is replaced, and filled with He to atmospheric pressure, the water trap is opened to atmosphere prior to the CO traps via a Swagelock<sup>®</sup> fitting to allow venting and drying of the water trap. The other end of the fitting (attached to the rest of the extraction line) is sealed from the air by a piece of plugged tubing. The high flow rate through the chamber (160 ml /min) is used to push the water vapour through the water trap while the trap is heated (ca. 150 °C) via heat tape for 10 to 15 minutes. It was found to be important that this cleaning happened after each sample. If this cleaning was not performed, instrumental performance was found to degrade rapidly.

Once dry, the water trap is refitted into the Swagelock<sup>®</sup> fitting and sealed. This joint is then leaked tested by pressurizing the chamber (ca. 20 psi) and using a gas leak detector (Gow Mac Instrument Co.) on the union. As an additional note about leaks, it is

important to protect the instrumental set-up against all forms of vibration, which will loosen unions over time. To protect against this, the set-up was hard mounted and isolated from sources of vibrations (e.g. rotary pumps, fans, etc.).

## 2.2. Age scale

Ice sheet margins are potentially easily-accessed sources of ancient ice. Snow deposited on the top of the ice sheet will compact to ice, flow through the ice sheet, and eventually emerge in the ablation zone, with the oldest ice located closest to the margin (Figure 1.4.1) [Reeh et al., 2002]. The Pákitsoq location (Section 1.4.1) offers ancient ice at the surface in large-scale, ablation zone outcrops. These outcrops exhibit features similar to rock outcroppings, including synclines and anticlines, as well as sections that have folded back upon themselves [Petrenko et al., 2006; Schaefer et al., 2009]. Field measurements of CH<sub>4</sub> concentration (conducted on-site with GC-FID) were used to correlate the basic stratigraphy with that of GISP2 for ice sampling [Petrenko et al., 2006]. To establish the age of the air bubbles within the Pákitsoq ice stratigraphy, it is necessary to utilize records of other ice cores from similar locations, both geographically and of similar characteristics, such as temperature and accumulation rate, to the snow deposition zone for Pákitsoq ice. Ice sheet flow modelling determined the location of snow deposition, for Pákitsoq up to the Last Glacial Maximum (LGM), to be located about 190 km south and 40 km west of the GISP2 site (Figure 1.3.2) [Reeh et al., 2002]. Four parameters are used to determine the age scale of the Pákitsoq ice [Petrenko et al., 2006]: 1)  $\delta^{15}\text{N}$  of atmospheric N<sub>2</sub>; 2)  $\delta^{18}\text{O}_{\text{ice}}$  from the ice matrix; 3) methane concentration, all from GISP2, Greenland; and 4)  $\delta^{18}\text{O}_{\text{atm}}$  of atmospheric O<sub>2</sub> record from Siple Dome, Antarctica [Severinghaus et al., 2009].

The present day  $\delta^{18}\text{O}_{\text{ice}}$  value at the Pákitsoq deposition site is about 3‰ lower than at GISP2. Since the  $\delta^{18}\text{O}_{\text{ice}}$  value is recording variations in local temperature, seasonality of precipitation, moisture sources, and other influences [Jouzel et al., 1997], this observed offset can be expected. However, the  $\delta^{18}\text{O}_{\text{ice}}$  values are useful as the magnitude of change in the  $\delta^{18}\text{O}_{\text{ice}}$  values of the climate transitions should be similar to that observed in GISP2 record. The Pákitsoq values are thus referenced to the Grootes and Stuiver (1997) GISP2 dataset.

The  $\delta^{15}\text{N}$  record is influenced by the diffusive column height (DCH), which in turn, is influenced by the deposition site's temperature and accumulation rate, and possibly wind speed [Sowers et al., 1992; Schwander et al., 1997; Severinghaus et al., 2003]. The DCH influences the  $\delta^{15}\text{N}$  values by changing the distance in the firm that gravitational fractionation can occur. Thermal fractionation also influences the  $\delta^{15}\text{N}$  values (see Section 2.3.1) and is dependent upon rapid temperature changes at the deposition site. Due to the proximity of the Pákitsoq and GISP2 sites, they are expected to have similar climatic history. The Pákitsoq measurements are compared to GISP2 values from J. Severinghaus (unpublished, 2009). This high-resolution dataset contained unpublished values, as well as, values from Kobashi et al., (2008a); Severinghaus et al., (1998); Headly, in prep. (2008); and Severinghaus and Brook (1999).

The  $\delta^{18}\text{O}_{\text{atm}}$  value is a measure of the history of climate through deviation of the  $\delta^{18}\text{O}_{\text{atm}}$  value from seawater  $\delta^{18}\text{O}$  (Dole effect). The  $\delta^{18}\text{O}_{\text{atm}}$  value is also sensitive to changes in seawater  $\delta^{18}\text{O}$ , which reflect global ice sheet volume changes. The  $\delta^{18}\text{O}_{\text{atm}}$  value is globally well-mixed, and has recently become available with high temporal

resolution and measurement precision (Figure 2.2.1)[Severinghaus et al., 2009]. This data set, from Siple Dome, Antarctica is chosen over the current GISP2 dataset

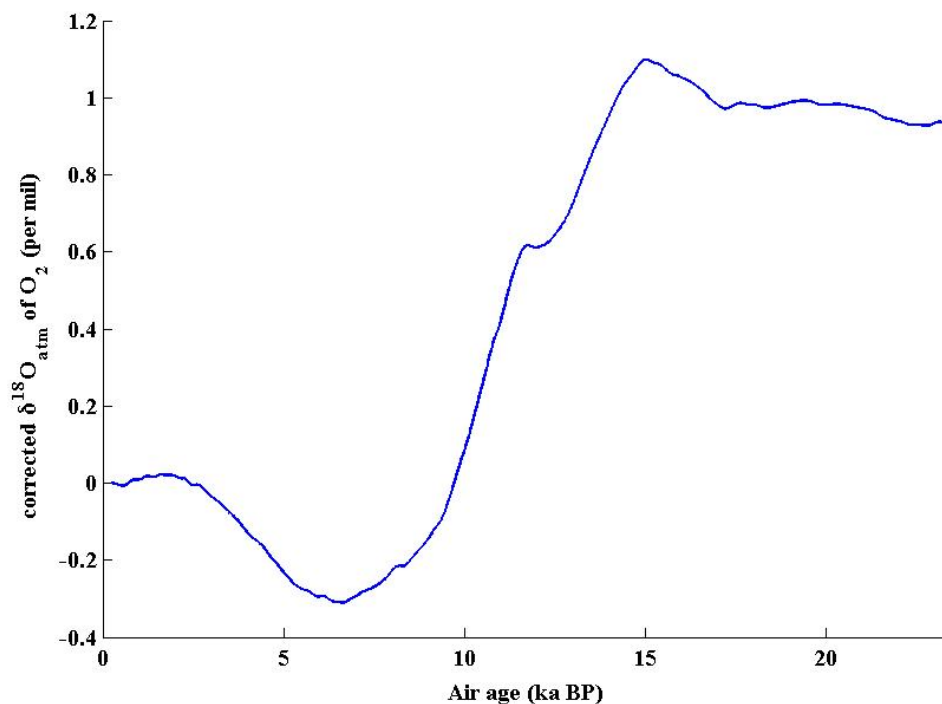


Figure 2.2.1: Subset of Siple Dome  $\delta^{18}\text{O}_{\text{atm}}$  dataset corrected for both gravitational and gas-loss fractionation [Severinghaus et al., 2009 Supplementary Material]. The high rate of change in the  $\delta^{18}\text{O}_{\text{atm}}$  value since ca. 15 ka BP makes it a useful parameter for age scaling.

[Bender et al., 1999], due to its greater precision and inclusion of a gas-loss correction. Ice fracturing can lead to an artifactual fractionation in the isotopes of Ar and  $\text{O}_2$ , due to the gas lost from the ice matrix [Severinghaus et al., 2009 supplementary material]. The fractionation is believed to occur in ice cores prior to annealing as they depressurize while being brought up the borehole, or cracking that can occur as the ice warms during handling on the surface. Both of these processes are not expected to have occurred to the Pákitsoq ice as the depressurization and warming would have occurred very gradually, avoiding the high stresses that allow for cracking and gas loss (J. Severinghaus, personal

communication, 2009). Thus, the  $\delta^{18}\text{O}_{\text{atm}}$  record from Siple Dome is assumed to more appropriately represent the global  $\delta^{18}\text{O}_{\text{atm}}$  record and should be identically recorded in the Pákitsoq ice, assuming that the correction used by Severinghaus et al. (2009) is correct.

Methane is a globally well-mixed gas with inter-hemispheric mixing times on the order of less than 1 year. Excluding any in-situ alterations (see Section 3.2), the methane record from GISP2 should be identical to that measured in the Pákitsoq ice. Both  $\delta^{18}\text{O}_{\text{atm}}$  and  $\text{CH}_4$  concentration have been used previously to correlate ice core records from Greenland and Antarctica based upon their well-mixed nature [Bender et al., 1994; Blunier and Brook, 2001].

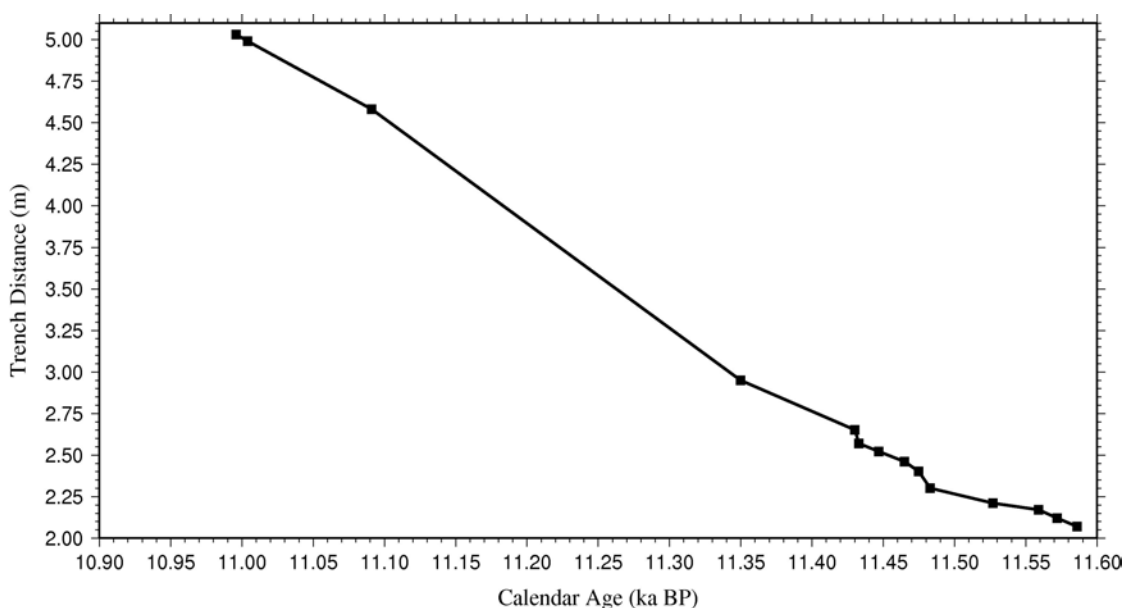


Figure 2.2.2: Example age tie-points for calendar age to Pákitsoq trench distance. The example below is for the 2003 sampling season and covers the termination of the Younger Dryas into the Preboreal. These tie-points are used to determine the trench distant to calendar age relationship used for samples in this thesis. The calendar age – trench distance relationships are based upon linear relationships between a minimum of 3 age tie-points (see text below)

To determine an age scale for the samples presented in Section 3.3, the protocols determined by Petrenko et al. (2006); Schaefer et al. (2006); and Petrenko (2008) are followed with a few exceptions. The uncertainties of the parameters and age tie points are

detailed in Appendix 7.1. The  $\delta^{15}\text{N}$  record is found to be the most consistent between GISP2 and Pákitsoq, implying similar temperature and accumulation rates between the sites. This close correlation is found across all years and sampling location and thus this parameter is relied upon extensively for age assignments (also noted by V. Petrenko, personal communication 2009). Due to the much improved  $\delta^{18}\text{O}_{\text{atm}}$  record, this parameter is used more extensively in this work than with other workers [Petrenko *et al.*, 2006; Schaefer *et al.* 2006]. The Siple Dome record has a very high precision, however the Pákitsoq measurements precision is not as good (see Appendix 7.1), thus the  $\delta^{18}\text{O}_{\text{atm}}$  values are used as a secondary constraint on age tie points from the  $\delta^{15}\text{N}$  data, especially in situations where the  $\delta^{15}\text{N}$  presents two possible ages (e.g. either side of a dip/peak in the record). The  $\delta^{18}\text{O}_{\text{ice}}$  parameter is primarily used in time sections where the other parameters do not exhibit sufficiently unique features for an age determination. Use of methane concentration for age tie-points is avoided except in regions with very well-behaved Pákitsoq methane records (e.g. the YD termination or the Bølling initiation, see Section 3.3). Figure 2.2.2 is an example calendar age-to-trench distance age scale.

Additionally, the age scaling between tie points in this work is treated in a different manner than Schaefer *et al.* (2006). In Schaefer *et al.* (2006), the ages are scaled directly between each pair of tie points, treating each tie point as an absolute time point. Several uncertainties are present in the age assigned to each tie point including: 1) interpolation between data points in the GISP2 and Pákitsoq records; 2) measurement uncertainty for both records; and, 3) age scale uncertainties in the GISP2 and Siple Dome age scales. Due to these uncertainties, for this work, linear interpolation with a minimum of three age tie points is used to determine the age of samples from the horizontal trench

scale. Applying this age scale scheme to the data of Schaefer *et al.* (2006) results in only minor changes from the ages originally assigned (maximum change of 140 years with a mean change of 30; Figure 2.3.1). The absolute age scale (GISP2 depth to calendar age) used for all ages is that of Schaefer *et al.* (2006). This age scale differs from the common GISP2 age scale of [Brook *et al.*, 2000] by fixing the date of the YD termination to  $11,570 \pm 0$  yr BP on the basis of tree ring records [Friedrich *et al.*, 1999]. The Pákitsoq  $\delta^{15}\text{N}$ ,  $\delta^{18}\text{O}_{\text{atm}}$ ,  $\delta^{18}\text{O}_{\text{ice}}$ , and laboratory measured  $[\text{CH}_4]$ , as well as information about instrumental techniques are available in Petrenko (2008) and Petrenko *et al.* (2006).

The age scale created in the manner described has differing levels of uncertainty depending on how unique are the parameters used for age correlation are within their respective records (e.g. using the peak OD-B transition  $\delta^{15}\text{N}$  value from GISP2 for age correlation allows a very certain correlation with the Pákitsoq maximum  $\delta^{15}\text{N}$  value. If a more intermediate value is chosen, then there is the added uncertainty of which side of the  $\delta^{15}\text{N}$  peak the Pákitsoq value matches), and how close the sample is to an inflection point in the tracers used to create the age scale. Age uncertainty close to, and within, abrupt climate transitions is estimated to be better than 1% absolute uncertainty for the Younger Dryas-Preboreal (YD-PB) transition, and less than 2% for the YD initiation and Oldest-Bølling (OD-B) transition [Petrenko, 2008]. The ages of samples older than the OD-Bølling transition, including the LGM, are not well constrained as there is little change in the four tracers used for the age tie-points. These data should be interpreted cautiously and possess absolute age uncertainties ranging up to several thousand years for the most uncertain LGM samples (see Appendix 7.3).

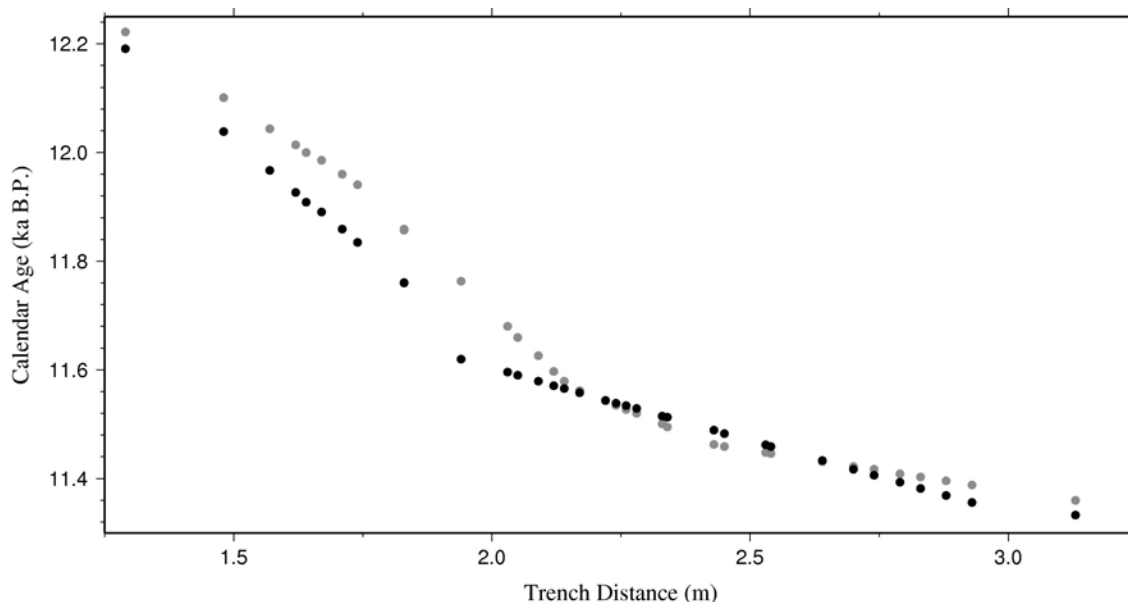


Figure 2.3.1: Difference in age scale between Schaefer et al. (2006)(grey dots) and this work (black dots) for the Schaefer et al. (2006) data.

### 2.3. Corrections to isotope values

As snow accumulates, it applies pressure to the snow layers below. This pressure results in a densification with depth, and thus with time. As the older snow, or firn, becomes denser, the pores within are compressed and the snow particles round. Eventually, the firn reaches a density where the pores close-off and the firn becomes ice with bubbles of trapped air (approximately 10% by volume [Raynaud et al., 1997]). Above this close-off point, air within the firn is able to communicate with the atmosphere. This leads to an age difference between the younger air within the bubbles and the older surrounding ice matrix. The depth of close-off varies with temperature and accumulation rate and is between 50 - 120 m for Greenland, with commonly deeper depths in colder, drier areas of Antarctica [Barnola et al., 1991]. The gas age-ice age difference is generally between 40 years for warm, high accumulation sites and 2700

years for cold and dry sites [Sowers et al., 1992]. During the time that gases are within the firn, but not yet sealed within pores, three main processes can influence the gases' isotope ratios: 1) gravitational settling, 2) thermal fractionation (Section 2.3.1), and 3) diffusion (Section 2.3.2). An additional effect, outside of the firn column, that requires correction is the isotopic disequilibrium that occurs during periods of rapidly changing concentration (Section 2.3.3)[Tans, 1997; Lassey et al., 2000].

### *2.3.1. Gravitational and thermal fractionation correction*

Gravitational fractionation is a process that will act upon species of differing masses to enrich the heavier species in the lower part of the firn. While gravitational fractionation is constant and dependent upon the mass of the isotope, thermal fractionation is dependent upon the thermal diffusion sensitivity of the species and the temperature difference between the surface and the close-off depth (with heavier species moving towards colder regions) [Grachev and Severinghaus, 2003]. Gases diffuse about 10 times faster than heat, so during a rapid climate change, the temperature difference between the surface and close-off is temporarily modified, promoting a detectable anomaly in the  $^{15}\text{N}/^{14}\text{N}$  ratios of  $\text{N}_2$  [Severinghaus et al., 1998]. These processes can be accommodated by using the separation of a 'constant' isotope tracer, such as the ratio of  $^{15}\text{N}/^{14}\text{N}$ . Since  $\delta^{15}\text{N}$  has been essentially constant for  $>10^6$  years [Mariotti, 1983], any firn measurements deviating from atmospheric value are related to gravitational settling and/or thermal fractionation. This ratio has been measured for the Pákitsoq ice (as in [Petrenko et al., 2006; Schaefer et al., 2006]) and used to correct the ice samples presented in Section 3.3 as has been done previously [Schaefer, 2005; Schaefer et al., 2006]. An example is provided in Figure 2.3.2.

Table 2.3.1: Parameters used as input for firn diffusion model. Methane concentration values are from Brook et al., (2000). The length of transition is calculated from the inflection points in the methane record. Accumulation rate is the GISP2 rate [Cuffey and Clow, 1997] with 50 % more accumulation added for the Pákitsoq site [Petrenko et al., 2006]. The surface temperature is 3 °C warmer than the GISP2 temperature [Severinghaus and Brook, 1999; Severinghaus et al., 1998]. The  $\alpha_T$  parameter is a linear interpolation between the values predicted by the Pákitsoq temperature and accumulation rate. For further information on this parameter, the reader is referred to Schaefer (2005) and Spahni et al., (2003). The  $\delta^{13}\text{CH}_4$  value is chosen to be representative of the values during the transition, although the value chosen for this parameter is not important (see Schaefer (2005) for logic).

Parameter	YD-PB transition	OD-B transition
Initial [ $\text{CH}_4$ ]	526	472
Final [ $\text{CH}_4$ ]	753	621
Length of transition (yr)	150	312
Accumulation rate (m ice / yr)	0.15	0.11
Surface temperature (°K)	237	233
$\alpha_T$	0.81	0.85
$\delta^{13}\text{CH}_4$ (‰)	-46.00	-46.70

### 2.3.2. *Firn diffusion correction*

Under circumstances of changing atmospheric concentration, the atmospheric signal of  $^{13}\text{CH}_4$  will reach the firn close-off zone delayed, with respect to the  $^{12}\text{CH}_4$  signal. This temporal offset is caused by the different diffusivities of the two species (see Trudinger et al. (1997) for more information about how this derived). This can be corrected by use of a model that calculates the density of the firn, its porosity, and thus its effective diffusion co-efficient. A model from Schaefer (2005) that performs these calculations, based upon the work of Herron and Langway (1980) and Schwander et al. (1993); Schwander et al. (1997), was used unadulterated for all time periods where it was required, i.e. during periods of rapidly changing atmospheric  $\text{CH}_4$  concentration. The model parameters for each time period are listed in Table 2.3.1. The values for the firn

diffusion correction are listed in Table 7.3.3 and an example time period is presented in Figure 2.3.2.

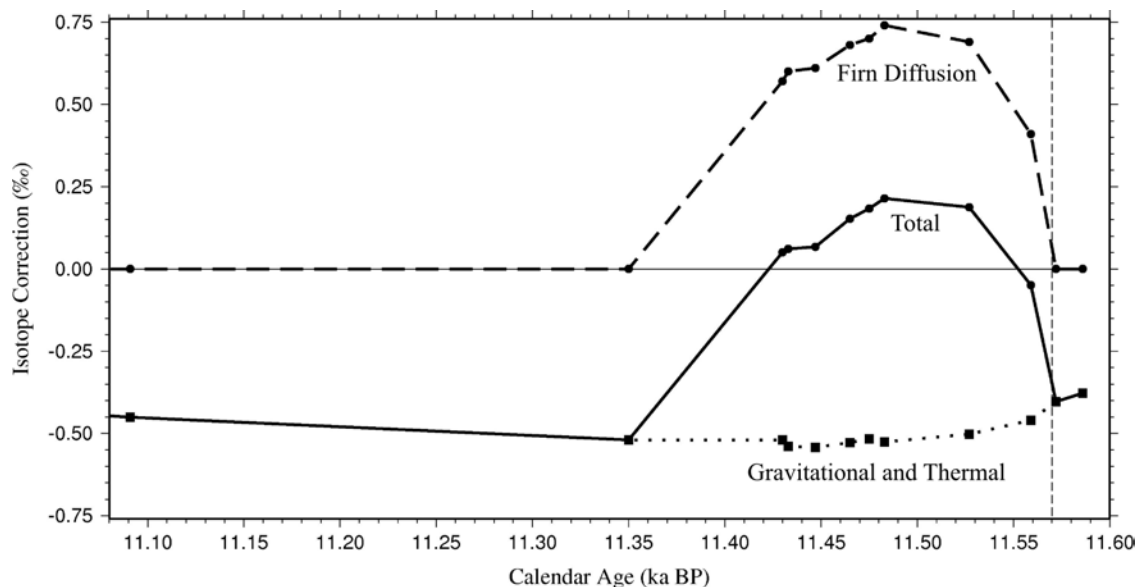


Figure 2.3.2: Younger Dryas - Preboreal transition methane isotope corrections for thermal, gravitational, and firm diffusional fractionation. The thin line at 0‰ indicates no correction from the measured  $\delta^{13}\text{CH}_4$  to the true atmospheric value. The gravitational and thermal fractionation correction (squares; dotted line) provided by the measured  $\delta^{15}\text{N}$  value consistently acts to correct the observed  $\delta^{13}\text{CH}_4$  to more negative values. The firm diffusion correction (circles; dashes) is non-zero only during the rapid concentration increase, and acts to correct the  $\delta^{13}\text{CH}_4$  to more positive values. The total correction to the measured  $\delta^{13}\text{CH}_4$  value is given by the solid line. The vertical dashed line is placed at the termination of the YD period (11.570 ka BP [Friedrich et al., 1999]).

### 2.3.3. Atmosphere disequilibrium

Atmospheric disequilibrium occurs when the atmospheric methane concentration and/or stable isotope values change rapidly, causing a temporary offset between the measured atmospheric value and the value of the aggregated sources. This was first described by Tans (1997) and later expanded by Lassey et al. (2000). The disequilibrium effect is evident in both concentration and stable isotope values with the latter exhibiting relatively slower adjustment to steady-state values.

Isotopic disequilibrium is important to accommodate if the measured atmospheric values are to be used to interpret the changes in the methane source during a time period of rapid changes. The offset between atmospheric values and values in steady-state can be significant, eg. it is calculated to be 101 ppbv and 0.62‰ in 1990 due to the disequilibrium initiated by the methane concentration increase since the Industrial Revolution [Lassey et al., 2000]. The model of Lassey et al. (2000) is applied to the Younger Dryas to Preboreal transition, as this is the only transition measured with extensive samples in the middle of the transition. The Lassey et al. (2000) model requires a source and sink budget for the time periods prior to- and post- transition. The YD and Preboreal source and sink budgets are from 4-box atmospheric methane model simulations (described in Section 2.4.1; results in Section 3.4). The transition period is set to 150 years (same value as used in the firn diffusion model, see Table 2.3.1) and the correction is applied with the start of the CH<sub>4</sub> rise assumed to occur at 11.570 ka BP, coeval with the climate warming at the end of the YD. This assumption should introduce a maximum uncertainty, in the matching of disequilibrium corrections to measurement values, of 30 years following Severinghaus et al. (1998) determination of a 0 – 30 year delay between the onset of warming and the rise in the atmospheric [CH<sub>4</sub>]. The correction factors, i.e., the magnitudes of disequilibrium between atmospheric value and the aggregated source, are then applied to the measured atmospheric values to determine the isotope value and concentration of the aggregated CH<sub>4</sub> source. The aggregated source  $\delta^{13}\text{CH}_4$  and concentration values for the YD termination are presented in Section 3.3.2. The model is also used to determine the aggregated source values of  $\delta\text{D-CH}_4$  from the Sowers (2006) data set (also presented in Section 3.3.2).

## 2.4. Atmospheric box model Monte Carlo simulations

To constrain methane emissions to the atmosphere from each source in the different time periods investigated, two steady-state atmospheric box models were created following Seinfeld (2006) and Fischer et al. (2008). The box models contain four and six boxes, respectively. The 6-box model (Figure 2.4.1) is described in detail in Appendix 7.2.1. These box models are not intended to investigate periods of rapid methane dynamics (such as the Younger Dryas- Preboreal transition), which would require a non-steady-state model.

### 2.4.1. Description of 4-Box atmospheric model

The 4-box model contains two troposphere and two stratosphere boxes separated into Northern and Southern hemispheres (Figure 2.4.2). The box models are applied during periods of stable methane concentration, and thus are in steady-state and can be solved analytically. The solution follows Seinfeld (2006) with prescribed air mass

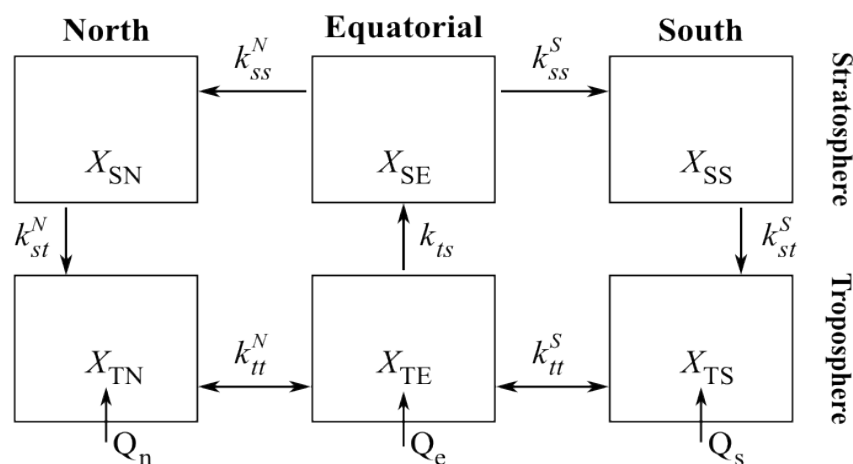


Figure 2.4.1: Schematic of 6-box atmospheric methane model. The mixing ratio of methane in each box,  $X$ , is balanced by sources,  $Q$ , in each box; by sink terms,  $\lambda$ , (not shown); and by transfers between boxes,  $k$ . Subscripts denote 1) stratosphere (S) or troposphere (T), 2) North (N), Equatorial (E), South (S). Subscripts of the transfers between boxes denote 1) box that flux is leaving, 2) box that flux is entering. Full details of the model are provided in Appendix 7.2.1.

exchange,  $k$ , between boxes (Table 7.2.2). The sources are emitted into the troposphere boxes based upon the prescribed hemispheric distribution of source flux (Table 7.2.3).

The removal processes are treated as a first-order rate constant,  $\lambda$ . The sink is initially

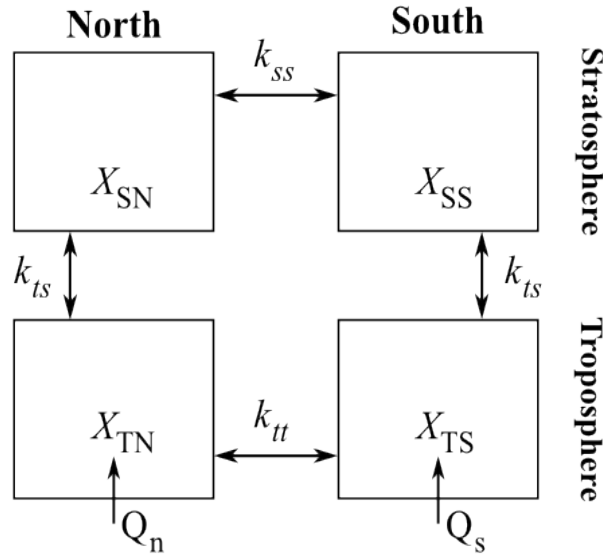


Figure 2.4.2: 4-box model of atmosphere methane cycle. The mixing ratio of methane in each box,  $X$ , is balanced by sources,  $Q$ , in each box; by sink terms,  $\lambda$ , (not shown); and by transfers between boxes,  $k$ . Subscripts are as in Figure 2.4.1.

prescribed with an atmospheric  $\text{CH}_4$  lifetime of 8.6 yrs, consistent with estimates [Denman et al., 2007]. The change in mixing ratio,  $X$ , with respect to time for the Northern troposphere ( $tn$ ) can be expressed as:

$$(2.4.1.) \quad dX_{tn}/dt = Q_n - \lambda X_{tn} - k_{ts}(X_{tn} - X_{sn}) - k_{tt}(X_{tn} - X_{ts})$$

where the sources ( $Q_n$ ) are countered by the troposphere loss ( $\lambda X_{tn}$ ), exchange with the Northern stratosphere ( $k_{ts}(X_{tn} - X_{sn})$ ), and exchange with the Southern troposphere ( $k_{tt}(X_{tn} - X_{ts})$ ). The other boxes can be expressed similarly, with the exception of no sources in the stratosphere:

$$(2.4.2.) \quad dX_{ts}/dt = Q_s - \lambda X_{ts} - k_{ts}(X_{ts} - X_{ss}) - k_{tt}(X_{ts} - X_{tn})$$

$$(2.4.3.) \quad dX_{sn}/dt = -\lambda X_{sn} - k_{ts}(X_{sn} - X_{tn}) - k_{ss}(X_{sn} - X_{ss})$$

$$(2.4.4.) \quad dX_{ss}/dt = -\lambda X_{ss} - k_{ts}(X_{ss} - X_{ts}) - k_{ss}(X_{ss} - X_{sn})$$

At steady state, the methane sources and sinks balance, thus the change in mixing ratio with respect to time is zero. Equations 2.4.1 through 2.4.4. can then be easily solved analytically. To incorporate isotope tracers, the less abundant isotope is treated as a separate tracer in a manner similar to Tans (1997). The  $^{13}\text{C}$  or D species is calculated as a mixing ratio ('isotopic methane'), in this case  $X^{13}$ , via:

$$(2.4.5.) \quad X^{13} = (\delta^{13}\text{C}/1000 + 1) * R_{std}^{13}$$

where the delta notation,  $\delta^{13}\text{C}$  or  $\delta\text{D}$  (as defined in Section 2.1.2), is used along with the  $R_{std}$  value ( $^{13}\text{C}/^{12}\text{C}$  ratio = 0.0112372, relative to VPBD; H/D ratio = 0.00015575, relative to VSMOW) [Craig, 1957]. The isotopic methane is treated in a similar manner to the total methane ( $^{13}\text{C} + ^{12}\text{C}$ ) as described previously:

$$(2.4.6.) \quad dX_{in}^{13}/dt = Q_n^{13} - \alpha \lambda X_{in}^{13} - k_{ts}(X_{in}^{13} - X_{sn}^{13}) - k_{tt}(X_{in}^{13} - X_{ts}^{13})$$

with the addition of a term for the kinetic fractionation factor,  $\alpha$ , to account for the slower destruction of isotopic methane, as compared to total methane. The sink terms in the troposphere include oxidation by OH radicals and uptake by methanotrophic bacteria in aerated soils. The sink term in the stratosphere is oxidation by OH, Cl, and O( $^1\text{D}$ ) radicals, which are treated as a single term sink. The sink provided by atomic chlorine in the marine boundary layer as described by Allan et al. (2001a); Allan et al. (2001b); Allan et al. (2005); and Allan et al. (2007) is not included. This sink has a large isotope effect for carbon ( $\epsilon = 66 \%$ ; where  $\epsilon = 10^3(\alpha - 1)$ ) [Saueressig et al., 1995] and is possibly important (estimated to be 5 % of the present day global atmospheric  $\text{CH}_4$  sink [Allan et al., 2007]). However, this sink has not been explicitly included in box model simulations.

The fractional proportion of the total sink contributed by each removal term is globally uniform, and fixed across all time periods at 0.879 for the OH radical, 0.052 for the soil sink, and 0.062 for stratospheric loss terms. This fractional distribution is consistent with other estimates [Denman et al., 2007]. The proportion of each sink and the  $\epsilon$  values from Table 2.4.4 are used to calculate the  $\alpha$  fractionation factors used in Equation 2.4.6. The remaining boxes follow the same approach using isotopic methane as in Equation 2.4.6. The deuterium tracer is formulated similarly and calculated independently of carbon.

The box model results are compared against polar records from both Antarctica and Greenland to determine the validity of the simulation. The use of polar records for comparison has been applied before [e.g. Chappellaz et al., 1997; Brook et al. 2005]. For methane concentration, it is an acceptable approximation that the southern box is homogeneous and will be well represented by measurements in the Antarctica core [Brook et al., 2005]. However, for the northern box, there exists a gradient in concentration within the Northern Hemisphere for present day. Following Chappellaz et al. (1997), and lacking any information about this gradient in other time periods, the difference between the concentration at the GISP2 site and the box average is set to 7 % of the total interhemispheric difference.

To parameterize the model, CH<sub>4</sub> emissions into the troposphere boxes are initially prescribed with fixed isotope values and source emission strengths (Table 2.4.4). These emissions levels are chosen to represent best present knowledge, are in line with total emission estimates [Denman et al., 2007], and measurements of fossil methane

proportion [Quay et al., 1999; Lassey et al., 2007; Etiope et al., 2008b]. The model is then parametrized (primarily through adjustment of the constants for exchange of air

Table 2.4.1: Isotopic fractionation values for the three sink terms. Values are referenced to VPDB for  $^{13}\text{C}$  and VSMOW for D.  $\epsilon$  values are defined:  $\epsilon = 10^3(\alpha - 1)$

Sink	$\epsilon_{\text{C}}$ (‰)	$\epsilon_{\text{D}}$ (‰)
OH oxidation	-3.9 <sup>a</sup>	-231 <sup>b</sup>
Soil uptake	-22 <sup>c</sup>	-80 <sup>d</sup>
Stratospheric Loss	-12 <sup>e</sup>	-160 <sup>f</sup>

<sup>a</sup>Sauerssig et al. (2001)  
<sup>b</sup>Gierczak et al. (1997)  
<sup>c</sup>King et al. (1989); Tyler et al. (1994); Reeburgh et al. (1997)  
<sup>d</sup>Snover and Quay, (2000)  
<sup>e</sup>Wahlen et al. (1989); Brenninkmeijer et al. (1995)  
<sup>f</sup>Irion et al. (1996)

masses between boxes; Table 7.2.2) to simulate output that will fall within modern (1990s) constraints for: 1) polar methane concentrations, 2) inter-polar concentration gradient [Quay et al., 1999; Dlugokencky et al., 2003], and 3)  $\delta^{13}\text{CH}_4$  and  $\delta\text{D-CH}_4$  for both hemispheres [Quay et al., 1999]. The model required little tuning from initial values.

The parameterized box model is then used for Monte Carlo simulations. The atmospheric lifetime and strength of each source is allowed to randomly vary within predefined limits (uniform distribution). The box model is run forward and compared to constraints provided by 1)  $\text{CH}_4$  concentration [Quay et al., 1999; Brook et al., 2000; Dällenbach et al., 2000], 2) inter-polar gradient [Quay et al., 1999; Dällenbach et al., 2000], 3)  $\delta^{13}\text{CH}_4$  from both hemispheres [this work; Fischer et al., 2008], and 4)  $\delta\text{D-CH}_4$  from the Northern hemisphere [Sowers, 2006, 2009]. The values of the constraints are described in Section 2.4.1. The simulation is successful if the scenario generated values that are: 1) within 10 ppbv of methane concentration, 2) within 15 ppbv for inter-polar

concentration gradient, 3) within 0.4‰ for  $\delta^{13}\text{CH}_4$  from both hemispheres, and 4) within 10‰ of the  $\delta\text{D-CH}_4$  value. The model is allowed to run until 10,000 possible realizations are achieved. The successful realizations define a probability distribution of possible values for methane atmospheric lifetime (years) and each source flux ( $\text{Tg CH}_4 \text{ yr}^{-1}$ ). For comparison between time periods, the distributions are normalized (Section 2.4.1).

Table 2.4.2: Box model stable time periods for Monte Carlo simulations. The temporal boundaries of each time period are listed. The time periods are chosen based upon periods of stable atmospheric methane mixing ratio.

Time Period		Ages included (ka BP)
1990s		
Preindustrial Holocene	PIH	0.6 - 1.2
Preboreal	PB	9.5 – 11.5
Younger Dryas	YD	11.63 – 12.5
Bølling-Allerød	BA	12.7 -14.5
Last Glacial Maximum	LGM	16.7 – 20.3

Monte Carlo simulations are run for 6 different time periods of stable methane dynamics (Table 2.4.2). For each period, slight adjustments are made in the source configurations between the boxes. This adjustment is necessary, as the model could not find acceptable realizations with constant source-configurations across the different time periods. The necessity of changing source flux-configurations is expected given the large changes in ice sheets, sea level, aridity etc. over the course of the deglaciation. The source configurations and  $\delta^{13}\text{CH}_4$  for each time period are listed in Table 7.2.3.

The  $\delta^{13}\text{CH}_4$  values are varied across time periods following Schaefer and Whiticar (2008) for wetland, aerobic plant methane (APM), biomass burning, ruminants, and termites. Geologic emissions of methane (GEM), aquatic, and marine gas hydrate sources

are assumed invariant due to insensitivity to vegetation change. When the modern  $\delta^{13}\text{CH}_4$  value chosen for a source is not the same as in Schaefer and Whiticar (2008), the source  $\delta^{13}\text{CH}_4$  value is still modulated across time periods in the same manner as their work. Additionally, Schaefer and Whiticar (2008) address only the present, PIH, and LGM, while Whiticar and Schaefer (2007) include the YD. To adjust for the other time periods investigated (PB and BA) the approach of Schaefer and Whiticar (2008) is used to account for changes in the  $\delta^{13}\text{C}$  of the precursor material; principally changes in the atmospheric  $\delta^{13}\text{CO}_2$  and changes in  $\text{C}_3 / \text{C}_4$  vegetation distribution. The  $\delta^{13}\text{CO}_2$  value for each time period are listed in Table 2.4.3. The globally summed changes in  $\text{C}_3 / \text{C}_4$  vegetation distribution for these time periods is presently unknown with numerous reports, often conflicting, from several regions world-wide [e.g. Huang et al., 2001; Hughen et al., 2004, Nordt et al., 2008]. To accommodate this uncertainty, the PB is first simulated by adjusting the PIH and YD source  $\delta^{13}\text{CH}_4$  values to changes in the  $\delta^{13}\text{CO}_2$  for the PB relative to the PIH, or YD, respectively. The simulation results for these two approaches are indistinguishable. Thus the YD  $\delta^{13}\text{CH}_4$  source values, adjusted for PB  $\delta^{13}\text{CO}_2$  values, are used for the simulations presented here. This same approach is also used for the BA period with  $\delta^{13}\text{CH}_4$  source values from the YD and LGM. The YD  $\delta^{13}\text{CH}_4$  source values, with adjustment for BA  $\delta^{13}\text{CO}_2$  values, is then chosen for the remainder of the simulations.

While the box model simulations account for changing  $\text{C}_3 / \text{C}_4$  vegetation distribution and  $\delta^{13}\text{CO}_2$ , the model does not account for changing isotopic fractionation in wetlands due to changing climatic conditions [Schaefer and Whiticar, 2008], changes in

the net to gross CH<sub>4</sub> production ratio [eg. Sowers, 2006], or changes in the sink fractionation due to changing climate or fractional sink contribution.

The  $\delta\text{D-CH}_4$  values for the methane sources are ultimately derived from the deuterium/hydrogen of the water in the source region [Whiticar, 1999] and is thus assumed to be invariant. Changes to global  $\delta\text{D-CH}_4$  due to ice sheet influence on the mean ocean  $\delta\text{D-H}_2\text{O}$  value (estimated to be 7.5 ‰ VSMOW during the LGM [Schrag et al., 2002]), as proposed by Sowers (2006), are not incorporated.

Gas hydrates can form from biogenic or thermogenic CH<sub>4</sub> depending on the source of the CH<sub>4</sub> that is being trapped by the hydrate stability zone. For the purpose of this box model analysis, all hydrates are assumed to be biogenic, primarily from the carbonate reduction pathway. Any hydrates that are of thermogenic origin are implicitly included as part of the geologic methane source.

Table 2.4.3: Mean  $\delta^{13}\text{CO}_2$  values for stable time periods simulated with atmospheric box model

Time period	Calendar Age Spread (ka BP)	Mean $\delta^{13}\text{CO}_2$ (‰)
PreIndustrial Holocene	0.6 - 1.2	-6.44 <sup>a</sup>
Preboreal	9.5 -11.5	-6.55 <sup>b</sup>
Younger Dryas	11.63- 12.5	-6.79 <sup>b</sup>
Bølling-Allerød	12.7 – 14.5	-6.81 <sup>b</sup>
LGM	16.7 – 20.3	-6.79 <sup>b</sup>

<sup>a</sup>Francey et al. (1999)

<sup>b</sup>Smith et al. (1999)

The variable space that the Monte Carlo is allowed to explore for each source was determined by several trials and inspection of the probability distribution function of the time period simulated. The upper and lower limits are set to ensure the variable space is adequately explored, while not being overly computationally expensive.

Each source has a distribution of carbon and hydrogen isotope ratios (e.g. boreal wetlands can vary over 20‰ [Chanton et al., 1995; Chasar et al., 2000]). The importance of the chosen representative values is investigated through sensitivity runs which vary the isotope ratios for different sources (Table 2.4.4). The sensitivity runs are also used to investigate the role of thermokarst lakes [Walter et al., 2006] and fen-dominated boreal peatlands [e.g. MacDonald et al. 2006] via adjustments in the 'boreal wetland' source  $\delta^{13}\text{CH}_4$  value (the model only distinguishes different sources by the characteristic isotope values and the hemispheric flux distribution, i.e. there is no mechanistic or geographic information that excludes either source). Sensitivity tests are also used to investigate the dynamics of terrestrial biogenic gas hydrates, which are believed to be characterized by a  $\delta\text{D-CH}_4$  value significantly  $^2\text{H}$ -depleted from that of marine biogenic gas hydrates. As gas hydrates function essentially as a gas storage reservoir, the source and characteristics of the gas that is stored in the clathrate form can vary widely. Terrestrial gas hydrates are assumed to have the same hemispheric flux distribution and  $\delta^{13}\text{CH}_4$  value as marine gas hydrates.

Table 2.4.4: Source methane flux and stable isotope ratios for the 1990s simulation. Source fluxes used to parameterize the model are as noted. Isotope ratios for sensitivity tests are in curved brackets. These sensitivity test values are assumed invariant across all time periods. Superscript symbols detail the source of the value chosen. The lower and upper methane flux limits for the Monte Carlo simulation of the 1990s are shown in brackets.

	Annual $\text{CH}_4$ flux (Tg $\text{CH}_4$ yr <sup>-1</sup> )	$\delta^{13}\text{CH}_4$ (‰ VPDB)	$\delta\text{D-CH}_4$ (‰ SMOW)
<b>Natural Sources</b>			
Tropical wetlands	98 [50 - 200]	-58.9 <sup>a</sup>	-315 <sup>b</sup>
Boreal wetlands	39 <sup>a</sup> [0 - 80]	-64.5	-360 <sup>b</sup>
-Thermokarst Lakes*		(-68.5)*	
-Fen dominated wetlands <sup>§</sup>		(-60) <sup>§</sup>	

(Continued on next page)

	Annual CH <sub>4</sub> flux (Tg CH <sub>4</sub> yr <sup>-1</sup> )	δ <sup>13</sup> CH <sub>4</sub> (‰ VPDB)	δD-CH <sub>4</sub> (‰ SMOW)
APM	25 [0 - 100]	-61 <sup>c</sup>	-348 <sup>d</sup>
Biomass burning	46 [0 - 100]	-24.6 <sup>a</sup> (-20)	-225 <sup>a</sup>
Gas hydrates -Terrestrial	13 [0 - 65]	-62.5 <sup>a</sup>	-190 <sup>a</sup> (-290)
Ruminants	80 <sup>a</sup> [40 - 120]	-60.5 <sup>a</sup>	-330 <sup>a</sup>
GEM	32 <sup>h</sup> [0 - 100]	-41.8 <sup>a</sup> (-25) <sup>‡</sup> (-50) <sup>‡</sup>	-200 <sup>a</sup>
Aquatic	14 <sup>e</sup> [5 - 25]	-56.8 <sup>e</sup>	-267 <sup>e</sup>
Termites	16 <sup>a</sup> [5 - 30]	-65 <sup>a</sup>	-390 <sup>a</sup>
<b>Anthropogenic Sources</b>			
Rice cultivation	66 <sup>f</sup> [30 - 100]	-63 <sup>a</sup>	-315 <sup>g</sup>
Landfills	40 <sup>a</sup> [20 - 60]	-55 <sup>a</sup>	-310 <sup>a</sup>
Natural gas	45 <sup>a</sup> [25 - 65]	-44 <sup>a</sup>	-180 <sup>a</sup>
Coal	45 [25 - 65]	-37 <sup>a</sup>	-140 <sup>a</sup>
<b>Global Total</b>	<b>559</b>		

<sup>a</sup> Values are from Whiticar and Schaefer (2007)

<sup>b</sup> Based upon estimate in Nakagawa et al. (2002)

<sup>c</sup> Value is an average based on Keppler et al. (2006) and Vigano et al. (2009) for detached plant material. Whole plant values are not used due to the non-biotic nature of the methane production. A weighted average between C<sub>3</sub> and C<sub>4</sub> plants was based upon 25% global grassland coverage with 57% of that C<sub>4</sub> plants [Collatz et al., 1998]

<sup>d</sup> The measurements of Vigano et al. (2009) are the only reported δD-CH<sub>4</sub> values. Value is a weighted average of C<sub>3</sub> and C<sub>4</sub> plants in same proportion as noted above.

<sup>e</sup> Aquatic is a weighted average of ocean sources (10 Tg) and freshwater (4 Tg). The isotopic values are weighted similarly [Schaefer and Whiticar, 2008]

<sup>f</sup> Value is consistent with Xiong et al. (2009)

<sup>g</sup> Value is assuming rice to behave similarly to C<sub>3</sub> grasslands and is then assigned the same as tropical wetlands

<sup>h</sup> Based upon Etiope et al. (2008b)

\*Thermokarst lake values are mean flux weighted values from Walter et al. (2006)

§MacDonald et al. (2006) suggest that boreal wetlands during the deglaciation would be likely characterized by minerotrophic fens (-50 to -73‰ [Bellisario et al., 1999]) rather than the present *Sphagnum* bog complexes.

‡Etiope et al. (2008b) Table 1 lists the range of values for the different geologic sources

### 3. Results

#### 3.1. GISP2 $\delta^{13}\text{CH}_4$ measurements

A section of the Greenland Ice Sheet Project (GISP2) core #139 is used to further establish the validity of the improved CF-IRMS method outlined in Section 2.1. The ice quality of these samples is, unfortunately, poor with much of the ice highly fractured. However, enough ice was available to measure 7 samples (Table 7.3.1). The ages of the samples are not accurately known; the ice core was previously cut for another use without notation as to which end (top or bottom) was removed, hence the age of the samples are either 223 – 225 yr BP or 229 – 231 yr BP. Fortunately, this time period does not exhibit rapid changes in either methane concentration or isotope value (Figure 1.2.2) and the diffusive column would smooth any large changes, thus this degree of age uncertainty is minor and of no impact.

The mean  $\text{CH}_4$  concentration of the samples from the CF-IRMS is  $703 \pm 43$  ppbv (where the standard deviation is given as  $1\sigma$ ). This value is comparable to that found by Schaefer and Whiticar (2007) for the same age ice ( $690 \pm 20$  ppbv) using an earlier CF-IRMS technique. The higher standard deviation of the new method possibly reflects the poor ice quality available for the measurements. The measured  $[\text{CH}_4]$  is in good agreement with that from the GISP2 Eurocore 235 ( $724 \pm 5$  ppbv) measured at 217 yr BP using conventional GC flame ionization detector (GC-FID) [Etheridge et al., 1998].

The mean  $\delta^{13}\text{CH}_4$  value is measured to be  $-49.37 \pm 0.58$  ‰. The measurement is corrected for gravitational fractionation (Section 2.3.1) using a value of 0.309 ‰ [Kobashi et al., 2008b]. The higher standard deviation, as compared to tests in Section 2.1.4, is a reflection of the sample quality and is supported by other workers findings for

measurements of fractured ice [Craig et al., 1988; Schaefer and Whiticar, 2007]. Two of the seven measurements were found to be  $^{13}\text{C}$ -enriched ( $\delta^{13}\text{CH}_4$  values of  $\sim -45$  ‰) and have been disregarded, based upon the unsuitability of these highly fractured samples (Table 7.3.1).

The previous measurements from the same ice core by Schaefer and Whiticar (2007) determined a  $\delta^{13}\text{CH}_4$  value of  $-49.7 \pm 0.3$  ‰. This value is more  $^{13}\text{C}$ -depleted than that measured with the improved instrumental set-up, although still within reported analytical uncertainty. Other isotope measurements are available from this time period including Craig et al. (1988) who measured a  $\delta^{13}\text{CH}_4$  value of  $-49.9 \pm 0.2$  ‰ for very large samples (25 kg / sample) with ice ages between 120 - 310 yr BP. The air within the ice of this age is younger than these ages due to the ice age – gas age difference (see Section 2.3) and thus is not appropriate for comparison without conversion to air age. Ferretti and coworkers measured a  $\delta^{13}\text{CH}_4$  value of  $-49.19 \pm 0.20$  ‰ at 228 yr BP, however these data are from the Law Dome core in Antarctica [Ferretti et al., 2005] and the inter-polar gradient in  $\delta^{13}\text{CH}_4$  has not been determined. A more recent, and appropriate,  $\delta^{13}\text{CH}_4$  record for comparison has been published using GISP2 ice [Sowers, 2009], which reports a  $\delta^{13}\text{CH}_4$  value of  $-49.24 \pm 0.30$  ‰ for 200 years BP. This  $\delta^{13}\text{CH}_4$  value is close to that measured using the improved instrumental set-up, providing support for its validity.

### 3.2. Contaminated and compromised samples

As outlined in Section 2.1.3, the CF-IRMS permits measurement of methane concentration in addition to determination of the  $\delta^{13}\text{CH}_4$  value. The  $[\text{CH}_4]$  can then be used as a check on the presence of contamination, both within the sample and the measurement process. The 148 Pákitsoq samples measured show high variability in CF-IRMS-derived  $\text{CH}_4$  concentrations (Figure 3.2.1). The  $[\text{CH}_4]$  samples are taken from the same trench positions as the  $\delta^{13}\text{CH}_4$  samples, and processed at Oregon State University (OSU) by GC-FID. The OSU samples also show instances of elevated  $[\text{CH}_4]$  (Figure 3.2.2). To investigate if these elevated  $\text{CH}_4$  concentrations were higher than would be

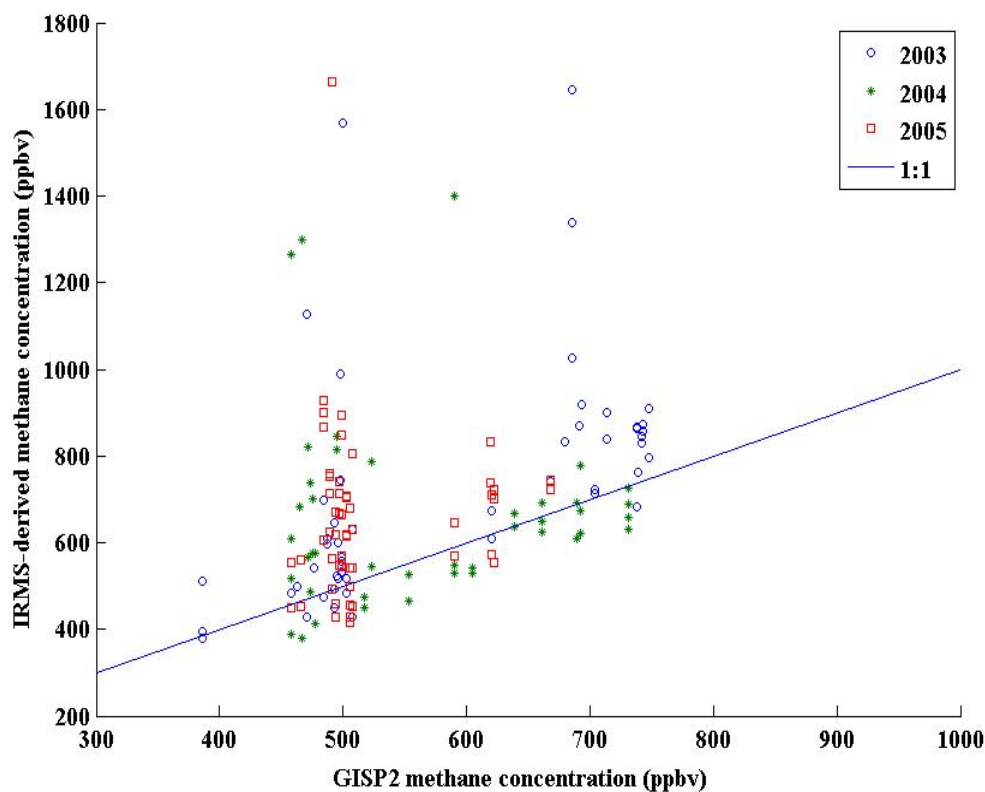


Figure 3.2.1: Pákitsoq IRMS-inferred  $[\text{CH}_4]$  plotted against the contemporaneous GISP2  $[\text{CH}_4]$  [Brook et al., 2000]. The plotted line is the 1:1 relationship, which appears to have a low slope due to differing axes length. All uncompromised data should plot close to the line.

expected, given the ages of the samples, the gas samples are first assigned an air age (as described in Section 2.2). The air age is used to compare against the GISP2 [CH<sub>4</sub>] for contemporaneous air. Figure 3.2.1 is a cross plot of the Pákitsoq CF-IRMS-inferred [CH<sub>4</sub>] and the GISP2 equivalent-age [CH<sub>4</sub>]. From inspection, it is apparent that some of the data are significantly higher than the 1:1 line. The appearance of aberrant points is also evident in the  $\delta^{13}\text{CH}_4$  values measured (see Table 7.3.2), with adjacent samples showing large changes in  $\delta^{13}\text{CH}_4$  value within short time periods (decades or less). These rapid changes can not be explained naturally considering the smoothing of the atmospheric record by the diffusive firn column [Schwander et al., 1997].

Inspection of the Pákitsoq GC-FID CH<sub>4</sub> concentration measurements performed at OSU (see Figure 3.2.2) and GC-FID measurements made while in the field (described in

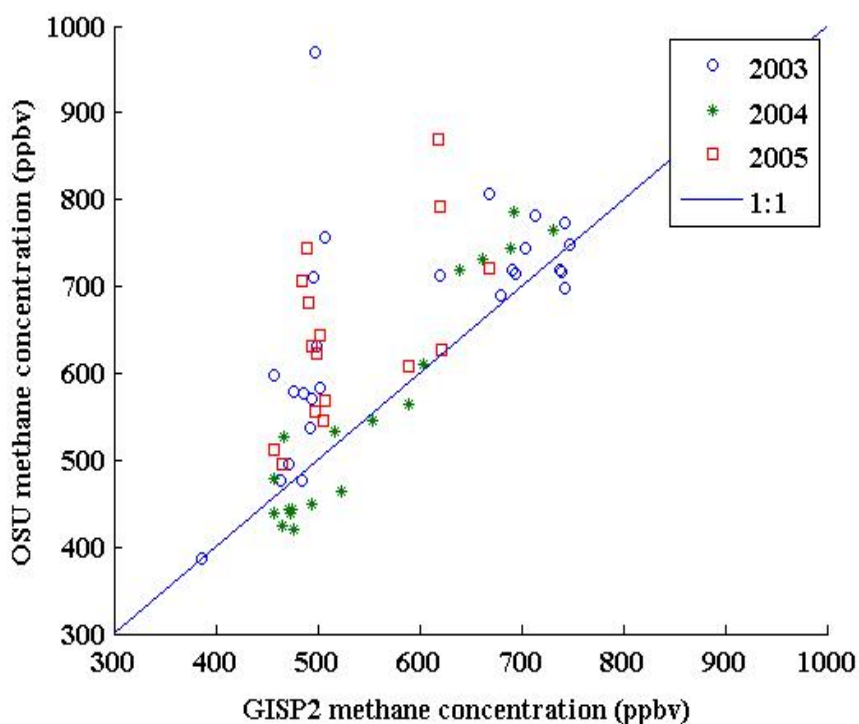


Figure 3.2.2: Pákitsoq methane concentration (as measured by GC-FID at OSU) versus GISP2 methane concentration for contemporaneous air [Brook et al., 2000]. The appearance of elevated methane concentrations would preclude the elevated methane concentrations to be an artifact of the IRMS concentration determination.

Petrenko et al., 2006), also reveal evidence of elevated  $\text{CH}_4$  concentrations in the horizontal trench (Figure 3.2.3; field measurements not plotted). The instances of anomalously elevated  $[\text{CH}_4]$  do not appear to be predictably located within the sampling trench, or across different sampling seasons.

Variability in the  $[\text{CH}_4]$  can also be observed in samples collected within the same sampling year. Samples from different depths (taken below the depth of surface contamination, usually 0.5 m [Petrenko et al., 2006]) for analysis in the field and at OSU have been measured at both expected and elevated  $[\text{CH}_4]$  for the same horizontal location, but different vertical depth (along the appropriate dip of the stratigraphy).

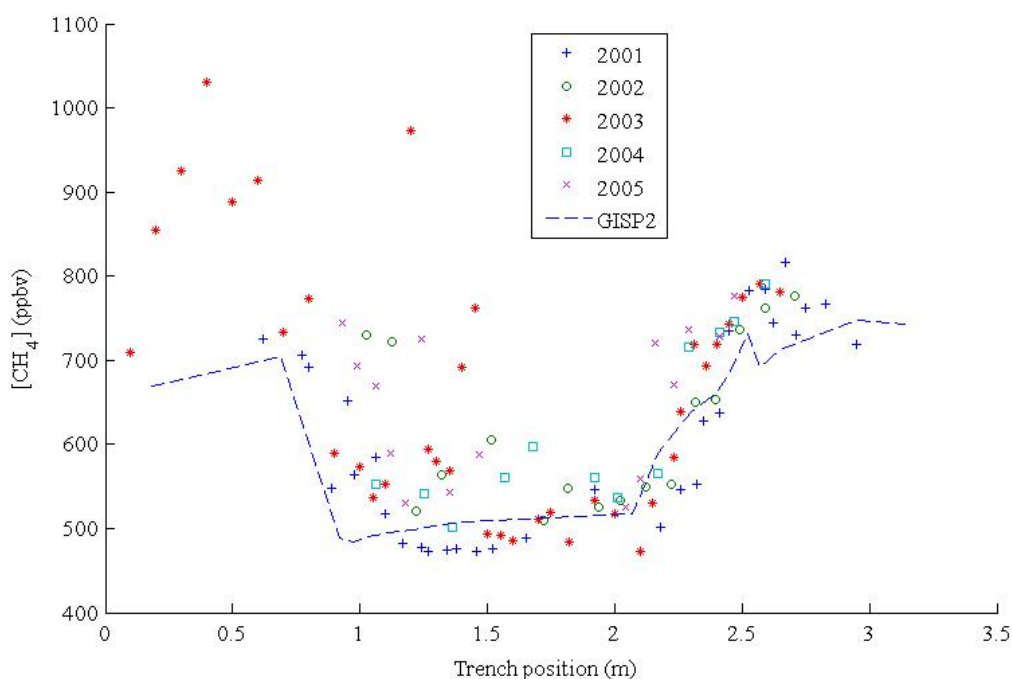


Figure 3.2.3: Pákitsoq  $[\text{CH}_4]$  measured at OSU across 5 sampling seasons plotted on the same horizontal trench scale. GISP2 methane has been assigned a trench distance (shown here for 2002 age scale) and plotted for reference. Gas ages were derived from the combination of  $\delta^{18}\text{O}_{\text{ice}}$ ,  $\delta^{15}\text{N}$ ,  $\delta^{18}\text{O}_{\text{atm}}$ , and  $[\text{CH}_4]$ . The GISP2  $[\text{CH}_4]$  demonstrate close correlation with the Pákitsoq values across all seasons during the termination of the YD (beginning at 2.07 m trench distance and increasing). A large number of elevated  $[\text{CH}_4]$  values are apparent during the Allerød period ( $< 0.69\text{m}$ ) and at the initiation of the YD cold interval ( $0.69\text{m}$ ). Note the lack of consistent sections of ice with elevated methane concentration values across years. OSU measurement uncertainty is described in Section 7.1

The  $\delta^{15}\text{N}$  values along the same transect (Figure 3.2.4) show the timeline of the transect to be consistent between sampling seasons and without small-scale folding, or changes in the stratigraphy. This precludes the possibility of the stratigraphy exhibiting large changes between sampling seasons, and suggests the elevated  $[\text{CH}_4]$  to be spot contamination with certain sections exhibiting higher (Allerød – YD transition) and lower (YD- PB transition) occurrences of contamination, but no consistent trend. It is important to ensure that samples with elevated  $[\text{CH}_4]$  are demarcated from samples exhibiting no contamination. Since the Pákitsoq  $[\text{CH}_4]$  is elevated above the expected methane concentration (as defined by contemporaneous air from GISP2), the excess  $\text{CH}_4$  can not be derived from atmospheric air at the time of bubble close-off. A methodology to filter

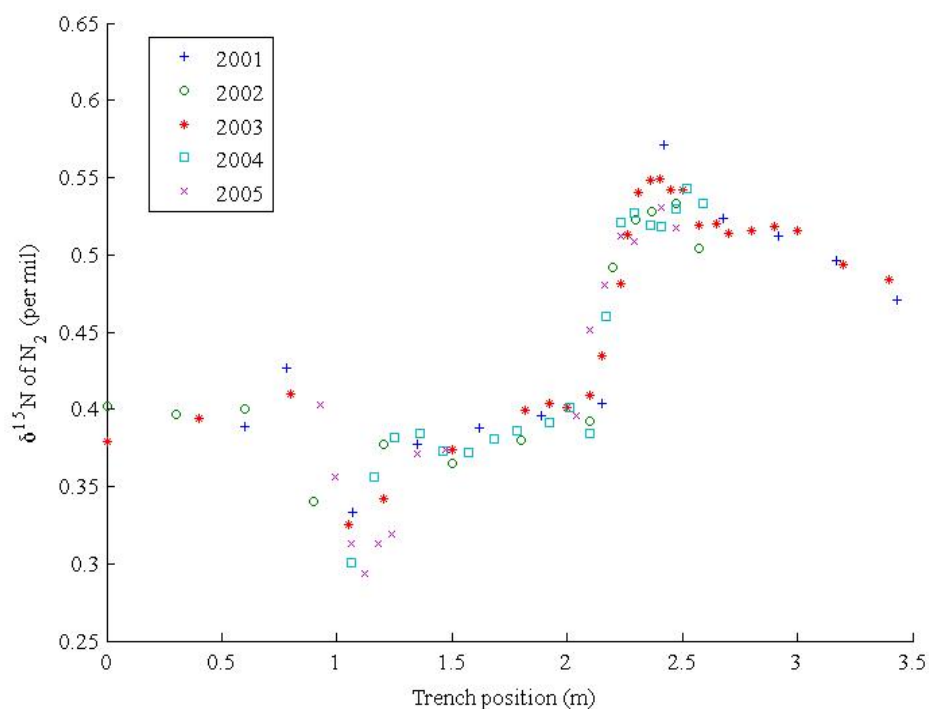


Figure 3.2.4: Pákitsoq  $\delta^{15}\text{N}$  of  $\text{N}_2$  measured at Scripps Institute of Oceanography (SIO) [Petrenko et al. 2006] across 5 sampling seasons plotted on the same horizontal trench scale. Note that there is no evidence of any major changes in the time scale across the sampling seasons, or time reversals due to small scale folding of the stratigraphy.

the Pákitsoq data and identify contaminated samples, using the CF-IRMS-derived  $[\text{CH}_4]$ , is described below.

To identify compromised samples using the CF-IRMS-derived  $\text{CH}_4$  concentration data, several assumptions are necessary:

1. The contamination is not consistent across distance, both horizontally and vertically, and through time. The lack of congruency, both spatially and temporally, for contamination is evident from the OSU  $[\text{CH}_4]$  measurements and other evidence already described.
2. Any contamination is expressed in elevated  $[\text{CH}_4]$ . Several processes can increase the  $[\text{CH}_4]$  in ice samples (e.g. in-situ production, CO break-through, or leaks during analysis (discussed in detail in Section 4.1), however few processes exist to decrease  $\text{CH}_4$  mixing ratio within ice. In-situ oxidation is possible, but has never been reported, and is unlikely due lack of liquid water and low temperatures [Hanson and Hanson, 1996]. Any contamination to the  $\delta^{13}\text{CH}_4$  values that does not change the  $[\text{CH}_4]$  will not be detected.
3. The CF-IRMS-derived  $[\text{CH}_4]$  uncertainty can be estimated and used to identify contaminated samples.

Table 3.2.1 lists the uncertainties associated with assigning a GISP2  $[\text{CH}_4]$  to the contemporaneous Pákitsoq CF-IRMS-derived  $[\text{CH}_4]$  measurement for identification of contaminated samples. To be conservative, the uncertainties are taken on the lower range of estimates, thus presenting a smaller range required for inclusion as a valid datum point. This approach, rather than assuming the upper limits of these uncertainties, has a greater risk of removing non-contaminated samples but should, most importantly, remove all

contaminated samples. The uncertainties estimated are derived from: 1) age scale uncertainties for the Pákitsoq dataset; 2) interpolation between data points; 3) uncertainty in the GISP2 [CH<sub>4</sub>]; 4) uncertainty in the Pákitsoq distance scale; and, 5) uncertainty in the CF-IRMS derived [CH<sub>4</sub>].

Table 3.2.1: Estimated uncertainties in comparison of CF-IRMS-derived [CH<sub>4</sub>] measurements to GISP2 [CH<sub>4</sub>] measurements as expressed in ppbv of methane

Source of Uncertainty	Estimated [CH <sub>4</sub> ] (ppbv)
Age scale uncertainties	ca. 30
Interpolation between data points	Small, ca. 10
GISP2 [CH <sub>4</sub> ] uncertainty	5 – 10
Uncertainty in Pákitsoq distance scale	Variable
IRMS-derived [CH <sub>4</sub> ] measurement	ca. 45
<b>Total assumed uncertainty</b>	<b>±100</b>

Errors in age assignments to the Pákitsoq samples increases uncertainty. This uncertainty in the sample age – trench distance relationship is, by definition, zero at age tie-points and increases with horizontal trench distance away from a tie-point (Section 2.2). The increasing uncertainty, with increasing distance from tie-points, is balanced by the smaller rate of change in the [CH<sub>4</sub>] farther from age tie points. The age scale contribution to uncertainty in the comparison of CF-IRMS-derived [CH<sub>4</sub>] measurements to GISP2 [CH<sub>4</sub>] measurements is estimated to be approximately 30 ppbv on average.

Within the Pákitsoq and GISP2 records, CH<sub>4</sub> dynamics in the regions between sample points is unknown, but assumed linear. This assumption is relatively safe due to the diffusive firn column smoothing of any rapid changes in CH<sub>4</sub> mixing ratio, yet increases uncertainty. Given the age-to-horizontal distance relationships in the Pákitsoq sampling trenches, it is apparent that the CH<sub>4</sub> concentration sampling frequency is

adequate to ensure this uncertainty is relatively small. The GISP2 [CH<sub>4</sub>] record is densely sampled at the points of greatest change in [CH<sub>4</sub>] minimizing the interpolation uncertainty. The combination of Pákitsoq and GISP2 interpolation uncertainty is estimated to be 10 ppbv.

The published measurement uncertainty for GISP2 is set at a maximum 5% difference between the sample concentration of duplicate samples, with most pairs differing by 1.2% [Brook et al., 2005]. This uncertainty ranges between a minimum of 4.2 ppbv and maximum of 40 ppbv for concentrations between 400 and 800 ppbv, respectively. Again choosing conservatively on the low end of the uncertainty estimate, together these errors are assumed small, and estimated as ca. 5 - 10 ppbv.

Each season the Pákitsoq horizontal trench reference pole was drilled 6 m into the ice, along the dip of stratigraphy into the exact same hole, to ensure reproducibility in ice sampling [Petrenko et al., 2006]. The possible shifting of this pole could introduce uncertainty, as well as measurement uncertainty during the actual sampling of the ice with electric chainsaw [Petrenko et al., 2006]. This uncertainty is assumed to be small, and included in the age scale uncertainty; and thus will be ignored.

The technique of measuring CH<sub>4</sub> concentration from air occluded in ice samples by CF-IRMS potentially presents the largest source of uncertainty. The uncertainty involved in this measurement is difficult to quantify. To determine concentration with the CF-IRMS, known volumes of atmospheric air are injected through the full instrumental setup and the instrumental response ( $m/z$  44 peak area) is recorded, and used to calibrate instrument response (mV /  $\mu\text{g C}$ ). Using this technique on ice samples relies upon knowledge of the atmospheric CH<sub>4</sub> mixing ratio at the ambient air sample site outside our

University of Victoria lab, the weight and bubble-air content of the ice sample, and the blank peak size for correction. The most uncertain of these is the bubble-air content of the ice sample, which is not measured during CF-IRMS analysis. Bubble-air content values for the Pákitsoq 2003 season and the GISP2 samples (Section 3.1) were assigned a fractional air content of 0.09 while ice from field seasons 2004 and 2005 were measured as part of the OSU CH<sub>4</sub> concentration measurements on ice samples taken from locations within the sampling trench. The combined uncertainty of the CF-IRMS CH<sub>4</sub> concentration determination is additionally difficult to quantify due to unknown sample effects from the wet extraction that air samples and artificial ice samples might not adequately replicate (though this appears insignificant; see Section 2.1.4).

The most appropriate determinant of the CF-IRMS CH<sub>4</sub> concentration uncertainty would be to measure numerous replicate samples of uncompromised glacial of 16 ppbv.

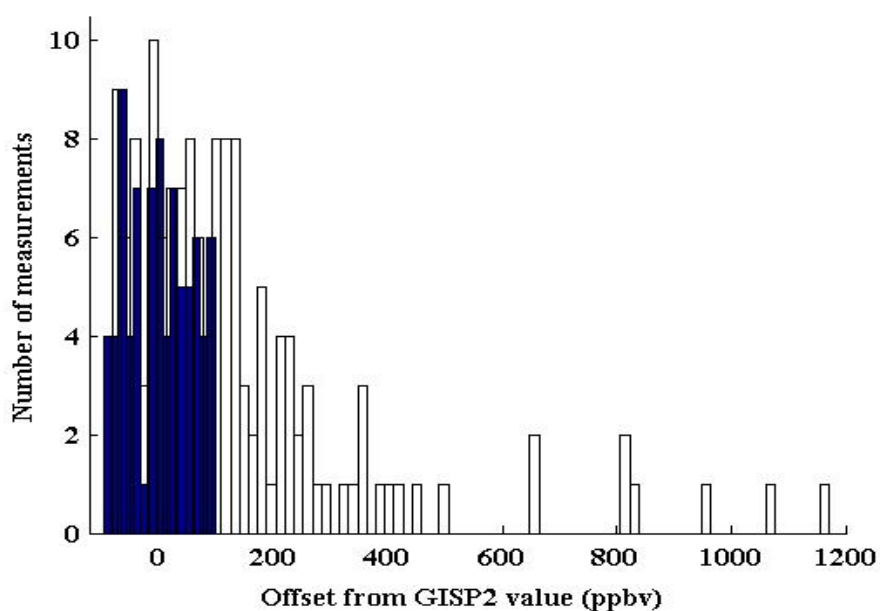


Figure 3.2.5: Histogram of the offset between the Pákitsoq IRMS-derived methane concentration and the contemporaneous GISP2 concentration [Brook et al., 2000]. Offset values from all samples are displayed with white bars, samples after filtering for contamination ( $> \pm 100$  ppbv) are blue filled bars. Note: no samples were offset greater than 100 ppbv below the GISP2 contemporaneous values. All Pákitsoq measurements for this study are presented.

ice containing a known concentration of methane. This was not available for a high number of samples, however the GISP2 samples present probably the best approximation. The standard deviation of these samples provides a maximum uncertainty of 69 ppbv and a minimum This uncertainty estimate is determined from offset to the Etheridge et al. (1998) EUROCORE value, assuming that to be the true value. Given the range, the uncertainty has been chosen to be 45 ppbv, which is close to the standard deviation of the measured GISP2 samples. This results in a total uncertainty of  $\pm 100$  ppbv when comparing Pákitsoq CF-IRMS-derived  $\text{CH}_4$  concentration to contemporaneous GISP2  $\text{CH}_4$  concentration (Figure 3.2.5).

The total uncertainty ( $\pm 100$  ppbv) is assumed invariant across all sample concentrations. This is justified since the errors associated with this grouped uncertainty

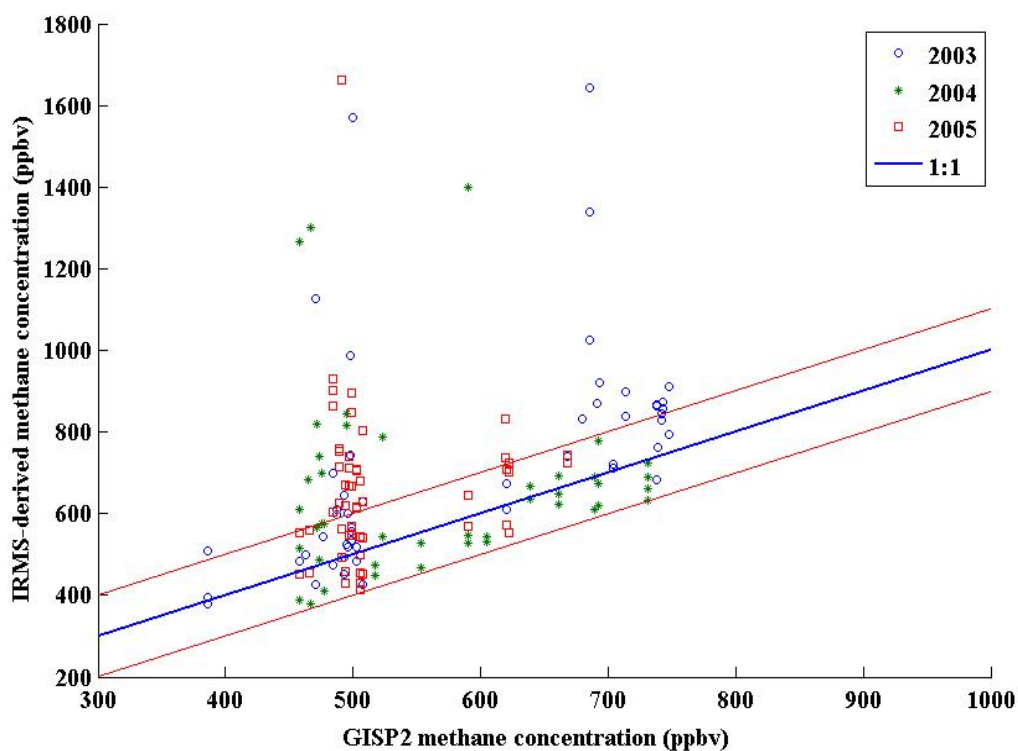


Figure 3.2.6: Pákitsoq IRMS-inferred  $[\text{CH}_4]$  plotted against the contemporaneous GISP2  $[\text{CH}_4]$  [Brook et al., 2000]. The plotted line is the 1:1 relationship, which appears to have a low slope due to differing axes length. Also plotted are the boundaries of the upper and lower 100 ppbv filter (red).

are also insensitive to sample concentration (see Figure 3.2.6, where the Pákitsoq CF-IRMS-derived samples  $[\text{CH}_4]$  values below the 1:1 line of GISP2 contemporaneous  $[\text{CH}_4]$  are evenly distributed across the GISP2 concentration spectrum). This contamination threshold is used to filter the Pákitsoq data for compromised samples ( $[\text{CH}_4] > \pm 100$  ppbv from the GISP2 contemporaneous value) with the full data set presented in Table 7.3.2. The filtering resulted in the discarding of 64 out of 148 samples. As support for the limit of the filter, no samples were more than 100 ppbv below contemporaneous GISP2  $[\text{CH}_4]$  values (Figure 3.2.6), as expected due to the lack of processes to decrease  $\text{CH}_4$  concentration within ice. The uncompromised samples are used in the remainder of this work.

### 3.3. Measurements spanning the LGM to Preboreal period

#### 3.3.1. $\delta^{13}\text{CH}_4$ measurements for the most recent deglaciation

The Pákitsoq  $\delta^{13}\text{CH}_4$  record spanning the last deglaciation is presented in Figure 3.3.1. The record shows relatively  $^{13}\text{C}$ -enriched methane during the LGM ( $\delta^{13}\text{CH}_4$   $-43.75 \pm 0.5$  ‰), when atmospheric  $\text{CH}_4$  concentrations were low, and a progressive enrichment of  $^{12}\text{C}$  as the deglaciation proceeds. This decrease in  $\delta^{13}\text{CH}_4$  values proceeds steadily from the Oldest Dryas (OD) ( $\delta^{13}\text{CH}_4$  values of ca.  $-43$  to  $-45$  ‰) through the transition into the Bølling warm period, and up to the abrupt cooling at the start of the Younger Dryas (YD)

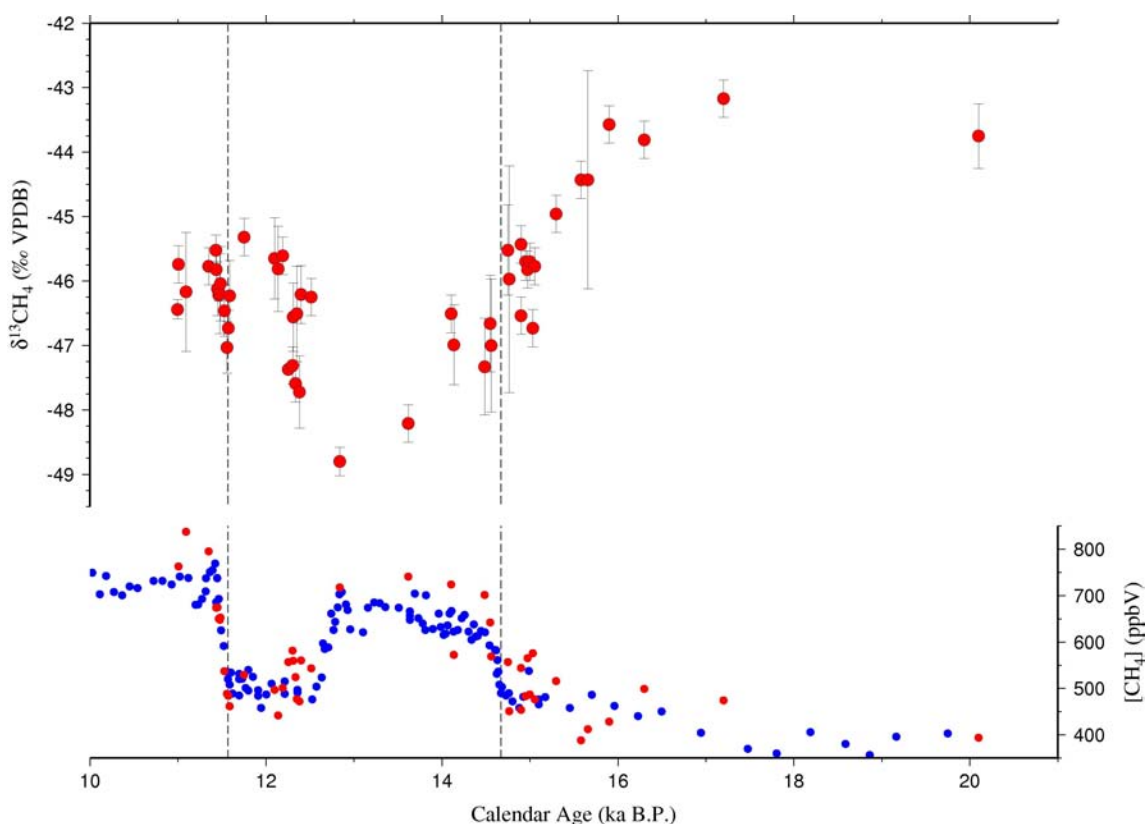


Figure 3.3.1: Pákitsoq  $\delta^{13}\text{CH}_4$  (top) and  $\text{CH}_4$  concentration (bottom) for the LGM to Preboreal time period (red dots). The GISP2  $\text{CH}_4$  record (blue dots; on the Schaefer et al. (2006) time scale) is shown for comparison [Brook et al. 2000]. Dashed lines are placed at the terminations of the Oldest Dryas (14.672 ka BP [Severinghaus and Brook, 1999]) and the Younger Dryas (11.570 ka BP [Friedrich et al., 1999]) time periods.

cold interval. The most  $^{13}\text{C}$ -depleted samples are measured just prior to the initiation of the YD cold interval, with a mean  $\delta^{13}\text{CH}_4$  value of  $-48.8 \pm 0.22$  ‰. The YD cold interval reverses the trend in the  $\delta^{13}\text{CH}_4$  with values becoming larger. The most  $^{13}\text{C}$ -enriched YD sample is measured to have a  $\delta^{13}\text{CH}_4$  value of  $-45.61 \pm 0.29$  ‰. The  $\delta^{13}\text{CH}_4$  values for the remainder of the deglaciation are more dynamic but remain between  $-45.3$  and  $-47.0$  ‰ and will be discussed in greater detail in the next section.

### 3.3.2. Younger Dryas – Preboreal transition

The Pákitsoq  $\delta^{13}\text{CH}_4$  record for the YD termination shows an interesting valley-like shape in the isotope values. The  $\delta^{13}\text{CH}_4$  values are observed to become  $^{13}\text{C}$ -enriched as the YD progresses (Sections 3.3.1 and 3.3.3) until about 11.75 ka BP. After this point,

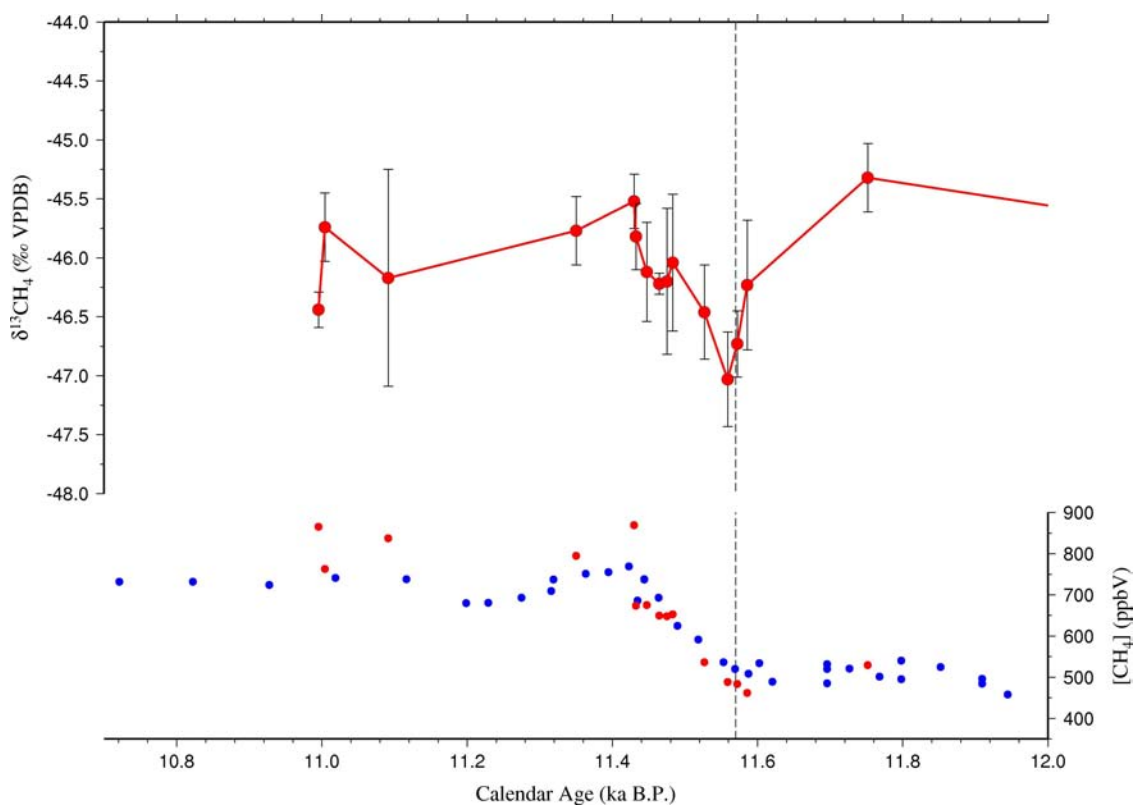


Figure 3.3.2: Pákitsoq  $\delta^{13}\text{CH}_4$  (top) and  $\text{CH}_4$  concentration (bottom) record (red dots) during the transition of the Younger Dryas to the Preboreal. The GISP2  $\text{CH}_4$  record (blue dots; on the Schaefer et al. (2006) time scale) is shown for comparison [Brook et al. 2000]. The dashed line is placed at the termination of the YD period (11.570 ka BP [Friedrich et al., 1999]).

the  $\delta^{13}\text{CH}_4$  values become progressively  $^{13}\text{C}$ -depleted. The lowest values occur at 11.6 ka BP with a  $\delta^{13}\text{CH}_4$  value of  $-47.03 \pm 0.4$  ‰. The timing of this reversal is close to the age of the termination of the YD ( $11,570 \pm 0$  yr BP [Friedrich et al., 1999]) and the subsequent increase in  $\text{CH}_4$  concentration 0 – 30 years, after the start of the warming [Severinghaus et al., 1998](Figure 3.3.2). As the  $[\text{CH}_4]$  increases, the  $\delta^{13}\text{CH}_4$  values become more  $^{13}\text{C}$ -enriched up to a maximum value of  $-45.52 \pm 0.23$  ‰ at 11.4 ka BP. The  $\delta^{13}\text{C}$  values then remain relatively stable into the Preboreal period. The magnitude of this  $\delta^{13}\text{CH}_4$  'valley' is almost five times greater than the measurement uncertainty. The dip of the methane  $^{13}\text{C}/^{12}\text{C}$  ratio prior to, and into, the YD termination is also evident in the work of Schaefer et al. (2006) (Figure 3.3.4).

The Pákitsoq data from the 2004 sampling season compare well against the Schaefer et al. (2006) measurements made with a different analytical setup (see Section 2.1 and Schaefer and Whiticar (2007)) and from different sampling seasons (2001 to 2003). The Schaefer et al. (2006) Pákitsoq data shows higher variability in the measurements. It is unclear if this is a result of the analytical procedure used, or that the data are not filtered using the procedure outlined in Section 3.2.

Decrease in the  $\delta^{13}\text{CH}_4$  values is observed to begin prior to the warming at the termination of the YD, as evident from the  $\delta^{15}\text{N}$  values recorded in the GISP2 core (Figure 3.3.3). The increase in methane concentration appears to coincide with the minimum value of  $\delta^{13}\text{CH}_4$  and the initiation of a trend towards increasing  $\delta^{13}\text{CH}_4$  values (within age scale uncertainty).

The late Preboreal period  $\delta^{13}\text{CH}_4$  record has been reported by Sowers (2009) for the GISP2 core (Figure 3.3.3). Sowers' (2009) GISP2 results show reasonable agreement in the few areas of overlap with the Pákitsoq measurements reported here. An additional record from Antarctica has been reported by Fischer *et al.* (2008). This record shows similar trends during the YD termination with a corresponding dip in  $\delta^{13}\text{CH}_4$  value

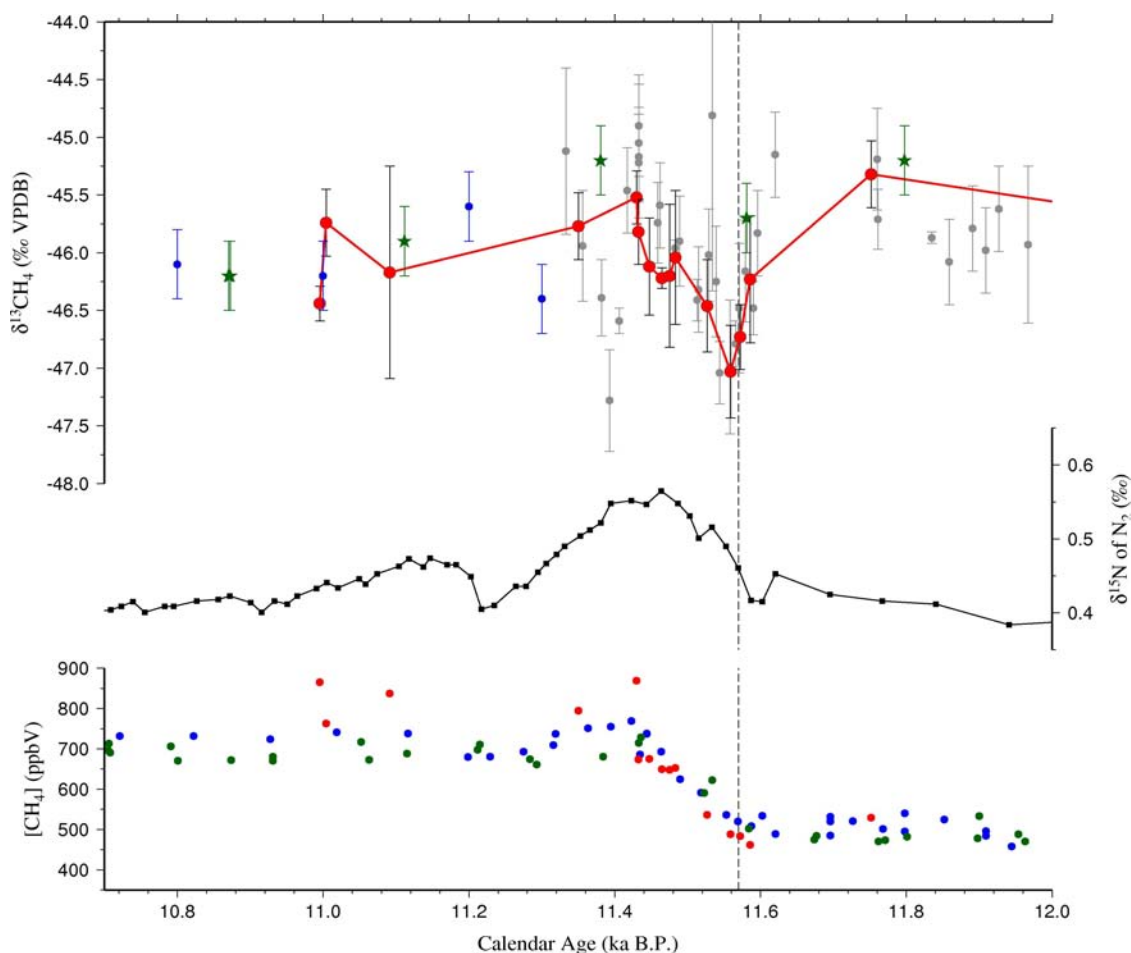


Figure 3.3.3: Abrupt temperature anomaly as recorded in the  $\delta^{15}\text{N}$  values (middle) from the GISP2 core [Severinghaus *et al.* 1998; Severinghaus and Brook, 1999]. This anomaly occurs in advance of the changes in  $[\text{CH}_4]$  (bottom; Pákitsoq IRMS-derived concentration (red dots), GISP2 (blue dots; Brook *et al.* 1996), and EDML, Antarctica (green dots; EPICA Community Members. 2006). For reference, Pákitsoq [this work (red dots), Schaefer *et al.* 2006 (gray dots)], GISP2 [Sowers, 2009 (blue dots)], and EDML, Antarctica [Fischer *et al.* 2008 (green stars)]  $\delta^{13}\text{CH}_4$  values are also plotted. Note, all data have been adjusted to the Schaefer *et al.* (2006) timescale. In the case of EDML, methane concentration was used to match the timing of the abrupt methane change, since it is a globally well-mixed signal. The dashed line is placed at the termination of the YD period (11.570 ka BP [Friedrich *et al.*, 1999]).

just prior to the  $\text{CH}_4$  concentration increase, and a recovery as the concentration rises. This trend is possibly not robust as it is only 3 data points with a 0.5‰ difference, between the two higher points and the low value, and the stated measurement accuracy is estimated to be better than 0.3 ‰.

Application of the atmospheric disequilibrium model (Section 2.3.3) to determine

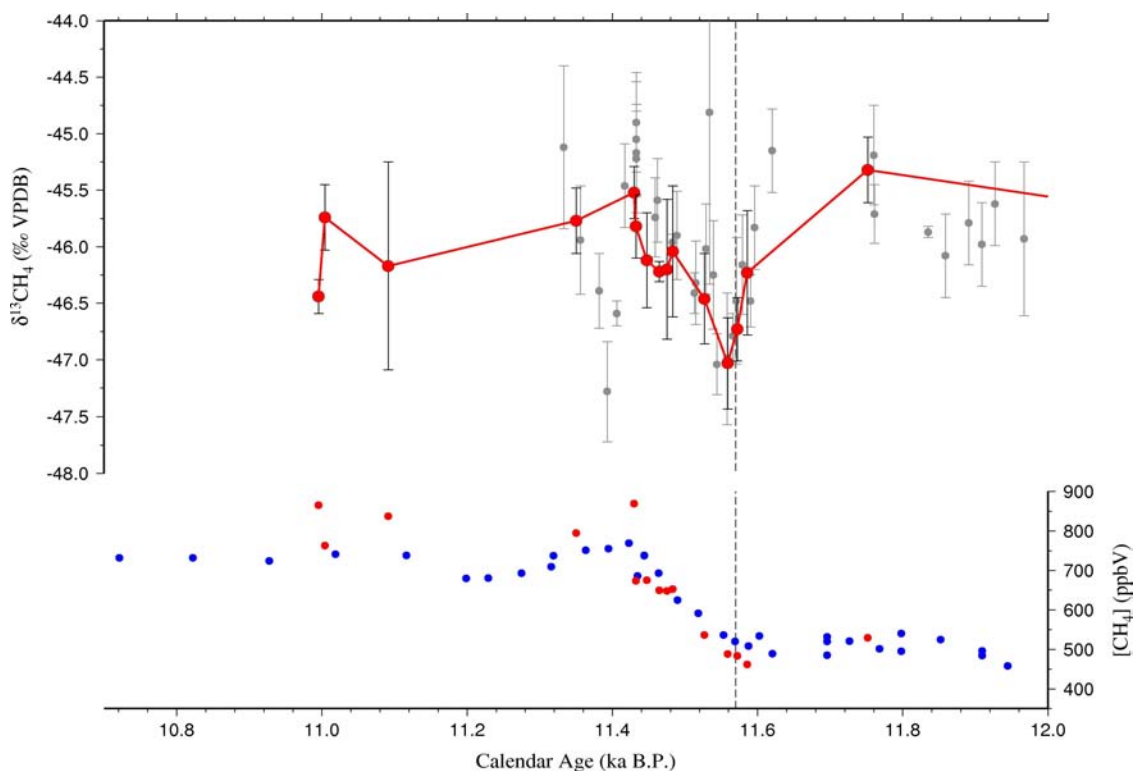


Figure 3.3.4: (Top) Pákitsoq  $\delta^{13}\text{CH}_4$  record from this work (red dots) and Schaefer et al. (2006) (grey dots). (Bottom) IRMS-derived methane concentration from this work (red dots) and GISP2 (blue dots) is shown for reference [Brook et al. 2000]. The dashed line is placed at the termination of the YD period (11.570 ka BP [Friedrich et al., 1999]). One point from Schaefer et al. (2006) does not appear on the figure for presentation purposes, it is -43.16‰ at 11.369 ka BP.

the value of the aggregated source for the YD termination results in a small adjustment of the atmospheric  $\delta^{13}\text{CH}_4$  value and concentration measured (maximum correction of 0.10 ‰ and 11 ppbv)(Figure 3.3.5). The corrected values show the change in the aggregated source, through the transition, to be slightly smaller in magnitude (values are less  $^{12}\text{C}$ -enriched) than that observed in the isotope record.

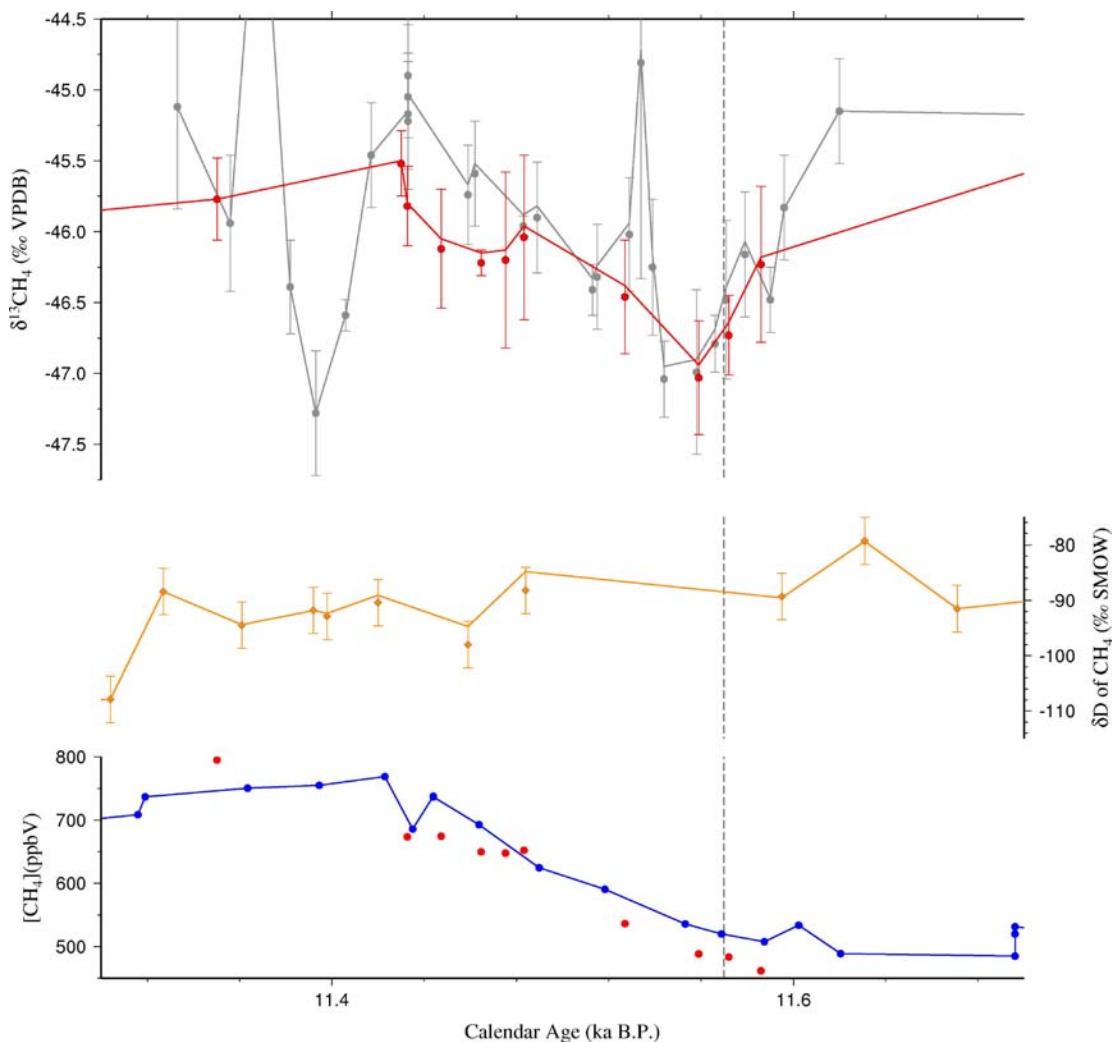


Figure 3.3.5: Disequilibrium correction applied to the YD - Preboreal transition  $\delta^{13}\text{CH}_4$  (top),  $\delta\text{D}-\text{CH}_4$  (middle) and  $[\text{CH}_4]$  (bottom) values. The measured atmospheric values are shown as discrete points, values corrected for atmosphere disequilibrium are shown as solid lines (concentration adjustments are too small to be visible at scale of plot).  $\delta^{13}\text{CH}_4$  values from Pákitsoq include this work (red) and Schaefer et al. (2006)(grey). The  $\delta\text{D}-\text{CH}_4$  values from Sowers (2006) have been corrected for both disequilibrium and diffusional fractionation (see Section 2.3). Concentration values from GISP2 (blue; Brook et al., 1996) and Pákitsoq (red, uncorrected; this work). The dashed line is placed at the termination of the YD period (11.570 ka BP [Friedrich et al., 1999]).

### 3.3.3. Younger Dryas Cold Interval

The Pákitsoq  $\delta^{13}\text{CH}_4$  record for the Younger Dryas (YD) cold interval is presented in Figure 3.3.6. The  $\delta^{13}\text{CH}_4$  record displays a general trend of progressive  $^{13}\text{C}$ -enrichment throughout the initial stages of the Younger Dryas. The general trend reverses at 11.75 ka

BP, as mentioned previously. No  $\delta^{13}\text{CH}_4$  values are retained in the actual cooling transition from the Allerød into the YD after application of the contamination filter (see Section 3.2). However, the  $\delta^{13}\text{CH}_4$  values bordering the transition indicate a move to more  $^{13}\text{C}$ -enriched  $\delta^{13}\text{CH}_4$  values. The  $\delta^{13}\text{CH}_4$  record shows a deviation from the trend of  $^{13}\text{C}$ -enriched values as the YD progresses in the period  $\sim 12.4 - 12.2$  ka BP. This period is marked by  $\delta^{13}\text{CH}_4$  values fluctuating between approximately  $-46.5$  and  $-47.5$  ‰ before moving to a  $\delta^{13}\text{CH}_4$  value of  $-45.61$  ‰ and remaining relatively stable until 11.75 ka BP.

Data from Antarctica for the same time period (Figure 3.3.7) display the same general pattern of more  $^{13}\text{C}$ -enriched isotope values as the YD progresses, though the data points are not closely positioned temporally to the YD initiation to make a strong

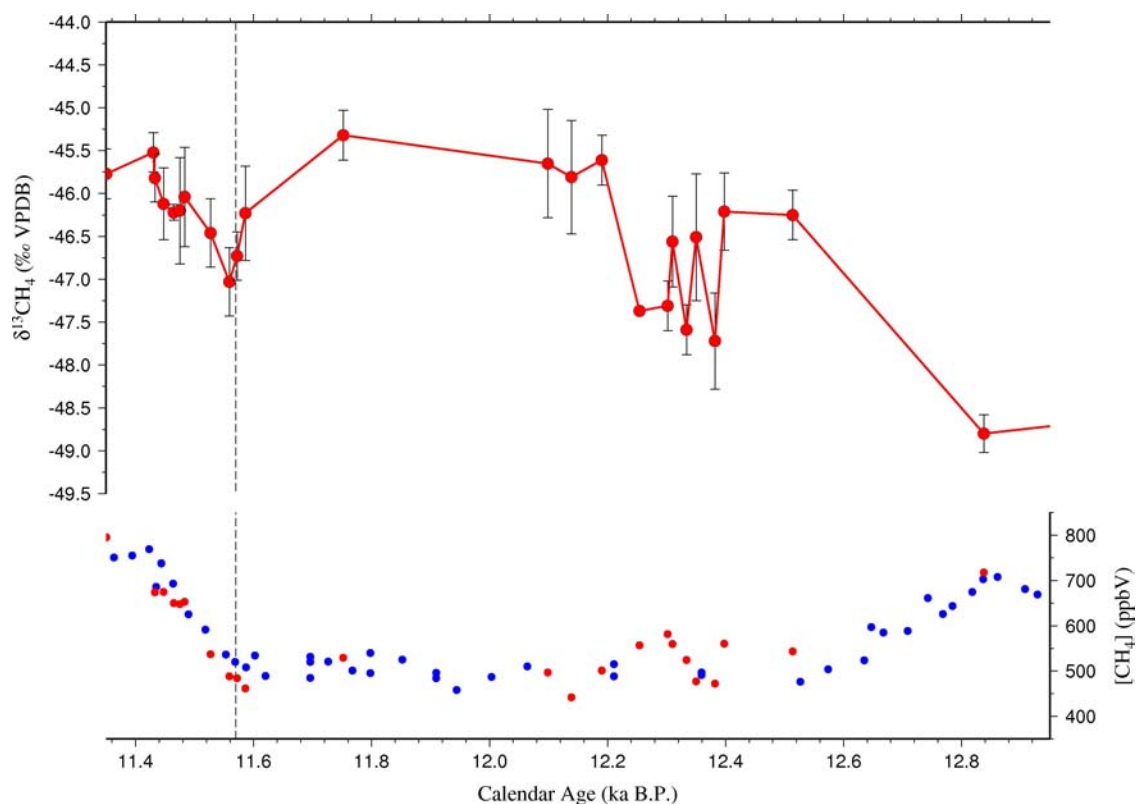


Figure 3.3.6: The Younger Dryas Cold Interval methane concentration (bottom; Påkitsoq IRMS-derived concentration (red dots), GISP2 (blue dots) [Brook et al. 1996]) and  $\delta^{13}\text{CH}_4$  from Påkitsoq (top). The dashed line is placed at the termination of the YD period (11.570 ka BP [Friedrich et al., 1999]).

inference. The previously published Pákitsoq data of Schaefer and coworkers (2006) show the same pattern of a relative stability in the  $\delta^{13}\text{CH}_4$  values for the latter half of the YD (12.2 – 11.8 ka BP) prior to the observed decrease in  $\delta^{13}\text{CH}_4$  values prior to the YD termination.

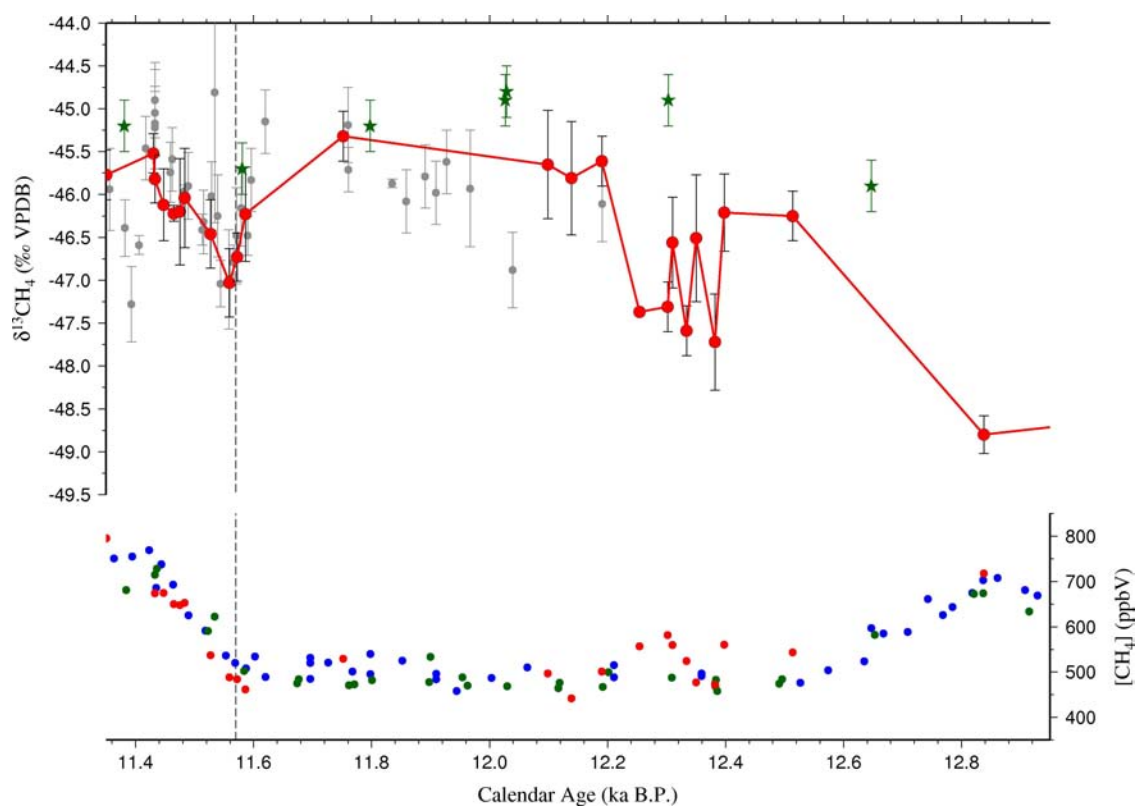


Figure 3.3.7: The Younger Dryas cold interval  $\delta^{13}\text{CH}_4$  (top) and  $\text{CH}_4$  mixing ratio (bottom).  $\delta^{13}\text{CH}_4$  data are from Pákitsoq, Greenland [this work (red dots); Schaefer et al., 2006 (grey dots)] and EDML, Antarctica [Fischer et al., 2008 (green stars)]. Methane concentration is from Pákitsoq [red dots; this work], GISP2 [Brook et al., 1996 (blue dots)], and EDML, Antarctica [EPICA Community Members, 2006 (green dots)]. The dashed line is placed at the termination of the YD period (11.570 ka BP [Friedrich et al., 1999]).

### 3.3.4. Oldest Dryas – Bølling transition

The methane stable isotope record of the transition from the Oldest Dryas (OD) cold period to the Bølling-Allerød (BA) warm interval is presented in Figure 3.3.8. The data from the OD period have higher age uncertainty (see Section 2.2) and will not be

interpreted closely. Even with the higher age uncertainty, the  $\delta^{13}\text{CH}_4$  record shows an almost continuous enrichment in  $^{12}\text{CH}_4$  from the OD through the BA warm period. This continual enrichment in  $^{12}\text{C}$  has a possible pause from the termination of the Bølling transition ( $\sim 14.5$  ka BP) until about 14.0 ka BP where the  $\delta^{13}\text{CH}_4$  values appear to remain relatively steady at ca.  $-46.5$  ‰.

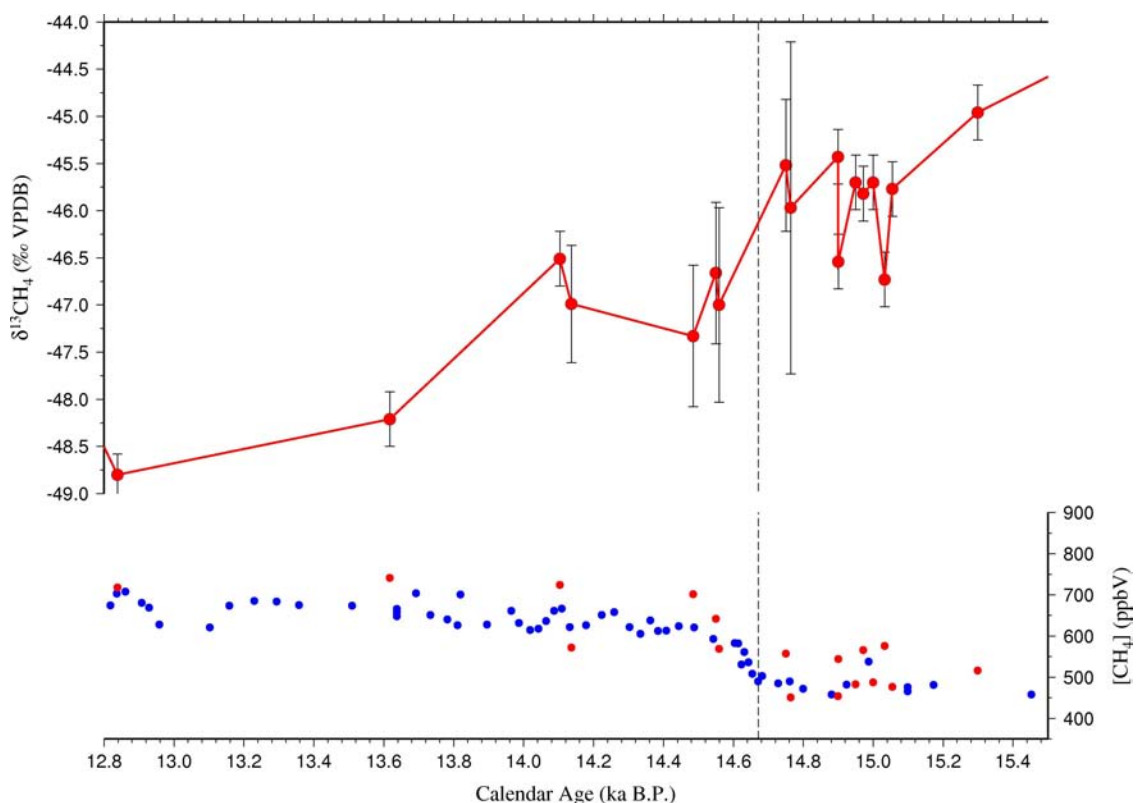


Figure 3.3.8: The Oldest Dryas - Bølling transition  $\delta^{13}\text{CH}_4$  and methane concentration record from Pákitsoq, Greenland (red dots). The GISP2 methane concentration record is provided for comparison (on the Schaefer et al. (2006) timescale) [Brook et al., 1996]. The dashed line is placed at the termination of the Oldest Dryas period (14.672 ka BP [Severinghaus and Brook, 1999]). The Pákitsoq samples older than  $\sim 14.8$  ka BP have large age uncertainty (hundreds of years) due to the lack of unique points in the age scale proxies (Section 2.2)

The OD-B transition has also been measured, but on Antarctica ice by Fischer et al. (2008). Their results indicate a similar pattern of progressive  $^{12}\text{C}$ -enrichment, however the offset between the Pákitsoq and Antarctica records is much smaller in the

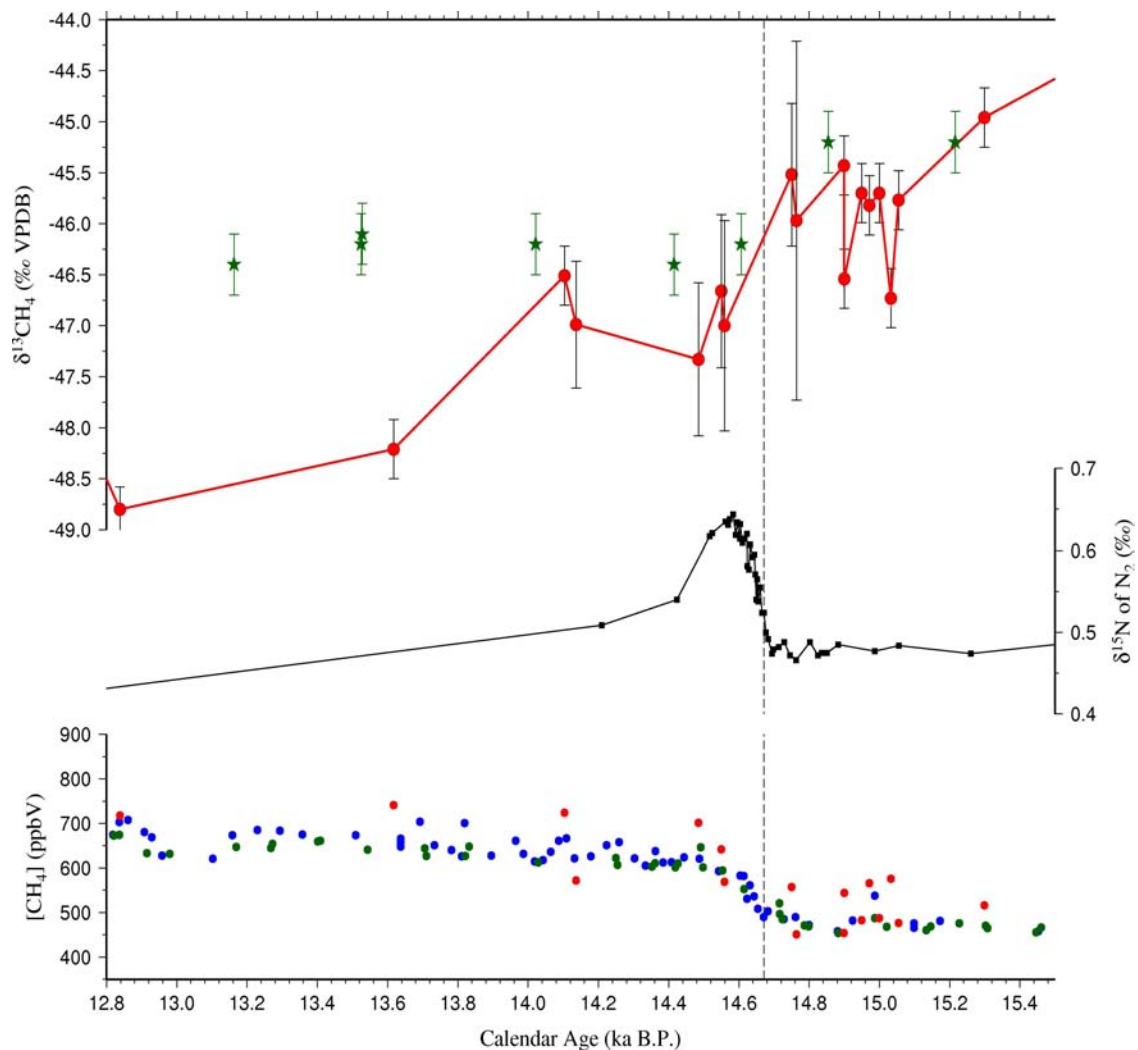


Figure 3.3.9: (top) Oldest Dryas to Bølling transition  $\delta^{13}\text{CH}_4$  record from Pákitsoq, Greenland (red dots) and EDML, Antarctica (green stars; Fischer et al., 2008). GISP2 temperature anomaly as recorded by  $\delta^{15}\text{N}$  (middle) [Severinhaus and Brook, 1999]. Methane concentration for Pákitsoq (red dots), GISP2 (blue dots; Brook et al., 1996), and EDML (green dots; EPICA Community Members, 2006)(bottom). All data are shown on the Schaefer et al. (2006) timescale.

OD than in other parts of the  $\delta^{13}\text{CH}_4$  records (Figure 3.3.9). This offset is initially close to 0 ‰ (the uncertainty in the Pákitsoq age scale for this time period does not allow for any definitive quantification) and increases to a large offset of  $>1.5$  ‰ in the BA period.

### 3.3.5. *Time-slice observations*

Select time periods of methane atmospheric concentration stability are chosen for analysis with steady-state Monte Carlo box model simulations (Section 2.4). The periods are chosen to coincide with previous work quantifying the inter-polar gradient in methane concentration (e.g. Chappellaz et al., 1997; Dällenbach et al., 2000; Brook et al., 2000). The time periods of atmospheric methane concentration stability are not necessarily periods of  $\delta^{13}\text{CH}_4$  stability (i.e. source fluxes can modulate in concert, resulting in the same atmospheric mixing ratio but different isotope values), which increases the uncertainty associated with the simulations. The time periods chosen, as well as representative isotope values for  $\delta^{13}\text{CH}_4$  and  $\delta\text{D-CH}_4$ , are listed in Table 3.3.1. The Northern Hemisphere  $\delta^{13}\text{CH}_4$  values are consistently  $^{13}\text{C}$ -depleted compared to those in the Southern Hemisphere. The  $\delta^{13}\text{CH}_4$  difference between the polar regions varies from little- to no difference (within standard uncertainty) during the LGM to ca. 1.5 ‰ during the Bølling-Allerød and YD, and then reducing to ca. 0.5 ‰ during the Preboreal.

The possibility of an inter-laboratory offset between the lab of Fischer et al. (2008) and that of the University of Victoria lab, could alter the magnitude of the inter-polar differences. This is being investigated via an inter-laboratory comparison and will be reported elsewhere. The values in Table 3.3.1 and the box model simulations were performed under the assumption of a 0.00 ‰ measurement offset between the Fischer and coworkers' and UVic labs.

Table 3.3.1: Stable time period CH<sub>4</sub> observations. These data provide the constraints for the Monte Carlo box model simulations (NH and SH denote Northern Hemisphere and Southern Hemisphere, respectively). Bold font indicates values provided by Påkitsoq measurements from this work. The Preboreal time period NH δ<sup>13</sup>CH<sub>4</sub> mean value is a combined record from Sowers (2009) and this work. In the area of overlap, the two records show no offset within uncertainty [Sowers (2009) -46.2 ± 0.3 ‰, this work -45.98 ± 0.26 ‰]. Curly brackets indicate the number of data points included.

Time Period (ka BP)	NH CH <sub>4</sub> concentration (μ ± 1σ ppbv) {n}	NH - SH concentration (μ ± 1σ ppbv)	NH δ <sup>13</sup> CH <sub>4</sub> value (μ ± 1σ ‰) {n}	SH δ <sup>13</sup> CH <sub>4</sub> value (μ ± 1σ ‰) {n}	NH δD-CH <sub>4</sub> value (μ ± 1σ ‰) {n}
1990s	1821 <sup>b</sup>	140 ± 6 <sup>a</sup>	-47.44 ± 0.04 <sup>b</sup>	-47.21 ± 0.04 <sup>b</sup>	-91 ± 5 (SH: -81 ± 3) <sup>b</sup>
PreIndustrial Holocene (0.6- 1.2)	710 ± 2 {31} <sup>c</sup>	35 ± 7 <sup>c</sup>	-48.4 ± 0.4 {7} <sup>d</sup>	-47.4 ± 0.2 {22} <sup>e</sup>	-95 ± 7 {7} <sup>d</sup> (SH: -83 ± 3 {9} <sup>e</sup> )
Preboreal (9.5 – 11.5)	718 ± 3 {26} <sup>c</sup>	44 ± 4 <sup>c</sup>	<b>-46.19 ± 0.43</b> {20}	-45.75 ± 0.43 {4} <sup>f</sup>	-101 ± 9 {20} <sup>g</sup>
YD (11.63– 12.5)	485 ± 4 {11} <sup>h</sup>	26 ± 9 <sup>h</sup>	<b>-46.51 ± 0.87</b> {11}	-44.92 ± 0.17 {4} <sup>f</sup>	-90 ± 8 {4} <sup>i</sup>
Bølling- Allerød 12.7 – 14.5	656 ± 6 {23} <sup>h</sup>	26 ± 10 <sup>h</sup>	<b>-47.57 ± 0.93</b> {5}	-46.18 ± 0.19 {6} <sup>f</sup>	-93 ± 4 {2} <sup>i</sup>
LGM (16.7 – 20.3)	362 ± 3 {19} <sup>h</sup>	-3 ± 4 <sup>h</sup>	<b>-43.46 ± 0.41</b> {2}	-42.91 ± 0.47 {7} <sup>f</sup>	-80 ± 6 {4} <sup>i</sup>

<sup>a</sup>Dlugokencky et al. (2003)  
<sup>b</sup>Quay et al. (1999)  
<sup>c</sup>Chappellaz et al. (1993)  
<sup>d</sup>Sowers (2009)  
<sup>e</sup>Mischler (2009)  
<sup>f</sup>Fischer et al., (2008)  
<sup>g</sup>Sowers (2006, 2009)  
<sup>h</sup>Dällenbach et al. (2000)  
<sup>i</sup>Sowers (2006)

### 3.4. Box model Monte Carlo simulations

Initially, two atmospheric box models consisting of 4 (Section 2.4.1) and 6 (Section 7.2.1) boxes were parametrized and used in Monte Carlo simulations. The 4-box model has the advantage of isotope ratio and concentration constraints in each box provided by the polar ice cores. Conversely, the 6-box model presents the opportunity for a more realistic atmospheric circulation pattern (including a crude representation of the Brewer-Dobson circulation) [Holton et al., 1997] and, with the inclusion of an equatorial box, allows recognition of the different methane emission conditions present in the tropics, as opposed to the extratropics. In initial trials, across all time periods, the 6-box model consistently shows smaller emissions from boreal wetlands. This decrease in boreal emissions is compensated by increased emissions from tropical wetlands. No other consistent difference is observed between the models. Due to the higher number of parameters in the 6-box model, as compared to the 4-box model, it possesses higher uncertainties associated with chosen parameter values. Due to the lack of reliable information about methane source configuration changes through time, and no constraint on methane concentration and isotope ratio within the equatorial box, the 4-box model is believed more reliable and is used for all the results presented here.

#### 3.4.1. *Modern Simulation*

The 4 box atmospheric methane model was first run in Monte Carlo mode for the 1990s time period. The mean and standard deviation of the successful realizations are presented in Figure 3.4.1. The model is able to adequately reproduce source emission fluxes close to those that were used to parameterize the model, as is expected (mean deviation of 3 Tg CH<sub>4</sub> yr<sup>-1</sup>; see Table 2.4.4 and Figure 3.4.1).

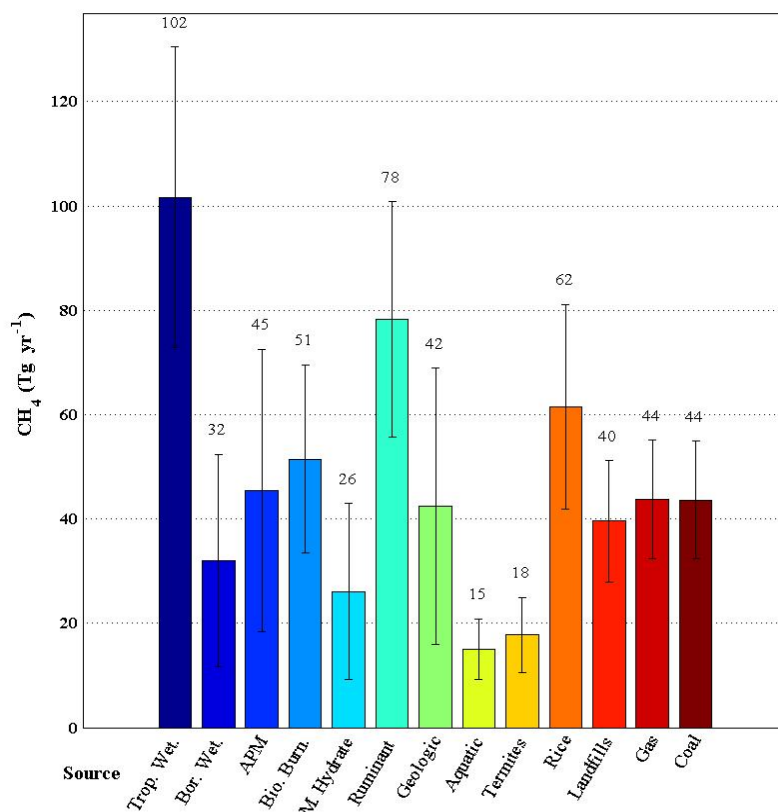


Figure 3.4.1: Monte Carlo box model simulation results for 1990s scenario. The standard deviations ( $1\sigma$ ) of the source fluxes for the 1990s are large. The range of possible source fluxes for the 1990s is larger than the other time periods investigated, which do not have the four additional anthropogenic sources of the 1990 time period (rice cultivation, landfills, natural gas, and coal; an exception is the Preindustrial Holocene (PIH) which allows for minor amounts of rice, landfill and coal methane).

The modern time period shows the importance of tropical wetlands as the strongest source, followed by ruminants (both wild and livestock), rice, and biomass burning.

### 3.4.2. 4-Box model simulation results across all time periods

The 4-box atmosphere model Monte Carlo simulations explores the predefined variable space of each source and the CH<sub>4</sub> atmospheric lifetime. The successful realizations define a probability distribution of possible values that satisfy the data

constraints. These probability distributions are normalized to allow comparison between time periods. The CH<sub>4</sub> atmospheric lifetime normalized probability distributions (NPDs) of the six time periods are presented in Figure 3.4.2. The box model mean CH<sub>4</sub> atmospheric lifetimes are listed in Table 3.4.1.

The longest CH<sub>4</sub> atmospheric lifetime is the modern scenario with the PIH, BA and LGM of similar length. The Preboreal and YD atmospheric lifetimes are almost two years shorter at ca. 5.5 years. The CH<sub>4</sub> atmospheric lifetimes of the different time periods are found to be stable under a large range of model CH<sub>4</sub> source variable space. An

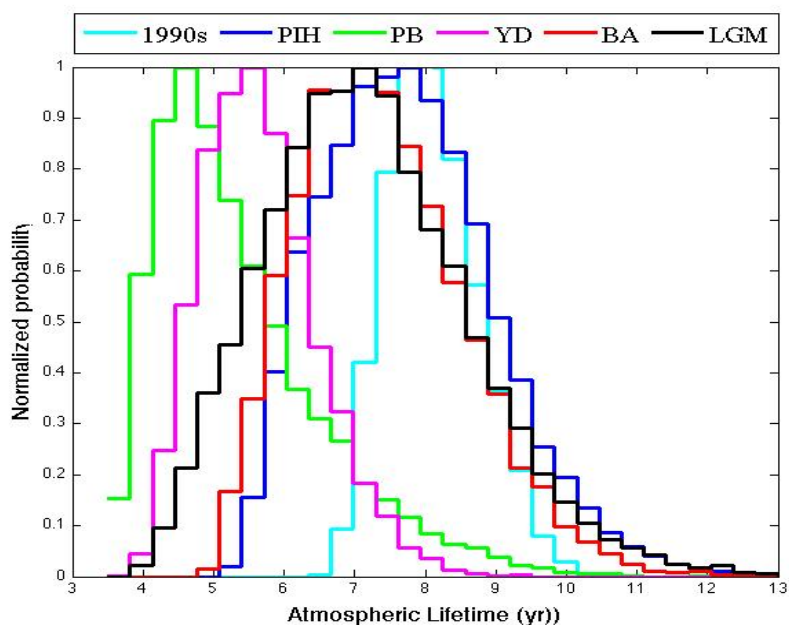


Figure 3.4.2: Probability distribution of atmospheric methane lifetime for the 6 time periods. These values represent only data-constrained Monte Carlo simulations. Note the Preboreal shows a greater tailing to higher CH<sub>4</sub> atmospheric lifetimes than all other periods.

exception is the Preboreal time period. The Preboreal CH<sub>4</sub> atmospheric lifetime is poorly constrained and decreases markedly if the source ranges are increased. This lack of a unique CH<sub>4</sub> lifetime, as opposed to the other time periods, is constrained by increasing

the minimum CH<sub>4</sub> atmospheric lifetime from 3.5 to 5.5 yrs ('best-guess'). This constraint results in a more stable methane atmospheric lifetime and better defined peaks for PB sources in the NPD.

Table 3.4.1: Methane atmospheric lifetimes determined by 4-box atmosphere model Monte Carlo simulations. The 'best-guess' constrained atmospheric lifetime for the Preboreal time period (> 5.5 years) is shown in curved brackets.

Time Period	CH <sub>4</sub> atmospheric lifetime (years)
1990s	8.1 ± 0.6
PIH	7.8 ± 1.2
Preboreal	5.5 ± 1.2 (6.7 ± 1.1)
YD	5.6 ± 0.8
Bølling-Allerød	7.4 ± 1.2
LGM	7.2 ± 1.5

The 4-Box model CH<sub>4</sub> fluxes of natural sources, as mean and standard deviation, for the 6 time periods simulated are presented in Figure 3.4.4. The results presented for the Preboreal use the 'best-guess' constrained atmospheric lifetime (> 5.5 yrs).

As a test of how well the mean Monte Carlo CH<sub>4</sub> flux and atmospheric lifetime values represent a plausible realization, as defined by the model (Table 3.4.2), the mean CH<sub>4</sub> source fluxes and atmospheric lifetime from the Monte Carlo simulations are fed back into the box model and run as a single simulation (non-Monte Carlo). All of the parameters are found to be within the constraint limits used in the Monte Carlo simulations, with the exception of Northern Hemisphere [CH<sub>4</sub>] that averaged 3.5 ppbv above the simulation tolerance of 10 ppbv (Table 3.3.1).

Total global and hemisphere CH<sub>4</sub> fluxes are presented in Table 3.4.3 and Figure 3.4.3. The LGM has the smallest fluxes, both globally and in each hemisphere, of all the time periods simulated. The LGM also has the smallest difference in CH<sub>4</sub> flux between

the N.H. and S.H, with 58 % of emissions originating in the N.H. The largest fluxes are for the 1990s, with a large difference between hemispheres; over 75 % of the CH<sub>4</sub> emissions are from the N.H. The other time periods show remarkable stability with all values, globally and for each hemisphere, within uncertainty limits.

Table 3.4.2: Results from the 4-box model, run as single simulation, for each time stable time period (1990s, PIH, PB, YD, BA, and LGM). Model input for each time period was from that time period's Monte Carlo simulation mean values for each CH<sub>4</sub> source and atmospheric lifetime. The single-simulation box model output for each of the model constraints (listed in column 1 including hemispheric CH<sub>4</sub> concentration, inter-polar gradient (IPG) and hemispheric stable isotope values for  $\delta^{13}\text{CH}_4$  and  $\delta\text{D-CH}_4$ ), is presented with the model constraint value for an acceptable realization (column 2), and the single-simulation results for all time periods. Single simulation values that are above Monte Carlo constraints are highlighted in bold. The  $\delta\text{D-CH}_4$  constraint is only available for the 1990s and PIH time periods.

Constraint	Limit	1990s	PIH	PB	YD	BA	LGM
N.H. [CH <sub>4</sub> ] (ppbv)	10	<b>10.3</b>	<b>16.0</b>	<b>15.3</b>	8	<b>14.8</b>	<b>16.5</b>
IPG [CH <sub>4</sub> ] (ppbv)	15	1.9	11.0	0.2	13.5	12.9	14.6
N.H. $\delta^{13}\text{CH}_4$ (‰ VPDB)	0.4	-0.09	0.32	-0.38	0.37	0.37	0.24
S.H. $\delta^{13}\text{CH}_4$ (‰ VPDB)	0.4	0.08	-0.31	0.02	-0.36	-0.36	-0.23
N.H. $\delta\text{D-CH}_4$ (‰ VSMOW)	10	-0.90	-0.55	1.17	-0.28	-0.54	-1.75
S.H. $\delta\text{D-CH}_4$ (‰ VSMOW)	10	2.2	-2.2	–	–	–	–

Table 3.4.3: Monte Carlo 4-box model simulated CH<sub>4</sub> flux (Tg yr<sup>-1</sup>) for hemisphere boxes and global total for all time periods investigated. (Mean values and 1σ standard deviations)

Time Period	1990s	PIH	PB	YD	BA	LGM
CH <sub>4</sub> flux (N. H.)	454 ± 30	175 ± 21	164 ± 24	160 ± 17	164 ± 20	90 ± 16
CH <sub>4</sub> flux (S. H.)	144 ± 17	74 ± 17	79 ± 18	71 ± 14	79 ± 17	65 ± 15
Global CH <sub>4</sub> flux	598 ± 35	249 ± 27	243 ± 30	230 ± 22	243 ± 26	155 ± 22

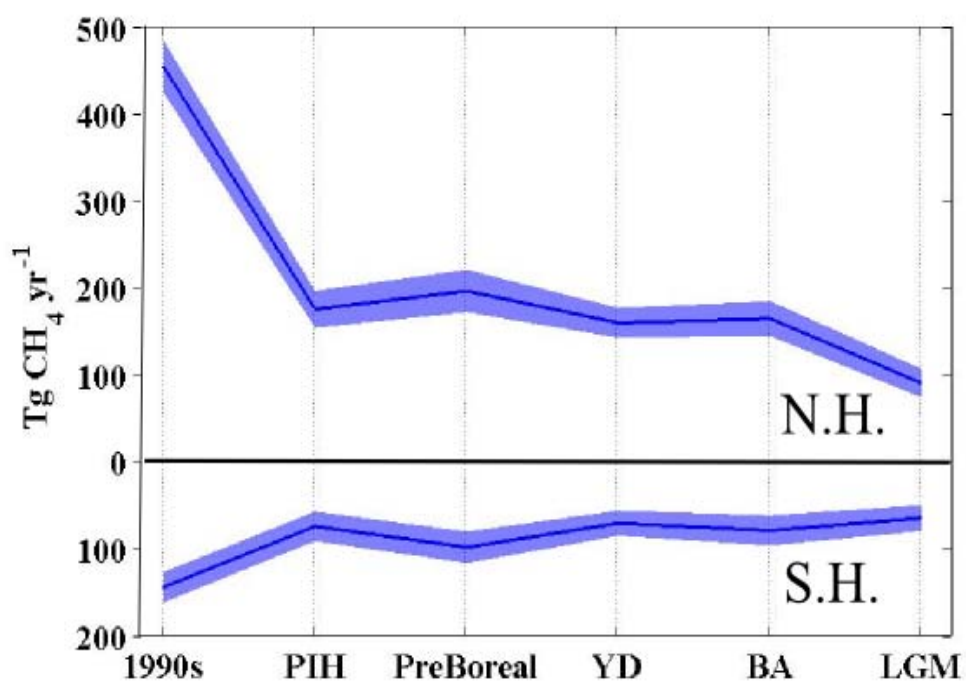


Figure 3.4.3: Monte Carlo box model simulated CH<sub>4</sub> flux from the Northern (N.H.) and Southern Hemisphere (S.H.) across all time periods investigated. 1σ uncertainty envelope is plotted in light blue.

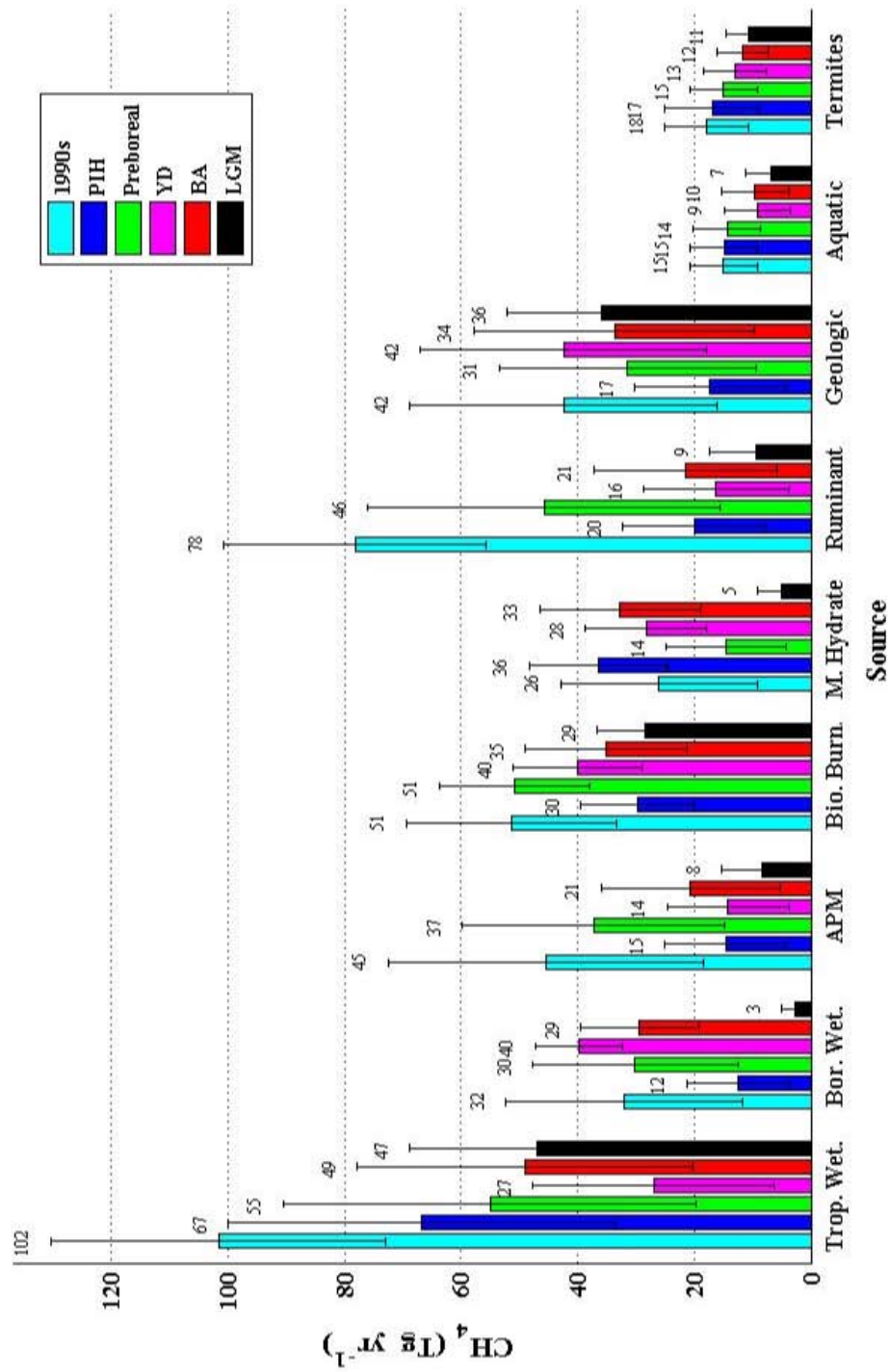


Figure 3.4.4: 4-Box model Monte Carlo simulation results for source strength over the stable time periods investigated.

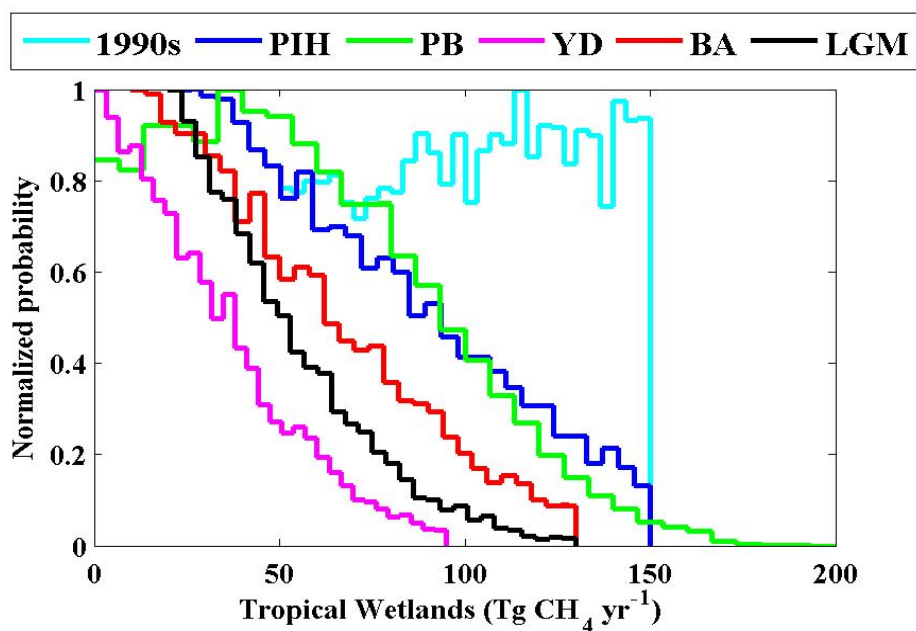


Figure 3.4.5: Normalized probability distribution (NPD) of tropical wetland methane flux across all time periods. The 1990s shows no peak in the NPD, but the mean value is stable over large changes in the Monte Carlo tropical wetlands flux variable space.

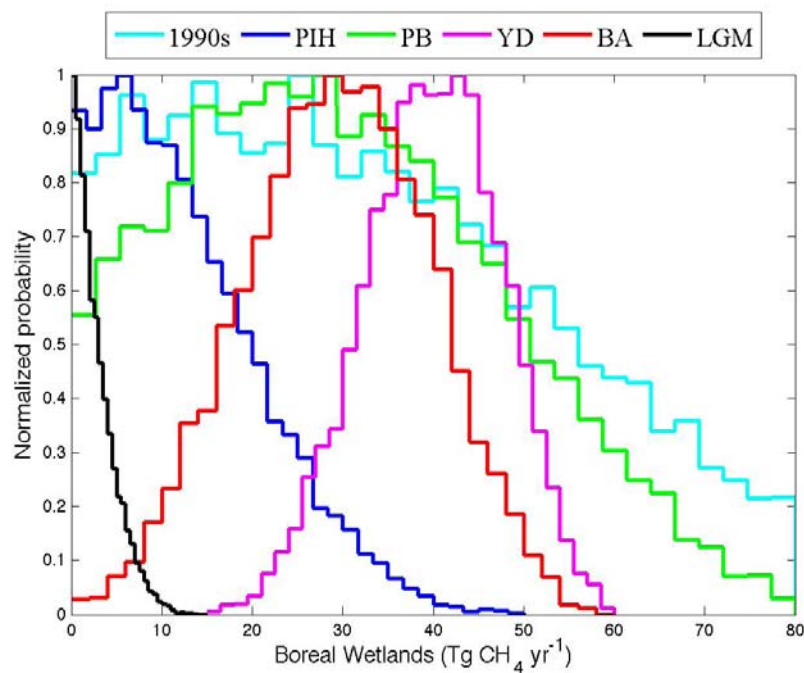


Figure 3.4.6: Normalized probability distribution (NPD) of boreal wetland methane flux across all time periods. Note the very tight peak for the LGM and the broad peaks of the PB and 1990s.

The tropical wetland CH<sub>4</sub> flux NPD shows a similar distribution across all time periods, with the exception of the 1990s (Figure 3.4.5). The 1990s time period does not show a defined peak in the NPD, but rather a roughly equal probability across the entire variable space. The variable space for the 1990s tropical wetlands was allowed in sensitivity tests to extend up to 250 Tg CH<sub>4</sub> yr<sup>-1</sup>. This extension of variable space shows the 1990s tropical wetland mean CH<sub>4</sub> flux to be reasonably robust. The mean tropical wetland flux of the simulation with the extended variable space does not extend beyond the standard deviation determined for a simulation with a tropical wetlands flux limit of 150 Tg CH<sub>4</sub> yr<sup>-1</sup>. Tropical wetlands also do not develop a sharper NPD peak with the extended variable space. The YD and LGM show a higher likelihood of lower tropical wetland CH<sub>4</sub> flux compared to the other periods (from the NPD at the 0.5 level). The mean CH<sub>4</sub> fluxes of the LGM and BA are similar, but the BA has a slightly wider NPD peak. The PB and PIH time periods appear indistinguishable in the NPD at the 0.5 level. The mean flux values show the YD to be the only time period that is obviously different, excluding the 1990s, however the large uncertainties prevent any firm conclusions. Tropical wetlands are the largest CH<sub>4</sub> source for the 1990s, PIH, PB, BA, and LGM (from mean values). However, the YD shows the tropical wetlands to be a relatively minor source, and in the PB tropical wetlands are approximately on par with biomass burning and ruminants.

The boreal wetlands show strongly an almost complete shut-off during the LGM with a narrow NPD peak and a CH<sub>4</sub> flux of  $3 \pm 2$  Tg yr<sup>-1</sup> (Figure 3.4.6). The warming of the BA time period shows an increase in the boreal wetland source up to about 30 Tg CH<sub>4</sub>

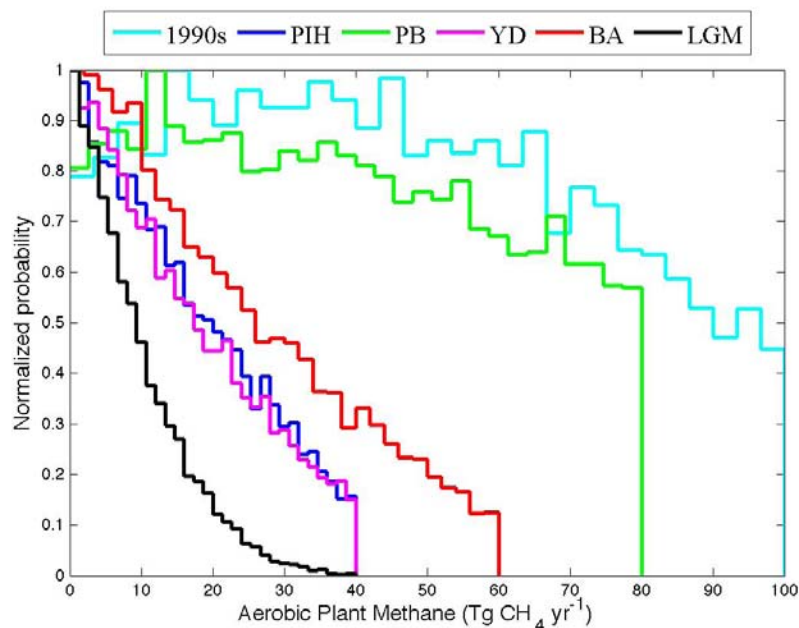


Figure 3.4.7: Normalized probability distribution (NPD) of aerobic plant methane (APM) flux across all time periods. The 1990s and PB time periods show no clear peaks in their respective NPDs

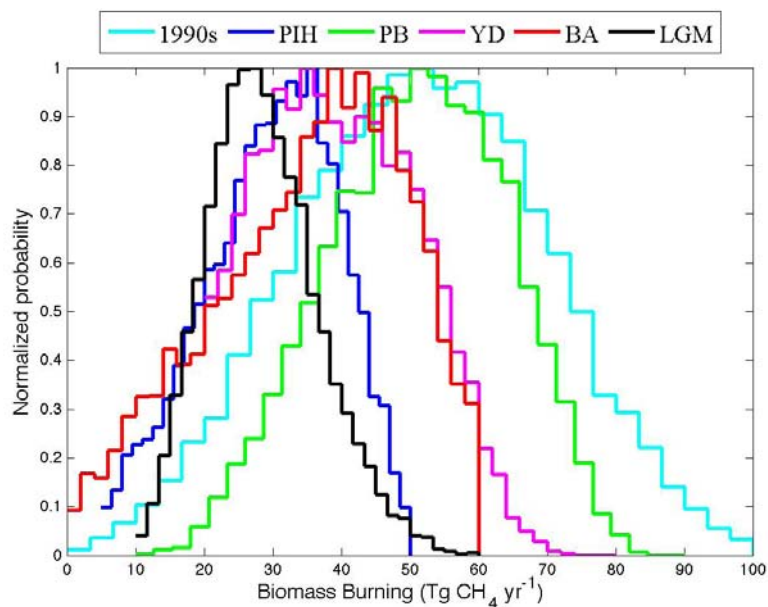


Figure 3.4.8: Normalized probability distribution (NPD) of biomass burning methane flux across all time periods. The NPD peaks for all time periods are relatively tight indicating well-constrained methane emission estimates.

yr<sup>-1</sup> with a slight increase in the YD, and a slight decrease into the PIH. The PB and 1990s time periods show broad NPD peaks indicating they are poorly constrained. The importance of boreal wetlands is most pronounced in the YD where they are amongst the three most important CH<sub>4</sub> sources. The other two CH<sub>4</sub> sources being geologic emissions of methane (GEM) and biomass burning.

The aerobic plant methane (APM) emissions NPD presents a similar pattern to the tropical wetlands, with smaller fluxes for the cooler time periods (LGM and YD) and the PIH, and slightly larger fluxes in the warmer periods (BA, PB, and 1990s) (Figure 3.4.4). However, the Preboreal and 1990s are poorly constrained with no clear peak in the NPD (Figure 3.4.7). The APM source appears to be consistently a minor component, with the largest mean values coinciding with the broadest NPD peaks (and thus the most uncertain flux estimates).

Biomass burning has some of the tightest NPD peaks of all sources, for all time periods (Figure 3.4.8). The six time periods do not show any strong shifts in methane flux with the mean values increasing slightly from the LGM through to the Preboreal. A smaller value is seen in the PIH. The 1990s, which are influenced by a mixture of natural and anthropogenic emissions, show an increase in CH<sub>4</sub> flux strength up to levels of the PB. The CH<sub>4</sub> flux values of the various time periods have significant overlap with the exception of the LGM and Preboreal (taken at 0.5 normalized probability (NP)). Biomass burning is the third most important methane source in the LGM (after tropical wetlands and GEM), and second most important in the BA and PB after tropical wetlands. During the YD, biomass burning is the most important source along with GEM.

Biogenic marine gas hydrates  $\text{CH}_4$  fluxes appear almost shut-off during the LGM, similar to the boreal wetlands, with a narrow peak in the NPD (Figure 3.4.9). The BA period shows a large increase in  $\text{CH}_4$  flux from marine gas hydrates up to a mean value of about  $33 \text{ Tg yr}^{-1}$  with a gradual decrease through the YD into the PB. The marine gas hydrate NPD shows a clear distinction (at the 0.5 NP level) between the  $\text{CH}_4$  flux of the BA and the PB time periods, and between the BA and LGM periods. The 1990s show a broad peak in the NPD with a mean value of ca.  $26 \text{ Tg CH}_4 \text{ yr}^{-1}$ .

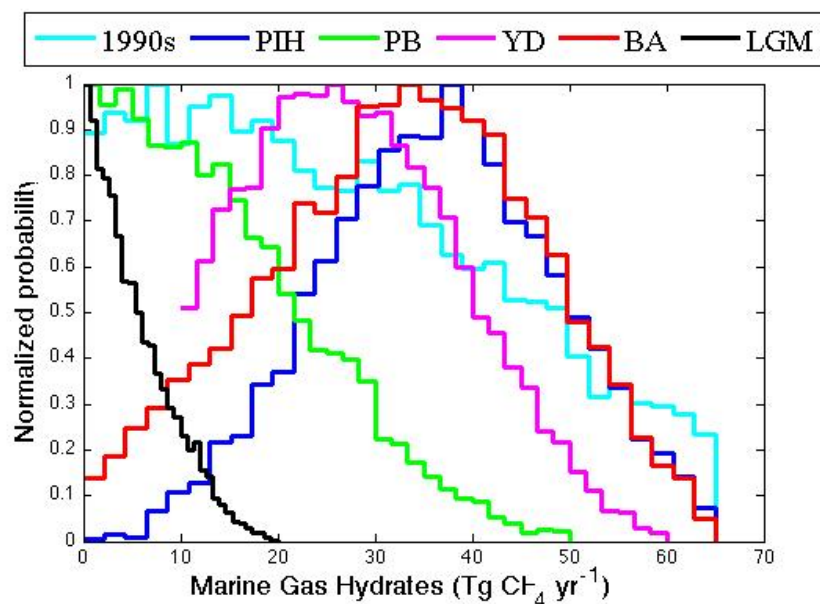


Figure 3.4.9: Normalized probability distribution (NPD) of biogenic marine gas hydrate methane flux across all time periods. The LGM NPD shows essentially no  $\text{CH}_4$  flux. The PB and PIH NPDs are broad and hence these flux estimates are poorly constrained.

Ruminant  $\text{CH}_4$  fluxes are highly influenced in the 1990s by anthropogenic activities such as livestock and dairy production. The 1990 ruminant mean  $\text{CH}_4$  flux is therefore much larger than the other time periods and its NPD is not shown on Figure 3.4.10. The PIH time period is also likely influenced by anthropogenic activities, but is

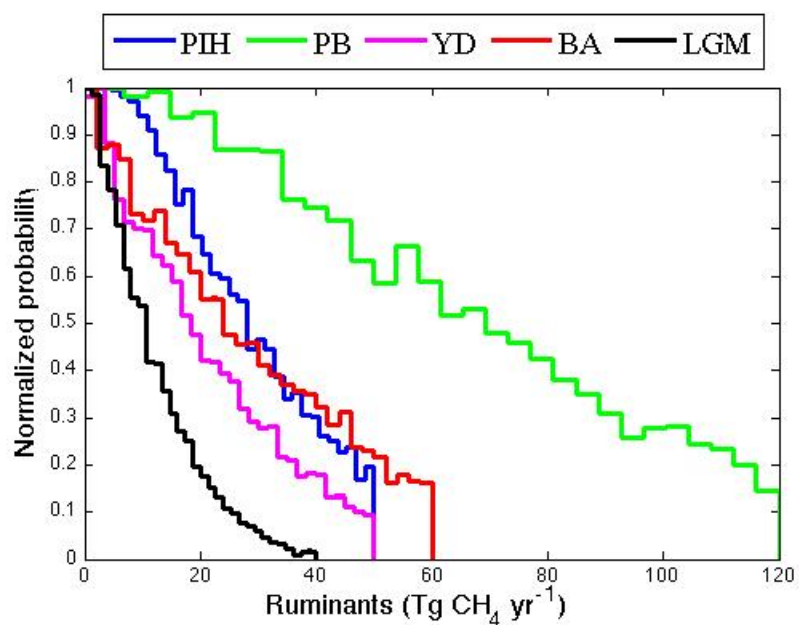


Figure 3.4.10: Normalized probability distribution (NPD) of ruminant methane flux across all time periods. The PB NPD is clearly different than the other periods with a very broad peak.

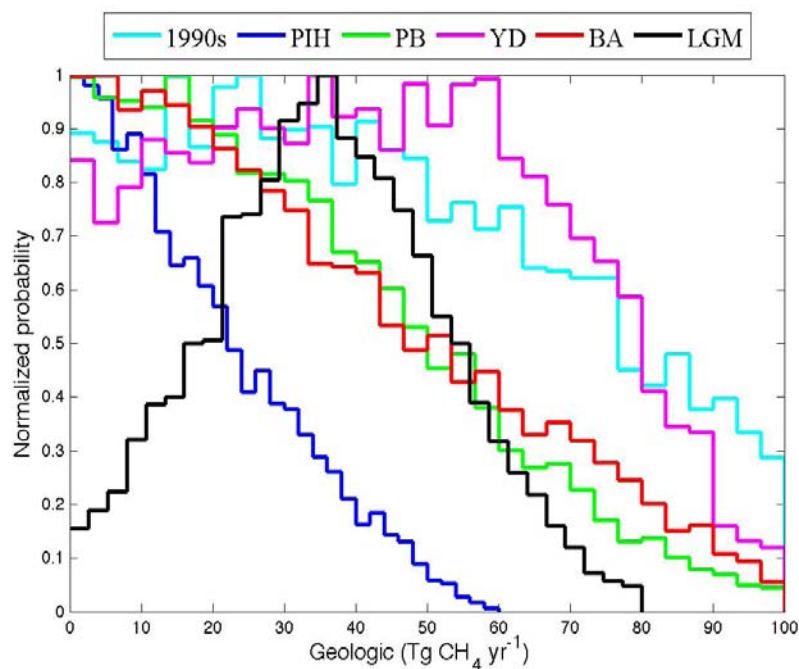


Figure 3.4.11: Normalized probability distribution (NPD) of geologic methane (GEM) flux across all time periods. The best constrained peaks in the NPD are for the PIH and LGM periods. Other time periods show relatively broad peaks.

plotted. Most time periods, excluding the 1990s, are essentially indistinguishable and show relatively small CH<sub>4</sub> fluxes between 10 and 20 Tg yr<sup>-1</sup>. The Preboreal has a larger mean CH<sub>4</sub> flux of 46 Tg yr<sup>-1</sup> (Figure 3.4.4), however it is poorly constrained due to a broad NPD peak (Figure 3.4.10).

The GEM mean CH<sub>4</sub> fluxes are relatively constant through time with the exception of the PIH flux about half that of the other time periods (Figure 3.4.6). However, the GEM NPD shows that the only well-defined peak to be the LGM (Figure 3.4.11).

Aquatic methane sources (which includes oceanic and freshwater) and termites show no peaks in their respective NPDs. These sources also show relatively constant mean values through the time periods investigated (Figure 3.4.4).

### 3.4.3. Sensitivity tests

Several different sensitivity tests were performed with the 4-box model. Results from Monte Carlo simulations for the five <sup>13</sup>C sensitivity tests are presented in Figures 3.4.12 and 3.4.13. The δ<sup>13</sup>CH<sub>4</sub> values chosen for the sensitivity tests, and initial (control) values, are listed in Table 2.4.4. The five sensitivity tests included:

- 'FEN': Boreal wetlands δ<sup>13</sup>CH<sub>4</sub> value changed to a value more typical of fen wetlands (-60‰; Bellisario et al., 1999; MacDonald et al., 2006)
- 'TK': Boreal wetland δ<sup>13</sup>CH<sub>4</sub> value changed to an average thermokarst lake δ<sup>13</sup>CH<sub>4</sub> value (-68.5 ‰; derived from Walter et al., 2006)
- 'BB': Biomass burning δ<sup>13</sup>CH<sub>4</sub> value increased to -20 ‰ [Stevens and Engelkemeir, 1988]

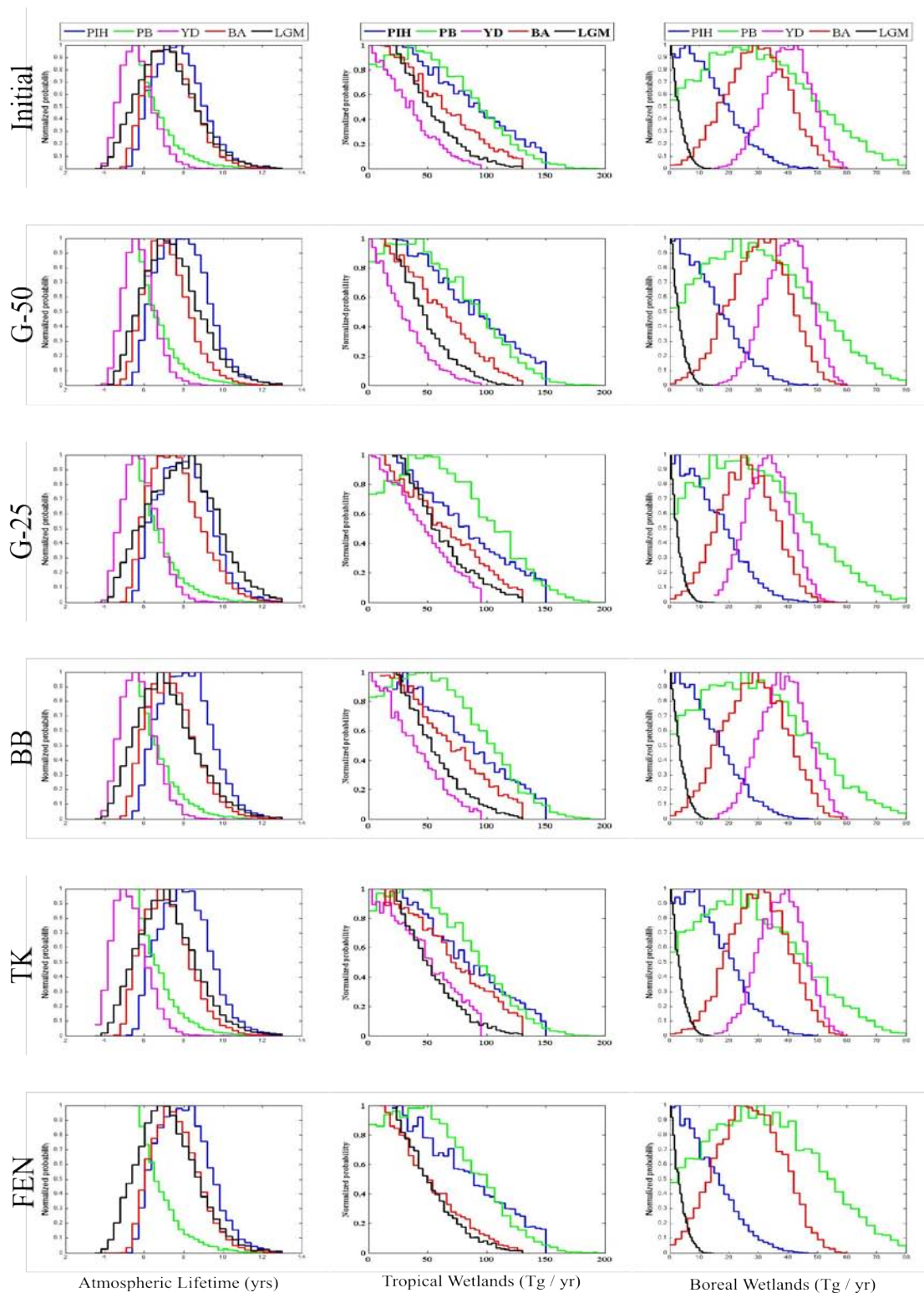


Figure 3.4.12: Normalized probability distributions (NPDs) of sensitivity tests for 4-Box Monte Carlo model. Atmospheric lifetime (left), tropical wetlands (centre), and boreal wetlands (right) for the five sensitivity tests (see text for further information) and initial conditions. Note the FEN simulations did not have any realizations for the YD.

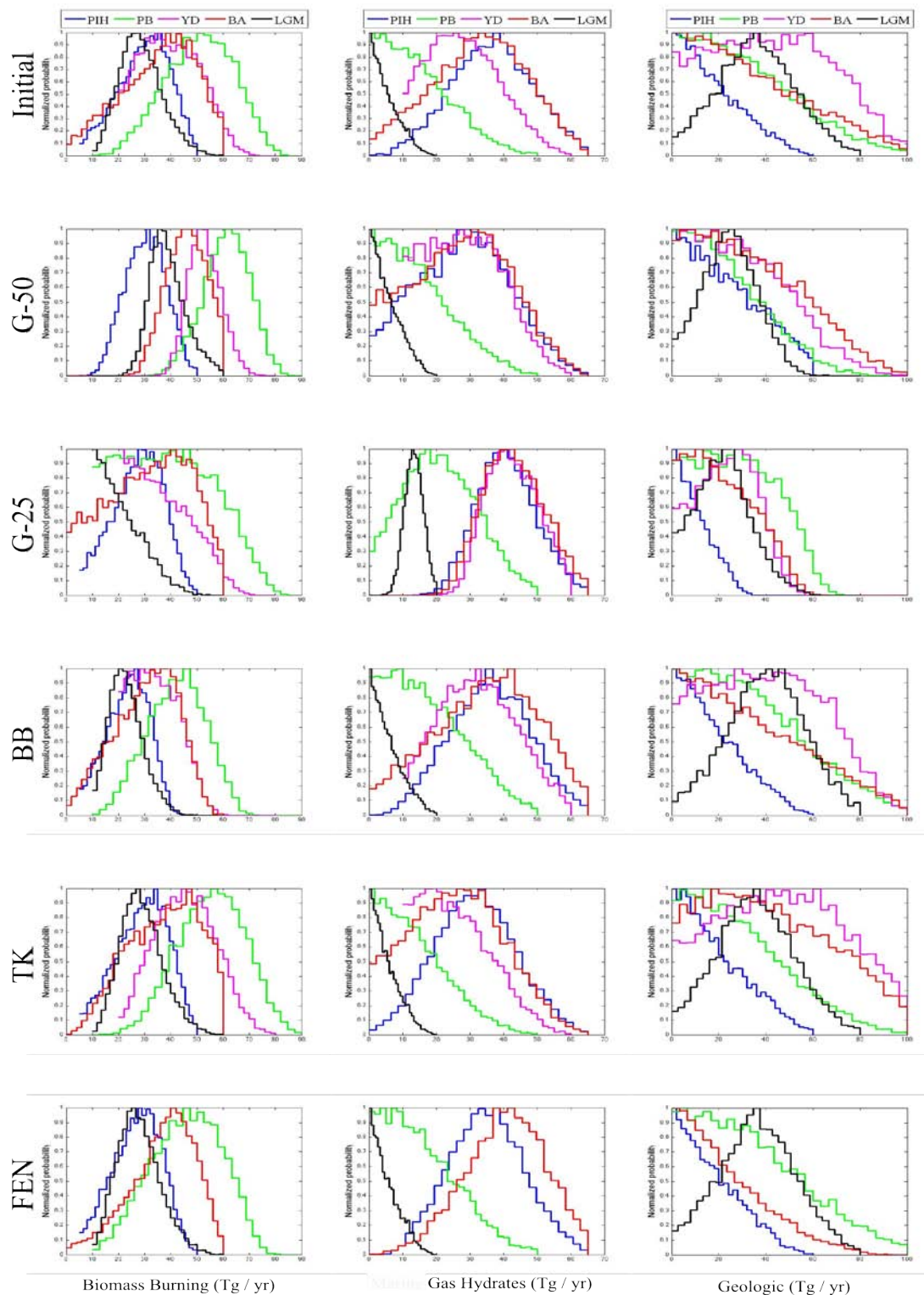


Figure 3.4.13: Normalized probability distributions (NPDs) of sensitivity tests for 4-Box Monte Carlo model. Biomass burning (left), biogenic marine gas hydrates (centre), and geologic emissions (right) for the five sensitivity tests (see text for further information) and initial conditions. Note the FEN simulations did not have any realizations for the YD.

- 'G-25': Geologic methane  $\delta^{13}\text{CH}_4$  value increased to the upper limit (-25 ‰) of data range in Etiope et al. (2008a)
- 'G-50': Geologic methane  $\delta^{13}\text{CH}_4$  value decreased to the lower limit (-50 ‰) of data range from Etiope et al. (2008a).

All simulations are able to complete 10,000 successful realizations except the YD FEN run. This run is not able to achieve  $> 200$  realizations in over 17 hours wall time. The run was thus aborted and no values for the FEN run of the YD time period are presented. The successful sensitivity tests are described below.

The  $\text{CH}_4$  atmospheric lifetime is observed to be stable across all sensitivity tests and time periods, with only subtle changes between tests (Figure 3.4.12). The largest changes are for the PIH and LGM time periods in the G-50 test, however these are too small to be considered significant.

The tropical wetlands are not highly influenced by the sensitivity tests (Figure 3.4.12). All sensitivity tests show approximately the same NPD as that from the initial conditions simulation. The boreal wetlands are also essentially unchanged by the differing  $\delta^{13}\text{CH}_4$  values of the sensitivity tests (Figure 3.4.12), in addition ruminants, aquatic emissions, APM, and termites display little sensitivity to the changing  $\delta^{13}\text{CH}_4$  values.

The biomass burning flux is essentially unchanged from the initial (control) simulations in the BB test, however the G-50 and G-25 tests show significant changes (Figure 3.4.13). The NPD spectrum of the G-50 test indicates a narrowing of all time periods' biomass burning peaks, and a small shift towards higher emissions of biomass burning methane for some periods (LGM, PB, and YD). The G-25 test is significantly

different (at the 0.5 NP level) from the initial and G-50 test results, for the LGM and YD with the G-25 test showing a strongly decreased biomass burning flux. The G-25 test also shows a strong tailing of the biomass burning NPD peaks towards smaller fluxes.

Biogenic marine gas hydrates  $\text{CH}_4$  fluxes are also highly influenced by the G-25 test scenario. The LGM  $\text{CH}_4$  emissions by biogenic marine gas hydrates are significantly larger (at the 0.5 NP level) than all other tests. As well, the marine gas hydrate NPD peaks of the other time periods are narrowed by the G-25 test compared to initial (control) simulations. The NPD peaks of the other tests are not largely changed except for a slight decrease in the YD  $\text{CH}_4$  flux peak value in the TK test, as compared to initial simulations.

The geologic source NPD shows only slight changes in the different time periods across the five tests. The largest changes are observed between the G-25 and BB tests with much narrower NPD peaks and smaller  $\text{CH}_4$  fluxes for the G-25 test across all time periods (decrease in mean fluxes of up to  $19 \text{ Tg CH}_4 \text{ yr}^{-1}$ , but not outside of standard uncertainty).

To test the model response to terrestrial, rather than marine gas hydrates, the  $\delta\text{D-CH}_4$  value of biogenic gas hydrates was changed from a representative marine value (-190 ‰) to a value chosen to be characteristic of a terrestrial gas hydrate (-290 ‰). The terrestrial  $\delta\text{D-CH}_4$  value can only be estimated as no measurements of terrestrial biogenic gas hydrates are currently available. Sensitivity tests using the terrestrial hydrate  $\delta\text{D-CH}_4$  value show no significant changes (outside of standard uncertainty) to any sources during the LGM and BA periods. During the YD, PB and PIH periods, the sensitivity tests show larger biomass burning  $\text{CH}_4$  fluxes in the marine gas hydrates scenario (Figure 3.4.14).

The terrestrial hydrate scenario for the same time periods shows increased GEM flux.

The fluxes of hydrates do not change if they are given  $\delta D-CH_4$  values characteristic of marine or terrestrial methane sources.

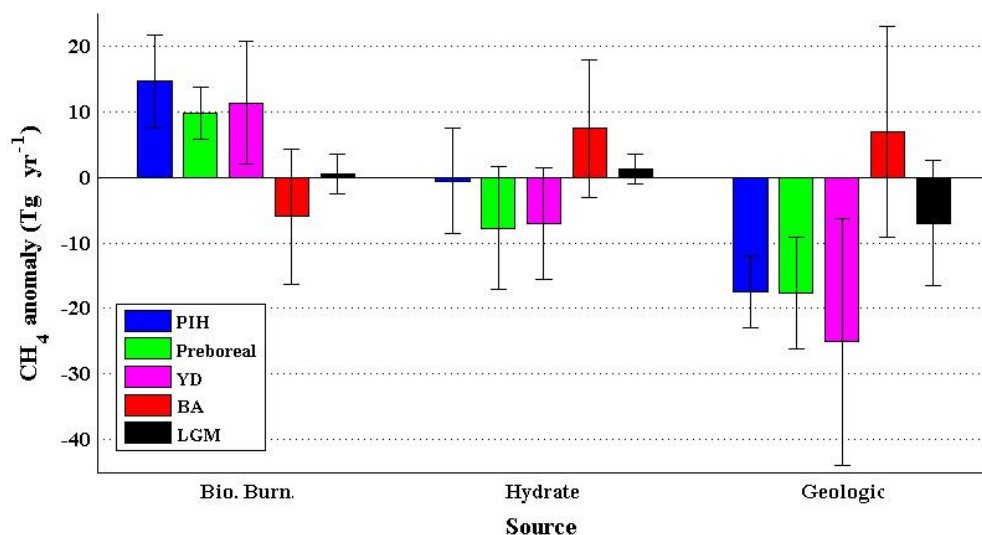


Figure 3.4.14: Sensitivity test for the effect of a marine (-190 ‰) versus terrestrial (-290 ‰) hydrate source  $\delta D-CH_4$  value across all time periods. The methane flux anomaly is the marine hydrate scenario minus the terrestrial hydrate scenario. The plot indicates that no change in hydrate flux is observed as the standard uncertainty estimate spans the 0-axis in all cases. . Biomass burning and GEM during the BA and LGM (outside of standard uncertainty) also do not show any change. During the YD, PB, and PIH, the terrestrial hydrate scenario indicates higher fluxes of GEM sources, while showing reduced fluxes of biomass burning methane.

## 4. Discussion

### 4.1. Sources of contamination

From the results presented in Section 3.2, the Pákitsoq ice appears to contain an irregular contamination that occurs in ice apparently free of other known problems, such as 'blue' bands (bubble-free ice) or dust bands (ice with high sediment load). Issues relating to these 'blue' and dust bands have been described in Petrenko et al. (2006) and Schaefer (2005). Blue bands are speculated to be refrozen cracks in the ice, with a resulting elevated  $[\text{CH}_4]$  in the interstitial air [Petrenko et al., 2006]. Any isotope effect on the  $\text{CH}_4$ , within the ice bubbles, due to these blue bands is unknown. Dust bands have been speculated to be caused by subglacial silt injection into fissures in the ice by subglacial meltwater [Petrenko et al., 2006]. This interpretation is supported by neodymium and strontium isotope analysis indicating a local, rather than Asian, source of the dust. Concentration measurements of air sampled from dust-band ice also show elevated  $[\text{CH}_4]$  with an unknown isotope effect. These two contamination sources are well known and easily identified, thus all samples measured for this study were carefully inspected for evidence of these features, and all occurrences removed prior to analysis. Since the Pákitsoq samples in the work presented here showed contamination, and known causes of contamination have been avoided, four possibilities will now be considered to explain the excess methane: 1) introduction of atmospheric air during sample analysis, 2) carbon monoxide (CO) break-through during analysis, 3) in-situ methane production, and 4) substrate depletion.

The instrumental set-up was carefully tested to exclude the possibility of introduction of modern atmospheric air (see Section 2.1.4). The numerous blank tests and

measurements of GISP2 ice (Section 3.1) preclude leaks in the system during Pákitsoq sample analysis. As further proof, one sample is measured at a higher concentration (2321 ppbv) than the present atmospheric methane mixing ratio (ca. 1850 ppbv; lab air measured with Isometric Instruments GYRO™ laser-based spectrometer), thus the excess methane could not have come from atmospheric air.

Petrenko (2008) notes that Pákitsoq contains high [CO] (800 – 2500 ppbv) compared to the modern atmosphere (40 - 200 ppbv)[Brenninkmeijer, 1993]. The source of this excess CO is suggested by Petrenko (2008) to be in-situ production by the slow H<sub>2</sub>O<sub>2</sub> oxidation of organic matter within the ice [Haan et al., 1996]. Other possible sources include photochemical production from organics in the ice by ultraviolet radiation generated in-situ by fast muons passing through deep ice [Colussi and Hoffmann, 2003]; and microbial production [e.g. Bowater et al., 2004; Price, 2007]. In the instrumental setup used here, the CO is stripped from the gas stream via two CO traps (where the CO is converted to CO<sub>2</sub>; detailed in Section 2.1.1). The CO removal is important because the oxidation oven will convert any residual CO to CO<sub>2</sub>, that will then be trapped with the oxidized CH<sub>4</sub>, causing an increase in the apparent [CH<sub>4</sub>]. Tests for Schutze reagent breakthrough by Petrenko (2008) showed 1% of the Pákitsoq CO was passing through unconverted, however his experimental set up was for the isolation of <sup>14</sup>CH<sub>4</sub> from very large samples (~100 L), and may not be analogous. In the setup used here, the gas stream first enters a Sofnocat™ 514 trap and then a Schutze reagent trap. Sofnocat™ 423, a similar catalyst to 514, was tested by Petrenko, (2008) to quantitatively convert CO to CO<sub>2</sub> in gas streams with [CO] up to 7000 ppbv. While the product used for this work is not identical (it appears to differ in particle conformation), similar

performance is expected. If it is assumed that the Sofnocat™ 514 trap has markedly poorer performance than Sofnocat™ 423, allowing 10 % of CO to pass through (this value is assumed to be much higher than expected under the worst circumstances) and the Schutze reagent also has a 1% breakthrough (using the value found by Petrenko, 2008), the maximum amount of contamination would be 2.5 ppbv CH<sub>4</sub> equivalent (from the highest [CO] value measured by Petrenko, (2008) for Pâkitsoq ice). This amount of CH<sub>4</sub>-equivalent CO could not account for the elevated [CH<sub>4</sub>] observed in the contaminated samples, and can be eliminated as a possible source.

Microorganisms have been shown to exist in icy habitats and have been isolated from the basal ice sections of the GISP2 ice core. These archaea have been shown to exist both in the network of liquid veins created by the exclusion of solutes from the polycrystalline ice matrix, and on the liquid film surfaces of clay particles entrained in ice matrices [Price, 2007]. Methane production in-situ by microorganisms is suggested by the very high concentrations of CH<sub>4</sub> found in silty ice at the bottom of ice cores, such as GRIP (6000 ppmv)[Tison et al., 1998] and GISP2 (>120 000 ppmv)[Price and Sowers, 2004], as well as in a low-latitude mountain glacier [Campen et al., 2003]. Analysis of the microbial cells found on the silt grains from GISP2 by F420 coenzyme autofluorescence found ca. 2.4 % to be methanogens, of which a ratio of 5 live to 1 dead was noted [Sheridan et al., 2003].  $\delta^{13}\text{CH}_4$  values in the basal ice sections of the GRIP ice core are measured to be -81 to -84 ‰ [Souchez et al., 2006].

It has also been noted by Price (2007) that irregular sections of the GISP2 ice core have highly elevated [CH<sub>4</sub>], up to 100 m vertically displaced from the silty ice. These same sections are found to have high numbers of methanogens (detected via F420

coenzyme autofluorescence). This ice is believed to have been entrained in the ice sheet by ice tectonic motion taking place over a frozen wetland at the bottom of the ice sheet [Price, 2007].

Some of the conditions of the basal ice of GISP2 and GRIP are similar to that found in Pákitsoq. The temperature of the basal ice at GISP2 is  $-9\text{ }^{\circ}\text{C}$  (as compared to  $-32\text{ }^{\circ}\text{C}$  in the top few hundred metres)[Meese et al., 1997], while Pákitsoq has been measured as warm as  $-7\text{ }^{\circ}\text{C}$  at a few metres depth [Petrenko, 2008]. Warmer ice promotes increased  $\text{CH}_4$  production due to increases in methanogen metabolism. For example, between temperatures at the top and bottom of GISP2, cell metabolism increases by about two orders of magnitude [Tung et al., 2005]. Furthermore, the incidence of dust bands in the Pákitsoq surface ice indicate close contact between underlying sediments and the ice as it flows from the deposition site to the ablation zone. Given these similarities, it appears possible that in-situ methanogenesis is involved with the elevated [ $\text{CH}_4$ ] values found in the air occlusions of Pákitsoq ice. However, given the  $\delta^{13}\text{CH}_4$  values reported for methane from silty basal ice, if the reported values are representative, it would be expected that all contamination would make the  $\delta^{13}\text{CH}_4$  values of the Pákitsoq contaminated samples more  $^{12}\text{C}$ -enriched than contemporaneous uncompromised samples. This is found to not be the case in 15 out of 26 of the samples where a duplicate uncompromised sample was available for comparison (using the filtering process as described in Section 3.2 to determine an uncontaminated sample). It is evident then, that in-situ production can not be solely responsible for the compromised samples measured. Interestingly, Schaefer (2005) reports contaminated samples from the 2001 sampling season that also gave  $^{13}\text{C}$ -enriched  $\delta^{13}\text{CH}_4$  values. These  $^{13}\text{C}$ -enriched  $\delta^{13}\text{CH}_4$  values are

attributed to the accidental inclusion of samples with a conspicuous clear (bubble-free) band, assumed to be a refrozen chainsaw cut, passing through them. There was no indication of any clear bands in the samples that were processed for this work. Thus a different explanation is required to explain the cause of the anomalous,  $^{13}\text{C}$ -enriched  $\delta^{13}\text{CH}_4$  values.

Due to the constraints of the ice matrix itself, it can be approximated as a closed system. Closed systems that experience continued, preferential removal of the lighter,  $^{12}\text{C}$  from the substrate carbon pool during methanogenesis become  $^{13}\text{C}$ -enriched in the remaining residual substrate [Whiticar, 1999]. As the substrate continues to be converted to  $\text{CH}_4$ , the methane produced is also progressively  $^{13}\text{C}$ -enriched. This progressive enrichment, by substrate depletion, commonly follows a Rayleigh distillation (fractionation) and the appropriate form of this relation is provided by [Whiticar, 1999]:

$$(4.1.1.) \quad \delta^{13}C_{\text{CH}_4, t} = \delta^{13}C_{\text{substrate}, i} + \varepsilon (1 + \ln(1 - (1 - f)))$$

where  $\delta^{13}\text{C}_{\text{CH}_4, t}$  is the value of the methane at time  $t$ ;  $\delta^{13}\text{C}_{\text{substrate}, i}$  is the value of the initial carbon substrate (assumed here to be  $\delta^{13}\text{CH}_4 = -27 \text{‰}$ );  $\varepsilon$  is the fractionation factor from substrate to methane (assumed to be acetate;  $\varepsilon = 24$  to  $27 \text{‰}$  [Whiticar, 1999]); and  $f$  is the fraction of the initial substrate remaining at time  $t$ . Choosing the most highly contaminated Pákitsoq sample (2321 ppbv with a contemporaneous uncompromised concentration of 489 ppbv) with a measured  $\delta^{13}\text{CH}_4$  value of  $-45.88 \text{‰}$ , and contemporaneous Pákitsoq samples measured at  $-47.00 \text{‰}$ , gives a  $\delta^{13}\text{C}_{\text{CH}_4, t}$  value of  $-42.50 \text{‰}$  for the contaminant  $\text{CH}_4$ . This would indicate that ca. 80 % of the substrate has been converted to  $\text{CH}_4$  in this particular sample. This is a high degree of methanogenesis, yet this does represent the most extreme case of the samples measured.

The combined processes of in-situ microbial methane production with subsequent substrate depletion could potentially explain the samples with elevated  $[\text{CH}_4]$ . However, both of these processes, while observed to occur in other similar environments, can only be considered speculative here without further evidence.

#### **4.2. Critique of Monte Carlo box model simulations**

Before the results of the Monte Carlo box model simulations are used to interpret the measured  $\delta^{13}\text{CH}_4$  record, it is important to outline the limitations of the box model. As previously mentioned (see Section 2.4.1 for a full description), the 4-box model is a steady state model with two troposphere and stratosphere boxes in the Northern and Southern hemispheres. Using this model for time periods in the past, exposes some necessary assumptions that may not be correct in these time periods. The assumptions include: 1) constant atmosphere mass-exchange rates, 2) constant proportional sink strengths, 3) prescribed portioning of each source's flux between the hemispheres through time, 4) equal sink strength in both hemispheres, and 5) stable isotope values chosen for each source.

The atmosphere mass-exchange rates were initially chosen following Warneck, (1988) and parameterized under modern conditions to the final values used (Table 7.2.2). Several general circulation model (GCM) studies have demonstrated higher wind speeds in glacial times [e.g. Kitoh et al., 2001; Shin et al., 2003]. These higher wind speeds could result in greater atmospheric mixing. The effect of enhanced mixing was tested by increasing atmospheric mass exchange rates (~10 %) in the 4-box model, but is found to not grossly affect the results presented (mean  $\text{CH}_4$  flux values are within the standard deviation of control runs).

In the box model, CH<sub>4</sub> sinks are each assigned a fixed fractional contribution to the total sink strength (see Table 7.2.2), which may not be correct across the different time periods.

Each source flux in the box model simulations is proportioned between the hemispheres. This partitioning is necessary (as described in Section 2.4.1), but is somewhat arbitrary. Hemispheric flux partitioning is made by reasonable estimation of the changes in the earth system relevant to each source through the different time periods. This is complicated by the observation that some sources do not have a reliable flux distribution between hemispheres even for present day, e.g. GEM [G. Etiope, personal communication 2009]. This is likely one of the greatest sources of uncertainty in the box model parameterization.

From modern observations, the tropospheric OH sink is not constant nor equally weighted between, or within, hemispheres [e.g. Prinn, 2003]. The distribution is a reflection of the atmospheric conditions of ultraviolet radiation (UV), water vapour, and the emissions of the trace gases that OH radicals destroy [Prinn, 2003]. Changes to the hemispheric distribution of the OH sink across the time periods simulated by the box models are not known.

Important box model parameters for each source are the representative  $\delta^{13}\text{CH}_4$  and  $\delta\text{D-CH}_4$  values chosen. Due to the large ranges of stable isotope values for each source (Figure 1.2.1), these choices will have impacts upon the model outcomes. As a result of this, careful selection of representative stable isotope values is important.

The box model results for the 1990s are not interpreted in the following discussion. The 1990s time period is likely heavily influenced by the initial conditions of

tuning and will reflect the bias of the initial prescribed-flux budget. As well, the 1990s has 4 extra anthropogenic CH<sub>4</sub> sources that allow for more degrees of freedom in the simulations, with a resulting lower constraint on source fluxes. The PIH time period also has some anthropogenic emissions allowed in the Monte Carlo simulations (coal, rice, and landfill), but the small fluxes of each of these (ca. 6 % of total flux) is assumed to not largely increase uncertainty.

The two smallest sources, termites and aquatic CH<sub>4</sub> emissions are not discussed in detail. Both of these sources show relatively small CH<sub>4</sub> fluxes with no peaks in the normalized probability distributions (NPDs). The lack of peaks in the NPDs of these sources preclude the interpretation of their flux strength.

Finally, the atmospheric lifetime constraint that is placed on the Preboreal Monte Carlo simulations (see Section 3.4.2) demonstrates the uncertainty associated with source CH<sub>4</sub> fluxes for this time period. While the 'best-guess constraint' (> 5.5 yr CH<sub>4</sub> lifetime limit) allows for a narrowing of the PB NPD source peaks, these estimates are no longer solely data-constrained.

#### **4.3. The $\delta^{13}\text{CH}_4$ record for the most recent deglaciation**

The combined Pákitsoq  $\delta^{13}\text{CH}_4$  record and other published  $\delta^{13}\text{CH}_4$  records [Ferretti et al., 2005; Schaefer et al., 2006; Fischer et al., 2008; Sowers, 2009] are presented in Figure 4.3.1. With these combined records, a fairly complete picture of methane dynamics through the most recent deglaciation is now available. Combining these  $\delta^{13}\text{CH}_4$  records with those available for [CH<sub>4</sub>] and  $\delta\text{D-CH}_4$  enables powerful insights into methane source dynamics.

Interpretation of the changes in methane sources and sinks responsible for the observed record is aided by the Monte Carlo box model simulations (Section 3.4). The sources commonly suggested as responsible for the observed changes in the methane record over the deglaciation are reviewed below, as well as the box model results for atmospheric lifetime. The special cases of the apparent large inter-polar gradient (IPG) in  $\delta^{13}\text{CH}_4$  during the Bølling-Allerød period and the high-resolution  $\delta^{13}\text{CH}_4$  measurements through the Younger Dryas - Preboreal abrupt warming are also discussed in detail.

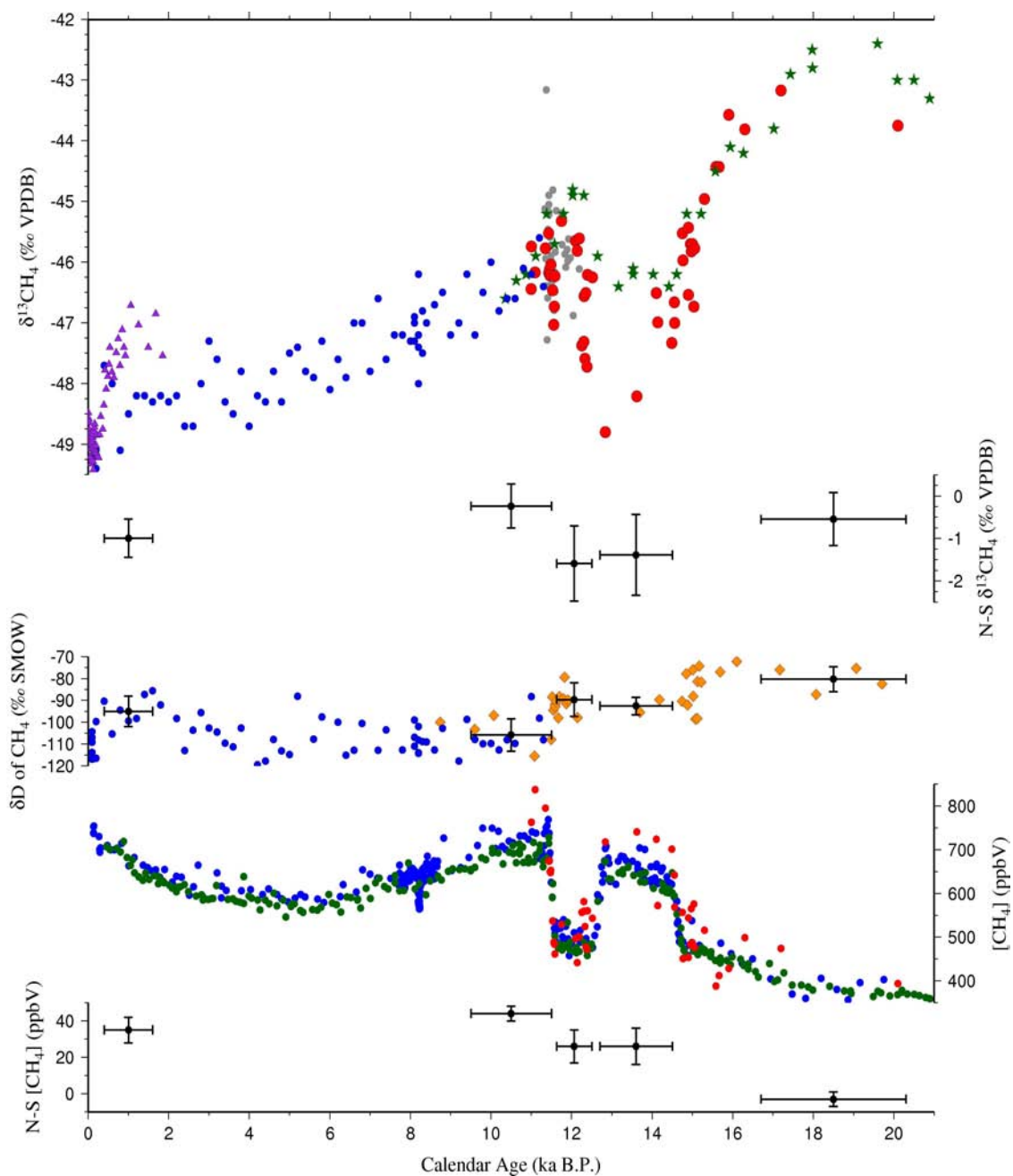


Figure 4.3.1:  $\delta^{13}\text{CH}_4$ ,  $\delta\text{D-CH}_4$  and  $\text{CH}_4$  concentration records spanning the LGM through the Holocene. The inter-polar gradient (IPG) in  $\delta^{13}\text{CH}_4$  (second from top) and  $\text{CH}_4$  concentration (bottom) for the box model stable time periods are also displayed.  $\delta^{13}\text{CH}_4$  data sources (top) include this work (red dots; P  kitsoq, Greenland), Fischer et al. (2008)(green stars; EDML, Antarctica), Schaefer et al. (2006)(grey circles; P  kitsoq, Greenland), Sowers (2009)(blue dots; GISP2, Greenland), and Ferretti et al. (2005)(purple triangles; Law Dome, Antarctica).  $\delta\text{D-CH}_4$  data are from Sowers (2006)(orange diamonds) and Sowers (2009)(blue dots). The stable period mean values used in the box model simulations are shown as discrete points with uncertainty bars.  $\text{CH}_4$  concentration data (second from bottom) are from this work (red dots; IRMS-derived concentration), Brook et al., 1996 (blue dots; GISP2, Greenland), and EPICA Community Members (2006)(green dots; EDML, Antarctica).  $[\text{CH}_4]$  IPG from D  llenbach et al. (2000); Chappellaz et al. (1993)

#### 4.3.1. Boreal Wetlands

Methane sources are predominantly terrestrial and approximately 85% of global land mass, at present day, is within the Northern Hemisphere. During the LGM, sea level was depressed by 120 – 135 m below present day sea level [Clark and Mix, 2002; Jansen et al., 2007] with the water displaced onto the continents as massive Northern Hemisphere (N.H.) ice sheets (Figure 4.3.2). The extent of the ice sheets was such that ca. 35 % of land in the N.H. was overlain by ice, as calculated using the ICE-5G model of Peltier (2004). This amount of ice and surface coverage will limit the boreal wetland methane flux due to cooler temperatures and decreased land surface available for boreal wetlands. In addition, it has been proposed from general circulation model simulations [Shin et al., 2003], paleovegetation data [Gajewski et al., 2001], and peatland basal  $^{14}\text{C}$  dates [MacDonald et al., 2006] that regions of Siberia, and possibly Beringia, that remained ice-free during the last glacial period (see Figure 4.3.2), were too cold and dry to support wetland development.

Conversely Beringia, with its large area of

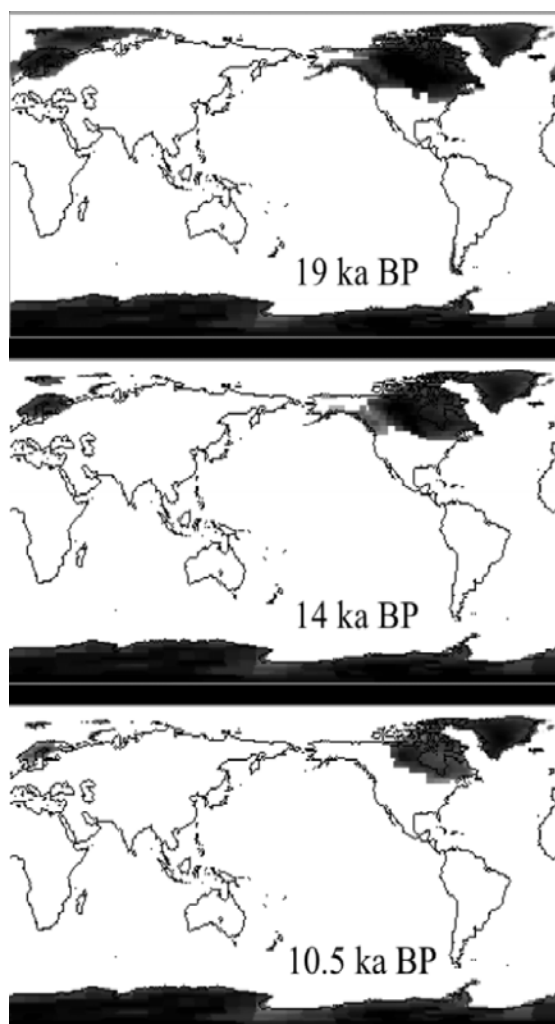


Figure 4.3.2: Continental ice sheet extents for the LGM, Bølling, and Preboreal time periods. Black filled areas are ice covered. Plots were created from the ICE-5G data set [Peltier, 2004]

exposed continental shelf, has been simulated by the BIOME4-TG global vegetation model driven by climate model output to have large wetland expanses during the LGM [Kaplan et al., 2006]. However, even if these areas did contain expansive wetland complexes, it is unlikely they would have been strongly CH<sub>4</sub> producing given the very low productivity of large boreal wetland expanses at more moderate latitudes, such as the present-day Hudson Bay lowlands [Roulet, 1994; Worthy et al., 2000].

Looking to the box model LGM results, the simulations do show, as expected, boreal wetland CH<sub>4</sub> flux to be almost completely shut off (Figure 3.4.6). This result confirms the Monte Carlo box model result of Fischer et al., (2008) and the work of earlier groups using [CH<sub>4</sub>] data and 3-box-model simulations [Chappellaz et al., 1997; Brook et al., 2000].

As the deglaciation progresses into the Bølling warm interval, the box model CH<sub>4</sub> flux from boreal wetlands increases almost ten-fold from the LGM value, as was also noted by Fischer et al., (2008). This is surprising as the ice sheets remained relatively large during this time period (Figure 4.3.2), indicating the increase is likely not attributable simply to a substantially larger boreal wetland areal extent, and would rather indicate the influence of a changing climate on the unglaciated boreal regions.

The establishment of new boreal peatlands as the ice sheet withdrew, and permafrost thawed, has been investigated using basal radiocarbon dating to establish boreal peatland establishment [Smith et al., 2004; Macdonald et al., 2006]. The peatland initiation dates show no boreal peatland basal dates older than about 16.5 ka BP, and the majority of initiation dates between 12 ka and 8 ka BP (Figure 4.3.3). To estimate CH<sub>4</sub> emissions from these young peatlands, Macdonald et al. (2006) argue that these young

peatlands would be more productive than present day boreal peatlands, due to being predominantly warm and wet minerotrophic fens, as opposed to ombrotrophic bogs in the regions at present. Nonetheless, their estimated boreal peatland CH<sub>4</sub> flux of 4 to 9 Tg yr<sup>-1</sup> after the end of the YD is only a small portion of the box model flux for the Preboreal (~30 ± 18 Tg CH<sub>4</sub> yr<sup>-1</sup>). However the upper end of the MacDonald et al. (2006) estimate almost falls within the lower value of the, albeit poorly constrained, 4-box model PB estimate.

To test the suggestion of Macdonald et al. (2006) that boreal wetlands in the early stage of development are more appropriately characterized as minerotrophic fens, rather than ombrotrophic *Sphagnum* bogs, the box model δ<sup>13</sup>CH<sub>4</sub> boreal wetland value was changed to a value characteristic of fen-dominated wetlands (-60 ‰; Table 2.4.4). This change does not significantly affect the boreal wetland flux for most time periods (Figure 3.4.12). The Younger Dryas (YD) is an exception, such that the Monte Carlo box model is not able to find acceptable realizations with a boreal wetlands source as <sup>13</sup>C-enriched as that of fen-dominated wetland. Barring some fundamental changes in model parameters for this time period (see Section 4.2), the model results indicate that it is unlikely that the Younger Dryas boreal wetland source could be characterized as a predominantly fen-dominated peatland complex.

In general, the box model results do agree well with the trend of a strongly increasing boreal wetland source through the YD and into the PB as proposed by Macdonald et al. (2006). Nonetheless, their source flux estimates are 3 – 6 times less than box model mean values. Also the box model simulations suggest that boreal wetland CH<sub>4</sub> fluxes in the BA period are much larger than the initiation dates of peatlands would

imply. This means that the peatlands would not have been capable of these levels of fluxes at this stage of their development and thus, the boreal peatlands could not have been responsible for the large increase in boreal wetland CH<sub>4</sub> flux during the BA period.

For the PIH time period, the boreal wetland value from the box model is possibly reflecting the Medieval Climate Anomaly (MCA; 800 – 1250 A.D.). The MCA was likely a global phenomenon [Broecker, 2001] and is believed to be related to persistent weak El Niños, a warm phase of the 'Atlantic Multidecadal Oscillation', as well as a positive North Atlantic Oscillation (NAO) [Seager et al., 2007]. These influences lead to a complex hydrological pattern of wet northern South America; dry mid-latitude South America; dry eastern Africa, albeit with strong Nile River floods; and a strong Indian Monsoon [Seager et al., 2007]. Western North America was characterized by severe droughts lasting for decades [Cook et al., 2004]. While most of the changes listed are for areas outside the boreal region, this complex pattern of changes to the hydrologic regime makes it likely that the boreal region hydrology is also influenced by the MCA. Due to the relatively mild perturbation of the MCA (especially as compared to the other climate events examined here), it perhaps more likely that the peatlands of the PIH exhibit smaller CH<sub>4</sub> productivity due to their maturation from minerotrophic fens to, many-times less productive, ombrotrophic *Sphagnum* bogs [MacDonald et al., 2006; Frolking and Roulet, 2007].

#### 4.3.2. *Thermokarst Lakes*

The box model uses hemispheric flux distribution, and prescribed  $\delta^{13}\text{CH}_4$  and  $\delta\text{D-CH}_4$  values, for model calculations and determination of source fluxes. Due to this, the boreal wetlands source could include other methane-producing processes, as long as they

approximate the prescribed characteristics of the boreal wetland source. Thermokarst lakes have the same hemispheric distribution,  $\delta D-CH_4$  values and similar  $\delta^{13}CH_4$  values to boreal wetlands [Walter et al. 2006, 2008]. Thus their contributions could be implicitly included in the model 'boreal wetland' term. Indeed, sensitivity tests where the initial boreal wetland  $\delta^{13}CH_4$  values are replaced with values of thermokarst  $CH_4$  show no significant change due to the  $^{13}C$ -depleted thermokarst  $\delta^{13}CH_4$  values (-68.5‰; [Walter et al., 2006]). This implies that the box model simulations do not exclude an important role of thermokarst lakes throughout the deglaciation.

Thermokarst lakes have only recently been discovered to be a large source of  $CH_4$ , estimated to presently contribute  $24.2 \pm 10.5 \text{ Tg yr}^{-1}$  to the global  $CH_4$  budget [Walter et al., 2008]. Walter et al. (2007) have proposed that thermokarst lakes could provide between 33 to 87% of the high latitude increase in  $[CH_4]$  over the course of the deglaciation. The available  $^{14}C$  basal dates from thermokarst lakes across Russia, Alaska, and northwestern Canada suggest thermokarst lakes began to form after 14 ka BP with lake initiation especially strong between 11.5 and 9 ka BP [Walter et al., 2007](Figure 4.3.3). The  $^{14}C$  basal initiation dates also show a more rapid increase in initiations than the boreal peatland basal dates of Macdonald et al. (2006)(Figure 4.3.3).

Walter et al. (2007) estimate the contribution from thermokarst methane during the BA to be slightly more than  $10 \text{ Tg } CH_4 \text{ yr}^{-1}$ , dropping slightly during the YD (8 – 9 Tg) and increasing to over 25 Tg during the Preboreal. The number of basal initiation dates and estimated  $CH_4$  fluxes from thermokarst lakes also drop significantly into the

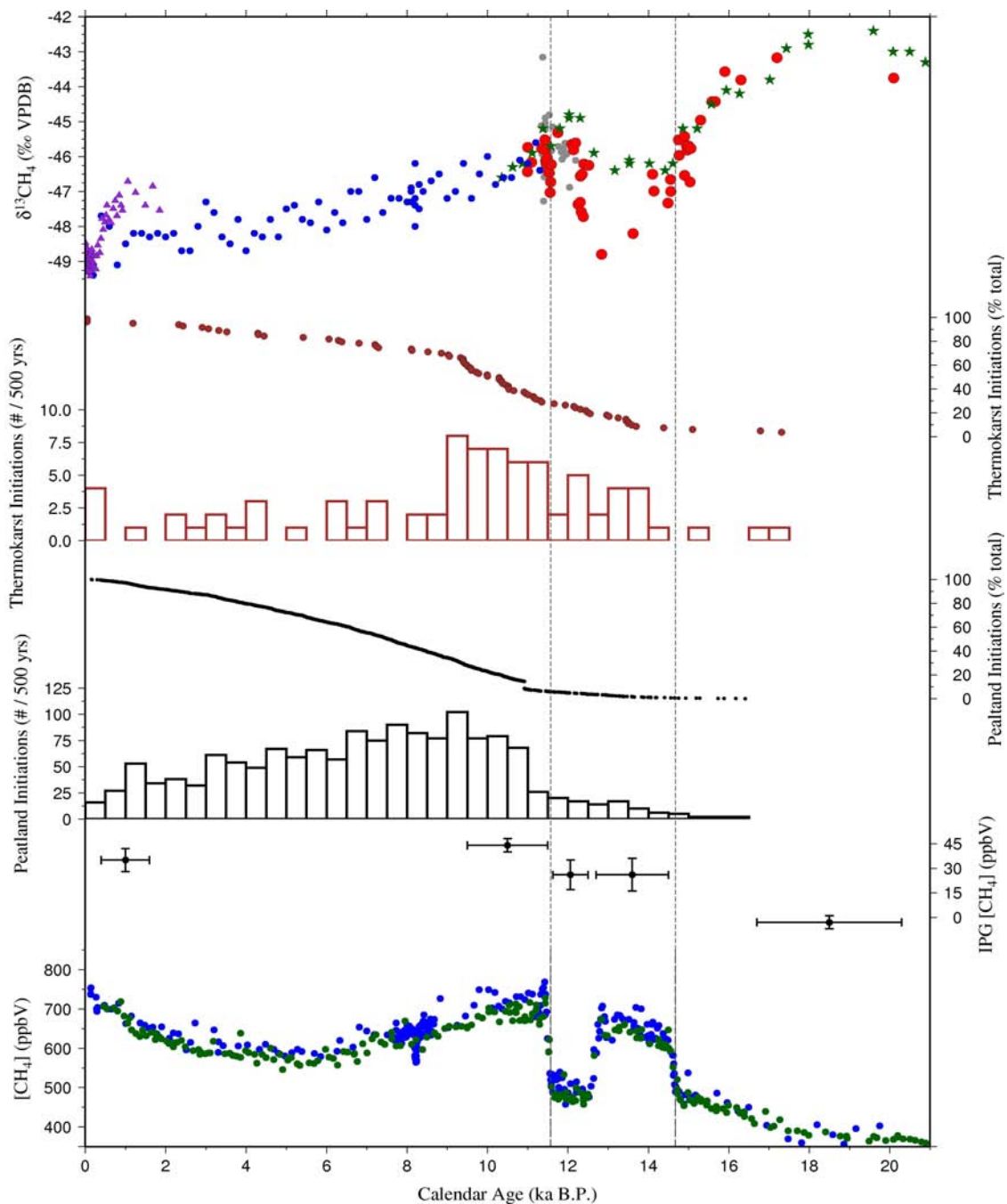


Figure 4.3.3: Plot of (listed in order from top to bottom) 1)  $\delta^{13}\text{CH}_4$  [this work (red dots; Pákitsoq, Greenland), Fischer et al. (2008)(green stars; EDML, Antarctica), Schaefer et al. (2006)(grey circles; Pákitsoq, Greenland), Sowers (2009)(blue dots; GISP2, Greenland), Ferretti et al. (2005)(purple triangles; Law Dome, Antarctica)], 2) thermokarst  $^{14}\text{C}$  basal initiation dates [Walter et al., 2007], 3) number of thermokarst  $^{14}\text{C}$  basal initiation dates binned every 500 years, 4) boreal peatland  $^{14}\text{C}$  basal initiation dates [MacDonald et al., 2006], 5) number of boreal peatland  $^{14}\text{C}$  basal initiation dates binned every 500 years, 6) inter-polar gradient (IPG) of [ $\text{CH}_4$ ] [Dällenbach et al., 2000; Chappellaz et al., 1993], and 7)  $\text{CH}_4$  concentration data [Brook et al., 1996 (blue dots; GISP2, Greenland), and EPICA Community Members (2006)(green dots; EDML, Antarctica)]. The vertical dotted lines represent the terminations of the Oldest Dryas (14.672 ka BP) and Younger Dryas (11,570 ka BP) periods.

PIH ( $< 5 \text{ Tg CH}_4 \text{ yr}^{-1}$ ). These estimates are consistent with the box model simulation results, particularly if the estimated boreal wetland emissions from Macdonald et al. (2006) are combined with the emissions of Walter et al. (2007). The box model results suggest that thermokarst lakes played an important role in Northern Hemisphere  $\text{CH}_4$  dynamics through the most recent deglaciation.

#### 4.3.3. *Tropical Wetlands*

Tropical wetlands are consistently estimated to be one of the largest  $\text{CH}_4$  sources from the box model simulations. Wet conditions (saturated soils) are the most important precondition for methane production in areas where there is an organic substrate available. Under wet conditions, commensurate warmer temperatures will act to enhance methanogenic rates and hence increase emissions. So, while it is important to note the tropical wetland  $\text{CH}_4$  flux NPDs are relatively poorly constrained (Figure 3.4.5), the box model outputs show an interesting pattern of relatively constant tropical wetland  $\text{CH}_4$  production.

A further outcome of the box model is the identification that tropical wetland  $\text{CH}_4$  fluxes during the LGM were only slightly reduced compared to the other time periods investigated. During the LGM, from model simulations, the tropical region appears to have cooled by about  $2^\circ\text{C}$  [Broccoli, 2000], with  $3^\circ\text{C}$  of continental cooling [Shin et al., 2003]. Climate proxy records from the tropical regions show the LGM to be cold and, importantly, dry (Figure 4.3.4 and references therein Thompson et al., 1995; Thompson et al., 1998; Peterson et al., 2000; Wang et al., 2001; Yuan et al., 2004; Dykoski et al., 2005; Wang et al., 2006; as well as Farrera et al., 1999; Jansen et al., 2007). In addition, the LGM experienced low global atmospheric concentrations of  $\text{CO}_2$  that could act to limit

substrate availability by reduced primary productivity [Kaplan, 2002b]. This suggests that CH<sub>4</sub> emissions from tropical wetlands would be depressed during the LGM, especially compared to a time period such as the relatively warm and wet Preboreal (Figure 4.3.4). However, the box model tropical wetland CH<sub>4</sub> flux for the Preboreal is only ca. 16% greater than the LGM. This surprisingly small change, given the different climate conditions, could be attributed to the large land surface available for wetlands on the exposed, low relief continental shelves during the LGM (Figure 4.3.5). Indeed, Kaplan et al., (2006) found very large and highly-productive wetland complexes on the exposed Sunda and Gulf of Carpentaria shelves. Thus while tropical wetland CH<sub>4</sub> flux was depressed during the LGM by cold and dry conditions on the whole, the additional area available for wetlands counteracted the unfavourable climatic conditions.

The YD is the only time period that stands out with a much reduced tropical wetland CH<sub>4</sub> flux. The climate conditions of the YD appear similar to the LGM (Figure 4.3.4), yet the box model tropical wetland CH<sub>4</sub> flux was reduced by over 50% from the LGM. This could possibly be attributed to loss of wetland area, as the YD had approximately 35% less exposed continental shelf than the LGM. This calculation is based solely upon sea level drop and does not account for tectonic processes, isostatic rebound, etc. The land surface submerged by the rising sea level may have been of lower relief, and thus more prone to water-logged soils. The land surface may also have been warmer due to proximity to the ocean, which has been modelled to not have cooled as much as continental areas [Shin et al., 2004]. As a consequence, the lands inundated between the YD and LGM, may have been more productive for CH<sub>4</sub> emissions than the lands that remain above eustatic sea level in the YD. At first order, this appears to be a

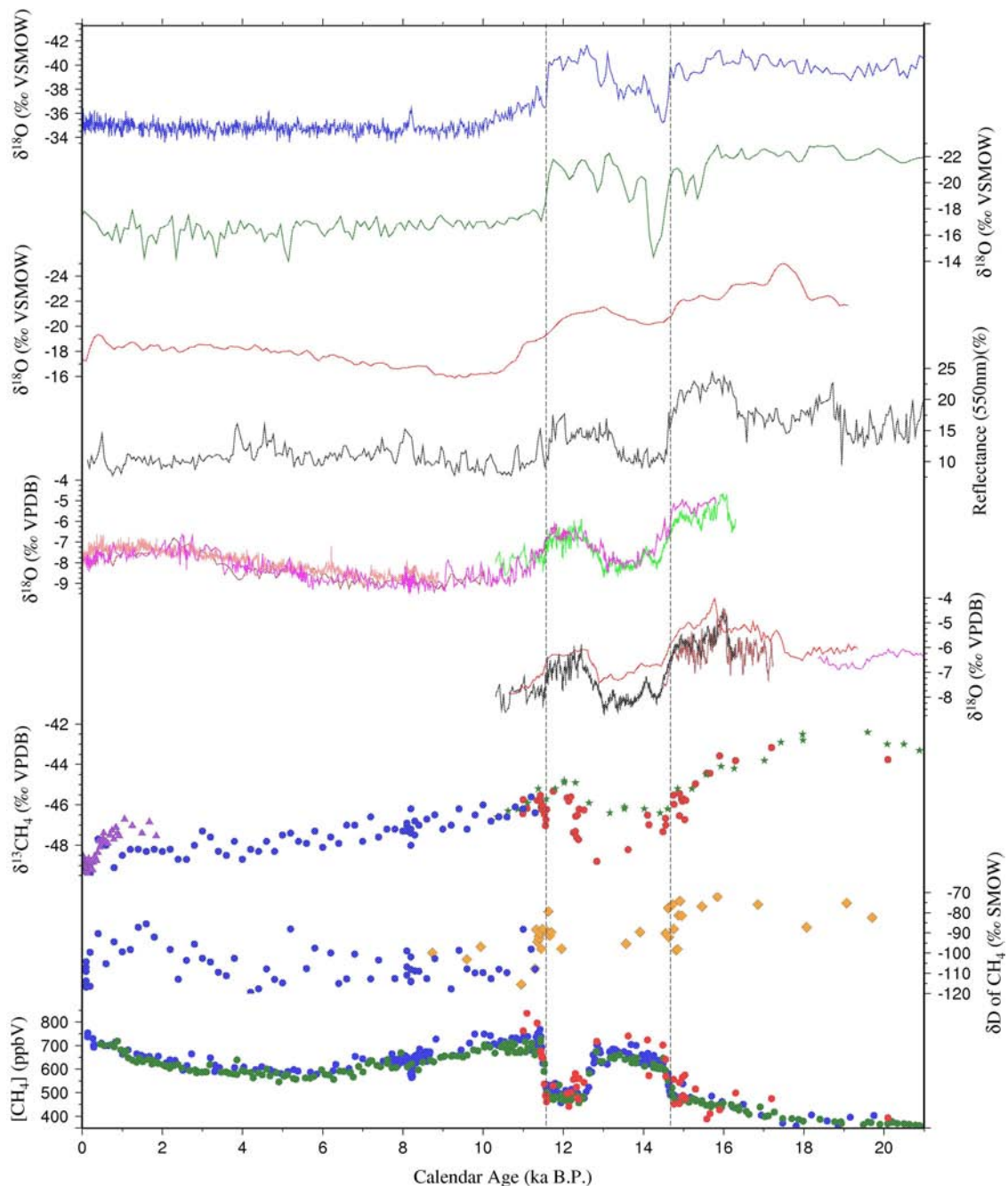


Figure 4.3.4: Collected global records of moisture and temperature.  $\delta^{18}\text{O}_{\text{ice}}$  records (inverted scale) from GISP2 [Grootes and Stuiver, 1997] and tropical mountain glacier records from Sajama, Bolivia [Thompson et al., 1998] and Huarascarán, Peru [Thompson et al., 1995]. Continental runoff from the coast of Venezuela from reflectance (at 550 nm) data [Peterson et al., 2000]. Monsoon records from Dongge [Yuan et al., 2004; Wang et al., 2006; Dykoski et al., 2006] and Hulu [Wang et al., 2001; Yuan et al., 2004] cave stalagmites. For comparison, the  $\delta^{13}\text{CH}_4$  records from this work (red dots); EDML, Antarctica [Fisher et al., 2008] (green stars); GISP2, Greenland [Sowers, 2009] (blue dots), and Law Dome, Antarctica [Ferretti et al., 2006] (purple triangles) are provided along with the  $\delta\text{D}-\text{CH}_4$  from GISP2, Greenland [Sowers, 2006; Sowers, 2009] and  $[\text{CH}_4]$ . Concentration data are from this work (red dots); EDML, Antarctica [EPICA community members, 2006], and GISP2 [Brook et al., 1996]. Note: all data are presented using the age scale of the dataset with the exception of the methane data which is all on the Schaefer et al. (2006) timescale. The vertical dotted lines represent the terminations of the Oldest Dryas (14.672 ka BP) and Younger Dryas (11.570 ka BP) periods.

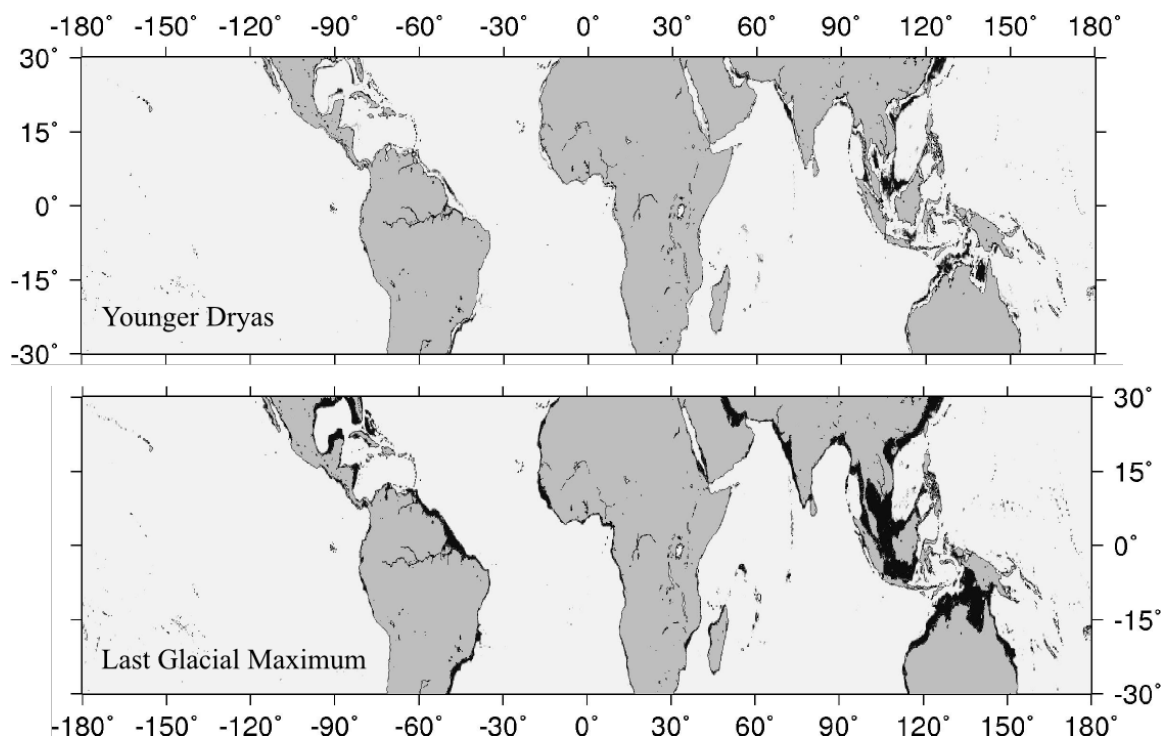


Figure 4.3.5: Map of exposed continental shelf at the YD (top) and LGM (bottom). Eustatic sea level was reduced by 60 m [Clark et al., 2002] from present day mean sea level for the YD and 125 m for the LGM [Clark and Mix, 2002; Jansen et al., 2007]. The rise of sea level between the time periods resulted in large losses of continental shelf particularly in Southeast Asia and the areas of present day Java and Arafura seas. Note map only shows changes due to a reduction in sea level from present day and should be considered only for illustrative purposes.

reasonable explanation for the YD tropical wetland flux decrease. After the YD, the Preboreal and PIH model output shows ever increasing tropical wetland  $\text{CH}_4$  fluxes, likely in response to increasing moisture availability [Maslin and Burns, 2000] and warm temperatures (Figure 4.3.4).

The combined emissions from tropical and boreal wetlands can be compared to other estimates for total wetlands provided by modelling studies (Table 4.3.1). The box model simulated PIH and LGM are both smaller than previous model results with values almost two-thirds and one-half of that proposed by other models respectively. However, all of these model simulations (with the exception of Bergamaschi et al. (2007), which did not separate wetland and APM emissions) were performed before the discovery of

aerobic plant methane (APM) production and this contribution might be have been 'double-counted' as a result. Combining the wetland and APM values from the box model simulations narrows the difference between the box model and other studies.

Table 4.3.1: Summary of model studies, for both forward and inverse models, of the global wetland flux through different time periods

Model Study	Modern	PIH	PB	YD	BA	LGM
Matthews and Fung (1987)	110					
Aselmann and Crutzen (1989)	80					
Fung et al. (1991)	115 <sup>‡</sup>					
Chappellaz et al. (1993)	115	136 <sup>‡</sup>				76
Bartlett and Harriss (1993)	109					
Cao et al. (1996)	92					
Hein et al. (1997)	227					
Houweling et al. (1999)	131	163 <sup>§</sup>				
Kaplan (2002a)	140					107
Kaplan et al. (2006)		110	~125 <sup>£</sup>			110
Mikaloff Fletcher et al. (2004)	92 – 237					
Valdes et al. (2005)		148 <sup>†</sup>				108
Bergamaschi et al. (2007)	192 - 216 <sup>§</sup>					
This Work (Wetlands)	134±35	79±34	85±39	67±22	78±31	50±22
(Wetlands + APM)	179±44	94±35	122±35	81±24	99±34	58±23

<sup>‡</sup>Scenario 7 of the study

<sup>‡</sup>PIH (9000 – 200 yr BP)

<sup>§</sup>PIH (1500 - 1800 CE)

<sup>†</sup>PIH (1700 CE)

<sup>£</sup>This simulation does not have a Younger Dryas event in the climatological driving, Preboreal value is taken from Figure 3 showing evolution of wetland emissions through deglaciation. Preboreal value is likely an over-estimate as a result.

<sup>§</sup>*A posteriori* model results informed by SCIAMACHY observations with NOAA ESRL measurements

#### 4.3.4. Gas Hydrates

Gas hydrate (clathrate) formation is constrained by the phase requirements of temperature, pressure, saturated gas concentrations, and the presence of liquid water [Kvenvolden, 1988]. The temperature conditions restrict methane hydrate stability, and hence formation and occurrence, to the deeper ocean shelf and terrestrial environments in the polar regions. For the purposes of the box model, all gas hydrates are treated as derived from biogenic, and not thermogenic source gases. All thermogenic gas hydrate emissions are implicitly included in the GEM source flux estimates.

Terrestrial gas hydrates likely possess much lower  $\delta D-CH_4$  values than marine hydrates [Whiticar, 1999]. To test the effect of these  $^2H$ -depleted  $\delta D-CH_4$  values, sensitivity tests were performed using the box model. An implicit assumption of the gas hydrate sensitivity tests is that only one reservoir of hydrates can be emitting in a scenario. Hence, if the  $\delta D-CH_4$  gas hydrate value is terrestrial, no marine hydrate emissions are permitted. These sensitivity tests then present end-member scenarios. The box model finds no change in flux of gas hydrates as the  $\delta D-CH_4$  value is changed from a characteristic marine value to that of a terrestrial source across all time periods. No changes are also observed in the other source fluxes during the LGM and BA. This indicates that gas hydrate emissions in the LGM and BA could have been either terrestrial or marine in origin. During the YD, PB, and PIH significant changes are observed to the  $CH_4$  fluxes from biomass burning and GEM. If the gas hydrate methane emitted was from a terrestrial source in those time periods, biomass burning  $CH_4$  flux is decreased and GEM flux is increased as compared to the marine gas hydrate scenario.

Gas hydrates, both terrestrial and marine, have been implicated in two prominent gas release hypotheses. Gas hydrates associated with terrestrial permafrost regions and off-shore continental shelves are suggested to become unstable under conditions of warming climate, or rising sea levels that transport comparatively warm sea water onto exposed continental shelves (Figure 4.3.6) [Kvenvolden, 1988; Nisbet, 1990; Kvenvolden, 1993; Kennett et al., 2003]. Conversely, oceanic hydrates are proposed to be destabilized during cold periods. Paull et al. (1996) propose that periods of low eustatic sea level will destabilize oceanic gas hydrate deposits, due to reduced hydrostatic pressure, resulting in large-scale slumping and release of CH<sub>4</sub>. Many proponents of gas hydrate release hypotheses have discussed this idea in the context of gas hydrates as a climate driver, i.e. rapid, even catastrophic, CH<sub>4</sub> hydrate release initiates warming. This mechanism was not responsible for at least the YD-PB and OD-B transitions, due to warming leading methane concentration increase (e.g. [Severinghaus et al., 1998; Severinghaus and Brook, 1999]). However, the possibility of CH<sub>4</sub> release due to warming remains valid. The size of the methane pool in the deep oceanic and permafrost reservoirs is large [Milkov, 2005], thus reservoir size is more than sufficient for the annual fluxes determined by the box model simulations (between 5 and 36 Tg CH<sub>4</sub> yr<sup>-1</sup>).

Box model simulated biogenic marine CH<sub>4</sub> hydrate flux during the LGM was similar to that of boreal wetlands, with almost no emissions ( $5 \pm 4$  Tg CH<sub>4</sub> yr<sup>-1</sup>). The <sup>13</sup>C-enriched atmospheric δ<sup>13</sup>CH<sub>4</sub> values of the LGM, and the small IPG in both atmospheric concentration and δ<sup>13</sup>CH<sub>4</sub>, precludes a strong flux from marine gas hydrates. For the LGM, the box model results do not support large-scale oceanic hydrate emissions as proposed by Paull et al. (1996). This is supported by another study that determined the

effect of changing eustatic sea level on timescales less than  $10^4$  years is likely insignificant compared to changes in sea floor temperature [Buffett and Archer, 2004]. The global oceans were cold in the LGM [Jansen et al., 2007] which would act to stabilize marine gas hydrates. Marine hydrates frequently released through slumping during the deglaciation (see for e.g. Maslin et al., 2004) can not be fully excluded, but are unlikely to have led to large  $\text{CH}_4$  releases. Furthermore, the ice core methane carbon and hydrogen isotope records during this period [Sowers, 2006; Schaefer et al., 2006; Petrenko, 2009], as well as their combination [Whiticar and Schaefer, 2007] do not support the hypothesis of large releases of biogenic marine gas hydrate.

The BA box model marine gas hydrate flux estimate is an increase of almost six-fold over the LGM. This large increase is also observed in the terrestrial gas hydrate sensitivity tests. This rapid increase could be related to rapid changes in sea-level. Meltwater Pulse 1A (MWP-1A;  $\sim 14.6$  ka BP)[Bard et al., 1996; Clark and Mix, 2002] led to a sea-level rise of ca. 20 m in less than 500 years, and has been hypothesized to be the trigger for the abrupt warming of the Bølling period [Weaver et al., 2003]. This sea level rise would have flooded large areas of the exposed continental shelf where hydrates existed in the permafrost. Due to this influx of warm water,  $\text{CH}_4$  would be emitted, although initially it was likely a small flux as the diffusion of heat through the permafrost to the gas hydrate stability zone ( $> 200$  m depth) is slow, –on the order of  $10^3$  years [Buffett, 2000]. However, if the warming of the Bølling-Allerød (BA) period propagates down to the hydrate stability zone over the course of the BA period, the cooling of the YD will not heavily influence the subsequent dissociation of permafrost hydrates, from the heat pulse of the BA, during the YD period. Once the cooling of the YD, greatly

delayed, is felt at the depth of the hydrate stability zone, it will then slow the dissociation of the gas hydrates, possibly long after the climate initially cooled. This delayed release, and delayed cessation, could be implicated in the relatively large gas hydrate emissions during the YD, and smaller emissions in the Preboreal. To explain the large hydrate flux in the BA period however, another hydrate reservoir, subglacial methanogenesis, is required.

The basal sediments of ice sheets can produce methane through in-situ methanogenesis, as has been observed at the bases of the GISP2 and GRIP ice cores (see Section 4.1). Organic carbon sequestered under advancing ice sheets is a potential carbon source to subglacial archaeal populations. This assumes that geothermal heating and the insulating effect of the ice sheet are sufficient to allow the base of the ice sheet to be warm enough for methanogenesis. If the ice sheet is sufficiently cold and several hundreds of metres thick, the pressure and temperature conditions at the base will allow methane clathrates to form this authigenic microbial  $\text{CH}_4$ , once its concentration is in excess of the solubility of  $\text{CH}_4$  in  $\text{H}_2\text{O}$ . These gas hydrates will continue to store the  $\text{CH}_4$  produced, assuming conditions continue to allow clathrate stability. A recent modelling study by Weitemeyer and Buffett (2006) uses a dynamic ice sheet model driven by climate model output to estimate the timing and magnitude of  $\text{CH}_4$  release from subglacial clathrates for two different assumptions about the original vegetation overlain by the advancing ice sheet (tundra or present day potential vegetation). Their analysis suggests large releases of  $\text{CH}_4$  at 14.4 (7 – 16  $\text{Tg yr}^{-1}$ ) and 11 ka BP (17-48  $\text{Tg yr}^{-1}$ ). The upper end of their  $\text{CH}_4$  flux estimates are for the scenario of present-day potential vegetation that is overlain by the ice sheet, and the lower end estimates assume the

vegetation overlain to be tundra. The clathrate releases from the Weitemeyer and Buffett (2006) model are not instantaneous one-time events (such as underwater slumps), but are spread over several hundred years as the ice sheet thins and retreats.

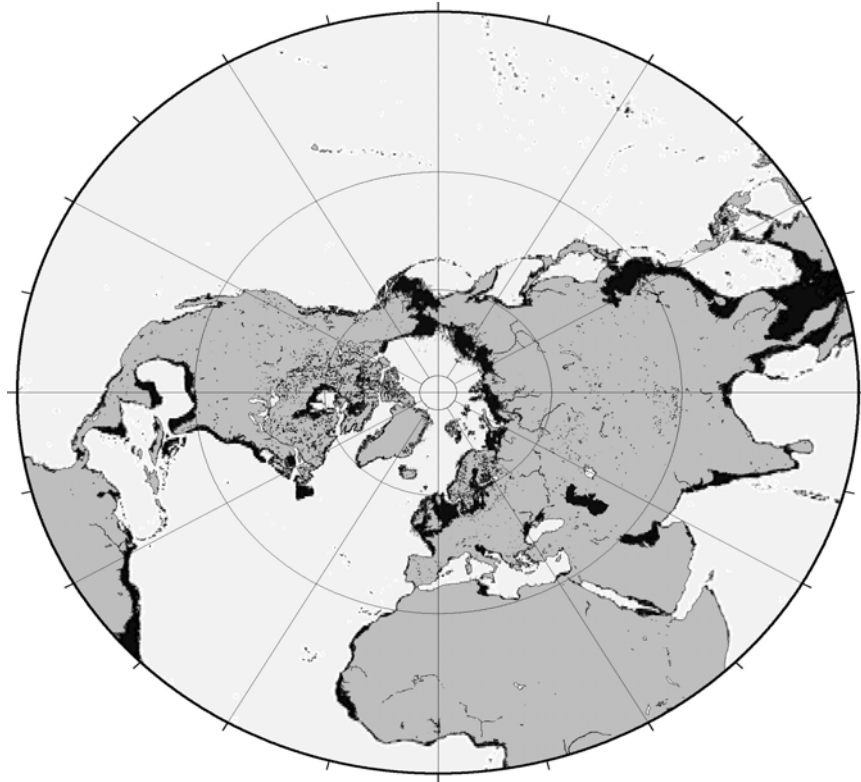


Figure 4.3.6: Exposed continental shelf during the LGM. Plot assumes LGM eustatic sea level to be 125 m below modern [Clark and Mix, 2002; Jansen et al., 2007] and does not account for tectonic changes (e.g. crustal deformation due to ice sheets, etc.). The figure is thus intended for illustrative purposes only.

The model-simulated timing and quantity of methane release from subglacial methanogenesis hydrates is reasonably consistent with the 4-box model simulated fluxes presented here. From this correlation, subglacial methanogenesis appears to have a potential role in the methane dynamics observed, especially during the early part of the BA period when other hydrate sources are assumed to be depressed.

During the PIH, the methane hydrate flux is modelled to be as high as that of the BA period. This could possibly relate to the warmth of the Medieval Climate Anomaly

(MCA), which was of sufficient length that permafrost hydrates would experience the propagated warming pulse down to the hydrate stability zone. However, the warming of the MCA was relatively subtle [Broecker, 2001] and against the backdrop of the stable, and already warm, climate of the late Holocene. The MCA influence is thus not a satisfactory, or likely, explanation. If the hydrates released are from marine sources, which is not excluded by the sensitivity tests, how the PIH period would have influenced marine gas hydrates is equally puzzling.

#### 4.3.5. *Geologic Methane (GEM)*

Geologic emissions of methane (GEM) is a source only recently suggested to be an important component of the global CH<sub>4</sub> budget [Lassey et al., 2007; Etiope et al., 2008a]. Global distribution (Figure 4.3.7) and fluxes are uncertain even for present day [G. Etiope, personal communication, 2009]. For the box model simulations, the geologic CH<sub>4</sub> fractional flux per hemisphere required adjustment between time periods to ensure the box model could find acceptable realizations (described in Section 2.4.1 and Table 7.2.4) thus it appears that the on-shore and off-shore GEM fluxes hemispheric distribution were not constant through time.

Looking to past climate periods, an interesting hypothesis for GEM flux modulation has been proposed involving off-shore seeps. Luyendyk et al. (2005) propose that during periods of low sea level, off-shore GEM seeps will be sub-aerial and able to vent directly to the atmosphere, thus avoiding water column oxidation. The decreased hydrostatic pressure, due to lowered sea level, is also anticipated to increase seepage rate. Thus during glacial periods GEM emissions from gas seeps on exposed continental shelves are proposed by Luyendyk et al., (2005) to emit 40 to 100 Tg CH<sub>4</sub> yr<sup>-1</sup>. For on-

shore seeps, different mechanisms control the methane emission rate. These are predominantly endogenic (geodynamic) processes that are not constant over geologic, or millennial time scales [Etiope et al., 2008b]. Endogenic processes include seismicity, neotectonics, and magmatism. How these forces have modulated geologic CH<sub>4</sub> flux through time is unknown and remains an open question [Etiope et al., 2008b].



Figure 4.3.7: Map of present day onshore and marine seeps of geologic methane (Reproduced with permission of G. Etiope 2009)

From the box model simulations, GEM fluxes appear to be relatively constant through time (after accounting for the relatively broad peaks in the NPD, with the exception of a well-defined LGM peak; Figure 3.4.11). The box model LGM GEM flux of  $36 \pm 16 \text{ Tg yr}^{-1}$  is consistent with the lower end of the GEM range proposed by Luyendyk et al. (2005) provided that on-shore CH<sub>4</sub> seeps emissions are small.

A slightly elevated GEM flux simulated by the box model during the YD, as compared to the other time periods, supports the findings of Whiticar and Schaefer (2007). From the  $\delta^{13}\text{CH}_4$  [Schaefer et al., 2006] and  $\delta\text{D-CH}_4$  [Sowers, 2006], Whiticar and Schaefer (2007) suggest an important role for thermogenic emissions during the YD,

when atmospheric  $[\text{CH}_4]$  is decreased. However, the broad NPD peak of the YD does not allow quantitative conclusions.

The PIH period shows a noticeably smaller GEM flux ( $\sim 17 \text{ Tg CH}_4 \text{ yr}^{-1}$ ), which is not in line with expectations. Petroleum exploitation has been shown to decrease GEM flux from nearby seeps and it is anticipated that PIH GEM flux should be higher than present-day [Etiope et al., 2008b]. It is possible that the, inferred, reduced volcanism of the PIH time period impacted upon the GEM fluxes as well [Crowley et al., 2000]. While the processes that control volcanism are not necessarily identical to those that control GEM emissions, the volcanic activity might be indicative of the level of activity of endogenic processes. The low PIH GEM flux is also potentially related to the prescribed GEM hemispheric source distribution in the box model, which is identical for the 1990s and PIH.

Two box model sensitivity tests for GEM are conducted with more  $^{13}\text{C}$ -enriched (G-25 = -25 ‰), and more  $^{13}\text{C}$ -depleted (G-50 = -50 ‰)  $\delta^{13}\text{CH}_4$  values compared with the initial representative GEM values. If the 'true'  $\delta^{13}\text{CH}_4$  value of geologic methane is -25‰, then GEM in the box model behaves similarly to a source isotopically identical to biomass burning, albeit with a slightly different hemispheric flux distribution. This results in an increase in the emissions of  $^{13}\text{C}$ -depleted sources with similar  $\delta\text{D-CH}_4$ , and hemispheric flux distribution as biomass burning, such as gas hydrates, to balance the addition from two sources of  $^{13}\text{C}$ -enriched methane. The G-50 scenario is similar to that of the G-25, however the GEM  $\delta^{13}\text{CH}_4$  value is now much less  $^{13}\text{C}$ -enriched. This causes the biomass burning  $\text{CH}_4$  flux to increase to offset the  $^{13}\text{C}$ -depleted sources in the isotope mass balance. It appears that these three sources –biomass burning, GEM, and gas

hydrates— represent end-members for the  $\delta^{13}\text{CH}_4$  budget, and thus their fluxes are able to cause dramatic changes in the aggregated source  $\delta^{13}\text{CH}_4$  value. The large 'isotope lever' provided by these sources ensures their emission fluxes are well constrained. This illustrates the importance of well-chosen, representative  $\delta^{13}\text{CH}_4$  values for the sources on the  $^{13}\text{C}/^2\text{H}$ -enriched and  $^{13}\text{C}/^2\text{H}$ -depleted end of the source  $\delta^{13}\text{CH}_4$  and  $\delta\text{D-CH}_4$  spectrum. The values chosen for the sensitivity tests represent extreme values and are thus illustrative 'worst-case' scenarios.

The box model results are not suitable for commenting on the hypothesis of Hill et al. (2006)(described in Section 1.1) as the model can not resolve the source of the GEM fluxes, i.e. hydrate-release mediated seeps vs. on-shore seep enhanced flux via endogenic processes vs. sub-aerial off-shore seeps, etc.

#### 4.3.6. *Biomass burning*

Biomass burning is one of the most well-constrained sources in the box model simulations (Figure 3.4.8), and shows a pattern of increasing  $\text{CH}_4$  flux through the LGM to Preboreal period. This result is contrary to that reported by Fischer et al. (2008), who find constant biomass burning over the same period (ca. 50 Tg  $\text{CH}_4$  yr<sup>-1</sup>). This discrepancy could be related to 4 different possibilities: 1) Fischer and coworkers' model is not constrained by Northern Hemisphere  $\delta^{13}\text{CH}_4$  values; 2) the Monte Carlo box model used in their study does not include GEM, termites, or aquatic sources; 3) their box model consistently converged to unlikely atmospheric lifetime values, as low as 3.7 years in LGM. Constraint of their model to atmospheric lifetime values > 5 years results in a decrease of biomass burning  $\text{CH}_4$  flux to 40 Tg yr<sup>-1</sup>[Fischer et al., 2008]; and, 4) their

hemispheric flux distributions for biomass burning across the time periods could have been significantly different from those used here.

Increasing biomass burning  $\text{CH}_4$  flux between the LGM to the PIH has been reported from a study using a dynamic global vegetation model (DGVM). The DGVM, with integrated fire module, is used to simulate fire and biomass burning  $\text{CH}_4$  emissions for time slices during the deglaciation [Thonicke et al., 2004]. Thonicke et al. (2004) report the LGM  $\text{CH}_4$  flux from biomass burning to be ca.  $30 \text{ Tg yr}^{-1}$  and the PIH flux to be  $41 \text{ Tg yr}^{-1}$ , close to the box model output of  $29 \pm 8 \text{ Tg yr}^{-1}$  and  $30 \pm 10 \text{ Tg yr}^{-1}$ , for the LGM and PIH respectively. Thonicke et al. (2004) attributed the decrease in  $\text{CH}_4$  flux to shifts of vegetation zones and decreases in woody cover. This pattern of increasing biomass burning through the deglaciation is also supported by a synthesis of global charcoal records that find depressed fire levels during the glacial as compared with preindustrial period [Power et al., 2008]. A North America specific fire record also shows an increase in fire activity through the deglaciation, with a gradual increase in fire activity from the glacial period to the start of the YD, and then a more rapid increase again after the YD [Marlon et al., 2009].

The PIH time period pyrogenic  $\text{CH}_4$  emissions are also simulated by Ferretti et al. (2005) using a box model informed by their  $\delta^{13}\text{CH}_4$  measurements from Law Dome, Antarctica. Ferretti et al. (2008) simulate  $\sim 25 \text{ Tg CH}_4 \text{ yr}^{-1}$  for the PIH period, consistent with the box model result of  $30 \pm 10 \text{ Tg CH}_4 \text{ yr}^{-1}$ .

Sensitivity tests using a  $^{13}\text{C}$ -enriched biomass burning  $\delta^{13}\text{CH}_4$  value of  $-20\text{‰}$  cause the box model to tighten the NPD peaks of biomass burning to reflect the even

stronger 'isotope lever' effect that these,  $^{13}\text{C}$ -enriched, values have on the isotope mass balance.

#### 4.3.7. *Ruminants*

Ruminants are a large source of methane for the modern period, due primarily to anthropogenic activities with smaller inputs from natural ruminant communities [Johnson et al., 2000]. Ruminant  $\text{CH}_4$  fluxes are reasonably constrained in the box model NPD across the different time periods, with the exception of a broad peak for the Preboreal simulation (Figure 3.4.10). The colder periods (YD and LGM) show relatively smaller ruminant  $\text{CH}_4$  flux than the other periods.

During the LGM, caecalids –species that use a larger caecum gut-diverticulum for food processing, eg. woolly mammoth, horse, woolly rhino– were widespread [Gill et al. 2009]. However, the caecalids produce less methane per animal due their gastrointestinal system lacking rumen (ruminants produce 95% of modern animal methane emissions [Johnson et al., 2000]). The reported predominance of caecalids and low population of ruminants, with high  $\text{CH}_4$  emissions, would likely result in low ruminant total  $\text{CH}_4$  emissions during the LGM. As the deglaciation progressed, the caecalids were replaced by ruminants resulting in small increases in methane flux [Gill et al., 2009]. The Preboreal ruminant flux is much larger than the PIH, although the large standard deviation and broad NPD peak of the PB would permit a similar  $\text{CH}_4$  flux to the BA and PIH periods.

#### 4.3.8. *Aerobic Plant Methane (APM)*

APM is reported to be generated by the interaction of UV light and plant matter, with the carbon substrate suggested to be the methoxyl groups of plant pectin [Keppler et

al., 2008; Vigano et al., 2009]. The production of APM is also reported to be influenced by temperature [Keppler et al., 2006; Vigano et al., 2009]. The exact mechanisms of this, only recently discovered, source remain to be elucidated.

Box model simulated APM fluxes appear to follow global climate with lower emissions during cold periods (LGM and YD) and greater emissions in warm periods (Figure 3.4.7). The largest fluxes are during the PB and 1990s, though both of these are poorly constrained and associated with large standard deviations and broad peaks in their NPDs. The dynamics of the APM emissions from the box model are expected to reflect changes in the global biosphere. The increased aridity, extensive ice cover, and low [CO<sub>2</sub>] reduced primary productivity during the LGM (Figure 4.3.4; Kaplan et al., 2002b; Valdes et al., 2005). This should lower APM emissions, if the mechanism behind APM production is indeed sensitive to changes in plant matter abundance and temperature. The box model APM LGM flux is, in fact, the lowest of the time periods investigated.

#### 4.3.9. *CH<sub>4</sub> Atmospheric Lifetime*

The box model simulated CH<sub>4</sub> atmospheric lifetime decreases from the BA through the PB time period and appears to increase again into the PIH and 1990s. The atmospheric CH<sub>4</sub> lifetime during the LGM and BA is only slightly lower than that of the 1990s at ca. 7.4 years. This pattern of decreasing CH<sub>4</sub> atmospheric lifetime with time is opposite to that reported by Fischer et al. (2008). Fischer and coworkers find atmospheric lifetime increases from ca. 3.7 years during the LGM, to ca. 8.1 years through the order of YD, PB, BA, and finally 1990s. Model simulations by others using global vegetation models combined with atmospheric chemistry models have suggested global concentrations of biogenic volatile organic compounds (BVOCs) were low during the

LGM and increased throughout the deglaciation [Valdes et al., 2005; Kaplan et al., 2006]. The primary sink of BVOCs in the troposphere is OH, which is also the primary sink of CH<sub>4</sub>. Reduction of the tropospheric OH radical content by these competitive sinks is assumed to increase the lifetime of CH<sub>4</sub> [Adams et al., 2001; Valdes et al., 2005; Kaplan et al., 2006].

There are several possible explanations for the opposite trend observed in this study. The first relates to a recently reported reaction pathway for OH recycling in pristine air [Lelieveld et al., 2008]. Lelieveld and coworkers (2008) deduced a previously unknown pathway for BVOC reaction with OH on the basis of observations, model simulations, and laboratory experiments. In unpolluted, low-[NO<sub>x</sub>] air oxidized BVOCs – in particular organic peroxy radicals– can directly recycle radicals with high efficiency (40 – 80 %). Thus BVOCs may not have a strong impact upon the CH<sub>4</sub> sink [J. Lelieveld, personal communication 2009].

Another possibility is based upon the control on OH concentrations exerted by humidity levels [Prinn, 2003; Drevet, 2008]. Since humidity levels were initially low in the cold and dry LGM [Shin et al., 2003; Bracconnot et al., 2007], the increase of humidity throughout the deglaciation as the climate warmed would have caused a related increase in OH concentrations, and a decrease in methane lifetime through the deglaciation. Lastly, increasing methane concentrations in the Post-Industrial period has been shown to increase the methane atmospheric lifetime by drawing down of its primary sink, OH radicals [Prather et al., 2001]

#### 4.4. The Bølling-Allerød period $\delta^{13}\text{CH}_4$ record

The transition from the Oldest Dryas into the Bølling (OD-B) period at ca. 14.7 ka BP marks the first observable pause, in the relatively steady enrichment of  $^{12}\text{C}$  to

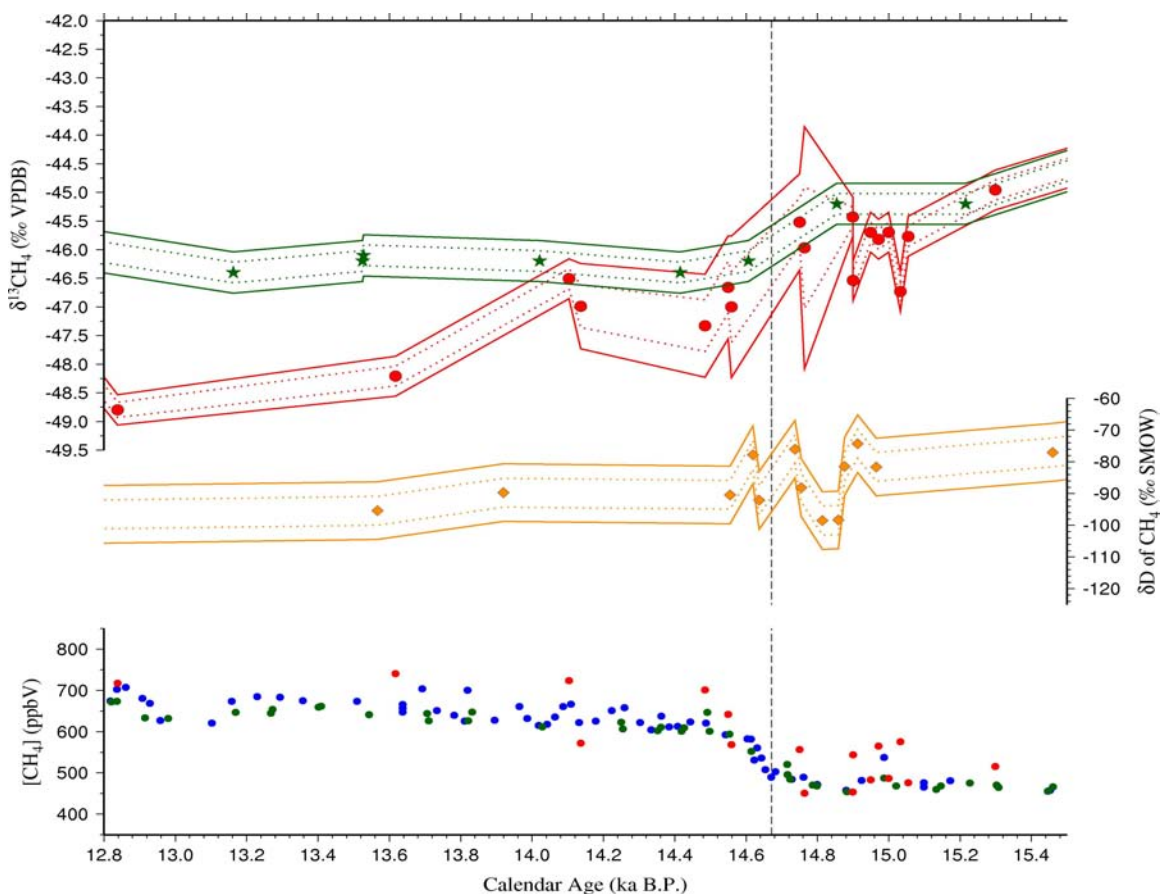


Figure 4.4.1: Uncertainty envelopes for the  $\delta^{13}\text{CH}_4$  record spanning the Oldest Dryas to Bølling transition. Uncertainty envelope is 1 $\sigma$  (dotted line) and 2 $\sigma$  (solid line).  $\delta^{13}\text{CH}_4$  data sources include this work (red dots; Påkitsoq, Greenland) and Fischer et al. (2008) (green stars; EDML, Antarctica).  $\text{CH}_4$  concentration data are from this work (red dots; IRMS-derived concentration), Brook et al., 1996 (blue dots; GISP2, Greenland), and EPICA Community Members (2006) (green dots; EDML, Antarctica). Dashed lines represent the OD-B transition at 14.672 ka BP

atmospheric methane, since the start of the deglaciation in both the Påkitsoq and EDML (Fischer et al., 2008)  $\delta^{13}\text{CH}_4$  records (Figure 4.4.1). The timing of this temporary  $\delta^{13}\text{CH}_4$  plateau appears to coincide with the end of the OD-B transition, although this timing is uncertain as the Påkitsoq samples are at the start- and end of the transition, with no

samples falling during the actual  $[\text{CH}_4]$  rise. Samples prior to, and after, the transition indicate that the increase in  $\text{CH}_4$  flux came from relatively  $^{13}\text{C}$ -depleted sources due to the observed  $^{13}\text{C}$ -depletion, assuming constant source strength as was found in the box model simulations.

This interpretation is supported by the box model results indicating a strong increase in emissions from both gas hydrates and boreal wetlands, both of which are relatively  $^{13}\text{C}$ -depleted sources. After the OD-B transition, an apparent balance was established between the sources and sinks to allow for relatively constant  $[\text{CH}_4]$  and

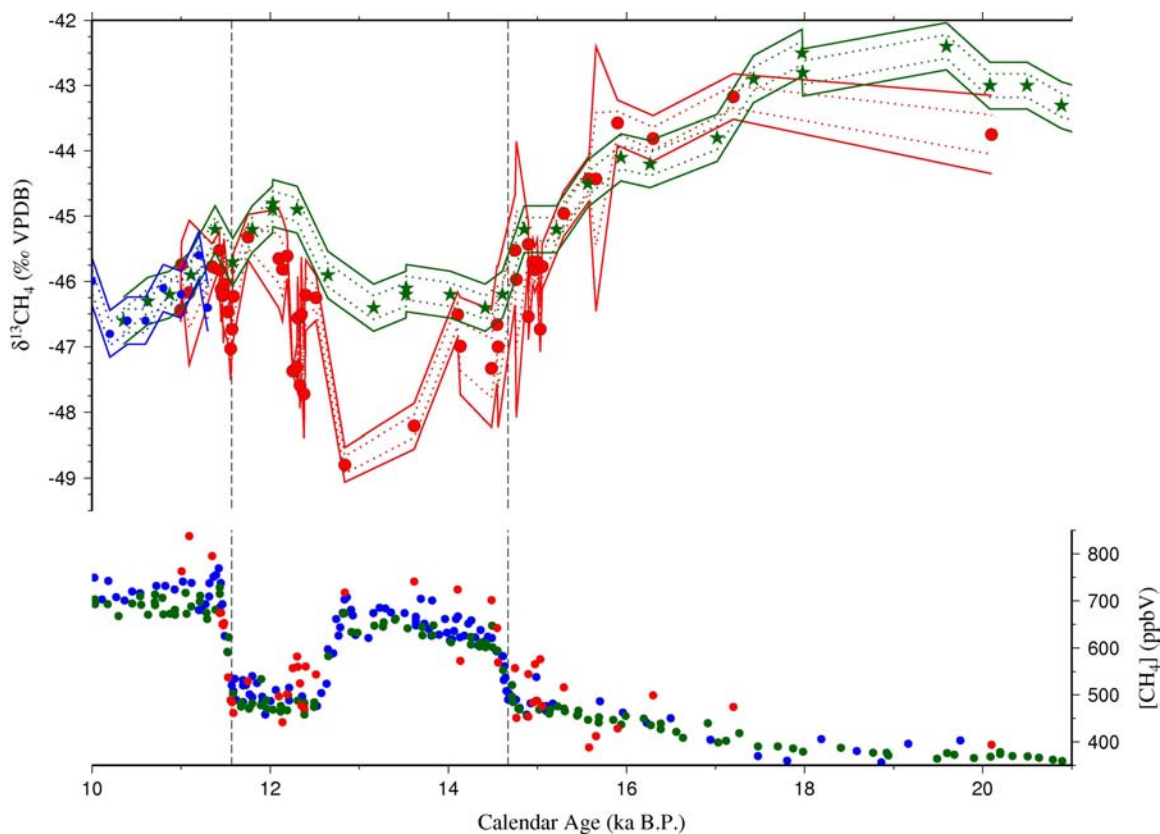


Figure 4.4.2: Uncertainty envelopes for the  $\delta^{13}\text{CH}_4$  record spanning the LGM to the start of the Holocene. Uncertainty envelope is  $1\sigma$  (dotted line) and  $2\sigma$  (solid line).  $\delta^{13}\text{CH}_4$  data sources include this work (red dots; Pákitsoq, Greenland), Fischer *et al.* (2008) (green stars; EDML, Antarctica), and Sowers (2009) (blue dots; GISP2, Greenland).  $\text{CH}_4$  concentration data are from this work (red dots; IRMS-derived concentration), Brook *et al.*, 1996 (blue dots; GISP2, Greenland), and EPICA Community Members (2006) (green dots; EDML, Antarctica).

$\delta^{13}\text{CH}_4$  values in both hemispheres. A greater number of  $\delta^{13}\text{CH}_4$  measurements are needed to confirm this apparent stability. As well,  $\delta\text{D-CH}_4$  and  $^{14}\text{CH}_4$  measurements are needed to detect changes in the methane system that are not apparent in the  $\delta^{13}\text{CH}_4$  of  $[\text{CH}_4]$  record.

The Pákitsoq and EDML [Fischer et al., 2008] samples from the Bølling-Allerød (BA) period show a widely diverging inter-polar gradient (IPG) in  $\delta^{13}\text{CH}_4$  values as the BA period proceeds. The  $\delta^{13}\text{CH}_4$  IPG appears to be almost 2 ‰ at the maximum divergence. The actual magnitude of the  $\delta^{13}\text{CH}_4$  IPG at its maximum is poorly defined due to the lack of contemporaneous data points in each hemisphere. Therefore, the  $\delta^{13}\text{CH}_4$  IPG is currently only an initial indication, while the true magnitude is unknown. As well, the area of the largest apparent  $\delta^{13}\text{CH}_4$  IPG is represented by only two datum points in the Pákitsoq dataset.

Acknowledging the uncertainty and paucity of data, the observed  $\delta^{13}\text{CH}_4$  IPG remains an interesting feature. Through the Bølling-Allerød period,  $[\text{CH}_4]$  is observed to rise gradually by  $\sim 85$  ppbv (corresponding to  $\sim 30$  Tg  $\text{CH}_4$   $\text{yr}^{-1}$  assuming constant sink strength) just prior to the initiation of the YD. Under three simultaneous conditions it would be possible to determine the  $\delta^{13}\text{CH}_4$  value of the increasing, and  $^{13}\text{C}$ -depleted, northern source: 1) the rise in atmospheric mixing ratio is solely attributed to one source; 2) that one source was also responsible for the large increase in the IPG of  $\delta^{13}\text{CH}_4$  through the BA period; and 3) the other sources aggregated  $\delta^{13}\text{CH}_4$  value remained constant through this period.

Mass balance shows the  $\delta^{13}\text{CH}_4$  value of this source to be about -68 ‰, after accounting for sink isotopic fractionation (using values in Table 2.4.1). The source also

must be almost exclusively in the Northern Hemisphere. From the hemispheric source distribution and calculated  $\delta^{13}\text{CH}_4$  value, boreal wetlands, and specifically, thermokarst lakes are the most likely sources to be primarily responsible for the large  $\delta^{13}\text{CH}_4$  IPG increase over the BA period. Due to methane's interhemispheric mixing time of ca. 1 year, to maintain a 2 ‰  $\delta^{13}\text{CH}_4$  IPG, would require the added Northern Hemisphere source(s) to have a relatively high flux. However to reiterate, these are initial observations and conclusions about this apparent large increase in  $\delta^{13}\text{CH}_4$  IPG during the BA are premature until more data are available to establish the relationships more rigorously.

#### 4.5. The termination of the Younger Dryas

The Younger Dryas – Preboreal (YD-PB) transition  $\delta^{13}\text{CH}_4$  values presented here have been corrected for isotopic disequilibrium (Section 2.3.3 and Figure 3.3.5). The corrected values permit a more detailed examination of the aggregated source  $\delta^{13}\text{CH}_4$

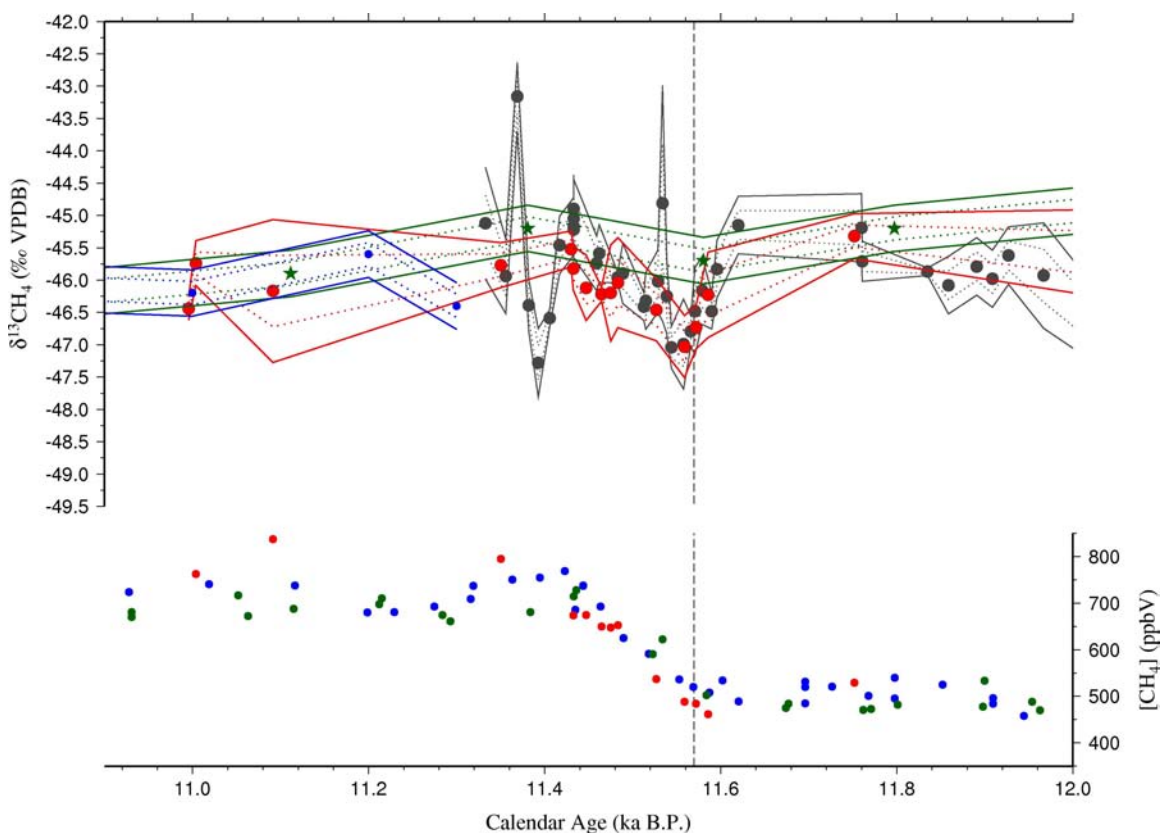


Figure 4.5.1: Uncertainty envelopes for the  $\delta^{13}\text{CH}_4$  record over the transition from the Younger Dryas to the Preboreal period. Uncertainty envelope is  $1\sigma$  (dotted line) and  $2\sigma$  (solid line).  $\delta^{13}\text{CH}_4$  data sources include this work (red dots; Pákitsoq, Greenland), Fischer et al. (2008) (green stars; EDML, Antarctica), and Schaefer et al. (2006) (grey circles; Pákitsoq, Greenland).  $\text{CH}_4$  concentration data are from this work (red dots; IRMS-derived concentration), Brook et al., 1996 (blue dots; GISP2, Greenland), and EPICA Community Members (2006) (green dots; EDML, Antarctica). Dashed line represents the termination of the YD at 11.570 ka BP

values through the transition.

The dynamics of the YD-PB transition were first explored by Schaefer et al. (2006), who, due to the precision of the measurements and sample coverage, chose to conservatively interpret a relatively constant  $\delta^{13}\text{CH}_4$  value of  $-46\text{‰}$  through the

transition. The augmenting Pákitsoq data provided by this work, using a substantially modified instrumental setup and samples from a different sampling season, provides evidence that confirms the broader conclusions of Schaefer et al. (2006). Figure 4.5.1 shows the datasets of this work and Schaefer et al. (2006) to overlap well. It is also possible with this expanded dataset to revisit Schaefer and coworkers' interpretation of no change in the  $\delta^{13}\text{CH}_4$  value through the transition.

While it is possible, but unlikely, that the visible  $^{13}\text{C}$ -enrichment in  $\delta^{13}\text{CH}_4$  values during the YD-Preboreal  $[\text{CH}_4]$  rise (after the dotted line in Figure 4.5.1) is a data artifact unique to the Pákitsoq site, it presents an interesting feature. Any strong interpretation of this feature will require validation by other ice sample measurements of high-resolution, precision, and accuracy. However, it is a worthwhile exercise to investigate the source/sink dynamics behind such a feature.

The atmospheric methane sinks have been commonly treated as invariant across the YD-PB transition (e.g. Sowers, 2006; Schaefer et al., 2006). This treatment is supported by the 4-box model results for the YD and PB periods (Table 3.4.1), which showed no change in the methane atmospheric lifetime in the solely data-constrained simulations. However, the Preboreal simulation demonstrated excessive tailing to higher atmospheric lifetime values and could be inaccurate. It can be anticipated that the main sink of atmospheric methane, OH, would react to an abrupt change in the climate. The increase in methane concentration will act to decrease the OH sink through OH radical destruction [Prather et al., 2001] resulting in a longer  $\text{CH}_4$  atmospheric lifetime. Increasing temperatures will increase humidity and OH concentrations thus decreasing  $\text{CH}_4$  atmospheric lifetime [Drevet, 2008]. As well, the vegetation response to changing

climate could alter the BVOC airborne concentrations, which may influence the OH sink [Valdes et al., 2005; Kaplan et al., 2006]. The relative importance of each of these mechanisms is difficult to ascertain.

For this analysis, it is assumed that the CH<sub>4</sub> sinks did not change significantly across the YD-PB transition. The assumption of no change in the methane sinks may not be a realistic assumption, however no reliable information about changes in the methane sinks over the transition is presently available. The increase in mixing ratios is then assumed solely due to an increase of ca. 82 Tg CH<sub>4</sub> yr<sup>-1</sup> over the course of the 150 year transition. The δ<sup>13</sup>CH<sub>4</sub> values measured would indicate a <sup>13</sup>C-enrichment of between 0.5 and 1.5 ‰. The difference in δ<sup>13</sup>CH<sub>4</sub> values and amount of [CH<sub>4</sub>] increase over the transition imply that the extra emissions have an atmospheric δ<sup>13</sup>CH<sub>4</sub> value of between -41 and -43 ‰ (not corrected for sink fractionation).

The δD-CH<sub>4</sub> record for this YD-PB transition has been measured from GISP2 ice by Sowers (2006) and shows a remarkably constant value of about -90 ‰. This would indicate the additional source emissions have a δ<sup>13</sup>CH<sub>4</sub> value of ca. -47‰ and a δD-CH<sub>4</sub> value of -307‰, after accounting for sink abstraction fractionation (ε<sub>C</sub> = 5.3 ‰; ε<sub>D</sub> = 217 ‰, see Table 2.4.1). No present day source has this δ<sup>13</sup>CH<sub>4</sub> and δD-CH<sub>4</sub> signature (Figure 4.5.2; note direction of δ<sup>13</sup>CH<sub>4</sub> scale is inverse of previous figures). However, due to the relatively high δ<sup>13</sup>CH<sub>4</sub> value calculated, only two sources are <sup>13</sup>C-enriched enough to use as input to the isotope mass balance: biomass burning and geologic methane (GEM)(see Table 2.4.4). Both of these sources have <sup>2</sup>H-enriched δD-CH<sub>4</sub>. These two sources then can not be reconciled to both the carbon and hydrogen isotope input mass balances, and therefore can not be the sole source(s) of the CH<sub>4</sub> increase. If one of these two <sup>13</sup>C-

enriched sources, i.e. biomass burning or GEM, can be ruled out, it will be possible to determine which other source is required to achieve the observed stable isotope values. Underpinning these calculations is the supposition that the increase in CH<sub>4</sub> mixing ratio was primarily caused by increases in only one or two sources.

Controls on GEM emission for on-shore and off-shore seeps vary and are poorly known [Etiope et al. 2008b]. Hypothesized controls depend on seep location, and can be sensitive to sea level change (off-shore) [Luyendyk et al., 2005] and/or endogenic (geodynamic processes)(both on-shore and off-shore). Both processes appear to be either insensitive to climate change, at least on the time scale of an abrupt climate transition, or are not capable of the rapid rate of change in CH<sub>4</sub> flux observed here. A third process for GEM flux variations has been discussed [Hill et al., 2006]. Hill et al. (2006) propose that climate-sensitive marine gas hydrates are able to modulate geologic off-shore seep flow and have done so during the last deglaciation. This hypothesis appears to have merit, as the YD termination was marked by a rapid warming *before* the [CH<sub>4</sub>] rise [Severinghaus et al. 1998]. However, if the gas hydrates associated with hydrocarbon seeps destabilized in response to the warming of the YD termination, it would be expected that other, biogenic, hydrates would also release to a similar extent, since they exhibit the same sensitivity to temperature. A mixture of emissions from both biogenic ( $\delta^{13}\text{CH}_4$  ca. -60 ‰) and thermogenic ( $\delta^{13}\text{CH}_4$  ca. -40 ‰) marine hydrates could balance out to the calculated source  $\delta^{13}\text{CH}_4$  value of -47 ‰. However, both hydrocarbon-seep and biogenic marine gas hydrates possess  $\delta\text{D-CH}_4$  values lower than -220 ‰. Thus together biogenic and thermogenic clathrates form a calculated source  $\delta\text{D-CH}_4$  value significantly too <sup>2</sup>H-enriched compared with the calculated  $\delta\text{D-CH}_4$  value of -307 ‰. The release of GEM

from hydrate-mediated reservoirs is thus unlikely to have contributed to the YD termination [CH<sub>4</sub>] rise.

Biomass burning is the other <sup>13</sup>C-enriched methane source, and it is capable of a rapid response to a changing climate [Westerling et al., 2006; Marlon et al., 2009]. As well, increased fire activity around 11 ka BP (1000 year sampling window) is evident from a large database of charcoal records [Power et al., 2008]. Marlon et al. (2009) also find a North American response to the YD termination with a large increase in fire activity. From this evidence, biomass burning appears a plausible source for <sup>13</sup>C-enriched methane at the YD termination.

If biomass burning is the <sup>13</sup>C-enriched source responsible for the rapid [CH<sub>4</sub>] increase, the other source (mixing end-member) would necessarily have a relatively <sup>2</sup>H-depleted δD-CH<sub>4</sub> value. This value must be more <sup>2</sup>H-depleted than the value of the mean source input δD-CH<sub>4</sub> (-307 ‰), in order to balance the <sup>2</sup>H-enriched biomass burning methane. Five potential methane sources have δD-CH<sub>4</sub> values more <sup>2</sup>H-depleted than the mean source input δD-CH<sub>4</sub> (using values from Table 2.4.4). As a test of which source is most likely to have contributed to the [CH<sub>4</sub>] rise, a mass balance is calculated for each of the stable isotope constraints (δ<sup>13</sup>CH<sub>4</sub> and δD-CH<sub>4</sub>):

$$(4.5.1.) \quad m_{inc} \delta^{13}C_{inc} = m_{BB} \delta^{13}C_{BB} + m_{src} \delta^{13}C_{src}$$

where  $m_{inc}$  is the mass flux of the additional CH<sub>4</sub>, (ca. 82 Tg yr<sup>-1</sup>)  $\delta^{13}C_{inc}$  is the δ<sup>13</sup>CH<sub>4</sub> value of the additional CH<sub>4</sub>,  $m_{BB}$  is the mass flux of additional CH<sub>4</sub> attributed to biomass burning,  $\delta^{13}C_{BB}$  is the δ<sup>13</sup>CH<sub>4</sub> value of biomass burning,  $m_{src}$  is the additional mass flux of CH<sub>4</sub> attributed to 1 of the 5 other possible sources, and  $\delta^{13}C_{src}$  is that source's δ<sup>13</sup>CH<sub>4</sub> value. The δD-CH<sub>4</sub> mass balance takes the same form and is calculated independently.

$$(4.5.2.) \quad m_{inc} \delta D_{inc} = m_{BB} \delta D_{BB} + m_{src} \delta D_{src}$$

The  $m_{BB}$  and  $m_{src}$  values necessarily sum to  $m_{inc}$ . The solutions to equations 4.5.1. and 4.5.2. are presented in Table 4.5.1. From this table, each end-member source has a calculated fractional contribution to the  $[\text{CH}_4]$  rise (the remaining end-member of the mass balance is taken to be biomass burning  $\text{CH}_4$ ). Sources with the most consistent fractional contribution estimates are thus more likely to have been the additional source along with biomass burning. Interestingly, based upon these stable isotope constraints, neither tropical wetlands [Brook et al., 1996] or gas hydrates [Kennett et al., 2003], as has

Table 4.5.1: Fractional contribution of each end-member of the 5 possible sources that could have contributed, along with biomass burning, to the  $[\text{CH}_4]$  rise at the termination of the Younger Dryas. The fractional contributions are for either the  $\delta^{13}\text{CH}_4$ , or the  $\delta\text{D-CH}_4$ , constraints. Sources with a low absolute value of the difference between  $\delta^{13}\text{CH}_4$  and  $\delta\text{D-CH}_4$  values will be those most likely to have contributed to the  $[\text{CH}_4]$  rise (in addition to biomass burning).

Constraint used	Trop. Wet	Bor. Wet.	Termites	Ruminants	APM
$\delta^{13}\text{CH}_4$	0.66	0.57	0.56	0.63	0.62
$\delta\text{D-CH}_4$	0.91	0.61	0.50	0.78	0.67
Absolute value of the difference between $\delta^{13}\text{CH}_4$ and $\delta\text{D-CH}_4$ constraints	0.25	0.04	0.06	0.15	0.05

been frequently purported, are likely to have been the additional source. The most likely sources include: boreal wetlands, APM and termites. This estimation is based solely on the  $\delta^{13}\text{CH}_4$  and  $\delta\text{D-CH}_4$  constraints of the sources and is not constrained by the rate at which the source can realistically change emitted flux strength or the size of its reservoir to produce the  $\text{CH}_4$ , etc. Thus the identification of the source responsible can be narrowed further.

Termites are a small source [Denman et al., 2007], and unlikely to respond to warming climate to such an extent, and thus are rejected. However, both APM and boreal wetlands are sensitive to climatic change and, potentially, large sources. Both sources

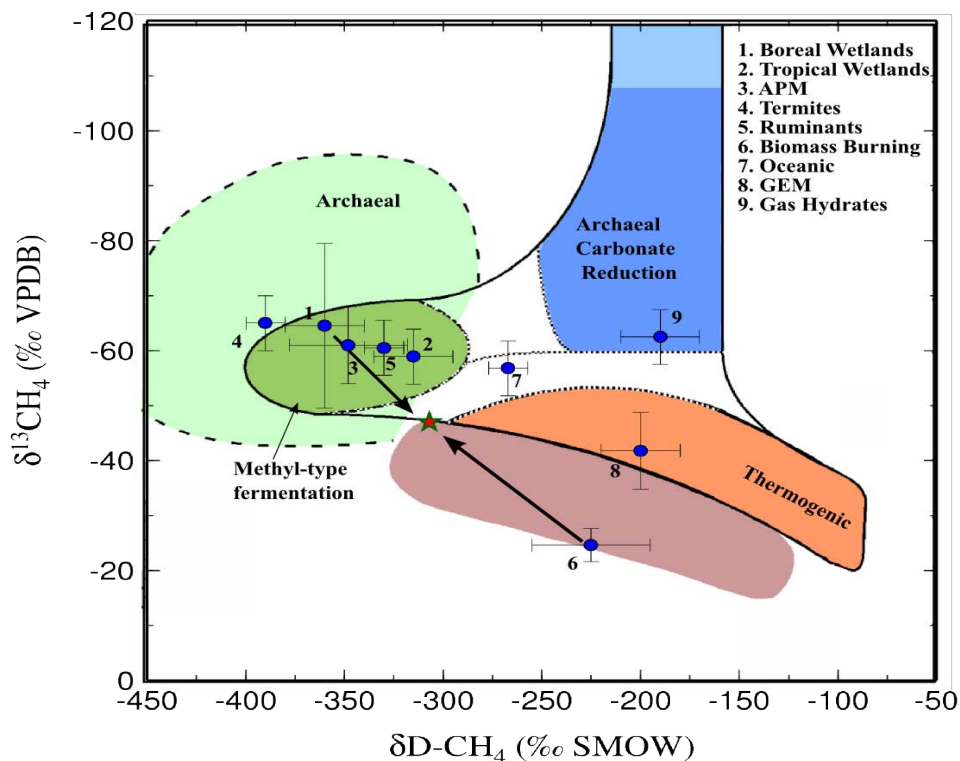


Figure 4.5.2: Combination  $\delta^{13}\text{CH}_4$  and  $\delta\text{D-CH}_4$  for the major sources of methane to the atmosphere, and the calculated value of the source responsible for the YD-Preboreal transition  $\text{CH}_4$  increase (red star). The mixing lines of the two most likely sources (boreal wetlands and biomass burning) responsible for the calculated source value are shown. Shaded regions denote methanogenic pathways (after Whiticar, 1999). Source stable isotope values and standard deviations are based upon from Quay et al., 1999; Whiticar, 1999; Vigano et al., 2009; Keppler et al., 2006; Milkov, 2005.

would, from these calculations, need to increase by around  $50 \text{ Tg CH}_4 \text{ yr}^{-1}$ , with the balance being generated by an increase biomass burning  $\text{CH}_4$  flux of ca.  $30 \text{ Tg yr}^{-1}$ . These estimates are likely maximum values considering that other  $\text{CH}_4$  sources may also be expected to change their fluxes in response to climate change, albeit with their own intrinsic rate of change and sensitivity to the changing climate.

A further constraint to differentiate the likelihood of either APM or boreal wetlands end-member components can be provided by  $^{14}\text{C}$  measurements of Pákitsoq  $\text{CH}_4$ . Petrenko et al. (2009) used large samples (ca. 1000 kg) of outcropping ice to determine the  $^{14}\text{CH}_4$  values for the YD, transition, and PB periods. Their results are complicated by  $^{14}\text{CH}_4$  values higher than predicted, attributed to in-situ direct cosmogenic  $^{14}\text{C}$  production. A correction is applied to their results to account for the in-situ production. From the corrected data they are able to infer only relative changes in the amount of fossil methane, dependent upon the assumed amount of fossil methane flux during the YD. Petrenko et al. (2009) present two different scenarios based upon 50 Tg  $\text{CH}_4 \text{ yr}^{-1}$  or 0 Tg  $\text{CH}_4 \text{ yr}^{-1}$  from fossil sources during the YD. The box model simulations performed for this study indicate a YD GEM  $\text{CH}_4$  flux of  $\sim 42 \text{ Tg yr}^{-1}$ , thus the 50 Tg  $\text{yr}^{-1}$  fossil  $\text{CH}_4$  scenario is assumed more realistic. From this 50 Tg  $\text{yr}^{-1}$  fossil  $\text{CH}_4$  scenario, the rise in fossil  $\text{CH}_4$  in the Preboreal period, over the YD, is between 18 and 30 Tg  $\text{yr}^{-1}$ . This amount of fossil methane will preclude the combination of APM and biomass burning from being the two largest sources for the  $[\text{CH}_4]$  increase, as both of these sources should contain appreciable  $^{14}\text{C}$ .

Boreal wetland  $\text{CH}_4$  flux (including in this category thermokarst lakes and boreal peatlands) can be expected to contain fossil methane. Thermokarst lake emissions have recently been measured to contain a range of  $^{14}\text{CH}_4$  ages from 5,600 to 43,000 years with the highest volume features ('hotspots') emitting gas of the oldest ages [Walter et al., 2007, 2008]. As a result, thermokarst emissions contain appreciable quantities of fossil methane and allow boreal wetland emissions to be consistent with the results of Petrenko et al. (2009). It is also likely that biomass burning initiated the  $[\text{CH}_4]$  rise as the  $^{14}\text{C}$

measurements indicate that the fossil source is only appreciable towards the end of the transition. If this is correct, the  $\Delta\delta^{13}\text{CH}_4$  should be initially large as biomass burning is the most  $^{13}\text{C}$ -enriched source. As the boreal wetland source increases through the transition and the  $^{12}\text{C}$ -depleted methane is added to the aggregated global source flux,  $\Delta\delta^{13}\text{CH}_4$  will decrease. The present data are, unfortunately, not of sufficient precision and accuracy for a thorough test of this hypothesis (Figure 3.3.5).

A final possibility is release of methane from subglacial hydrates as the additional source to biomass burning. Due to no available methane stable isotope values for subglacial methanogenesis gas hydrates, this methane source can not be tested using the mass balance approach adopted here. However, the  $^{14}\text{C}$  content and assumed ability to respond to climate warming [Weitemeyer and Buffett, 2006] make subglacial gas hydrates a potential candidate.

From the assumptions outlined, the most plausible source combination for the observed  $\text{CH}_4$  dynamics over the course of the YD-Preboreal transition is ca. 60 % boreal wetlands (mostly thermokarst lakes) and ca. 40 % biomass burning. However, given the complex nature of methane dynamics, it is unlikely that any change in the atmospheric methane record would be due solely to the actions of only one or two sources. With this in mind, and the many assumptions necessary to determine the sources responsible, the assessment that biomass burning and boreal wetlands were responsible for the YD termination atmospheric  $[\text{CH}_4]$  should be viewed as tentative.

Comparing the two abrupt warmings investigated in this study (the YD-Preboreal and Oldest Dryas- Bølling (OD-B)) it is apparent that the  $\delta^{13}\text{CH}_4$  dynamics across each transition are fundamentally different. While the OD-B transition is not sampled with

high resolution during the actual  $[\text{CH}_4]$  rise, it is likely that the trend in  $\delta^{13}\text{CH}_4$  across the transition is toward  $^{13}\text{C}$ -depleted values as opposed to  $^{13}\text{C}$ -enriched values as discussed for the YD-Preboreal transition. This difference reflects the fundamentally different state of the earth system between these two time periods, and serves as a reminder that all abrupt climate changes in methane are not readily attributable to the influence of a single source.

## 5. Conclusions

The work presented in this study aims to increase our understanding of methane dynamics spanning the most recent deglaciation. Special attention is paid to instances of abrupt changes in atmospheric methane concentration. To facilitate this goal, an improved on-line extraction and continuous flow- isotope ratio mass spectrometer (CF-IRMS) method was developed to allow ice samples containing air with low methane concentrations to be analysed with high precision and accuracy. The modified method improves on the setup of Schaefer and Whiticar (2007), with an approximately 2.5 times increase in sensitivity with a standard uncertainty for  $\delta^{13}\text{CH}_4$  estimated to be less than 0.3 ‰.

This improved setup was used to measure ice samples collected from the ablation -zone at Pákitsoq, Greenland. CF-IRMS measurement of the Pákitsoq samples reveal an irregular, spot contamination consisting of elevated  $\text{CH}_4$  concentrations in the interstitial air. This contamination is most likely a result of in-situ methanogenesis with some samples also displaying evidence of substrate depletion by the methanogens. All Pákitsoq data were filtered to identify and reject contaminated samples by comparison against contemporaneous  $\text{CH}_4$  mixing ratios from GISP2 ice core [Brook et al., 2000]. All Pákitsoq data that are 100 ppbv deviant from the baseline GISP2 mixing ratio are rejected. The remaining 84  $\delta^{13}\text{CH}_4$  samples cover the Last Glacial Maximum (LGM, ca. 20 ka BP) through to the Preboreal period (ca. 11 ka BP), with the Younger Dryas-Preboreal (YD-PB) transition measured in higher resolution.

The Pákitsoq  $\delta^{13}\text{CH}_4$  values are the first from the Northern Hemisphere for time periods older than the YD-PB transition. This  $\delta^{13}\text{CH}_4$  record shows a general pattern of

$^{13}\text{C}$ -depletion as the deglaciation progresses. Compared with other time periods, methane during the LGM is highly enriched in  $^{13}\text{C}$ , with  $\delta^{13}\text{CH}_4$  values about -43 ‰. As the atmospheric  $\text{CH}_4$  mixing ratio slowly rises through the Oldest Dryas (OD), the Pákitsoq  $\delta^{13}\text{CH}_4$  values become steadily  $^{13}\text{C}$ -depleted. During the OD to Bølling warm period transition, the  $[\text{CH}_4]$  rapidly increases over a ca. 300 year period, while the Pákitsoq  $\delta^{13}\text{CH}_4$  values are observed to possibly plateau at ca. -47 ‰ after the transition is complete (the actual transition itself is not well-sampled). As the Bølling-Allerød (BA) period progresses, the Pákitsoq  $\delta^{13}\text{CH}_4$  values eventually continue  $^{13}\text{C}$ -depletion, reaching a  $\delta^{13}\text{CH}_4$  value of -48.8 ‰, immediately prior to the initiation of the YD cold interval.  $\delta^{13}\text{CH}_4$  values  $^{13}\text{C}$ -depleted to this extent are not observed again through the deglaciation until the late Preindustrial Holocene (PIH) [Ferretti et al., 2005]. This high level of  $^{13}\text{C}$ -depletion is suggested to be due to enhanced  $\text{CH}_4$  emissions from thermokarst lakes. Through the YD period, the  $\delta^{13}\text{CH}_4$  values shift to more  $^{13}\text{C}$ -enriched values, most likely as a result of the cooling climate reducing emissions from  $^{13}\text{C}$ -depleted biogenic  $\text{CH}_4$  sources. The  $\delta^{13}\text{CH}_4$  record shows some rapid dynamics during the termination of the YD, with a potential  $^{13}\text{C}$ -enrichment visible in the densely-sampled transition.

Further information is gained from the Pákitsoq  $\delta^{13}\text{CH}_4$  record through comparison with the Antarctica  $\delta^{13}\text{CH}_4$  record of Fischer et al. (2008). This is the first look at the  $\delta^{13}\text{CH}_4$  inter-polar gradient (IPG) for the deglaciation and, while much more data are required to make a complete picture, what is presently available reveals some interesting features.

During the LGM, the  $\delta^{13}\text{CH}_4$  values in both hemispheres show a small ( $< 0.5$  ‰)  $\delta^{13}\text{CH}_4$  IPG that remains very small, or zero, through the OD period. The Bølling

transition marks the first period during the deglaciation with an obvious increase in the IPG, due to  $^{13}\text{C}$ -depleted  $\delta^{13}\text{CH}_4$  values in the Northern Hemisphere. As the BA period progresses, a large  $\delta^{13}\text{CH}_4$  IPG of approximately 2 ‰ develops prior to the initiation of the YD cold interval. Through the YD period, an appreciable  $\delta^{13}\text{CH}_4$  IPG is maintained at about 1.5 ‰, with a decrease after the YD-PB transition to less than 0.5 ‰. The pattern of  $^{13}\text{C}$ -depleted  $\delta^{13}\text{CH}_4$  values in the Northern Hemisphere is consistent across the deglaciation.

Interpretation of the source and sink dynamics behind the observed record is aided by a 4-box steady-state atmospheric methane model run in Monte Carlo mode. The model uses source emissions and  $\text{CH}_4$  atmospheric lifetime, randomly chosen within reasonable limits, as input. The model calculated results are then compared to ice core data constraints for inclusion as one of the 10,000 possible realizations. The model realizations define a quantitative probability distribution of source  $\text{CH}_4$  fluxes and  $\text{CH}_4$  atmospheric lifetime.

From the box model, tropical wetlands show relatively consistent  $\text{CH}_4$  flux across all time periods with the exception of the YD. The cold, dry climates of the LGM and YD decrease wetland  $\text{CH}_4$  output, however the LGM is likely compensated by the additional wetland area available on the exposed continental shelves; area that is less available to the YD resulting in lower  $\text{CH}_4$  emissions. Boreal wetlands are essentially shut-off during the LGM with a rapid turn-on into the BA. The contribution of thermokarst lakes is likely important starting in the BA period with additional, smaller, emissions from boreal peatlands after the YD termination. Biomass burning is found to increase through the deglaciation, approaching  $\text{CH}_4$  emission levels during the Preboreal period, close to those

of present day. Gas hydrates are similar to boreal wetlands with essentially no CH<sub>4</sub> flux in the LGM followed by a large increase into the BA period. The gas hydrate emissions are likely the result of subglacial methanogenesis for the BA period with terrestrial permafrost hydrate emissions during the YD cold period. The Preboreal gas hydrates CH<sub>4</sub> flux is less than the YD, likely due to less subglacial methanogenesis and a delayed response to the YD cooling from permafrost hydrates.

The Pâkitsoq  $\delta^{13}\text{CH}_4$  measurements from this work and Schafer et al. (2006) are used, in conjunction with  $\delta\text{D-CH}_4$  [Sowers, 2006] and  $^{14}\text{CH}_4$  [Petrenko et al., 2009] records, to evaluate the main sources responsible for the rapid [CH<sub>4</sub>] rise during the YD-Preboreal transition. A mixture of methane sources comprised of 40 % biomass burning and 60 % boreal wetlands is suggested to be responsible for the rapid [CH<sub>4</sub>] increase. Additionally, the boreal wetland source appears to be likely from thermokarst lake emissions. The analysis presented here is not consistent with an important role for methane hydrates or tropical wetlands in the [CH<sub>4</sub>] rise at the termination of the YD, as has been intensely debated [e.g. Brook et al., 1996; Kennett, 2003].

The methane record through the deglaciation and the YD-Preboreal abrupt climate transition demonstrate important aspects of the methane system and its response to changing climate. As the climate warms into the future as projected [IPCC, 2007], special attention should be paid to the dynamics of northern sources such as thermokarst lakes and terrestrial gas hydrates. Both of these methane sources appear capable of responding to changing climate with large increases in methane flux. Additionally, biomass burning appears to be capable of rapid response to abrupt changes in climate.

## 6. References

- Adams, J. M., et al. (2001) An estimate of natural volatile organic compound emissions from vegetation since the Last Glacial Maximum, *Chemosphere -Global Change Science*, 3, 73-91.
- Allan, W. et al. (2001a), Modelling the variation of  $\delta^{13}\text{C}$  in atmospheric methane: Phase ellipses and the kinetic isotope effect, *Global Biogeochemical Cycles*, 15(2), 467-481.
- Allan, W., et al. (2001b), Active chlorine in the remote marine boundary layer: Modelling anomalous measurements of  $\delta^{13}\text{C}$  in methane, *Geophysical Research Letters*, 28(17), 3239-3242.
- Allan, W., et al. (2005), Interannual variation of  $^{13}\text{C}$  in tropospheric methane: Implications for a possible atomic chlorine sink in the marine boundary layer, *Journal of Geophysical Research*, 110(D11306), doi:10.1029/2004JD005650.
- Allan, W., et al. (2007), Methane carbon isotope effects caused by atomic chlorine in the marine boundary layer: Global model results compared with Southern Hemisphere measurements, *Journal of Geophysical Research*, 112(D4), 1-10, doi:10.1029/2006JD007369.
- Alley, R. B., et al. (1998), Timing of abrupt climate change at the end of the Younger Dryas interval from thermally fractionated gases in polar ice, *Nature*, 391, 141-147.
- Alley, R. B. (2000), The Younger Dryas cold interval as viewed from central Greenland, *Quaternary Science Reviews*, 19, 213-226.
- Aselmann, I., and P. J. Crutzen (1989), Global distribution of natural freshwater wetlands and rice paddies, their net primary productivity, seasonality and possible methane emissions, *Journal of Atmospheric Chemistry*, 8,307-358.
- Assonov, S. S., and C. A. Brenninkmeijer (2003), On the  $^{17}\text{O}$  correction for  $\text{CO}_2$  mass spectrometric isotopic analysis., *Rapid Communications in Mass Spectrometry*, 17(10), 1007-16, doi:10.1002/rcm.1012.
- Bard, E., et al. (1996), Deglacial sea-level record from Tahiti corals and the timing of global meltwater discharge, *Nature*, 382,241-245
- Barnola, J., et al. (1991),  $\text{CO}_2$ -climate relationship as deduced from the Vostok ice core: a re-examination based on new measurements and on a re-evaluation of the air dating, *Tellus, Series A*, 43(2), 83.
- Bartlett, K. B., and R. C. Harriss (1993), Review and assessment of methane emissions from wetlands, *Chemosphere*, 26, 261-320
- Beerling, D. J., et al. (2005), The ice age methane budget, *Geophysical Research Letters*, 32(L02704), 1-4, doi:10.1029/2004GL021004.
- Bellisario, L. M., et al. (1999), Controls on  $\text{CH}_4$  emissions from a northern peatland, *Global Biogeochemical Cycles*, 13(1), 81-91.

- Bender, M. L., et al. (1999), High precision correlations of Greenland and Antarctica ice core records over the last 100 kyr, in *Mechanisms of Global Climate Change at Millennial Timescales*, (ed.) P. U. Clark, R. Webb, and L. Keigwin, pp. 149-164, American Geophysical Union, Washington, D.C.
- Bender, M. L., et al. (1994), The Dole effect and its variations during the last 130,000 years as measured in the Vostok ice core, *Global Biogeochemical Cycles*, 8(3), 363-376.
- Bergamaschi, P., et al. (2007), Satellite cartography of atmospheric methane from SCIAMACHY on board ENVISAT: 2. Evaluation based on inverse model simulations, *Journal of Geophysical Research*, 112, D02304, doi:10.1029/2006JD007268.
- Blunier, T., and E. J. Brook (2001), Timing of millennial-scale climate change in Antarctica and Greenland during the last glacial period., *Science*, 291(5501), 109-112, doi:10.1126/science.291.5501.109.
- Bowater, L. (2004), *Bacillus subtilis* YxaG is a novel Fe-containing quercetin 2,3-dioxygenase., *FEBS Letters*, 557, 45-48.
- Braconnot, P., et al. (2007), Results of PMIP2 coupled simulations of the Mid-Holocene and Last Glacial Maximum – Part 1: experiments and large-scale features, *Climate of the Past*, 3, 261-277.
- Brenninkmeijer, C. A. M. (1993), Measurement of the abundance of  $^{14}\text{C}$  in the atmosphere and the  $^{13}\text{C}/^{12}\text{C}$  and  $^{18}\text{O}/^{16}\text{O}$  ratio of atmospheric CO with applications in New Zealand and Antarctica, *Journal of Geophysical Research*, 98 (D6), 10,595-10,614.
- Brenninkmeijer, C. A. M., et al. (1995), The  $^{13}\text{C}$ ,  $^{14}\text{C}$ , and  $^{18}\text{O}$  isotopic composition of CO, CH<sub>4</sub>, and CO<sub>2</sub> in the higher southern latitudes lower stratosphere, *Journal of Geophysical Research*, 100(D12), 26,163 – 26,172
- Broccoli, A. J. (2000), Tropical cooling at the Last Glacial Maximum: An atmosphere-mixed layer ocean model simulation, *Journal of Climate*, 13, 951-976.
- Broecker, W., et al. (1989), Routing of meltwater from the Laurentide Ice Sheet during the Younger Dryas cold episode, *Nature*, 341, 318-321.
- Broecker, W. (2001), Was the Medieval Warm Period global?, *Science*, 291(5508), 1497-1499.
- Brook, E. J., et al. (1996), Rapid variations in atmospheric methane concentration during the past 110,000 years, *Science*, 273,1087-1095.
- Brook, E. J., et al. (2000), On the origin and timing of rapid changes in atmospheric methane during the last glacial period, *Global Biogeochemical Cycles*, 14(2), 559-572.
- Brook, E. J., et al. (2005), Timing of millennial-scale climate change at Siple Dome, West Antarctica, during the last glacial period, *Quaternary Science Reviews*, 24(12-13), 1333-1343, doi:10.1016/j.quascirev.2005.02.002.
- Buffett, B., (2000), Clathrate Hydrates, *Annual Review of Earth and Planetary Science*, 28,477-507

- Buffett, B., and D. Archer (2004), Global inventory of methane clathrate: sensitivity to changes in the deep ocean, *Earth and Planetary Science Letters*, 227, 185-199
- Campen, R. K., et al. (2003), Evidence of microbial consortia metabolizing within a low-latitude mountain glacier, *Geology*, 31, 231-234, doi:10.1130/0091-7613(2003)031<0231.
- Cao, M., et al. (1996), Global carbon exchange and methane emissions from natural wetlands: Application of a process-based model, *Journal of Geophysical Research*, 101 (D9), 14,399-14,414
- Chanton, J. P., et al. (1995), Radiocarbon evidence for the substrates supporting methane formation within northern Minnesota peatlands, *Geochimica et Cosmochimica Acta*, 59(17), 3663-3668, doi:10.1016/0016-7037(95)00240-Z.
- Chappellaz, J., et al. (1990), Ice-core record of atmospheric methane over the past 160,000 years, *Nature*, 345, 127-131, doi:10.1038/345127a0.
- Chappellaz, J., et al. (1993a), Synchronous changes in atmospheric CH<sub>4</sub> and Greenland climate between 40 and 8 kyr BP, *Nature*, 366, 443-445, doi: 10.1038/366443a0.
- Chappellaz, J., et al. (1993b), The atmospheric CH<sub>4</sub> increase since the Last Glacial Maximum: (1) Source estimates, *Tellus*, 45B, 228-241.
- Chappellaz, J., et al. (1997), Changes in the atmospheric CH<sub>4</sub> gradient between Greenland and Antarctica during the Holocene, *Journal of Geophysical Research*, 102(D13), 15,987-15,997.
- Chasar, L., et al. (2000), Methane concentration and stable isotope distribution as evidence of rhizospheric processes: Comparison of a fen and bog in the glacial Lake Agassiz peatland complex, *Annals of Botany*, 86(3), 655-663, doi:10.1006/anbo.2000.1172.
- Clark, P. U., et al. (2001), Freshwater forcing of abrupt climate change during the last deglaciation, *Science*, 293, 283-288.
- Clark, P. U., and A. C. Mix (2002), Ice sheets and sea level of the Last Glacial Maximum, *Quaternary Science Reviews*, 21, 1-7, doi:10.1016/S0277-3791(01)00118-4
- Collatz, G. J., et al. (1998), Effects of climate and atmospheric CO<sub>2</sub> partial pressure on the global distribution of C<sub>4</sub> grasses: present, past, and future, *Oecologia*, 114, 441-454.
- Colussi, A. J., and M. Hoffmann (2003), In situ photolysis of deep ice core contaminants by Čerenkov radiation of cosmic origin, *Geophysical Research Letters*, 30(4), 1195, doi:10.1029/2002GL016112.
- Cook, E. R., et al. (2004), Extra-tropical Northern Hemisphere land temperature variability over the last 1000 years, *Quaternary Science Reviews*, 23, 2063-2074
- Craig, H. (1957), Isotopic standards for carbon and oxygen and correction factors for mass spectrometric analysis of carbon dioxide, *Geochimica et Cosmochimica Acta*, 12, 133-149.

- Craig, H., et al. (1988), The isotopic composition of methane in polar ice cores, *Science*, 242(4885), 1535–1539.
- Crowley, T. J., (2000), Causes of climate change over the past 1000 years, *Science*, 289, 270-279, doi: 10.1126/science.289.5477.270
- Cuffey, K.M., and G. D. Clow (1997), Temperature, accumulation and ice sheet elevation in central Greenland through the last deglacial transition, *Journal of Geophysical Research*, 102 (C12), 26,383-26,396.
- Curry, C. L. (2009), The consumption of atmospheric methane by soil in a simulated future climate, *Biogeosciences (Submitted)*.
- Dällenbach, A., et al. (2000), Changes in the atmospheric CH<sub>4</sub> gradient between Greenland and Antarctica during the Last Glacial and the transition to the Holocene, *Geophysical Research Letters*, 27(7), 1005, doi:10.1029/1999GL010873.
- Denman, K. L. et al. (2007), Couplings between changes in the climate system and biogeochemistry, in *Climate Change 2007: The Physical Science Basis. Contribution of Working Group I to the Fourth Assessment Report of the Intergovernmental Panel on Climate Change*, S. Solomon, D. Qin, M. R. Manning, Z. Chen, M. Marquis, K. Averyt, M. Tignor, and H. L. Miller, pp. 1-90, Cambridge University Press, Cambridge UK and New York, NY, USA.
- Dias, R. F., et al. (2002),  $\delta^{13}\text{C}$  of low-molecular-weight organic acids generated by the hydrous pyrolysis of oil-prone source rocks, *Geochimica et Cosmochimica Acta*, 66(15), 2755-2769, doi:10.1016/S0016-7037(02)00871-2.
- Dlugokencky, E. J., et al. (1994), The growth rate and distribution of atmospheric methane, *Journal of Geophysical Research*, 99(D8), 17,021-17,043.
- Dlugokencky, E. J., et al. (2003), Atmospheric methane levels off: Temporary pause or a new steady- state?, *Geophysical Research Letters*, 30(19), 1-4, doi:10.1029/2003GL018126.
- Dlugokencky, E. J. et al. (2009), Observational constraints on recent increases in the atmospheric CH<sub>4</sub> burden, *Geophysical Research Letters*, 36(18), 1-5, doi:10.1029/2009GL039780.
- Drevet, J. (2008) *Modeling study of the interannual variability in global tropospheric hydroxyl radical and methane concentrations over the last two decades*, Ph.D. Thesis, École Polytechnique Fédérale de Lausanne, 133.
- Dykoski, C.A., et al. (2005), A high-resolution, absolute-dated Holocene and deglacial Asian monsoon record from Dongge Cave, China, *Earth and Planetary Science Letters*, 233, 71-86
- EPICA Community Members, (2006), One-to-one coupling of glacial climate variability in Greenland and Antarctica, *Nature*, 444, 195-199, doi:10.1038/nature05301.
- Etheridge, D. M., et al. (1998), Atmospheric methane between 1000 A.D. and present: Evidence of anthropogenic emissions and climatic variability, *Journal of Geophysical Research*, 103(D13), 15979-15993, doi:10.1029/98JD00923.

- Etiopio, G., and R. W. Klusman (2002), Geologic emissions of methane to the atmosphere, *Chemosphere*, 49, 777-789
- Etiopio, G., et al. (2008a), Reappraisal of the fossil methane budget and related emission from geologic sources, *Geophysical Research Letters*, 35(9), 1-5, doi:10.1029/2008GL033623.
- Etiopio, G., et al. (2008b), Did geologic emissions of methane play any role in Quaternary climate change?, *Global and Planetary Change*, 61, 79-88.
- Fanning, A.F., and A. J. Weaver, (1997), Temporal-geographical meltwater influences on the North Atlantic Conveyor: Implications for the Younger Dryas, *Paleoceanography*, 12(2), 307-320.
- Ferretti, D. F. et al. (2005), Unexpected changes to the global methane budget over the past 2000 years., *Science*, 309(5741), 1714-7, doi:10.1126/science.1115193.
- Fischer, H. et al. (2008), Changing boreal methane sources and constant biomass burning during the last termination, *Nature*, 452, 864-868, doi:10.1038/nature06825.
- Fischer, H. et al. (2008), Supplementary Information: Changing boreal methane sources and constant biomass burning during the last termination., *Nature*, 452(7189), 864-7, doi:10.1038/nature06825.
- Flückiger, J., et al. (2004), N<sub>2</sub>O and CH<sub>4</sub> variations during the last glacial epoch: Insight into global processes., *Global Biogeochemical Cycles*, 18, GB1020, doi: 10.1029/2003GB002122.
- Forster, P. et al. (2007), Changes in atmospheric constituents and in radiative forcing, in *Climate Change 2007: The Physical Science Basis. Contribution of Working Group I to the Fourth Assessment Report of the Intergovernmental Panel on Climate Change*, vol. 20, M. A. [Solomon, S., D. Qin, M. Manning, Z. Chen, M. Marquis, K.B. Averyt, Cambridge University Press, Cambridge UK and New York, NY, USA.
- Francey, R. J., et al. (1999), A 1000-year high precision record of  $\delta^{13}\text{C}$  in atmospheric CO<sub>2</sub>, *Tellus*, 51B, 170-193.
- Fraser, P. J., et al. (1986), Termites and global methane – Another assessment, *Journal of Atmospheric Chemistry*, 4, 295-310.
- Friedrich, M., et al. (1999), Paleo-environment and radiocarbon calibration as derived from Lateglacial/Early Holocene tree-ring chronologies, *Quaternary International*, 61(1), 27-39, doi:10.1016/S1040-6182(99)00015-4.
- Frolking, S. and N. Roulet, (2007), Holocene radiative forcing impact of northern peatland carbon accumulation and methane emissions, *Global Change Biology*, 13, 1079–1088, doi: 10.1111/j.1365-2486.2007.01339.x.
- Fung, I., et al. (1991), Three-dimensional model synthesis of the global methane cycle, *Journal of Geophysical Research*, 97 (D7), 13,033-13,065.

- Gajewski, K., et al. (2001), *Sphagnum* peatland distribution in North America and Eurasia during the past 21,000 years, *Global Biogeochemical Cycles*, 15(2), 297-311.
- Gierczak, T., et al. (1997), Rate coefficients for the reactions of hydroxyl radicals with methane and deuterated methanes, *Journal of Physical Chemistry A*, 101, 3125-3134.
- Grachev, A. M., and J. P. Severinghaus (2003), Determining the thermal diffusion factor for  $^{40}\text{Ar}/^{36}\text{Ar}$  of abrupt climate change in air to aid paleoreconstruction, *Journal of Physical Chemistry A*, 107, 4636-4642.
- Grootes, P., and M. Stuiver (1997), Oxygen 18/16 variability in Greenland snow and ice with  $10^3$  to  $10^5$  year time resolution, *Journal of Geophysical Research*, 102(C12), 26,455-26,470.
- Gill, J.L., et al. (2009), Pleistocene megafaunal collapse, novel plant communities, and enhanced fire regimes in North America, *Science*, 326, 1100-1105, doi: 10.1126/science.1179504
- Haan, D., et al. (1996), Ice core data of atmospheric carbon monoxide over Antarctica and Greenland during the last 200 years, *Geophysical Research Letters*, 23(17), 2235, doi:10.1029/96GL02137.
- Hanson, R. S., and T. E. Hanson (1996) Methanotrophic bacteria, *Microbiological Reviews*, 60 (2), 439-471
- Hein, R., et al. (1997), An inverse modeling approach to investigate the global atmospheric methane cycle, *Global Biogeochemical Cycles*, 11 (1), 43-76
- Herron, M. M., and C. C. Langway (1980), Firn densification: an empirical model, *Journal of Glaciology*, 25(93), 373-385.
- Hill, T. M., et al. (2006) Climatically driven emissions of hydrocarbons from marine sediments during deglaciation, *Proceedings of the National Academy of Science*, 103(37), 13570-13574.
- Holton, J. R., et al. (1997), Stratosphere-troposphere exchange, *Review of Geophysics*, 33(4), 403-439
- Houweling, S., et al. (1999), Inverse modeling of methane sources and sinks using the adjoint of a global transport model, *Journal of Geophysical Research*, 104(D21), 26,137-26,160
- Huang, Y., et al. (2001), Climate change as the dominant control on glacial-interglacial variations in  $\text{C}_3$  and  $\text{C}_4$  plant abundance, *Science*, 293, 1647-1651.
- Hughen, K. A., et al. (2004), Abrupt tropical vegetation response to rapid climate changes, *Science*, 304, 1955-1960.
- Irion, F. W., et al. (1996), Stratospheric observations of  $\text{CH}_3\text{D}$  and HDO from ATMOS infrared solar spectra: Enrichments of deuterium in methane and implications for HD, *Geophysical Research Letters*, 23 (17), 2381-2384.

- Johnson, D.E., and G. M. Ward (1996), Estimates of animal methane emissions, *Environmental Monitoring and Assessment*, 42, 133-141
- Johnson, D. E., et al. (2000), Ruminants and other animals, in *Atmospheric Methane: Its Role in the Global Environment*. M.A.K. Khalil (Ed), 112 – 134, Springer-Verlag, Berlin
- Jouzel, J. et al. (1997), Validity of the temperature reconstruction from water isotopes in ice cores, *Journal of Geophysical Research*, 102(C12), 26471-26487, doi:10.1029/97JC01283.
- Jouzel, J., et al. (2007), Orbital and millennial Antarctic climate variability over the past 800,000 years., *Science*, 317, 793-796. doi: 10.1126/science/1141038.
- Kaplan, J. O. (2002a), Wetlands at the Last Glacial Maximum: Distribution and methane emissions, *Geophysical Research Letters*, 29(6), doi: 10.1029/2001GL013366.
- Kaplan, J. O., et al. (2002b), Modeling the dynamics of terrestrial carbon storage since the Last Glacial Maximum, *Geophysical Research Letters*, 29 (22), 2074, doi:10.1029/2002GL015230.
- Kaplan, J. O., et al. (2006), Role of methane and biogenic volatile organic compound sources in late glacial and Holocene fluctuations of atmospheric methane concentrations, *Global Biogeochemical Cycles*, 20(GB2016), 1-16, doi:10.1029/2005GB002590.
- Kennett, J. P., et al. (2003), *Methane hydrates in Quaternary climate change: the Clathrate Gun hypothesis*, AGU Special Publication 54.
- Keppler et al., (2006), Methane emissions from terrestrial plants under aerobic conditions, *Nature*, 439, 187-192. doi:10.1038/nature04420.
- Keppler et al., (2008), Methoxyl groups of plant pectin as a precursor of atmospheric methane: evidence from deuterium labelling studies, *New Phytologist*, doi: 10.1111/j.1469-8137.2008.02411.x
- King, S. T., et al. (1989), The  $^{13}\text{C}/^{12}\text{C}$  kinetic isotope effect for soil oxidation of methane at ambient atmospheric concentrations, *Journal of Geophysical Research*, 9 (D15), 18,273-277.
- Kitoh, A., et al. (2001), A simulation of the Last Glacial Maximum with a coupled atmosphere-ocean GCM, *Geophysical Research Letters*, 28(11), 2221-2224, doi:10.1029/2000GL012271.
- Kobashi, T., et al. (2008a),  $4\pm 1.5$  °C abrupt warming 11,270 yr ago identified from trapped air in Greenland ice, *Earth and Planetary Science Letters*, 268(3-4), 397-407, doi:10.1016/j.epsl.2008.01.032.
- Kobashi, T., et al. (2008b), Argon and nitrogen isotopes of trapped air in the GISP2 ice core during the Holocene epoch (0–11,500 BP): Methodology and implications for gas loss processes, *Geochimica et Cosmochimica Acta*, 72(19), 4675-4686, doi:10.1016/j.gca.2008.07.006.

- Kvenvolden, K. (1988), Methane hydrate — A major reservoir of carbon in the shallow geosphere?, *Chemical Geology*, 71, 41-51, doi:10.1016/0009-2541(88)90104-0.
- Kvenvolden, K. (1993), Gas hydrates—geological perspective and global change, *Reviews of Geophysics*, 31(2), 173–187.
- Lassey, K. R., et al. (2000), The trend in atmospheric methane  $\delta^{13}\text{C}$  and implications for isotopic constraints on the global methane budget, *Global Biogeochemical Cycles*, 14(1), 41-49.
- Lassey, K. R., et al. (2007), Centennial evolution of the atmospheric methane budget: what do the carbon isotopes tell us?, *Atmospheric Chemistry and Physics*, 7, 2119-2139.
- Leckrone, K. J., and J. M. Hayes (1997), Efficiency and temperature dependence of water removal by membrane dryers., *Analytical Chemistry*, 69(5), 911-918
- Lehner, B., and P. Döll (2004), Development and validation of a global database of lakes, reservoirs, and wetlands, *Journal of Hydrology*, 296, 1-22
- Lelieveld, J., et al. (1993), Climate effects of atmospheric methane, *Chemosphere*, 26(1-4), 739-768.
- Lelieveld, J., et al. (1998), Changing concentration, lifetime and climate forcing of atmospheric methane, *Tellus B*, 50(2), 128–150.
- Lelieveld, J. et al. (2008), Atmospheric oxidation capacity sustained by a tropical forest., *Nature*, 452(7188), 737-40, doi:10.1038/nature06870.
- Loulergue, L., et al. (2008), Orbital and millennial-scale features of atmospheric  $\text{CH}_4$  over the past 800,000 years., *Nature*, 453, 383-387, doi: 10.1038/nature06950
- Luyendyk, B., et al. (2005), Hypothesis for increased atmospheric methane input from hydrocarbon seeps on exposed continental shelves during glacial low sea level, *Marine and Petroleum Geology*, 22, 591 -596.
- Macdonald, G. M., et al. (2006), Rapid early development of circumArctic peatlands and atmospheric  $\text{CH}_4$  and  $\text{CO}_2$  variations:, *Science*, 314, 285-288.
- Mapsofworld.com, (2009), Web resource, *Top Ten Rice Producing Countries*, Compare Infobase Limited, Accessed December 10<sup>th</sup>, 2009.
- Mariotti, A. (1983), Atmospheric nitrogen is a reliable standard for natural  $^{15}\text{N}$  abundance measurements, *Nature*, 303, 685-687.
- Marlon, J. R., et al. (2009), Wildfire responses to abrupt climate change in North America, *PNAS*, 106 (8), 2159-2524, doi:10.1073/pnas.0808212106
- Maslin, M. A., and S. J. Burns (2000), Reconstruction of the Amazon basin effective moisture availability over the past 14,000 years, *Science*, 290, 2285-2289, doi: 10.1126/science.290.5500.2285
- Maslin, M.A., et al. (2004), Linking continental-slope failures and climate change: Testing the clathrate gun hypothesis, *Geology*, 32 (1), 53-56, doi:10.1130/G20114.1

- Matthews, E., and I. Fung (1987), Methane emission from natural wetlands: Global distribution, area, and environmental characteristics of sources, *Global Biogeochemical Cycles*, 1(1), 61-86.
- Meese, D. A., et al. (1997), The Greenland Ice Sheet Project 2 depth-age scale: Methods and results, *Journal of Geophysical Research*, 102(C12), 26,411-26,423.
- Merritt, D. A., et al. (1995), Performance and optimization of a combustion interface for isotope ratio monitoring gas chromatography/mass spectrometry, *Analytical Chemistry*, 67, 2461-2473.
- Mikaloff-Fletcher, S. E., et al. (2004), CH<sub>4</sub> sources estimated from atmospheric observations of CH<sub>4</sub> and its <sup>13</sup>C/<sup>12</sup>C isotopic ratios: 1. Inverse modeling of source processes, *Global Biogeochemical Cycles*, 18, doi:10.1029/2004GB002223
- Mischler, et al. (2009), Carbon and hydrogen isotopic composition of methane over the last 1000 years, *Global Biogeochemical Cycles*, 23, GB4024, doi:10.1029/2009GB003460.
- Milkov, A. (2005), Molecular and stable isotope compositions of natural gas hydrates: A revised global dataset and basic interpretations in the context of geological settings, *Organic Geochemistry*, 36(5), 681-702, doi:10.1016/j.orggeochem.2005.01.010.
- Nakagawa, F., et al. (2002), Production of methane from allasses in eastern Siberia: Implications from its <sup>14</sup>C and stable isotopic compositions, *Global Biogeochemical Cycles*, 16(3), doi: 10.1029/2000GB001384
- NEO (2009), NASA Earth Observatory, Web resource:<http://earthobservatory.nasa.gov/GlobalMaps/>. Accessed December 10<sup>th</sup>, 2009.
- Nisbet, E. (1990), The end of the ice age, *Canadian Journal of Earth Sciences*, 27(1), 148-157, doi:10.1139/e90-012.
- Nordt, L., et al. (2008), Coherent changes in relative C<sub>4</sub> plant productivity and climate during the late Quaternary in the North American Great Plains, *Quaternary Science Reviews*, 27, 1600-1611.
- Paull, C. K., et al. (1996), Increased continental-margin slumping frequency during sea-level lowstands above gas hydrates-bearing sediments, *Geology*, 24, 143-146.
- Peltier, W. (2004), Global glacial isostasy and the surface of the ice-age earth: the ICE-5G (VM2) model and GRACE, *Annual Review of Earth and Planetary Sciences*, 32, 111-149, doi:10.1146/annurev.earth.32.082503.144359.
- Peterson, L.C., et al. (2000), Rapid changes in the hydrologic cycle of the tropical atlantic during the Last Glacial, *Science*, 290, 1947-1952
- Petit, J. R., et al. (1999), Climate and atmospheric history of the past 420,000 years from the Vostok ice core, Antarctica, *Nature*, 399, 429-437.
- Petrenko, V. V., et al. (2006), Gas records from the West Greenland ice margin covering the Last Glacial Termination: a horizontal ice core, *Quaternary Science Reviews*, 25(9-10), 865-875.

- Petrenko, V. V. (2008), *A study of carbon-14 of paleoatmospheric methane for the last glacial termination from ancient glacial ice*, PhD. Thesis, Scripps Institute of Oceanography, 291.
- Power, M. J., et al. (2008), Change in fire regimes since the Last Glacial Maximum: an assessment based on a global synthesis and analysis of charcoal data, *Climate Dynamics*, 30, 887-907, doi:10.1007/s00382-007-0334-x
- Prather, M., et al. (2001), *Atmospheric Chemistry and Greenhouse Gases* in IPCC 2001: The scientific basis. Cambridge Press, Ch. 4, 239-288.
- Price, P. B. (2007), Microbial life in glacial ice and implications for a cold origin of life, *FEMS Microbiology Ecology*, 59(2), doi:10.1111/j.1574-6941.2006.00234.x.
- Price, P. B., and T. Sowers (2004), Temperature dependence of metabolic rates for microbial growth, maintenance, and survival., *Proceedings of the National Academy of Sciences*, 101(13), 4631-4636, doi:10.1073/pnas.0400522101.
- Prinn, R.G. (2003), The cleansing capacity of the atmosphere, *Annual Reviews of Environmental Resources*, 28, 29-57. doi:10.1146/annurev.energy.28.011503.163425.
- Quay, P., et al. (1999), The Isotopic Composition of Atmospheric Methane, *Global Biogeochemical Cycles*, 13(2), 445-461, doi:10.1029/1998GB900006.
- Raynaud, D., et al. (1997), Air content along the Greenland Ice Core Project core: A record of surface climatic parameters and elevation in central Greenland, *Journal of Geophysical Research*, 102(C12), 26607-26613, doi:10.1029/97JC01908.
- Reeburgh, W.S., et al. (1997), Carbon kinetic isotope effect accompanying microbial oxidation of methane in boreal forest soils, *Geochimica Cosmochimica Acta*, 61 (22), 4761-4767.
- Reeh, N., and H. Thomsen (1994), Introduction to the Paakitsoq 1994 field programme, West Greenland, in *Field Report on Palaeo-environmental Studies at the Greenland Ice Sheet Margin, Paakitsoq, West Greenland*, H. Thomsen and N. Reeh, Geological Survey of Greenland, Copenhagen.
- Reeh, N., et al. (2002), Comparison between Greenland ice-margin and ice-core oxygen-18 records, *Annals of Glaciology*, 35, 136-144.
- Reeh, N., et al. (2005), *Mapping layer sequence and folds of Pre-Holocene ice at the Pakitsoq 'horizontal ice coring' site, West Greenland*, American Geophysical Union Fall Meeting, San Francisco.
- Rigby, M. et al. (2008), Renewed growth of atmospheric methane, *Geophysical Research Letters*, 35(22), doi:10.1029/2008GL036037.
- Rogner, H-H., (1996), An Assessment of World Hydrocarbon Resources, *Working Paper (WP-96-56) from International Institute for Applied Systems Analysis, Laxenburg Austria*, 45
- Rohrer, F., and H. Berresheim (2006), Strong correlation between levels of tropospheric hydroxyl radicals and solar ultraviolet radiation, *Nature*, 442, 184-187. doi: 10.1038/nature04924.

- Romanovskii, N.N., et al. (2004), Permafrost of the east Siberian Arctic shelf and coastal lowlands, *Quaternary Science Reviews*, 23, 1359-1369.
- Roulet, N. T., et al. (1994), Role of the Hudson Bay lowland as a source of atmospheric methane, *Journal of Geophysical Research*, 99(D1),1431-1454.
- Saueressig, G., et al. (1995), Carbon kinetic isotope effect in the reaction of CH<sub>4</sub> with Cl atoms, *Geophysical Research Letters*, 22 (10), 1225-1228.
- Saueressig, G., et al. (2001), Carbon 13 and D kinetic isotope effects in the reactions of CH<sub>4</sub> with O(<sup>1</sup>D) and OH: New laboratory measurements and their implication for the isotopic composition of stratospheric methane, *Journal of Geophysical Research*, 106(D19), 23,127-23,138.
- Schaefer, H. (2005), *Stable Carbon Isotopic Composition of Methane from Ancient Ice Samples*, Ph.D. Thesis, University of Victoria, Victoria, Canada. 201.
- Schaefer, H. et al., (2006), Ice record of δ<sup>13</sup>C for atmospheric CH<sub>4</sub> across the Younger Dryas–Preboreal transition, *Science*, 313, 1109-1113.
- Schaefer, H., and M. J. Whiticar (2007), Measurement of stable carbon isotope ratios of methane in ice samples, *Organic Geochemistry*, 38(2), 216-226, doi:10.1016/j.orggeochem.2006.10.006.
- Schaefer, H., and M. J. Whiticar (2008), Potential glacial-interglacial changes in stable carbon isotope ratios of methane sources and sink fractionation, *Global Biogeochemical Cycles*, 22 (GB1001), doi: 10.1029/2006GB002889
- Schaefer, H., et al. (2009), Ice stratigraphy at the Pâkitsoq ice margin, West Greenland, derived from gas records, *Journal of Glaciology*, 55(191), 411-421.
- Schrag, D.P., et al. (2002), The oxygen isotopic composition of seawater during the Last Glacial Maximum, *Quaternary Science Reviews*, 21, 331-342
- Schwander, J., et al. (1993), The Age of the Air in the Firn and the Ice at Summit, Greenland, *Journal of Geophysical Research*, 98(D2), 2831-2838, doi:10.1029/92JD02383.
- Schwander, J., et al. (1997), Age scale of the air in the summit ice: Implication for glacial-interglacial temperature change, *Journal of Geophysical Research*, 102(D16), 19483-19493, doi:10.1029/97JD01309.
- Seager, R., et al. (2007), Blueprints for Medieval hydroclimate, *Quaternary Science Reviews*, 26, 2322-2336.
- Seinfeld, J. H. (2006), Global cycles: Sulfur and carbon, in *Atmospheric Chemistry and Physics: From Air Pollution to Climate Change*, (eds) H. Seinfeld, John and S. N. Pandis, pp. 1003-1025, John Wiley & Sons, Ltd Bracknell.
- Severinghaus, J. P., et al., (1998), Timing of abrupt climate change at the end of the Younger Dryas interval from thermally fractionated gases in polar ice., *Nature*, 391, 141-147.
- Severinghaus, J. P., and E. J. Brook (1999), Abrupt climate change at the end of the last glacial period inferred from trapped air in polar ice, *Science*, 286(5441), 930-934.

- Severinghaus, J. P., A. Grachev, and M. Battle (2001), Thermal fractionation of air in polar firn by seasonal temperature gradients, *Geochemistry Geophysics Geosystems*, 2(7), doi:10.1029/2000GC000146.
- Severinghaus, J. P., et al. (2003), A method for precise measurement of argon 40/36 and krypton/argon in trapped air in polar ice with applications to past firn thickness and abrupt climate change in Greenland and at Siple Dome, Antarctica, *Geochimica et Cosmochimica Acta*, 67(3), 325-343.
- Severinghaus, J. P., et al. (2006), Ice record of  $\delta^{13}\text{C}$  for atmospheric  $\text{CH}_4$  across the Younger Dryas-Preboreal transition., *Science*, 313(5790), 1109-12, doi:10.1126/science.1126562.
- Severinghaus, J. P., et al. (2009), Oxygen-18 of  $\text{O}_2$  records the impact of abrupt climate change on the terrestrial biosphere., *Science*, 324(5933), 1431-4, doi:10.1126/science.1169473.
- Sheridan, P. P., et al. (2003), Phylogenetic Analysis of Anaerobic Psychrophilic Enrichment Cultures Obtained from a Greenland Glacier Ice Core, *Applied and Environmental Microbiology*, 69(4), 2153-2160, doi:10.1128/AEM.69.4.2153.
- Shin, S., et al. (2003), A simulation of the Last Glacial Maximum climate using the NCAR-CCSM, *Climate Dynamics*, 20(2), 127–151, doi:10.1007/s00382-002-0260-x.
- Smith, H.J., et al. (1999), Dual modes of the carbon cycle since the Last Glacial Maximum, *Nature*, 400, 248-251.
- Smith, L., et al. (2004), Siberian peatlands a net carbon sink and global methane source since the early Holocene, *Science*, 303(5656), 353-356, doi:10.1126/science.1090553.
- Snover, A. K., and P. D. Quay (2000) Hydrogen and carbon kinetic isotope effects during soil uptake of atmospheric methane, *Global Biogeochemical Cycles*, 14(1), 25-39.
- Souchez, R., et al. (2006), Gas isotopes in ice reveal a vegetated central Greenland during ice sheet invasion, *Geophysical Research Letters*, 33(L24503), doi:10.1029/2006GL028424.
- Sowers, T. (2006), Late Quaternary atmospheric  $\text{CH}_4$  isotope record suggests marine clathrates are stable., *Science*, 311(5762), 838-40, doi:10.1126/science.1121235.
- Sowers, T. (2009), Atmospheric methane isotope records covering the Holocene period, *Quaternary Science Reviews*, 1-9, doi:10.1016/j.quascirev.2009.05.023.
- Sowers, T., et al. (1992),  $\delta^{15}\text{N}$  of  $\text{N}_2$  in air trapped in polar ice: a tracer of gas transport in the firn and a possible constraint on ice age-gas age differences, *Journal of experimental botany*, 97(D14), 15,683 – 15,697.
- Spahni, R., et al., (2003), The attenuation of fast atmospheric  $\text{CH}_4$  variations recorded in polar ice cores, *Geophysical Research Letters*, 30(11), 1571-1575.

- Stevens, C.M., and A. Engelkemeir (1988), Stable carbon isotopic composition of methane from some natural and anthropogenic sources, *Journal of Geophysical Research*, 93 (D1), 725-733
- Stevens, C.M., and F.E. Rust (1982) The carbon isotopic composition of atmospheric methane, *Journal of Geophysical Research*, 87,4879-4882.
- Stuiver, M., et al. (1995), The GISP2  $\delta^{18}\text{O}_{\text{atm}}$  climate record of the past 16,500 year and the role of the sun, ocean, and volcanoes, *Quaternary Research*, 44, 341-354.
- Tans, P. P. (1997), A note on isotopic ratios and the global atmospheric methane budget, *Global Biogeochemical Cycles*, 11(1), 77-81.
- Thompson, L.G., et al. (1995), Late glacial stage and Holocene tropical ice core records from Huascarán, Peru, *Science*, 269 (5220), 46-50
- Thompson, L.G., et al. (1998), A 25,000-year tropical climate history from Bolivian ice cores, *Science*, 282, 1858-1865
- Thonicke, K., et al. (2004), Modeling glacial-interglacial changes in global fire regimes and trace gas emissions, *Global Biogeochemical Cycles*, 19, doi:10.1029/2004GB002278
- Tison, J., et al. (1998), Is a periglacial biota responsible for enhance dielectric response in basal ice from the Greenland Ice Core Project ice core?, *Journal of Geophysical Research*, 103(D15), 18885-18,894.
- Trudinger, C. M., et al. (1997), Modeling air movement and bubble trapping in firn, *Journal of Geophysical Research*, 102(D6), 6747-6763
- Tung, H. C., et al. (2005), Microbial origin of excess methane in glacial ice and implications for life on Mars., *Proceedings of the National Academy of Sciences of the United States of America*, 102(51), 18292-6, doi:10.1073/pnas.0507601102.
- Tyler, S. C., et al. (1994),  $^{13}\text{C}/^{12}\text{C}$  fractionation of methane during oxidation in a temperate forested soil, *Geochimica Cosmochimica Acta*, 58(6), 1625-1633.
- Valdes, P.J., et al. (2005) The ice age methane budget, *Geophysical Research Letters*, 32, L02704, doi: 10.1029/2004GL021004.
- Vigano, I., et al. (2009), The stable isotope signature of methane emitted from plant material under UV radiation, *Atmospheric Environment*, 43, 5637-5646.
- Wahlen, M., et al. (1989), Profiles of  $\delta^{13}\text{C}$  and  $\delta\text{D}$  of  $\text{CH}_4$  from the lower stratosphere, *EOS Transactions AGU*, 70, 1017, 1989.
- Walter, K. M., et al. (2006), Methane bubbling from Siberian thaw lakes as a positive feedback to climate warming., *Nature*, 443(7107), 71-75, doi:10.1038/nature05040.
- Walter, K. M., et al. (2007), Thermokarst lakes as a source of atmospheric  $\text{CH}_4$  during the last deglaciation., *Science*, 318(5850), 633-636, doi:10.1126/science.1142924.
- Walter, K.M., et al. (2008), Methane production and bubble emissions from Arctic lakes: Isotopic implications for source pathways and ages, *Journal of Geophysical Research*, 113, doi: 10.1029/2007JG000569

- Wang, Y. J., et al. (2001), A high-resolution absolute-dated late Pleistocene monsoon record from Hulu Cave, China, *Science*, 294, 2345-2349
- Wang, X., et al. (2006), Interhemispheric anti-phasing of rainfall during the last glacial period, *Quaternary Science Reviews*, 25, 3391-3403
- Warneck, P. (1988), Bulk composition, physical structure and dynamics of the atmosphere, in *Chemistry of the Natural Atmosphere*, pp. 1-45, Academic Press, San Diego.
- Weaver, A.J., et al. (2003), Meltwater pulse 1A from Antarctica as a trigger of the Bølling-Allerød warm interval, *Science*, 299, 1709-1714
- Weitemeyer, K. A., and B. A. Buffett (2006), Accumulation and release of methane from clathrates below the Laurentide and Cordilleran ice sheets, *Global and Planetary Change*, 53, 176-187
- Westerling, A. L., et al. (2006), Warming and earlier spring increase western U.S. forest fire activity, *Science*, 313, 940-945, doi:10.1126/science.1128834.
- Whiticar, M. J. (1999), Carbon and hydrogen isotope systematics of bacterial formation and oxidation of methane, *Chemical Geology*, 161(1-3), 291-314, doi:10.1016/S0009-2541(99)00092-3.
- Whiticar, M. J., and H. Schaefer, (2007), Constraining past global tropospheric methane budgets with carbon and hydrogen isotope ratios in ice, *Philosophical Transactions of the Royal Society A*, 365, 1793-1828, doi: 10.1098/rsta.2007.2048.
- Wuebbles, D. J., and K. Hayhoe, (2002) Atmospheric methane and global change, *Earth-Science Reviews*, 57, 177-210.
- Xiong, X., et al. (2009), Methane plume over south Asia during the monsoon season: satellite observation and model simulation, *Atmospheric Chemistry and Physics*, 9, 783-794
- Yuan, D., et al. (2004), Timing, duration, and transitions of the Last Interglacial Asian Monsoon, *Science*, 304, 575-580.

## 7. Appendix

### 7.1. Age scale tie points

The age scale tie points for Pâkitsoq are listed in Tables 7.1.1 and 7.1.2. Values for comparison are as described in Section 2.2. Measurement uncertainty of the Pâkitsoq parameters are 0.005 ‰ for  $\delta^{15}\text{N}$ , 0.028 ‰ for  $\delta^{18}\text{O}_{\text{atm}}$ , and 20 ppbv for  $[\text{CH}_4]$ .

Table 7.1.1: Age tie points for the Allerød to Preboreal period for the 2001 sampling trench. Sampling points from the 2003 sampling season for the Preboreal period are indicated.  $\delta^{18}\text{O}_{\text{atm}}$  values measured for Pâkitsoq samples have relatively poor precision; thus each age tie point using  $\delta^{18}\text{O}_{\text{atm}}$  was determined by adding the  $\delta^{18}\text{O}_{\text{atm}}$  value plus /minus its standard deviation (SD) and then comparing those values. The 2001 sampling season was assigned an age scale, and this age scale was adjusted to any year-by-year changes to the ice stratigraphy (very small adjustments).

Pâkitsoq Trench Distance (m)	Climate proxy for age determination	Possible ages of tie point (ka BP)	Final age of tie point (ka BP)
0.69	$[\text{CH}_4]$	12.838	12.838
0.97	$\delta^{18}\text{O}_{\text{ice}}$	12.426	12.426
1.62	$\delta^{15}\text{N}$	11.928	11.928
	$\delta^{18}\text{O}_{\text{atm}}$	12.783 11.710(-SD) 12.710(+SD)	
1.74	$\delta^{18}\text{O}_{\text{ice}}$	11.938	11.938
1.92	$[\text{CH}_4]$	11.602	11.602
2.15	$\delta^{15}\text{N}$	11.570	11.570
	$\delta^{18}\text{O}_{\text{atm}}$	11.515(-SD) 12.510(+SD)	
2.18	$[\text{CH}_4]$	11.587	11.587
2.42	$\delta^{15}\text{N}$	11.468	11.468
	$\delta^{18}\text{O}_{\text{atm}}$	11.260(-SD)	
	$[\text{CH}_4]$	11.450(+SD) 11.464 11.490	
3.2	$\delta^{15}\text{N}$	11.339	11.339
	$\delta^{18}\text{O}_{\text{atm}}$	11.300(-SD) 11.500(+SD)	

(Continued on next page)

Påkitsoq Trench Distance (m)	Climate proxy for age determination	Possible ages of tie point (ka BP)	Final age of tie point (ka BP)
3.43	$\delta^{15}\text{N}$	11.311 11.154	11.311
	$\delta^{18}\text{O}_{\text{atm}}$	11.400(-SD) 11.690(+SD)	
3.68	$\delta^{15}\text{N}$	11.193 11.084	11.193
	$\delta^{18}\text{O}_{\text{atm}}$	11.295(-SD) 11.490(+SD)	
3.90 (2003)	$\delta^{15}\text{N}$	11.211	11.210
4.20 (2003)	$\delta^{15}\text{N}$	10.962	10.962
4.33	$\delta^{18}\text{O}_{\text{ice}}$	11.181	11.181

Table 7.1.2: Age tie points for the LGM to Allerød period for the 2003 to 2005 sampling trenches. Sampling points from the 2003 sampling season for the Preboreal period are indicated.  $\delta^{18}\text{O}_{\text{atm}}$  values are less unique in this time period, thus values are only used for approximate ages (denoted by significant figures). 2004 trench is denoted BAN with details in Schaefer et al., (2009). Schaefer et al. (2009) give full details of the fold structure of the Påkitsoq ice and the reader is referred there.

Påkitsoq Trench Distance (m)	Climate proxy	Possible ages of tie point (ka BP)	Final age of tie point (ka BP)
2004			
0.70	$\delta^{18}\text{O}_{\text{ice}}$	14.991	14.991
1.27	$\delta^{15}\text{N}$	14.760	14.760
1.33	[CH <sub>4</sub> ]	14.881	14.881
1.46	$\delta^{15}\text{N}$	14.584	14.584
1.61	[CH <sub>4</sub> ]	14.488	14.488
1.70	$\delta^{18}\text{O}_{\text{ice}}$	14.180	14.180
2.14	$\delta^{18}\text{O}_{\text{ice}}$	13.938	13.938
2003			
15.18	$\delta^{18}\text{O}_{\text{ice}}$	13.938	13.938
15.58	$\delta^{18}\text{O}_{\text{ice}}$	14.180	14.180
16.25	[CH <sub>4</sub> ]	14.488	14.488
16.38	$\delta^{18}\text{O}_{\text{ice}}$	14.991	14.991

(Continued on next page)

Påkitsoq Trench Distance (m)	Climate proxy	Possible ages of tie point (ka BP)	Final age of tie point (ka BP)
16.54	$\delta^{15}\text{N}$	14.760	14.760
16.59	$\delta^{18}\text{O}_{\text{atm}}$	~14.9	~14.9
16.70	[CH <sub>4</sub> ]	14.881	14.881
16.98	$\delta^{18}\text{O}_{\text{ice}}$	15.553	15.553
19.11	$\delta^{18}\text{O}_{\text{atm}}$	~20.9	~20.9
2005			
13.84	$\delta^{18}\text{O}_{\text{ice}}$	13.938	13.938
14.05	$\delta^{18}\text{O}_{\text{ice}}$	14.180	14.180
14.34	$\delta^{15}\text{N}$	14.584	14.584
14.70	[CH <sub>4</sub> ]	14.488	14.488
14.85	[CH <sub>4</sub> ]	14.881	14.881
14.85	$\delta^{15}\text{N}$	14.764	14.764
15.01	$\delta^{18}\text{O}_{\text{ice}}$	14.991	14.991
15.72	$\delta^{18}\text{O}_{\text{ice}}$	15.553	15.553

## 7.2. Box model parameters

### 7.2.1. 6-Box model description

The 6-box steady-state model contains three troposphere (t) and three stratosphere boxes (s) separated into Northern (n), Equatorial (e), and Southern (s) boxes. The latitudinal range of the Northern and Southern boxes is 90 to 30° and the Equatorial is 30 °N to 30 °S. The 6-box model schematic is presented in Figure 2.4.1. The 6-box model is similar to the 4-box model described in Section 2.4.1, and is applied during the same time periods. The change in mixing ratio,  $X$ , with respect to time for the Northern troposphere (tn) can be expressed as:

$$(7.2.1) \quad dX_{tn}/dt = Q_n - \lambda X_{tn} - k_{ne}^{TT}(X_{tn} - X_{te}) + k_{nn}^{ST}(X_{sn})$$

where the sources ( $Q_n$ ) are countered by the troposphere sinks ( $\lambda X_{tn}$ ), exchange with the Equatorial troposphere ( $k_{ne}^{TT}(X_{tn} - X_{te})$ ), and input from the stratosphere ( $k_{nn}^{ST}(X_{sn})$ ). The superscripts denote direction of exchange, i.e. ST is exchange from the stratosphere to troposphere. Subscript denote latitudinal boxes in exchange, i.e. ne is north-equatorial. The other boxes can be expressed similarly, with the exception of no sources in the

$$dX_{te}/dt = Q_e - \lambda X_{te} - k_{ne}^{TT}(X_{tn} - X_{te}) - k_{es}^{TT}(X_{ts} - X_{te}) - k_{se}^{TS}(X_{se})$$

stratosphere:

$$(7.2.2.)$$

$$(7.2.3.) \quad dX_{ts}/dt = Q_s - \lambda X_{ts} - k_{se}^{TT}(X_{ts} - X_{te}) + k_{ss}^{ST}(X_{ss})$$

$$(7.2.4.) \quad dX_{sn}/dt = -\lambda X_{sn} + k_{ne}^{SS}(X_{sn} - X_{se}) - k_{nn}^{ST}(X_{sn})$$

$$(7.2.5.) \quad dX_{se}/dt = -\lambda X_{se} - k_{ne}^{SS}(X_{se} - X_{sn}) - k_{es}^{SS}(X_{se} - X_{ss}) + k_{ee}^{TS}(X_{te})$$

$$(7.2.6.) \quad dX_{ss}/dt = -\lambda X_{ss} + k_{se}^{SS}(X_{ss} - X_{se}) - k_{ss}^{ST}(X_{ss})$$

where equation 7.2.2. and 7.2.3. are equatorial troposphere and south troposphere, respectively. Equations 7.2.4 – 7.2.6. are stratospheric north, equatorial, and south, in that order. The remainder of the 6-box model formulation was applied identically to that of the 4-box model. The air mass exchange rates are provided in Table 7.2.1.

Table 7.2.1: Air mass exchange rates between compartments of atmosphere 6-box model. These values were tuned from values found in Warneck, (1988) and Holton et al., (1997)

Exchange between boxes (k)	Air mass exchange rate (yr <sup>-1</sup> )
Within the troposphere	
North to Equatorial	2.41
Equatorial to North	1.2
Equatorial to South	1.22
South to Equatorial	2.4
Between troposphere and stratosphere	
North	3.1
South	3.1
Equatorial	0.28
Within the stratosphere	
Equatorial to North	0.26
Equatorial to South	0.2

## 7.2.2. 4-Box model parameters

Table 7.2.2: Air mass exchange rates between compartments of atmosphere 4-box model. These values were tuned from values found in Warneck, (1988)

Exchange between boxes (k)	Air mass exchange rate (yr <sup>-1</sup> )
Troposphere - Troposphere	0.9
Stratosphere - Stratosphere	0.28
Troposphere – Stratosphere	0.74
Stratosphere – Troposphere	3.43

Table 7.2.3: Source and sink distribution parameters for 4-box atmosphere methane model scenarios of 1990s

	Hemisphere Fractional Distribution	
	North Hemisphere	South Hemisphere
<b>Natural Sources</b>		
Tropical wetlands <sup>a</sup>	0.55	0.45
Boreal wetlands <sup>a</sup>	1	0
Aerobic plant methane (APM) <sup>b</sup>	0.8	0.2
Biomass burning <sup>c</sup>	0.65	0.35
Gas hydrates <sup>d</sup>	0.8	0.2
Ruminants <sup>e</sup>	0.7	0.3
Geologic <sup>f</sup>	0.83	0.17
Aquatic <sup>g</sup>	0.6	0.4
Termites <sup>h</sup>	0.6	0.4
<b>Anthropogenic Sources</b>		
Rice cultivation <sup>i</sup>	0.85	0.15
Landfills <sup>j</sup>	0.65	0.35
Natural gas <sup>k</sup>	0.85	0.15
Coal <sup>k</sup>	0.94	0.06

<sup>a</sup> Estimate drawn from Figure 5 in Lehner and Döll, 2004

<sup>b</sup> Based upon vegetation index maps averaged for Northern and Austral summers from NEO, 2009

<sup>c</sup> Based upon present day fire distribution derived from NEO, 2009. Averaged for Northern and Austral summers

<sup>d</sup> Average of Kvenvolden, 1993 and Rogner, 1996

<sup>e</sup> From table V in Johnson and Ward, 1996. Based only upon domestic ruminants.

<sup>f</sup> Distribution is based upon Figure 2 of Etiope and Klusman, 2002

<sup>g</sup> Distribution is from ocean productivity maps averaged from Northern and Austral summer (NEO, 2009)

<sup>h</sup> Distribution is based upon hemisphere proportion of land area (NEO, 2009) and Fraser et al., 1986

<sup>i</sup> Hemispheric distribution based upon world map of rice production (Mapsofworld, 2009)

<sup>j</sup> Landfills assumed to be represented by population density. Population density from NEO, 2009

<sup>k</sup> Hemispheric distribution is based upon tables in Rogner, 1996

Table 7.2.4: 4-Box model simulation parameters for all time periods. NH and SH denote Southern and Northern Hemispheres respectively.

Source	Time period	$\delta^{13}\text{CH}_4$ (‰ VPDB)	NH flux fraction	SH flux fraction	Flux ranges (Tg $\text{CH}_4\text{yr}^{-1}$ )	
					Lower	Upper
Tropical wetlands	PIH	-56.8	0.55	0.45	20	150
	PB	-57	0.5	0.5	20	200
	YD	-57.2	0.5	0.5	0	95
	BA	-57.4	0.5	0.5	10	130
	LGM	-58	0.5	0.5	20	130
Boreal wetlands	PIH	-63.4	1	0	0	50
	PB	-64.2	1	0	0	60
	YD	-64.4	1	0	0	60
	BA	-64.4	1	0	0	60
	LGM	-65.4	1	0	0	15
APM	PIH	-59.2	0.8	0.2	0	40
	PB	-59.4	0.7	0.3	0	60
	YD	-59.6	0.65	0.35	0	40
	BA	-59.6	0.65	0.35	0	40
	LGM	-59.8	0.6	0.4	0	40
Biomass burning	PIH	-25.6	0.65	0.35	5	50
	PB	-26	0.62	0.38	10	60

(Continued on next page)

Source	Time period	$\delta^{13}\text{CH}_4$ (‰ VPDB)	NH flux fraction	SH flux fraction	Flux ranges (Tg $\text{CH}_4\text{yr}^{-1}$ )	
					Lower	Upper
	YD	-26.2	0.62	0.38	20	80
	BA	-26.2	0.62	0.38	10	60
	LGM	-25.7	0.62	0.38	10	60
Gas hydrates	PIH	-62.5	0.85	0.15	0	65
	PB	-62.5	0.85	0.15	0	50
	YD	-62.5	0.85	0.15	10	60
	BA	-62.5	0.85	0.15	0	65
	LGM	-62.5	0.85	0.15	0	20
Ruminants	PIH	-56.8	0.75	0.25	3	50
	PB	-57.6	0.7	0.3	3	50
	YD	-57.8	0.65	0.35	0	50
	BA	-57.8	0.65	0.35	0	60
	LGM	-57.6	0.6	0.4	0	40
Geologic	PIH	-41.8	0.85	0.15	0	60
	PB	-41.8	0.65	0.35	0	60
	YD	-41.8	0.6	0.4	0	100
	BA	-41.8	0.65	0.35	0	100
	LGM	-41.8	0.6	0.4	0	80
Aquatic	PIH	-56.8	0.6	0.4	5	25
	PB	-56.8	0.55	0.45	5	25
	YD	-56.8	0.55	0.45	0	20
	BA	-56.8	0.55	0.45	0	20
	LGM	-56.8	0.55	0.45	0	15
Termites	PIH	-64.2	0.6	0.4	5	30
	PB	-64.8	0.55	0.45	5	25
	YD	-65	0.55	0.45	5	25
	BA	-65	0.55	0.45	5	20
	LGM	-65	0.55	0.45	5	20

### 7.2.3. 4-Box Model Algorithm

#### Main Driver Program for Matlab Monte Carlo Simulation: Main4MC.m

```

%October 24 2009
% Joe Melton

% This is the central driver program of the methane box model.

% Choose the kind of simulation by uncommenting the simulation to run
% then run Main.

clear; %prepare for this run

%Choose the simulation
timeperiod = 'LGM'; %Options: modern, PIH, PB, YD, Bolling, LGM
boxmodel = '4box'; %Options: 4box, 6box

%% Set parameters
j = 1; %initialize counter
k = 1;
n = 10001; %Number of successful simulations required
Tg2ppb = 0.35979; %Conversion used for Tg CH4 to ppbV
lim_con = 10; %Threshold for simulation acceptance for concentration
%measurements (ppbV)
lim_cIH = 15; %Threshold for interhemi conc grad.
lim_13C = 0.4; %Threshold for 13C simulation acceptance (per mil)
lim_i13IH = 0.4; %Threshold for 13C inter-hemi grad. (per mil)
lim_dD = 10; %Threshold for dD (per mil)
atm_mass = 5.0194e21; %Mass of atmosphere (g)
trop_mass = 4.129e21; %Mass of troposphere (g)
stra_mass = atm_mass - trop_mass - (0.01 * atm_mass); %mass of stratosphere (g)
M_air = 28.964; %molec. mass of air (g/mol)
M_CH4 = 16.042; %molec. mass of CH4 (g/mol)
RDstd = 0.00015575; %R std for deuterium (VSMOW)
R13std = 0.0112372; % R std value for 13C (VPDB)
max_lam = 13; %longest CH4 lifetime allowed
min_lam = 3.5; %shortest

% Choose number of variables to store at end.

src_num = 16; %Number of stored variables from MC simulation
% Create array to dump variables
sim_array = zeros(src_num,n);

% The sources are numbered as follows:
% 1. tropical wetlands
% 2. boreal wetlands
% 3. Aerobic plant methane
% 4. Biomass burning
% 5. Gas hydrates
% 6. Ruminants
% 7. Geologic
% 8. Ocean

```

```

% 9. Termites

% 10. Rice Cultivation
% 11. Landfills
% 12. Gas
% 13. Coal

% 14. Atmospheric lifetime (yrs)

%% Select time period's boundaries

      LGM %calls the constants in file LGM.m
      MC_LGM4 = zeros(src_num,n);
      LGM_fos4 = zeros(1,n);

%% Read in isotopic ratios (REQ)
isotopes

%% Read in the exchange rates

      ktt = 0.9; %exchange rate for tropo-tropo (yr-1)
      kss = 0.28; %exchange rate for strato-strato (yr-1)
      kts = 0.74; %exchange tropo to strato (yr-1) 0.74
      kst = 5.2*0.66; %exchange strato to tropo (yr-1)
      %there is about 5.2 times the mass in the tropo as
      %the strato

%% Describe the sinks
%Values are originally in epsilon (delta_reactant - delta_product)

% Convert to alpha values
%epsilon / 1000 + 1 = alpha

a13_tOH = d13_tOH / 1000 + 1;
adD_tOH = dD_tOH / 1000 + 1;

a13_strat = d13_strat / 1000 + 1;
adD_strat = dD_strat / 1000 + 1;

a13_soil = d13_soil / 1000 + 1;
adD_soil = dD_soil / 1000 + 1;

a13_Cl = d13_Cl / 1000 + 1;
adD_Cl = dD_Cl / 1000 + 1;

%% Fractionation (alpha) weighted by source contribution
%set equal between hemispheres
      alph13t_NH = (tropOH_NH * a13_tOH + soil_NH * a13_soil + mbICL_NH * a13_Cl) / (tropOH_NH
+ soil_NH + mbICL_NH);
      alph13t_SH = (tropOH_SH * a13_tOH + soil_SH * a13_soil + mbICL_SH * a13_Cl) / (tropOH_SH +
soil_SH + mbICL_SH);

      alphdDt_NH = (tropOH_NH * adD_tOH + soil_NH * adD_soil + mbICL_NH * adD_Cl) /
(tropOH_NH + soil_NH + mbICL_NH);
      alphdDt_SH = (tropOH_SH * adD_tOH + soil_SH * adD_soil + mbICL_SH * adD_Cl) / (tropOH_SH
+ soil_SH + mbICL_SH);

```

```

% stratosphere
alph13s = a13_strat;
alphdDs = aD_strat;

%% Start loop for MC simulations

while (j <= n) % Perform until 'n' acceptable realizations

    %% Read in the source/sink strengths and isotope values (REQ)
    sources4_MC

    %% Run the box model calculation

    CH4_4_boxMC

    %% Write the variables to the array
    if strcmp(valid,'true')
        sim_array(1,j) = trop_wet;
        sim_array(2,j) = bor_wet;
        sim_array(3,j) = APM;
        sim_array(4,j) = bio_burn;
        sim_array(5,j) = mar_gasH;
        sim_array(6,j) = ruminant;
        sim_array(7,j) = geo;
        sim_array(8,j) = ocean;
        sim_array(9,j) = termite;
        sim_array(10,j) = rice;
        sim_array(11,j) = landfill;
        sim_array(12,j) = gas;
        sim_array(13,j) = coal;
        sim_array(14,j) = lifeT;
        sim_array(15,j) = S_north;
        sim_array(16,j) = S_south;

        % Since validity passes, keep the simulation and move on to the next
        % one.

        j = j + 1;

        if ((j/100)==floor(j/100))
            j
        end

    end
    % validity fail so retry with new scenario
end

% Transfer results out of temporary array and determine amount of
% fossil carbon

MC_LGM4 = sim_array;
LGM_fos4 = sim_array(7,:) + sim_array(5,:);

%% Sort out results and create normalized probability distribution
% functions

```

```
bin = 30; %set number of bins for histograms  
histogram
```

```
save 4box_LGM_GH1.mat
```

```
exit
```

```
>> LGM.m
```

```
% LGM source and sink configuration
```

```
% tropical wetlands
```

```
min_tw = 20;  
max_tw = 130;  
NH_tw = 0.5;  
SH_tw = 0.5;  
d13_tw = -58;  
dD_tw = -315;
```

```
% boreal wetlands
```

```
min_bw = 0;  
max_bw = 15;  
NH_bw = 1.0;  
SH_bw = 0.0;  
d13_bw = -65.4;  
dD_bw = -360;
```

```
% Aerobic plant methane
```

```
min_AP = 0;  
max_AP = 40;  
NH_AP = 0.6;  
SH_AP = 0.4;  
d13_AP = -59.8;  
dD_AP = -348;
```

```
% Biomass burning
```

```
min_bb = 10;  
max_bb = 60;  
NH_bb = 0.62;  
SH_bb = 0.38;  
d13_bb = -25.7;  
dD_bb = -225;
```

```
% Gas hydrates
```

```
min_gasH = 0;  
max_gasH = 20;
```

```
NH_gasH = 0.85;  
SH_gasH = 0.15;  
d13_gasH = -62.5;  
dD_gasH = -190;
```

```
% Ruminants
```

```
min_rum = 0;
max_rum = 40;
NH_rum = 0.6;
SH_rum = 0.4;
d13_rum = -57.6;
dD_rum = -330;
```

```
% Geologic
min_geo = 0;
max_geo = 80;
NH_geo = 0.6;
SH_geo = 0.4;
d13_geo = -41.8;
dD_geo = -200;
```

```
% Ocean
min_oc = 0;
max_oc = 15;
NH_oc = 0.55;
SH_oc = 0.45;
d13_oc = -56.8;
dD_oc = -267.1;
```

```
% Termites
min_term = 5;
max_term = 20;
NH_term = 0.55;
SH_term = 0.45;
d13_term = -65;
dD_term = -390;
```

```
%% Anthropogenic =====
```

```
%NO ANTRHO in LGM: DUMMY VALUES
```

```
% Rice Cultivation
```

```
min_rice = 0;
max_rice = 0;
NH_rice = 1;
SH_rice = 1;
d13_rice = -63;
dD_rice = -320;
```

```
% Landfills
```

```
min_land = 0;
max_land = 0;
NH_land = 1;
SH_land = 1;
d13_land = -50;
dD_land = -310;
```

```
% Gas
```

```
min_gas = 0;
max_gas = 0;
NH_gas = 1;
SH_gas = 1;
d13_gas = -43;
dD_gas = -185;
```

```
% Coal
```

```
min_coal = 0;
```

```

max_coal = 0;
NH_coal = 1;
SH_coal = 0;
d13_coal = -36;
dD_coal = -140;

%%Sinks =====
tropOH_NH = 0.879;%
tropOH_SH = 0.879;%
soil_NH = 0.052;%
soil_SH = 0.052;
% No partitioning here
mblCL_NH = 0;
mblCL_SH = 0;

strat = 0.062;

%% Boundary Conditions =====

NH_d13C_bound = -43.46; % +/- 0.41, n = 2

SH_d13C_bound = -42.91; % +/- 0.47 (n = 7) from 16.7 - 20.3

c13grad_bound = NH_d13C_bound - SH_d13C_bound;

NH_dD_bound = -80.23; % +/- 5.71 (n = 4)

conc_NHbound = 392; %Dallenbach 2000, 16.7 - 20.3ka

conc_grad_bound = -3; %Dallenbach 2000, 16.7 - 20.3ka (+/- 4)

>> Isotopes.m

%% Put sources in isotope-Tans notation
%(a la Tans 1997)

% C13
%delta = (Rsample / Rstd - 1) * 1000
%Rstd (VPDB) = 0.0112372
%Rsample = delta / 1000 + 1 * Rstd

R13_tw = (d13_tw / 1000 + 1) * R13std;
R13_bw = (d13_bw / 1000 + 1) * R13std;
R13_AP = (d13_AP / 1000 + 1) * R13std;
R13_bb = (d13_bb / 1000 + 1) * R13std;
R13_gasH = (d13_gasH / 1000 + 1) * R13std;
R13_rum = (d13_rum / 1000 + 1) * R13std;
R13_geo = (d13_geo / 1000 + 1) * R13std;
R13_oc = (d13_oc / 1000 + 1) * R13std;
R13_term = (d13_term / 1000 + 1) * R13std;
R13_rice = (d13_rice / 1000 + 1) * R13std;
R13_land = (d13_land / 1000 + 1) * R13std;
R13_gas = (d13_gas / 1000 + 1) * R13std;
R13_coal = (d13_coal / 1000 + 1) * R13std;

```

%Convert the Rsample from 13C/12C to 13C/(12C + 13C)

%Rsample = 13C/12C

%13C = Rsample \* 12C

%12C + 13C = (Rsample \* 12C) + 12C

%= 12C \* (Rsample + 1)

% 13C / (12C+13C) = Rsample / (Rsample + 1)

Rt13\_tw = R13\_tw / (R13\_tw + 1);

Rt13\_bw = R13\_bw / (R13\_bw + 1);

Rt13\_AP = R13\_AP / (R13\_AP + 1);

Rt13\_bb = R13\_bb / (R13\_bb + 1);

Rt13\_gasH = R13\_gasH / (R13\_gasH + 1);

Rt13\_rum = R13\_rum / (R13\_rum + 1);

Rt13\_geo = R13\_geo / (R13\_geo + 1);

Rt13\_oc = R13\_oc / (R13\_oc + 1);

Rt13\_term = R13\_term / (R13\_term + 1);

Rt13\_rice = R13\_rice / (R13\_rice + 1);

Rt13\_land = R13\_land / (R13\_land + 1);

Rt13\_gas = R13\_gas / (R13\_gas + 1);

Rt13\_coal = R13\_coal / (R13\_coal + 1);

%dD

RD\_tw = (dD\_tw / 1000 + 1) \* RDstd;

RD\_bw = (dD\_bw / 1000 + 1) \* RDstd;

RD\_AP = (dD\_AP / 1000 + 1) \* RDstd;

RD\_bb = (dD\_bb / 1000 + 1) \* RDstd;

RD\_gasH = (dD\_gasH / 1000 + 1) \* RDstd;

RD\_rum = (dD\_rum / 1000 + 1) \* RDstd;

RD\_geo = (dD\_geo / 1000 + 1) \* RDstd;

RD\_oc = (dD\_oc / 1000 + 1) \* RDstd;

RD\_term = (dD\_term / 1000 + 1) \* RDstd;

RD\_rice = (dD\_rice / 1000 + 1) \* RDstd;

RD\_land = (dD\_land / 1000 + 1) \* RDstd;

RD\_gas = (dD\_gas / 1000 + 1) \* RDstd;

RD\_coal = (dD\_coal / 1000 + 1) \* RDstd;

%Convert the Rsample from D/H to D/(H + D)

RtD\_tw = RD\_tw / (RD\_tw + 1);

RtD\_bw = RD\_bw / (RD\_bw + 1);

RtD\_AP = RD\_AP / (RD\_AP + 1);

RtD\_bb = RD\_bb / (RD\_bb + 1);

RtD\_gasH = RD\_gasH / (RD\_gasH + 1);

RtD\_rum = RD\_rum / (RD\_rum + 1);

RtD\_geo = RD\_geo / (RD\_geo + 1);

RtD\_oc = RD\_oc / (RD\_oc + 1);

RtD\_term = RD\_term / (RD\_term + 1);

RtD\_rice = RD\_rice / (RD\_rice + 1);

RtD\_land = RD\_land / (RD\_land + 1);

RtD\_gas = RD\_gas / (RD\_gas + 1);

RtD\_coal = RD\_coal / (RD\_coal + 1);

%-----

%% Describe the sinks

%Values are in epsilon (delta\_reactant - delta\_product)

d13\_tOH = -3.9; %Saueressig et al. 2001 -3.9

dD\_tOH = -231;

```

d13_strat = -12;
dD_strat = -160;

d13_soil = -22;
dD_soil = -80;

d13_Cl = -66;
dD_Cl = -100; %DUMMY VALUE! No known value available.

>> sources4_MC.m

% Describes the sources and ranges.
% This calls the individual scenario files and creates the general
% version that is fed into the 6 or 4 box model monte carlo

%% Find value for simulation if MC run

% Generate a random uniform distribution
% r = a + rand(1) * (b-a)
% a : minimum
% b : maximum

trop_wet = min_tw + rand(1) * (max_tw - min_tw); %
bor_wet = min_bw + rand(1) * (max_bw - min_bw);
APM = min_AP + rand(1) * (max_AP - min_AP);
bio_burn = min_bb + rand(1) * (max_bb - min_bb);
mar_gasH = min_gasH + rand(1) * (max_gasH - min_gasH);
ruminant = min_rum + rand(1) * (max_rum - min_rum);
geo = min_geo + rand(1) * (max_geo - min_geo);
ocean = min_oc + rand(1) * (max_oc - min_oc);
termite = min_term + rand(1) * (max_term - min_term);
switch timeperiod
case {'modern','PIH'} %PIH has no gas allowed.
    rice = min_rice + rand(1) * (max_rice - min_rice);
    landfill = min_land + rand(1) * (max_land - min_land);
    gas = min_gas + rand(1) * (max_gas - min_gas);
    coal = min_coal + rand(1) * (max_coal - min_coal);
case {'PB', 'YD','Bolling','LGM'}
    rice = 0;
    landfill = 0;
    gas = 0;
    coal = 0;
end

%% Find the source strength weighted by isotopic value in each hemisphere

%% 4 Box
%Carbon-13 source in Tans-notation
S_S13 = trop_wet * Rt13_tw * SH_tw + bor_wet * Rt13_bw * SH_bw + APM...
    * Rt13_AP * SH_AP + bio_burn * Rt13_bb * SH_bb...
    + mar_gasH * Rt13_gasH * SH_gasH + ruminant * Rt13_rum * SH_rum...
    + geo * Rt13_geo * SH_geo + ocean * Rt13_oc * SH_oc...
    + termite * Rt13_term * SH_term + rice * Rt13_rice * SH_rice...
    + landfill * Rt13_land * SH_land + gas * Rt13_gas * SH_gas...
    + coal * Rt13_coal * SH_coal;

```

%Deuterium sources in Tans-notation

```
S_SD = trop_wet * RtD_tw * SH_tw + bor_wet * RtD_bw * SH_bw + APM...
      * RtD_AP * SH_AP + bio_burn * RtD_bb * SH_bb...
      + mar_gasH * RtD_gasH * SH_gasH + ruminant * RtD_rum * SH_rum...
      + geo * RtD_geo * SH_geo + ocean * RtD_oc * SH_oc...
      + termite * RtD_term * SH_term + rice * RtD_rice * SH_rice...
      + landfill * RtD_land * SH_land + gas * RtD_gas * SH_gas...
      + coal * RtD_coal * SH_coal;
```

%Source strengths in Tg CH4/yr

```
S_south = trop_wet * SH_tw + bor_wet * SH_bw + APM * SH_AP + bio_burn * SH_bb...
          + mar_gasH * SH_gasH + ruminant * SH_rum + geo * SH_geo + ocean * SH_oc...
          + termite * SH_term + rice * SH_rice + landfill * SH_land + gas * SH_gas...
          + coal * SH_coal;
```

```
S_ND = trop_wet * RtD_tw * NH_tw + bor_wet * RtD_bw * NH_bw + APM...
       * RtD_AP * NH_AP + bio_burn * RtD_bb * NH_bb...
       + mar_gasH * RtD_gasH * NH_gasH + ruminant * RtD_rum * NH_rum...
       + geo * RtD_geo * NH_geo + ocean * RtD_oc * NH_oc...
       + termite * RtD_term * NH_term + rice * RtD_rice * NH_rice...
       + landfill * RtD_land * NH_land + gas * RtD_gas * NH_gas...
       + coal * RtD_coal * NH_coal;
```

```
S_N13 = trop_wet * Rt13_tw * NH_tw + bor_wet * Rt13_bw * NH_bw + APM...
         * Rt13_AP * NH_AP + bio_burn * Rt13_bb * NH_bb...
         + mar_gasH * Rt13_gasH * NH_gasH + ruminant * Rt13_rum * NH_rum...
         + geo * Rt13_geo * NH_geo + ocean * Rt13_oc * NH_oc...
         + termite * Rt13_term * NH_term + rice * Rt13_rice * NH_rice...
         + landfill * Rt13_land * NH_land + gas * Rt13_gas * NH_gas...
         + coal * Rt13_coal * NH_coal;
```

```
S_north = trop_wet * NH_tw + bor_wet * NH_bw + APM * NH_AP + bio_burn * NH_bb...
           + mar_gasH * NH_gasH + ruminant * NH_rum + geo * NH_geo + ocean * NH_oc...
           + termite * NH_term + rice * NH_rice + landfill * NH_land + gas * NH_gas...
           + coal * NH_coal;
```

%% Loss rate (yr-1)

```
lam = 1 / (min_lam + rand(1) * (max_lam - min_lam));
```

>> CH4\_4\_boxMC.m

% 4-Box model of atmospheric methane isotope dynamics

%This model has 4 boxes, troposphere and stratosphere for both  
%hemispheres. Fluxes per year are parameterized.

=====

%% Concentration

```
B1 = lam + kts + ktt;
```

```
B2 = ktt;
```

```
B3 = kst;
```

```
B4 = lam + kts + ktt;
```

```
B5 = ktt;
```

```
B6 = kst;
```

```
B7 = lam + kst + kss;
```

```

B8 = kss;
B9 = kts;
B10 = lam + kst + kss;
B11 = kss;
B12 = kts;

K1 = ((B8/B7)*(B12/B10))/(1 - (B8/B7)*(B11/B10));
K2 = (B9/B7)/(1 - (B8/B7)*(B11/B10));
K3 = ((B11/B10)*(B8/B7)*(B12/B10))/(1 - (B8/B7)*(B11/B10)) + (B12/B10);
K4 = ((B9/B7)*(B11/B10))/(1 - (B8/B7)*(B11/B10));

%So then per box the Tg CH4 is:
c_tn = ((B2 + B3*K1)*S_south - (B6*K3-B4)*S_north) / ((B3*K2-B1)*(B6*K3-B4)-
(B5+B6*K4)*(B2+B3*K1));
c_ts = ((B5+B6*K4)*S_north - (B3*K2-B1)*S_south) / ((B3*K2-B1)*(B6*K3-B4)-
(B5+B6*K4)*(B2+B3*K1));
c_sn = K1*c_ts + K2*c_tn;
c_ss = K3*c_ts + K4*c_tn;

c_tot = c_tn + c_ts + c_sn + c_ss;

% Life time of CH4 in atm. (yrs)
lifeT = c_tot / (S_south + S_north);

% Put into ppb from Tg CH4
ppb_tn = c_tn * 1e12 / M_CH4 / (trop_mass * 0.5 / M_air) * 1e9;
ppb_ts = c_ts * 1e12 / M_CH4 / (trop_mass * 0.5 / M_air) * 1e9;

ppb_tot = c_tot * 1e12 / M_CH4 / (atm_mass / M_air) * 1e9;

% Find the inter-hemi conc grad.
ppb_IH = ppb_tn - ppb_ts;

%Increase the ppb_tn by 7% of the IH conc gradient (al a Brook et
%al. This is due to the N.H. being not well mixed.
inc_Greenland = ppb_IH * 0.07;
ppb_tn = ppb_tn + inc_Greenland;
ppb_IH = ppb_tn - ppb_ts;

%% Perform validity check of the output
if ((abs(ppb_IH - conc_grad_bound) > lim_cIH)) % inter-hemi conc.
    valid = 'fail';
    return
end
if ((abs(ppb_tn - conc_NHbound) > lim_con)) %N.H. conc.
    valid = 'fail';
    return
end

%% Carbon-13
B1 = alph13t_NH * lam + kts + ktt;
B2 = ktt;
B3 = kst;
B4 = alph13t_SH * lam + kts + ktt;
B5 = ktt;
B6 = kst;

```

```

B7 = alph13s * lam + kst + kss;
B8 = kss;
B9 = kts;
B10 = alph13s * lam + kst + kss;
B11 = kss;
B12 = kts;

K1 = ((B8/B7)*(B12/B10))/(1 - (B8/B7)*(B11/B10));
K2 = (B9/B7)/(1 - (B8/B7)*(B11/B10));
K3 = ((B11/B10)*(B8/B7)*(B12/B10))/(1 - (B8/B7)*(B11/B10)) + (B12/B10);
K4 = ((B9/B7)*(B11/B10))/(1 - (B8/B7)*(B11/B10));

%So then conc_iso values are:
c13_tn = ((B2 + B3*K1)*S_S13 - (B6*K3-B4)*S_N13) / ((B3*K2-B1)*(B6*K3-B4)-
(B5+B6*K4)*(B2+B3*K1));
c13_ts = ((B5+B6*K4)*S_N13 - (B3*K2-B1)*S_S13) / ((B3*K2-B1)*(B6*K3-B4)-
(B5+B6*K4)*(B2+B3*K1));
c13_sn = K1*c13_ts + K2*c13_tn;
c13_ss = K3*c13_ts + K4*c13_tn;
c13_tot = c13_tn + c13_ts + c13_sn + c13_ss;

% Now get out the d13C isotopic ratios;
ci13_tn = ((c13_tn/(c_tn - c13_tn) / R13std) - 1) * 1000;
ci13_ts = ((c13_ts/(c_ts - c13_ts) / R13std) - 1) * 1000;
%ci13_sn = ((c13_sn/(c_sn - c13_sn) / R13std) - 1) * 1000;
%ci13_ss = ((c13_ss/(c_ss - c13_ss) / R13std) - 1) * 1000;

ci13IH = ci13_tn - ci13_ts;
ci13_tot = ((c13_tot/(c_tot - c13_tot) / R13std) - 1) * 1000;

% Validity check of the outcome
if ((abs(ci13_tn - NH_d13C_bound) > lim_13C)) %N.H. d13C
    valid = 'fail';
    return
end
if ((abs(ci13_ts - SH_d13C_bound) > lim_13C)) %S.H. d13C
    valid = 'fail';
    return
end

%% Deuterium
B1 = alphdDt_NH * lam + kts + ktt;
B2 = ktt;
B3 = kst;
B4 = alphdDt_SH * lam + kts + ktt;
B5 = ktt;
B6 = kst;
B7 = alphdDs * lam + kst + kss;
B8 = kss;
B9 = kts;
B10 = alphdDs * lam + kst + kss;
B11 = kss;
B12 = kts;

K1 = ((B8/B7)*(B12/B10))/(1 - (B8/B7)*(B11/B10));
K2 = (B9/B7)/(1 - (B8/B7)*(B11/B10));

```

```

K3 = ((B11/B10)*(B8/B7)*(B12/B10))/(1 - (B8/B7)*(B11/B10)) + (B12/B10);
K4 = ((B9/B7)*(B11/B10))/(1 - (B8/B7)*(B11/B10));

```

```

%So then the conc_iso value is:

```

```

cdD_tn = ((B2 + B3*K1)*S_SD - (B6*K3-B4)*S_ND) / ((B3*K2-B1)*(B6*K3-B4)-
(B5+B6*K4)*(B2+B3*K1));
cdD_ts = ((B5+B6*K4)*S_ND - (B3*K2-B1)*S_SD) / ((B3*K2-B1)*(B6*K3-B4)-
(B5+B6*K4)*(B2+B3*K1));
cdD_sn = K1*cdD_ts + K2*cdD_tn;
cdD_ss = K3*cdD_ts + K4*cdD_tn;
cdD_tot = cdD_tn + cdD_ts + cdD_sn + cdD_ss;

```

```

% Now get out the dD isotopic ratios

```

```

cidD_tn = ((cdD_tn/(c_tn - cdD_tn) / RDstd) - 1) * 1000;
cidD_ts = ((cdD_ts/(c_ts - cdD_ts) / RDstd) - 1) * 1000;
%cidD_sn = ((cdD_sn/(c_tn - cdD_sn) / RDstd) - 1) * 1000;
%cidD_ss = ((cdD_ss/(c_ts - cdD_ss) / RDstd) - 1) * 1000;

```

```

cdDIH = cidD_tn - cidD_ts;
cidD_tot = ((cdD_tot/(c_tot - cdD_tot) / RDstd) - 1) * 1000;

```

```

% Validity check

```

```

switch timeperiod

```

```

    case {'modern', 'PIH'}

```

```

        if (abs(cidD_tn - NH_dD_bound) > lim_dD)      %N.H. dD
            valid = 'fail';

```

```

        return

```

```

        % For PIH and Modern this additional constraint can be
        % invoked

```

```

    end

```

```

    if (abs(cidD_ts - SH_dD_bound) > lim_dD)      %S.H. dD
        valid = 'fail';

```

```

    return

```

```

    else

```

```

        valid = 'true';

```

```

    end

```

```

    case {'PB','YD','Bolling','LGM'}

```

```

        if (abs(cidD_tn - NH_dD_bound) > lim_dD)      %N.H. dD
            valid = 'fail';

```

```

        return

```

```

    else

```

```

        valid = 'true';

```

```

    end

```

```

end

```

### 7.3. Ice core $\delta^{13}\text{CH}_4$ ratio measurement data

Table 7.3.1:  $\delta^{13}\text{CH}_4$  measurement values for samples from GISP2 core #139. Excluded values are in curved brackets.

Sample Number	Sample Mass (g)	$m/z$ 44 signal (mV)	$\text{CH}_4$ concentration (ppbv)	$\delta^{13}\text{CH}_4$ value (‰ VPDB)
1A	158.19	1109	728	-49.40
2A	185.33	1302	677	-49.87
3A	140.32	1087	762	-48.70
4A	141.65	1030	699	-48.39
5A	160.15	969	(576*)	(-44.86)
6A	125.17	1068	(901*)	(-45.00)
7A	146.81	1024	650	-48.97

\*Values are excluded due to unsuitability of highly fractured ice (see Section 3.1)

Table 7.3.2: Complete Pákitsoq CF-IRMS measurement results. Methane concentration is derived from CF-IRMS. Trench distance is from arbitrary reference location that is invariant across sampling seasons. GISP2 methane concentration from contemporaneous air to Pákitsoq samples is linearly interpolation from Brook et al. (2000). Values excluded due to contamination (as outlined in Section 3.2) are in curved brackets.

Sampling Season	Trench Distance (m)	Air age (kyr BP)	GISP2 $^{\text{y}}$ [ $\text{CH}_4$ ] (ppbv)	Sample Mass (g)	$m/z$ 44 signal (mV)	$\text{CH}_4$ concentration (ppbv)	$\delta^{13}\text{CH}_4$ value (‰ VPDB)
YD-Preboreal							
2003	2.65	11.430	713	79.7	557	840	-45.73
				96.5	696	899	-45.41
	2.95	11.350	748	106.5	681	795	-45.25
				75.5	524	(910)	(-45.48)
				211.6	1415	(856)	(-46.14)
	3.14	11.332	743	195.4	1259	(873)	(-46.95)
				135.1	892	(920)	(-43.85)
	3.52	11.278	694	66.4	463	(871)	(-44.73)
	3.57	11.270	692	196.9	1235	(832)	(-46.53)
	4.08	11.198	680				

(Continued on next page)

Sampling Season	Trench Distance (m)	Air age (kyr BP)	GISP2 <sup>‡</sup> [CH <sub>4</sub> ] (ppbv)	Sample Mass (g)	<i>m/z</i> 44 signal (mV)	CH <sub>4</sub> concentration (ppbv)	δ <sup>13</sup> CH <sub>4</sub> value (‰ VPDB)
2004	4.58	11.091	742	155.6	966	830	-45.07
				170.9	1193	845	-46.37
	4.99	11.004	739	48.4	(280*)	682	(-44.59)
				88.1	559	763	-45.32
	5.03	10.996	738	96.1	622	864	-46.13
				104.8	701	866	-45.92
	2.07	11.586	517	165.0	650	449	-46.24
				114.0	473	475	-45.47
	2.12	11.572	554	150.0	621	466	-46.13
				188.0	779	527	-46.53
	2.17	11.559	590	113.0	-- <sup>§</sup>	--	--
				135.0	542	429	-46.70
	2.21	11.527	605	172.8	2453	(2321)	(-45.88)
				179.0	765	548	-47.27
	2.21	11.527	605	116.0	514	530	-46.37
				174.4	1440	(709)	(-47.44)
	2.30	11.483	639	169.0	771	543	-46.93
				169.0	871	636	-46.66
	2.40	11.475	662	201.0	1133	669	-45.84
				145.0	829	693	-45.55
	2.40	11.475	662	139.0	941	648	-46.38
				179.0	836	623	-46.76
	2.46	11.465	690	127.5	1366	(918)	(-45.99)
				170.0	902	691	-46.31
2.46	11.465	690	137.0	(264*)	(286)	(-45.52)	
			124.0	654	609	-46.43	
2.52	11.447	731	142.5	853	690	-45.52	
			156.8	764	660	-46.10	
2.52	11.447	731	128.0	653	632	-46.26	
			143.0	793	726	-46.49	

(Continued on next page)

Sampling Season	Trench Distance (m)	Air age (kyr BP)	GISP2 <sup>‡</sup> [CH <sub>4</sub> ] (ppbv)	Sample Mass (g)	<i>m/z</i> 44 signal (mV)	CH <sub>4</sub> concentration (ppbv)	δ <sup>13</sup> CH <sub>4</sub> value (‰ VPDB)
	2.57	11.433	692	134.0	762	778	-46.59
				179.8	1200	620	-46.40
				121.0	651	674	-46.27
Allerød – Younger Dryas							
2005	0.92	12.551	489	136.4	1183	(784)	(-45.64)
				137.0	760	(651)	(-45.15)
				114.6	661	(739)	(-44.60)
				198.2	1775	(776)	(-43.93)
	0.97	12.450	484	129.6	1350	(952)	(-44.20)
				143.0	984	(889)	(-43.96)
				127.5	838	(631)	(-43.62)
				129.2	1255	(925)	(-45.34)
				137.0	748	(721)	(-45.24)
	1.03	12.398	491	148.7	2498	(1656)	(-45.49)
				193.8	1171	492	-46.19
				146.5	768	563	-45.56
	1.09	12.350	494	138.5	679	459	-45.68
				160.1	879	(656)	(-47.00)
				131.8	1100	(707)	(-45.59)
				136.0	566	429	-46.73
	1.15	12.302	497	128.6	716	548	-47.01
				138.3	781	(681)	(-45.25)
				194.9	1144	(751)	(-46.37)
				140.8	920	(725)	(-46.33)
	1.21	12.254	499	139.0	1101	(670)	(-46.68)
				94.8	620	(844)	(-46.36)
				235.9	1041	568	-47.07
				125.0	616	546	-47.04
				120.4	1060	(890)	(-46.75)
	1.29	12.191	503	118.5	810	(654)	(-47.69)

(Continued on next page)

Sampling Season	Trench Distance (m)	Air age (kyr BP)	GISP2 <sup>‡</sup> [CH <sub>4</sub> ] (ppbv)	Sample Mass (g)	<i>m/z</i> 44 signal (mV)	CH <sub>4</sub> concentration (ppbv)	δ <sup>13</sup> CH <sub>4</sub> value (‰ VPDB)
				132.3	754	(744)	(-46.88)
				160.2	1219	(651)	(-46.83)
				169.1	740	(713)	(-46.76)
				211.0	1190	(742)	(-47.23)
	1.36	12.139	506	116.8	811	(569)	(-46.62)
				162.9	871	(704)	(-45.27)
				144.7	833	499	-45.88
				140.0	556	415	-45.80
				133.8	642	456	-45.08
				115.7	572	428	-44.48
	1.41	12.099	508	259.0	1256	452	-45.72
				111.0	535	542	-44.83
				117.3	745	(830)	(-44.33)
				255.6	1931	(657)	(-46.05)
2003	0.16	13.618	668	158.1	1186	741	-47.83
	0.42	13.235	685	118.4	1115	(1259)	(-41.79)
				187.6	2095	(1571)	(-42.65)
				98.8	1385	(1877)	(-44.89)
	0.69	12.838	704	200.9	1463	722	-48.55
				171.7	1174	713	-48.24
	0.91	12.514	476	204.2	1170	543	-45.88
	0.99	12.430	487	197.6	1255	(843)	(-49.74)
				189.2	1810	(830)	(-48.94)
	1.05	12.382	493	134.5	736	451	-47.00
				106.3	602	493	-47.80
				112.3	728	(878)	(-48.34)
	1.11	12.334	495	215.1	1252	524	-47.26
	1.14	12.310	496	113.8	636	518	-46.60
				97.7	608	601	-45.86
	1.19	12.270	498	168.7	1566	(1221)	(-44.51)

(Continued on next page)

Sampling Season	Trench Distance (m)	Air age (kyr BP)	GISP2 <sup>‡</sup> [CH <sub>4</sub> ] (ppbv)	Sample Mass (g)	<i>m/z</i> 44 signal (mV)	CH <sub>4</sub> concentration (ppbv)	δ <sup>13</sup> CH <sub>4</sub> value (‰ VPDB)
				218.5	1587	(976)	(-45.70)
	1.23	12.238	500	137.7	1815	(1802)	(-42.18)
	1.29	12.191	503	202.8	1182	517	-46.17
				76.4	422	485	-44.34
	1.44	11.752	508	115.7	603	428	-44.95
				102.8	639	630	-44.95
<b>Oldest Dryas - Bølling</b>							
2004	-0.07	15.74	486	194.3	2412	(1224)	(-44.87)
	0.13	15.66	477	166.4	722	412	-42.78
				192.0	1296	577	-45.17
	0.21	15.63	475	162.8	1384	(729)	(-47.46)
	0.33	15.58	458	194.2	2493	(1265)	(-45.49)
				178.4	742	398	-43.98
	0.43	15.300	458	112.2	623	538	-44.49
				178.3	847	(637)	(-42.82)
	0.54	15.060	467	201.1	820	495	-45.31
				121.5	1602	(1300)	(-46.93)
	0.6	15.030	475	143.5	758	(738)	(-42.94)
				116.4	561	607	-46.27
	0.66	15.007	473	163.7	851	513	-45.24
				157.5	873	(778)	(-44.17)
	0.75	14.972	472	192.5	974	578	-45.37
				139.6	872	(838)	(-43.30)
	0.81	14.948	495	132.9	774	(814)	(-44.81)
				143.1	887	(844)	(-44.09)
	0.93	14.900	523	193.2	782	545	-46.06
				167.7	938	(788)	(-44.05)
2005	14.98	14.900	466	159.6	619	561	-44.97
				172.7	679	454	-44.97
	14.81	14.760	458	154.1	623	553	-47.11

(Continued on next page)

Sampling Season	Trench Distance (m)	Air age (kyr BP)	GISP2 <sup>‡</sup> [CH <sub>4</sub> ] (ppbv)	Sample Mass (g)	<i>m/z</i> 44 signal (mV)	CH <sub>4</sub> concentration (ppbv)	δ <sup>13</sup> CH <sub>4</sub> value (‰ VPDB)
				132.2	523	451	-44.62
	14.56	14.559	590	161.8	752	569	-46.06
				154.2	723	647	-47.51
	14.47	14.485	622	148.4	717	723	-46.73
				138.6	653	702	-45.61
				190.1	840	553	-47.04
	14.08	14.166	619	137.4	628	(750)	(-46.87)
				142.8	779	(841)	(-45.50)
	14.05	14.137	620	148.3	701	709	-46.88
				151.9	695	572	-46.00
	14.01	14.104	668	139.0	918	(794)	(-48.57)
				150.0	798	724	-45.98
2003	17.53	17.2	484	224.1	802	474	-42.71
				166.2	853	(698)	(-42.22)
	16.96	16.3	463	175.3	667	499	-43.35
	16.72	15.9	471	182.5	1531	(1126)	(-54.43)
				247.8	802	428	-43.11
	16.46	14.882	458	176.4	608	483	-45.23
	16.22	14.678	499	141.9	594	533	-46.19
				123.0	520	557	-45.49
				200.0	853	566	-44.78
	16.00	14.491	620	132.2	630	609	-46.64
				166.2	846	675	-45.59
Last Glacial Maximum							
2003	19.35	20.1	~400	188.2	627	510	-44.08
				178.4	512	378	-43.14
				185.7	553	394	-43.32

<sup>‡</sup>GISP2 methane concentration from contemporaneous air of Pákitsoq samples

\* Sample signal below shot noise threshold of 290 mV (0.97 nA)

§ Sample lost during analysis due to capillary breakage.

Table 7.3.3: Final results for Pákitsoq ice measurements of  $\delta^{13}\text{CH}_4$ .

Sampling Season	Trench Distance (m)	Calendar Age (ka BP)	Median measured $\delta^{13}\text{CH}_4$ (‰ VPDB)	$\delta^{15}\text{N}$ correction (‰)	Diffusion Correction (‰)	Corrected $\delta^{13}\text{CH}_4$ (‰ VPDB)	Standard uncertainty (‰)	IRMS [CH <sub>4</sub> ] (ppbV)
2003	5.03	10.996	-46.03	0.42	0.00	-46.44	0.15	865
2003	4.99	11.004	-45.32	0.42	0.00	-45.74	0.29	763
2003	4.58	11.091	-45.72	0.45	0.00	-46.17	0.92	838
2003	2.95	11.350	-45.25	0.52	0.00	-45.77	0.29	795
2003	2.65	11.430	-45.57	0.52	0.57	-45.52	0.23	870
2004	2.57	11.433	-46.40	0.54	0.60	-45.82	0.28	674
2004	2.52	11.447	-46.18	0.54	0.61	-46.12	0.42	675
2004	2.46	11.465	-46.22	0.53	0.68	-46.22	0.09	650
2004	2.40	11.475	-46.38	0.52	0.70	-46.20	0.62	648
2004	2.30	11.483	-46.25	0.53	0.74	-46.04	0.58	653
2004	2.21	11.527	-46.65	0.50	0.69	-46.46	0.40	537
2004	2.17	11.559	-46.99	0.46	0.41	-47.03	0.40	488
2004	2.12	11.572	-46.33	0.40	0.00	-46.73	0.28	497
2004	2.07	11.586	-45.85	0.38	0.00	-46.23	0.55	462
2003	1.44	11.752	-44.95	0.37	0.00	-45.32	0.29	529
2005	1.41	12.099	-45.27	0.37	0.00	-45.65	0.63	497
2005	1.36	12.139	-45.44	0.37	0.00	-45.81	0.66	442
2003	1.29	12.191	-45.26	0.35	0.00	-45.61	0.29	501
2005	1.21	12.254	-47.05	0.32	0.00	-47.37	0.02	557
2005	1.15	12.302	-47.01	0.30	0.00	-47.31	0.29	581
2003	1.14	12.310	-46.23	0.34	0.00	-46.56	0.53	560
2003	1.11	12.334	-47.26	0.33	0.00	-47.59	0.29	524
2005	1.09	12.350	-46.21	0.30	0.00	-46.51	0.74	477
2003	1.05	12.382	-47.40	0.33	0.00	-47.72	0.56	472
2005	1.03	12.398	-45.88	0.33	0.00	-46.21	0.45	560
2003	0.91	12.514	-45.88	0.37	0.00	-46.25	0.29	543
2003	0.69	12.838	-48.40	0.41	0.00	-48.80	0.22	718
2003	0.16	13.618	-47.83	0.38	0.00	-48.21	0.29	741
2005	14.01	14.104	-45.98	0.53	0.00	-46.51	0.29	724

(Continued on next page)

Sampling Season	Trench Distance (m)	Calendar Age (ka BP)	Median measured $\delta^{13}\text{CH}_4$ ( $\text{‰ VPDB}$ )	$\delta^{15}\text{N}$ correction ( $\text{‰}$ )	Diffusion Correction ( $\text{‰}$ )	Corrected $\delta^{13}\text{CH}_4$ ( $\text{‰ VPDB}$ )	Standard uncertainty ( $\text{‰}$ )	IRMS [ $\text{CH}_4$ ] (ppbV)
2005	14.05	14.137	-46.44	0.54	0.00	-46.99	0.62	641
2005	14.47	14.485	-46.73	0.60	0.00	-47.33	0.75	702
2003	16.00	14.550	-46.11	0.54	0.00	-46.66	0.75	642
2005	14.56	14.559	-46.79	0.56	0.52	-46.83	1.03	569
2003	16.22	14.750	-45.49	0.51	0.49	-45.52	0.70	557
2005	14.81	14.764	-45.87	0.49	0.39	-45.97	1.76	452
2005	14.98	14.900	-44.97	0.47	0.00	-45.43	0.29	454
2004	0.93	14.900	-46.06	0.48	0.00	-46.54	0.29	544
2003	16.46	14.950	-45.23	0.51	0.00	-45.70	0.29	483
2004	0.75	14.972	-45.37	0.45	0.00	-45.82	0.29	565
2004	0.66	15.000	-45.24	0.45	0.00	-45.70	0.29	487
2004	0.60	15.033	-46.27	0.46	0.00	-46.73	0.29	576
2004	0.54	15.055	-45.31	0.46	0.00	-45.77	0.29	477
2004	0.43	15.299	-44.49	0.46	0.00	-44.96	0.29	516
2004	0.33	15.581	-43.98	0.45	0.00	-44.43	0.29	388
2004	0.13	15.66	-43.97	0.46	0.00	-44.43	1.69	412
2003	16.72	15.9	-43.11	0.46	0.00	-43.57	0.29	428
2003	16.96	16.3	-43.35	0.46	0.00	-43.81	0.29	499
2003	17.53	17.2	-42.71	0.45	0.00	-43.17	0.29	474
2003	19.35	20.1	-43.32	0.43	0.00	-43.75	0.50	394